![U.S.NRC logo] **U.S.NRC**
United States Nuclear Regulatory Commission
Protecting People and the Environment

Nuclear Data Assessment for Advanced Reactors

Office of Nuclear Reactor Regulation

AVAILABILITY OF REFERENCE MATERIALS
IN NRC PUBLICATIONS

United States Nuclear Regulatory Commission

Protecting People and the Environment

Nuclear Data Assessment for Advanced Reactors

Prepared by:

F. Bostelmann
G. Ilas
C. Celik
A. M. Holcomb
W. A. Wieselquist

Oak Ridge National Laboratory
Oak Ridge, TN 37831-6283

Timothy Drzewiecki, NRC Project Manager

Office of Nuclear Reactor Regulation

ABSTRACT

Advanced reactor concepts being developed throughout the industry are significantly different from light-water reactor (LWR) designs with respect to geometry, materials, and operating conditions, and consequently, with respect to their reactor physics behavior. Given the limited operating experience with non-LWRs, the accurate simulation of reactor physics and the quantification of associated uncertainties are important for ensuring that the nuclear design for advanced reactor concepts include appropriate margins. Nuclear data are a major source of input uncertainties in reactor physics analysis. As part of a project sponsored by the US Nuclear Regulatory Commission at Oak Ridge National Laboratory (ORNL), key nuclear data relevant to reactor safety analysis in selected advanced reactor technologies[1] were identified, and their impacts on important key figures of merit were assessed based on (1) a review of available advanced reactor specifications, (2) analysis of previous studies performed at ORNL and other research institutions, and (3) sensitivity and uncertainty analyses performed for six selected benchmarks—three experimental and three computational—to quantify the impacts of the identified key nuclear data on several key metrics.

This report summarizes the key nuclear data—nominal data and nuclear data uncertainties—considering the most important nuclear reactions in the fuel and in various materials for the moderator, coolant, and structure of the considered advanced reactors.

The major nominal missing data that were identified consist of thermal scattering data and ^{135m}Xe cross section data for molten salt reactor (MSR) analysis. The identified major gaps with respect to nuclear data uncertainties are (1) the missing uncertainties in the thermal scattering data for high-temperature gas-cooled reactors and moderated MSR systems, and (2) the incomplete uncertainties on angular distributions, particularly for fast spectrum systems such as sodium-cooled fast reactors, fast molten salt reactors, and heat pipe reactors.

Large uncertainties of reactions that are not commonly considered to be relevant in LWR studies were found to be significant for several advanced reactor systems. The large uncertainty of ^{238}U inelastic scattering in the fast energy range contributes significantly to large output uncertainties in all fast spectrum systems. The large uncertainty of ^{235}U (n,γ) in the fast energy range causes significant reactivity uncertainties in fast neutron spectrum systems that use ^{235}U-enriched fuel. A large uncertainty of ^{7}Li (n,γ) causes a large fraction of uncertainty in the output quantities investigated for MSR systems in which lithium is part of the salt.

Special attention should be paid to differences in cross section and uncertainties of different evaluated nuclear data library releases. Significant differences were found in nuclear data that can lead to major differences in reactivity calculations, even for well-known nuclides. In particular, differences in ^{235}U, ^{238}U, and ^{239}Pu nominal and uncertainty data between the Evaluated Nuclear Data File (ENDF)/B-VII.1 and ENDF/B-VIII.0 nuclear data releases are the major causes of differences in calculations when using these libraries.

For MSR systems containing a large amount of FLiBe salt, the update from the ENDF/B-VII.0 to the ENDF/B-VII.1 release of the tritium production cross section for ^{6}Li is significant. Similarly, the update of the ^{12}C capture cross section from ENDF/B-VII-0 to ENDF/B-VII.1 can have a significant impact on reactivity calculations of graphite-moderated systems, and the update of

---

[1] Selected advanced reactor technologies: graphite moderated high temperature gas-cooled reactor, fluoride salt-cooled high temperature reactor, graphite-moderated molten salt reactor, molten chloride fast spectrum reactor, fast-spectrum heat pipe reactor, sodium-cooled fast reactor

the ^{35}Cl (n,p) cross section between these libraries have an impact on fast spectrum molten chloride MSRs.

Given the limited amount of experimental measurement data, no conclusion regarding the better performance of either investigated ENDF/B library is drawn. The presented sensitivity analyses inform about nuclear data for which a change could cause a significant change in the calculated metric of interest. The uncertainty analyses, in particular the ranking of contribution to the output uncertainties, can be used to guide future measurement and evaluation efforts to reduce the significant nuclear data uncertainties and thereby significantly reduce the overall observed uncertainties of key figures of merit.

TABLE OF CONTENTS

LIST OF FIGURES

x

LIST OF TABLES

ABBREVIATIONS AND ACRONYMS

2D	two-dimensional
3D	three-dimensional
ABR	Advanced Burner Reactor
ABTR	Advanced Breeder Test Reactor
BOEC	beginning-of-equilibrium-cycle
CD	control drum
CE	continuous-energy
C/E	calculated vs. experimental
CLUTCH	contribution-linked eigenvalue sensitivity/uncertainty estimation via track length importance characterization
CR	control rod
CSEWG	Cross Section Evaluation Working Group
DOE	US Department of Energy
EBC	equivalent boron concentration
EBR	experimental breeder reactor
EFR	European Fast Reactor
ENDF/B	Evaluated Nuclear Data File B
EOEC	end-of-equilibrium-cycle
FHR	fluoride salt-cooled high-temperature reactor
GFR	Gas-cooled fast reactor
GWd	gigawatt day
HPR	heat pipe reactor
HTGR	high-temperature gas-cooled reactor
ICSBEP	International Criticality Safety Benchmark Evaluation Project
IFP	iterated fission probability
INL	Idaho National Laboratory
IRPhEP	International Reactor Physics Experiment Evaluation Project
JEFF	Joint Evaluated Fission and Fusion File
JENDL	Japanese Evaluated Nuclear Data Library
LANL	Los Alamos National Laboratory
LFR	Lead-cooled fast reactor
LWR	light-water reactor
MG	multigroup
MOX	mixed-oxide
MSR	molten salt reactor
MSRE	Molten Salt Reactor Experiment
MTIHM	metric tons of initial heavy metal
MW	megawatt
MWth	megawatt thermal

NEA	Nuclear Energy Agency
NRC	US Nuclear Regulatory Commission
OECD	Organisation for Economic Co-operation and Development
ORNL	Oak Ridge National Laboratory
PB	pebble bed
PWR	Pressurized water reactor
PyC	pyrolitic carbon
QOI	quantity of interest
SiC	silicon carbide
SFR	sodium-cooled fast reactor
SFR-FT	Sodium Fast Reactor Core Feedback and Transient
TENDL	TALYS-Based Nuclear Data Library
TRISO	tristructural isotropic
UAM-SFR	Uncertainty Analysis in Modeling for Design, Operation and Safety Analysis of SFRs
UCB	University of California, Berkeley
VHTR	Very-high temperature gas rector
VHTRC	Very-high temperature reactor critical experiment

ACKNOWLEDGMENTS

1   INTRODUCTION

Uncertainty analyses are an essential component in the design and analysis of advanced reactors, especially due to the growing interest in new reactor concepts for which scant operational data are available. The advanced reactor concepts currently being developed throughout the industry are significantly different from light-water reactor (LWR) designs with respect to geometry, materials, and operating conditions, and consequently, with respect to their reactor physics behavior. Given the limited operating experience with non-LWRs, the accurate simulation of reactor physics and the quantification of associated uncertainties are critical for ensuring that advanced reactor concepts operate within the appropriate safety margins.

Nuclear data are a major source of input uncertainties in reactor physics analyses. They provide the basis for every reactor physics calculation. The nuclear interaction cross sections, fission yields, and decay data used in these calculations have uncertainty resulting from measurements and subsequent data evaluations. Nuclear data used with reactor physics codes result from extensive data evaluations, including validation studies performed with criticality experiments. The most common evaluated nuclear data libraries are the European Joint Evaluated Fission and Fusion File (JEFF) (Sublet et al., 2003), the Japanese Evaluated Nuclear Data Library (JENDL) (Shibata et al., 2012) files, and the US Evaluated Nuclear Data File / B (ENDF/B) (Chadwick et al., 2006; Chadwick et al., 2011; Brown et al., 2018). These libraries are undergoing continuous modifications based on additional measurements or improved evaluations, and new revisions are being released on a regular basis. Figure 1-1 illustrates how cross section data for one nuclide and reaction (inelastic scattering in ^{23}Na) can differ significantly across different nuclear data libraries, including JENDL-4.0, JEFF-3.3, and ENDF/B-VII.1. Moreover, when comparing the data from these libraries with measurements from the EXFOR database (Otuka et al., 2014), significant disagreement can be observed between the individual measurements and between measurements and evaluations.
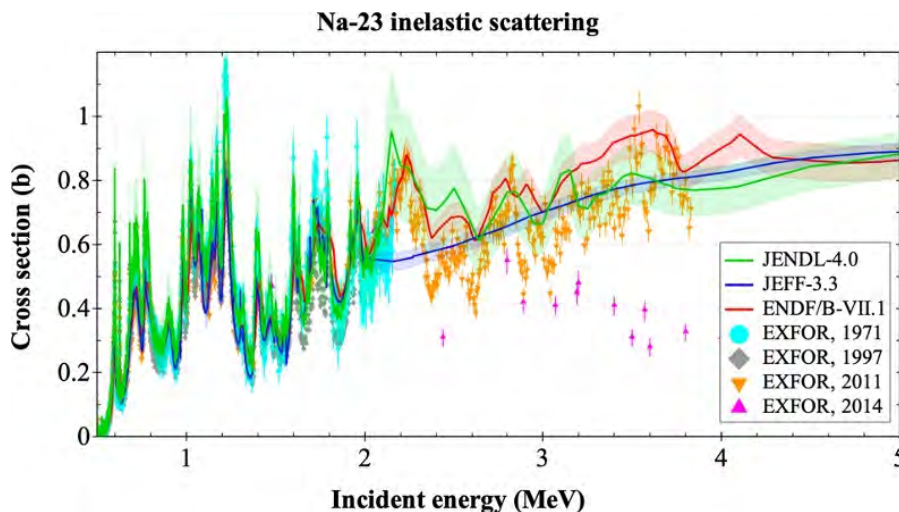
Figure 1-1 Measured and Evaluated ^{23}Na Inelastic Scattering Cross Section[1]

---

[1] The bands represent the 1σ uncertainties as given in the evaluated nuclear data libraries.

To express the uncertainty in the nominal cross section values, the evaluated nuclear data files contain information about the associated nuclear data uncertainties in the form of covariance matrices. As an example, the energy-dependent covariance matrix in 56 neutron energy groups—an energy group structure optimized for thermal spectrum systems as used in the SCALE code system (Wieselquist et al., 2020)—for ^{23}Na inelastic scattering based on ENDF/B-VII.1 data, is illustrated in Figure 1-2. The diagonal elements describe the variance of the cross sections in the individual energy groups. The square root of the variance is the standard deviation that is the uncertainty of the cross section. The values in the ith row and j^{th} columns are the covariances between the scattering cross section in the ith and j^{th} energy group. The covariance is a measure of the joint variability of two cross sections. In addition to covariance matrices of individual reactions, the libraries include covariance with correlations between different reactions within a nuclide (e.g., between elastic scattering and neutron capture of ^{238}U) and correlations between reactions of different nuclides (e.g., between fission of ^{235}U and neutron capture of ^{238}U). Figure 1-3 shows the uncertainty of ^{23}Na inelastic scattering corresponding to the covariance matrix in Figure 1-2. Data from the latest three ENDF/B releases are displayed, as well as the corresponding nominal data.
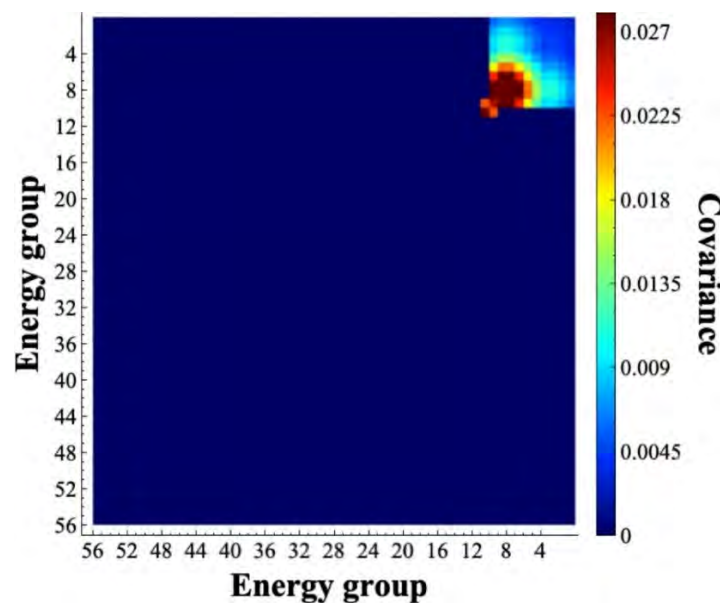
Figure 1-2 ^{23}Na Inelastic Scattering 56-Group Covariance Matrix Based on ENDF/B-VII.1
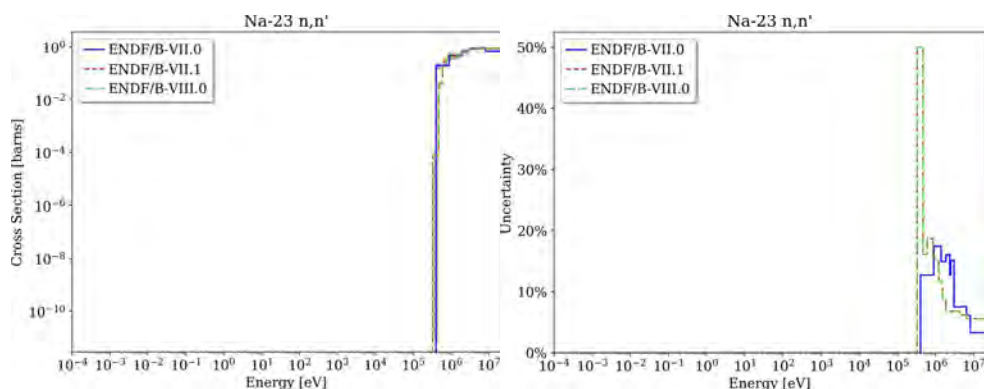
Figure 1-3 ^{23}Na Inelastic Scattering Nominal Data and Uncertainty from the Three Latest ENDF/B Releases

To improve understanding of uncertainties that result from nuclear data in the calculation of safety-relevant output quantities and to determine where additional efforts should focus to reduce relevant nuclear data uncertainties, these data need to be propagated to key figures of merit that impact nuclear safety. This is a challenging task because uncertainty information is not available for all nuclear data used in reactor physics analysis. To ensure a thorough analysis the missing data must be identified and the potential impact of missing nominal data, as well as the missing uncertainty information, must be assessed.

As part of the project entitled "Nuclear Data Assessment for Advanced Reactors," which was funded by the US Nuclear Regulatory Commission (NRC), the impact of nuclear data uncertainties on key figures of merit associated with advanced reactor safety was assessed for selected advanced non-LWR technologies.

Based on current interest and relevant activities seen throughout the industry, several advanced reactor technologies were selected for consideration in this project: high-temperature gas-cooled reactor (HTGR), molten salt reactor (MSR), fluoride salt-cooled high-temperature reactor (FHR), heat pipe reactor (HPR), and sodium-cooled fast reactor (SFR). Table 1 provides an overview of the selected technologies, along with the corresponding fuel types, moderators, and coolants.

The project included four phases:

- Phase 1: Identify key nuclear data impacting reactivity in non-LWRs,

- Phase 2: Assess key nuclear data impacting reactivity in non-LWRs,

- Phase 3: Identify relevant benchmarks applicable to the nuclear data identified in Phases 1 and 2, and

- Phase 4: Assess the impact of nuclear data uncertainty through propagation to key figures of merit associated with reactor safety for the relevant benchmarks selected in Phase 3.

Under Phase 1, key nuclear data that impact key figures of merit were identified for each selected advanced reactor technology presented in Table 1-1. For Phase 2, the impact of the

identified key nuclear data, including their corresponding uncertainties on the key figures of merit, was assessed.

Table 1-1   Overview of Selected Advanced Reactor Technologies

Reactor type	Reactor technology	Fuel	Moderator	Coolant
Thermal spectrum, HTGR	Pebble-bed HTGR	UCO or UO_2	Graphite	Helium
Thermal spectrum, MSR	FHR	UCO or UO_2 graphite	FLiBe	
Thermal spectrum MSR	Graphite-moderated MSR	$LiF\text{-}BeF_2\text{-}UF_4$	Graphite	Fuel serves as coolant
Fast spectrum MSR	Molten chloride fast spectrum reactor	$PuCl_3\text{-}NaCl$, $UCl_3\text{-}NaCl$	–	Fuel serves as coolant
Fast spectrum, oxide and metal fueled, stationary microreactor	HPR	UO_2, UN, or U-10Zr	–	Potassium, sodium
Fast spectrum, metal and oxide fueled, sodium-cooled reactor	SFR	U/TRU-Zr or U/TRU oxide	–	Sodium

Phases 1 and 2 included the following steps:

1. Explored publicly available literature and identified descriptions of representative geometrical and material definitions relevant to reactor physics analysis of the selected advanced reactor technologies.

2. Interrogated modern evaluated nuclear data libraries to identify important updates in nominal values and uncertainties of relevant nuclear data.

3. Reviewed results from previous studies performed by Oak Ridge National Laboratory (ORNL) and other research institutions with respect to the impact of nuclear data on the key figures of merit associated with advanced reactor safety.

4. Based on the literature review and previous studies, identified key nuclides and nuclear data impacting reactivity during operation—considering both fresh and irradiated fuel—and assessed their impacts on the selected advanced reactor technologies.

In Phase 3, available benchmark resources were identified for each relevant advanced reactor technology and were reviewed to select benchmarks for consideration in Phase 4. Because publicly accessible measurement data were limited, benchmarks based on reported experiments were considered, as well as computational benchmarks. The following steps were included in Phase 3:

1. Investigated various Organisation for Economic Co-operation and Development (OECD)/Nuclear Energy Agency (NEA) databases to identify applicable benchmarks, and searched for additional publicly available sources of applicable measurements.

2. Identified theoretical or simplified computational models from publicly available reports that are representative of the reactor technologies of interest.

3. Assessed the benchmarks with respect to the reported measurements of quantities of interest (QOIs), their applicability to the reactor technology of interest, and the corresponding modeling and computation efforts.

4. Selected the benchmarks for each reactor technology of interest, including the QOIs to be investigated for each case.

In Phase 4, the impact of uncertainties in nuclear data was assessed for the benchmarks selected in Phase 3. This was accomplished by calculating the selected QOIs using various nuclear data libraries and then propagating nuclear data uncertainties to these QOI. All calculations within this project were performed using methods, tools, and libraries from the SCALE code system (Wieselquist et al., 2020). The following steps were included in Phase 4:

1. Collected and adapted for use in the current study existing SCALE models that were generated under previous ORNL modeling efforts.

2. Developed new SCALE models for the benchmarks for which no SCALE model existed.

3. Performed neutron transport calculations with the SCALE models to confirm agreement with existing benchmark results or other published results.

4. Selected QOI for each of the considered benchmarks, based on availability of measurements and key figures of merit associated with reactor safety, and the estimated modeling and computational effort.

5. Identified relevant nuclear data for the selected QOI through calculations with different nuclear data library releases and through nuclear data sensitivity analyses.

6. Quantified the QOI's uncertainties due to nuclear data uncertainties and identified the top contributing nuclear data to the observed uncertainties.

The main QOIs selected for performing in-depth uncertainty analysis in Phase 4 for the considered advanced reactor technologies include the following: (1) core reactivity, (2) control rod (CR) worth, (3) temperature and expansion coefficients, and (4) power distribution, including axial or radial peak power. The QOI's level of importance to reactor safety can differ between various advanced reactor concepts. While all these quantities were considered during the literature research in Phases 1 and 2 and the selection of benchmarks in Phase 3, the availability of measured quantities for comparison with calculated results was found to be very limited for the advanced reactor technologies of interest. Therefore, only a few comparisons with measurement data from evaluated benchmarks were possible for the calculated QOIs. Other assessments were based on theoretical benchmark models, and representative perturbations of compositions or the geometry were applied to these models to calculate reactivity effects.

This report summarizes the findings of all four phases. First, Section 2.1 describes the different advanced reactor technologies considered in this study and provides details on their main characteristics. The outcome of the literature research to identify relevant benchmarks is summarized in Section 2.2. The approach followed for the nuclear data performance assessment is presented in Section 3, and the selected benchmarks are described in Section 4.

Section 5 presents the results of the nuclear data assessments. The conclusions in Section 6 provide a brief overview of the relevant findings for each selected advanced reactor technology.

2   BACKGROUND

2.1   Relevant Advanced Reactor Technologies

Based on current interest and relevant activities throughout the industry, several advanced reactor technologies were selected for consideration in this study as listed in Table 1. The following section briefly describes the main characteristics of the selected reactor technologies with respect to the materials used, geometry, and temperatures.

2.1.1   Pebble-Bed High-Temperature Gas-Cooled Reactor

An HTGR is a graphite-moderated, helium-cooled reactor with a thermal neutron spectrum. An HTGR pebble-bed reactor operates at several hundred megawatts (MW) of power. Its core contains hundreds of thousands of fuel pebbles and moderator (graphite) pebbles (Figure 2-1). The fuel pebbles are moving towards the core and are replaced with fresh fuel pebbles once they reach their final discharge burnup. Therefore, the core consists of a mixture of fuel pebbles at different burnups. The core is surrounded by graphite reflector structures (DOE, 2002; Zhang et al., 2006; Ilas et al., 2012; IAEA, 2013; NEA, 2015). A fuel pebble consists of a fuel zone that is ~5 cm in diameter, with many thousands of tristructural isotropic (TRISO) fuel particles distributed randomly in a graphite matrix, surrounded by a 5 mm graphite layer, resulting in a pebble with an outer diameter of 6 cm. A representative TRISO fuel particle is roughly 1 mm in diameter and consists of a microsphere fuel kernel composed of uranium in oxycarbide form. The fuel kernel is enclosed by concentric coatings that may include porous graphite buffers, pyrolytic carbon (PyC) layers, or ceramic silicon carbide (SiC) layers, for example. The fuel enrichment ranges up to 19.75 wt% ^{235}U, depending on the reactor design. High inlet and outlet temperatures of the helium coolant (e.g., 640 and 1,000°C, respectively) result in high fuel temperatures of up to 1,200°C under normal operating conditions (DOE, 2002). Reactivity control is achieved with absorber rods containing boron in the outer reflector. Burnups beyond 150 gigawatt days (GWd) / metric tons of initial heavy metal (MTIHM) are targeted (Mulder and Boyes, 2020).
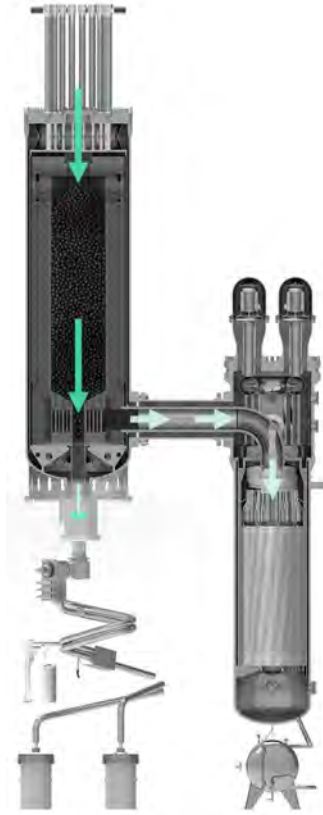
Figure 2-1 X-energy's 165 MWth Xe-100 Reactor Design (X-energy, 2021, Used with Permission)

2.1.2   Fluoride Salt-Cooled High-Temperature Reactor

An FHR combines the HTGR fuel form with liquid fluoride salt coolant in a graphite-moderated environment (Cisneros, 2013). A pebble-bed FHR has an annular core filled with a large number of graphite moderator and fuel pebbles (Figure 2-2). As for the pebble-bed HTGR, the core contains a mixture of fuel pebbles at different burnups. The annular core is contained in graphite reflector structures. Like an HTGR, the fuel pebbles contain thousands of TRISO particles distributed in a graphite matrix. However, the pebbles in an FHR are significantly smaller at $\sim$3 cm diameter, and the fuel particles within the pebble are tightly packed in a spherical shell that is 1.5 mm thick. The fuel material is either UCO or UO_2 that is enriched up to 19.9 wt% ^{235}U. The coolant salt is FLiBe, which is a mixture of Li_2F and BeF. Core inlet and outlet temperatures are approximately 600 and 700°C, respectively, and a common fuel temperature range is between 700 and 800°C. Burnups reaching up to 180 GWd/MTIHM are intended. Reactivity control is achieved using CRs and blades containing boron carbide (Cisneros, 2013; Andreades et al., 2014; Qualls et al., 2017; Latta et al., 2019).
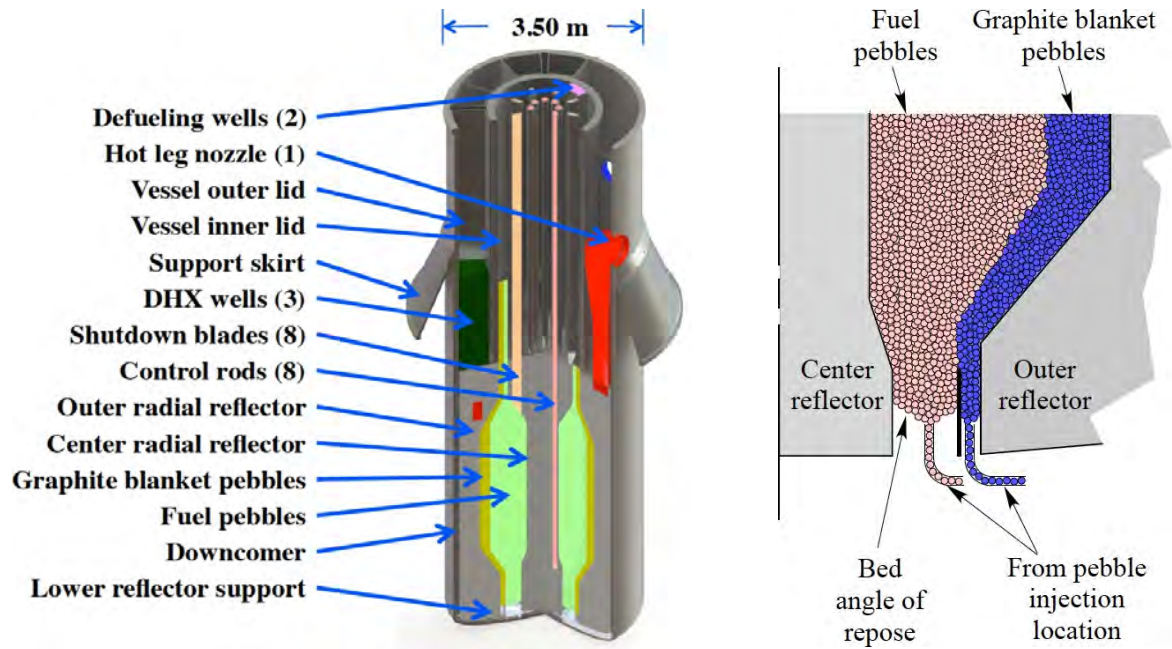
Figure 2-2 Mark-1 Pebble-Bed FHR Reactor (Andreades et al., 2014)

2.1.3 Molten Salt Reactor

Several different MSR systems currently being pursued by industry vary widely with respect to the fuel salt and/or moderator. MSRs have a variety of spectral conditions that can change further during fuel depletion. The FHR concept presented in Section 2.1.2 is also addressed in the literature as a molten salt system that uses solid fuel and molten salt as coolant. Two selected representative concepts in which the salt contains the fuel itself are briefly described in the following subsections.

2.1.3.1 Graphite-Moderated MSR

A graphite-moderated MSR core consists of a graphite structure within a cylindrical reactor vessel. The fuel salt is pumped through the graphite and flows through the plena below and above the graphite structure (Figure 2-3). The salt is either a mixture of LiF-BeF_2-UF_4 or a mixture of NaF-RbF-UF_4 that serves the dual purpose of carrying the low-enriched fuel (less than 5 wt% ^{235}U) and cooling the core. Common fuel salt inlet and outlet temperatures are ~560 and 700°C, respectively (Choe et al., 2018; Shen et al., 2019).
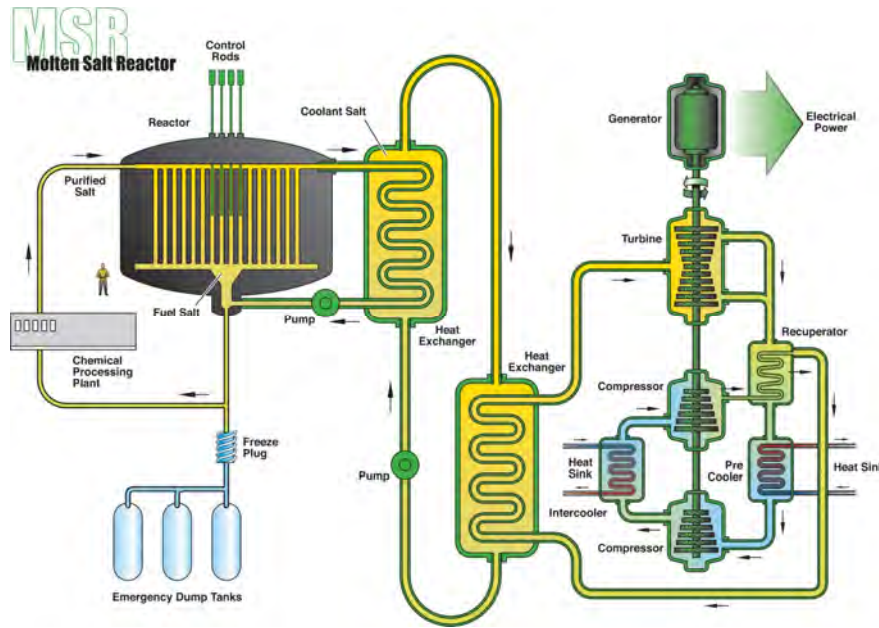
Figure 2-3 Molten Salt Reactor Concept (DOE, 2002)

2.1.3.2   Molten chloride fast spectrum reactor

A molten chloride fast spectrum reactor uses NaCl as the carrier salt in UCl_3-NaCl and $PuCl_3$-NaCl fuel salts, for example. The fuel salt is located at the center of the cylindrical reactor and circulates within the core region. In axial and radial directions, the core is surrounded by neutron reflectors made of materials such as steel or magnesium oxide. Molten chloride fast reactors with powers between 700 and 3,700 MW and salt temperatures between 750 and 1,000 K were proposed in previous work (Holcomb et al., 2011; Betzler et al., 2017b; Cisneros 2021; Mausolff et al., 2021). An example molten chloride reactor is shown in Figure 2-4.

2.1.4 Heat Pipe Reactor

HPRs are small reactor systems, typically with thermal power of less than 100 MW. These reactors mainly consist of a reactor core with a reflector, shielding, and a heat removal system. Different HPR concepts are currently under development. Most of these systems use 19.75 wt% ^{235}U enriched UO_2, UN, or U-10Zr fuel with heat pipes that use potassium (K), sodium (Na), or NaK as the working fluid. Reflector materials placed above the fuel and radially surrounding the core include BeO, steel, and/or Al_2O_3. Reactivity control is performed using boron-containing control drums (CDs) and/or boron-containing CRs. Depending on the design, the temperature of the coolant in the heat pipes is in the range of 620–730°C, and the fuel temperature is only slightly higher than that of the coolant and under 800°C (Sterbentz et al., 2018; Maioli et al., 2019; Matthews et al., 2019; Clark et al., 2020; Yan et al., 2020). An example HPR is shown in Figure 2-5.

2.1.5 Sodium-Cooled Fast Reactor

The core of an SFR (Figure 2-6) consists of a grid of hexagonal assemblies. The fuel assemblies at the center of the core consist of fuel pins with an inner fuel zone surrounded by cladding. The fuel pins are arranged in a tight hexagonal lattice surrounded by a metal wrapper

or duct. The active height is usually on the order of a few tens of cm, whereas the radius of the core can be on the order of meters (NEA, 2016; Lum et al., 2018). The fuel in an SFR can be mixed-oxide (MOX) fuel or a mixed uranium-transuranic-zirconium (U-TRU-Zr) metal alloy. Axial reflectors and gas plena are located above and below the fuel region. The structural materials, including the cladding and the wrapper, are made of iron-based alloys containing nickel, chromium, manganese, and/or molybdenum. Sodium is used as the coolant (CSEWG, 2018). A core can have multiple fuel zones with different fuel compositions. The fuel zone in the core is surrounded by hexagonal reflector assemblies, and an absorbing shield may also be included. Reactivity control is maintained by moving control and safety assemblies into locations not occupied by fuel assemblies. The typical inlet and outlet temperatures of a metal core are 350 and 510°C, respectively, and for an oxide core, they are ~400 and 550°C, respectively. The metal fuel temperature is ~530°C, and the oxide fuel temperature is ~1,200°C. Burnups in the range of 150–200 GWd/MTHM have been experimentally demonstrated (DOE, 2002).
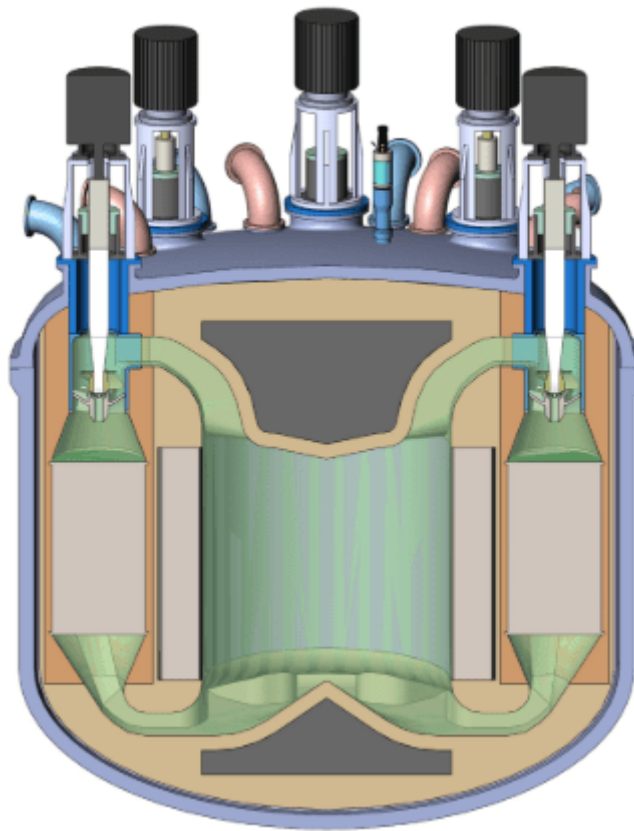
Figure 2-4 Molten Salt Fast Reactor Configuration (Terrapower, 2021)
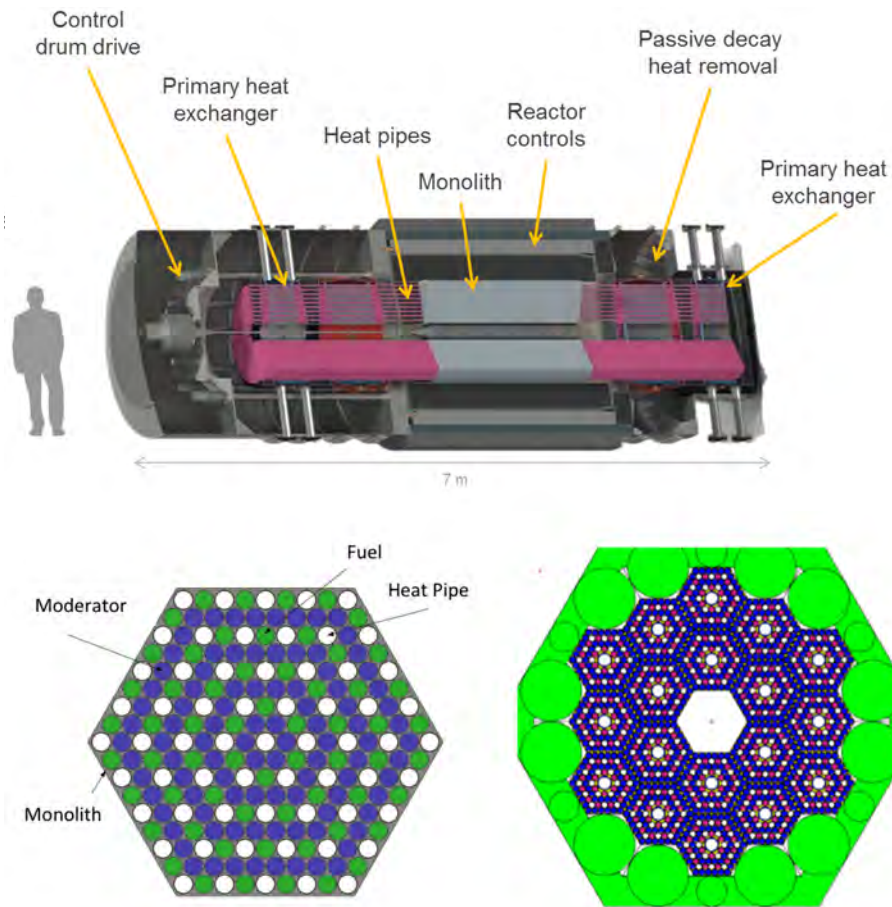
Figure 2-5 EMPIRE Heat Pipe Reactor Assembly (Left) and Core Design (Matthews et al., 2019)
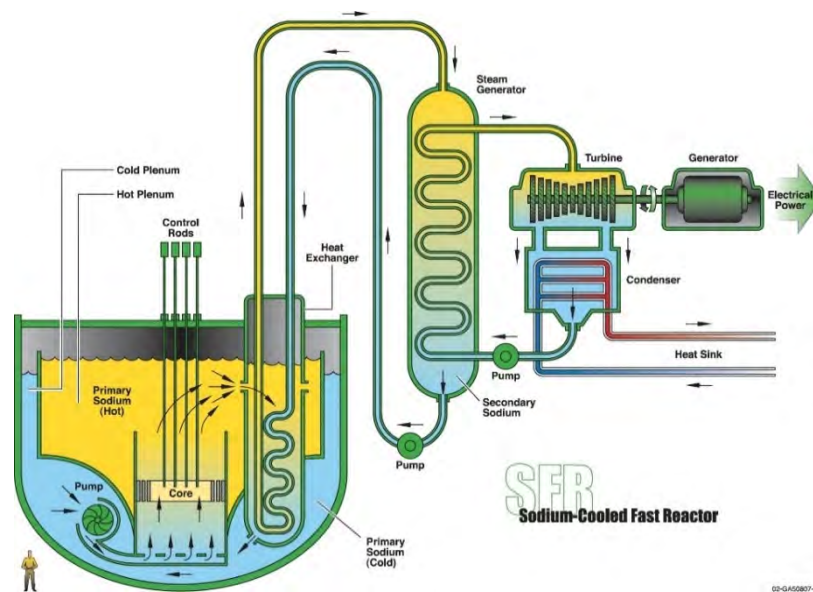
Figure 2-6 Sodium-Cooled Fast Reactor Concept (DOE, 2002)

2.2   **Literature Review**

Studies on nuclear data have been performed through NEA for the advanced breeder test reactor (ABTR), SFR, European fast reactor (EFR), gas-cooled fast reactor (GFR), lead-cooled fast reactor (LFR), accelerator-driven minor actinide burner (ADMAB), very-high temperature gas rector (VHTR), and pressurized water reactor (PWR) with extended burnup (Salvatores and Jacqmin, 2008). These studies determined that, for the designs evaluated, the uncertainty in the reactivity balance was less than 2% (except for the accelerator-driven systems), reactivity coefficient uncertainties were less than 20%, and power distribution uncertainties were also relatively small except for the accelerator driven systems. The work in this report extends the work done at NEA by investigating different reactor technologies and evaluating specific QOIs through benchmark assessments.

Identification of key nuclear data relevant for simulation of the selected reactor technologies and the assessment of their impact on important QOIs was based on a review of publicly available resources and interrogation of the available evaluated nuclear data libraries to reveal important updates in nominal values and associated uncertainties in the key nuclear data. Key nominal data and uncertainties are summarized in this section. Details on the methods used for sensitivity and uncertainty analyses are described in Section 3.

2.2.1   Key Nominal Data

This section summarizes key nominal nuclear data (i.e., mean values of cross sections, decay data, and fission yields without their uncertainties) that are impactful for advanced reactor physics analysis. This summary includes insights from various advanced reactor studies, applicable conclusions from existing LWR studies, and important observations from evaluated nuclear data library comparisons. This summary also identifies relevant data that are not currently available for use in advanced reactor physics analysis. This section is structured according to the considered advanced reactor concept; relevant conclusions are repeated if applicable. The most recent ENDF/B-VIII.0 release indicates major differences compared to the previous ENDF/B-VII.1 release for some nuclide reactions relevant to the investigated advanced reactor concepts.

2.2.1.1   *Pebble-bed high-temperature gas-cooled reactor*

For graphite-moderated systems such as pebble-bed HTGRs, the capture cross section of carbon changed significantly between ENDF/B-VII.0 and VII.1 (Figure 2-7). Due to the abundance of graphite in the fuel material and the reflector in this reactor concept, a change in a cross section of carbon is highly relevant. Depending on the size of the simulated reactor model, an impact of more than 1,000 pcm on the multiplication factor can be observed. For example, for a small 30MWth HTGR experiment, the ENDF/B-VII.1 calculations show good agreement with measurements (Bostelmann et al., 2020; Fujimoto et al., 2021), whereas ENDF/B-VII.0 calculations show a significant overestimation of 1,300 pcm (Bostelmann et al., 2020).
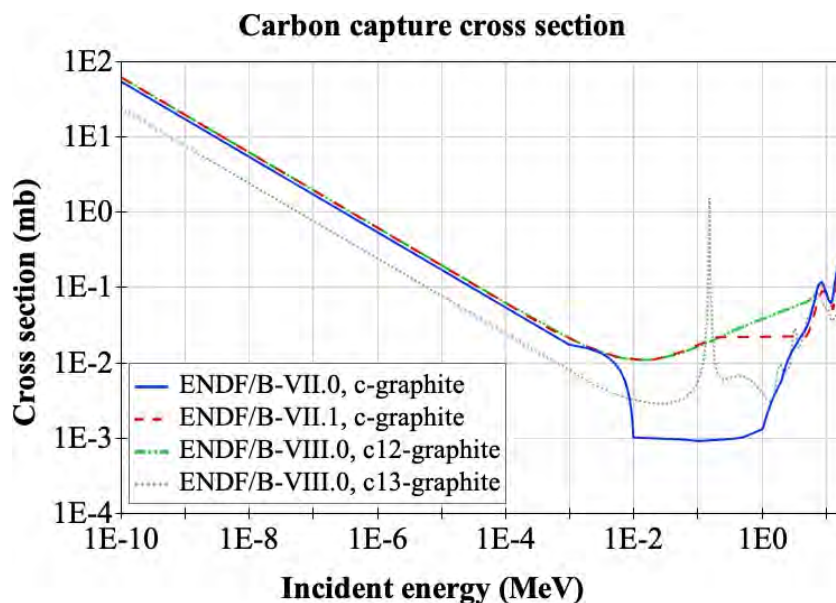
Figure 2-7 Comparison of Carbon Capture Cross Section in ENDF/B Releases[1]

Prior to and including the ENDF/B-VII.1 release, available graphite evaluations considered graphite as a perfect crystal with respect to its thermal scattering cross sections. However, with the release of the ENDF/B-VIII.0 library, data for nuclear-grade graphite became available. In addition to an evaluation for graphite as a perfect crystal (i.e., 0% porosity), graphite evaluations assuming 10 and 30% porosity were made available (Hawari and Gillete, 2014). Because of the amount of graphite in graphite-moderated systems and the importance of graphite as moderator, the availability of additional data is highly relevant to neutron moderation and therefore to reactivity. When changing the porosity of graphite in the fuel and dummy pebbles in criticality calculations of the HTR-10 benchmark (Terry et al., 2007), an increase of several hundred pcm in the multiplication factor was observed at room temperature. In contrast, when changing the porosity only in the surrounding graphite reflector, the multiplication factor did not change (Bostelmann et al., 2018) for the same HTR-10 benchmark. A similar study for the HTR-PM reactor arrived at similar conclusions (Zhang et al., 2020). For adequate consideration of the porosity, detailed information about the graphite porosity and the temperatures in the included materials is needed because (1) the impact at higher temperatures can be different than at lower temperatures, (2) the graphite porosity is a function of the neutron fluence (Campbell et al., 2016), and (3) the graphite porosity is not always known for each graphite component of the reactor.

For the first time in the ENDF/B evolution, the ENDF/B-VIII.0 library contains thermal scattering data for SiC. These data could be relevant for the analysis of systems fueled with TRISOs that contain a SiC layer. For graphite-rich reactor configurations, special attention must be focused on the impurities in the graphite—particularly the neutron capture in these impurities. Although the impurities usually include several nuclides Takahashi et al., 1999), graphite impurities are often provided as an equivalent boron concentration (EBC) quantifying their aggregate effect instead of specifying the individual nuclide concentrations of several impurities. Therefore, the

---

[1] ENDF/B-VII.0 and ENDF/B-VII.1 contain natural carbon data, whereas ENDF/B-VIII.0 contains isotopic data for ^{12}C and ^{13}C. The natural abundances are 12C ~98.9% and 13C ~1.1%

nuclear data for boron become more relevant when these systems are simulated. For example, a 2% change in EBC of 4.866 ppm—which corresponds to a change of 2% in the total boron cross section— in the reflector graphite leads to a 100 pcm change in the multiplication factor for the HTR-10 benchmark (Terry et al., 2007). Accurate estimations of the EBC and the boron absorption cross section are relevant for HTGR analysis.

Additional relevant nuclide reactions that are important to the reactivity of HTGRs were identified based on a review of publications on uncertainty analysis using sensitivity coefficients. In addition to the analysis of the nuclides available in the various materials in a reactor's design, some of these studies describe the importance of the nuclides' individual reactions. For the fuel material, the neutron multiplicity, fission, capture and scattering of uranium nuclides were found important for fresh fuel. Furthermore, the nuclear data of plutonium nuclides were deemed important for depleted fuel. In terms of the structural materials, the capture and scattering reactions in graphite and absorption in boron, as previously mentioned, were also found to be significant (Rochman et al., 2017; Bostelmann and Strydom, 2017; Bostelmann et al., 2019a; Cheng et al., 2020a).

In a previous ORNL study, significant differences of a few hundred pcm in multiplication factors for advanced reactor models were noted when comparing results obtained with ENDF/B-VII.1 data to results obtained with ENDF/B-VIII.0 (Bostelmann et al., 2020). By starting with an ENDF/B-VII.1 calculation and replacing the nuclear data of individual nuclides with data from ENDF/B-VIII.0 one nuclide at a time, updates in the cross sections of ^{235}U and ^{238}U (Figure 2-8 through Figure 2-10) were found to be responsible for most of the observed differences in multiplication factors (Bostelmann et al., 2019b). Even though these are among the most common nuclides in traditional reactor fuel, and their nuclear data are therefore assumed to be very well known, significant changes in the capture, fission, and scattering cross sections were introduced in the latest ENDF/B-VIII.0 release when compared to ENDF/B-VII.1.

HTGR concepts are intended to achieve burnups that are significantly higher than those in traditional LWRs. The importance of the nuclear data for higher actinides, in addition to that for uranium and plutonium, is potentially amplified. However, the available benchmarks involving neutron interaction reactions of minor actinides—particularly capture, fission, and inelastic scattering reactions—are scarce in the literature (Bernstein et al., 2019; Salvatores, 2002).
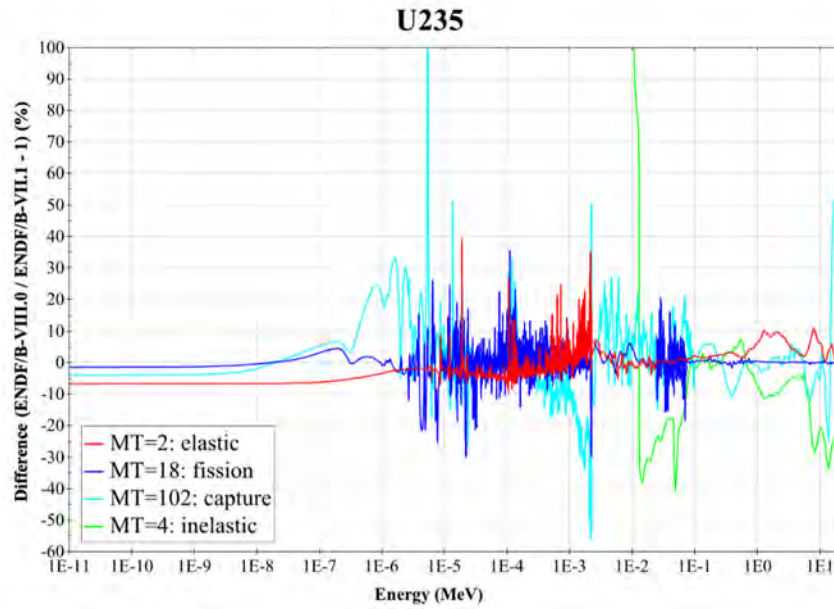
Figure 2-8 Relative Differences Between ENDF/B-VII.1 and ENDF/B-VIII.0 for ^{235}U Cross Sections
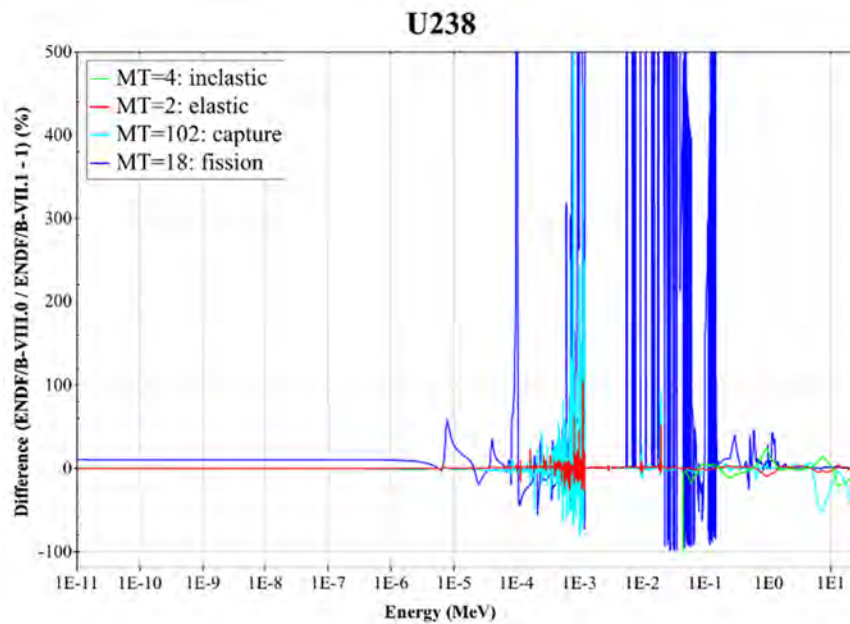
Figure 2-9 Relative Differences between ENDF/B-VII.1 and ENDF/B-VIII.0 for ^{238}U Cross Sections
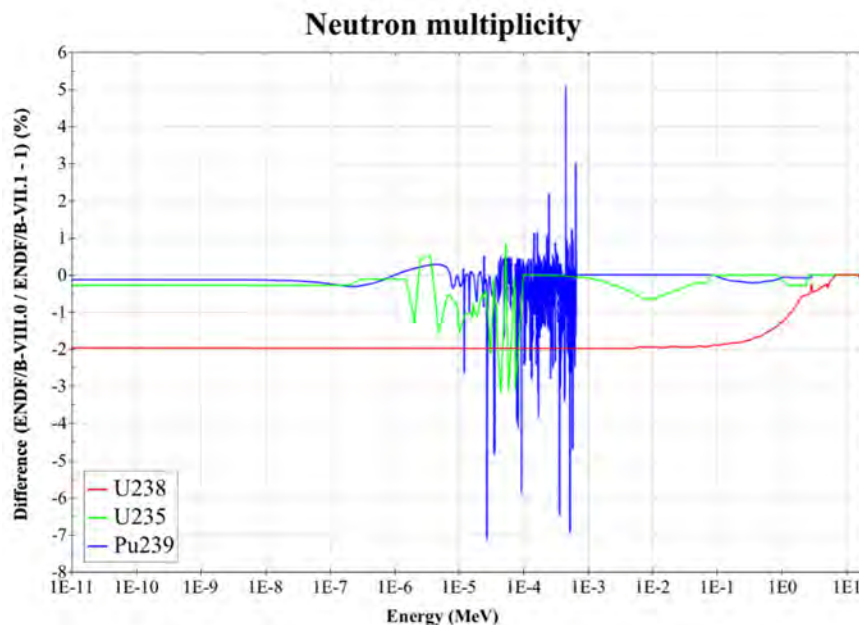
Figure 2-10 Relative Differences of the ^{235}U, ^{238}U, and ^{239}Pu Neutron Multiplicities $\bar{\nu}$ between ENDF/B-VIII.0 and ENDF/B-VII.1

2.2.1.2 *Fluoride salt-cooled high-temperature reactor*

FHRs are graphite-moderated systems, so the same conclusions regarding carbon/graphite that were identified for the pebble-bed HTGR (Section 2.2.1.1) generally apply. In particular, the change of the carbon capture cross section from ENDF/B-VII.0 to ENDF/B-VII.1 and the use of different graphite porosities in ENDF/B-VIII.0 will have a significant impact on the reactivity.

For nuclides acting as moderators like the carbon in graphite just mentioned, improved thermal scattering data are available, including upscattering on these nuclides. However, thermal scattering data are not yet available for the various salts used in FHRs. Thermal scattering data for FLiBe—a compound combining LiF and BeF$_2$—is currently under preparation and planned to be included in the next ENDF/B release (Zhu and Hawari, 2017). Reported studies in which researchers processed their own FLiBe data showed an impact in the range of 260–800 pcm for the multiplication factor in a molten salt system containing FLiBe, with the magnitude of the effect being dependent on the temperature (Mei et al., 2013).

Data for individual salt components are relevant and must be considered. However, no data are available for LiF and BeF$_2$ in FLiBe; the only data available are for the individual nuclides in these salt components. Furthermore, thermal scattering data over the entire temperature range that is applicable to the systems of interest is desirable. For example, in ENDF/B-VII.1, graphite thermal scattering data are available for temperatures up to 2,000 K. The presently available thermal scattering data were generally developed based on theoretical models and did not benefit from extensive comparison with experimental results.

Naturally occurring lithium is composed of two stable isotopes: ^{6}Li with 7.59% abundance, and ^{7}Li with 92.41% abundance. When lithium is part of the salt mixture, particularly LiF, the concentration of the isotope ^{6}Li can have a significant impact on reactivity. ^{6}Li is a strong

neutron absorber with a significant cross section for radiative neutron capture (n,γ) reaction, and in particular, a very large cross section for neutron capture reactions, with subsequent decay leading to emission of tritium (n,t) (Figure 2-11). To avoid this strong neutron absorption, even for small concentrations of ^{6}Li, lithium in MSRs is usually enriched to contain an abundance of ^{7}Li above 99.995% (Andreades et al., 2014). The radiative neutron capture in ^{7}Li (Figure 2-11) is also highly relevant due to the large amount of this nuclide in the reactor coolant (Shi et al., 2018; Fratoni, 2019).
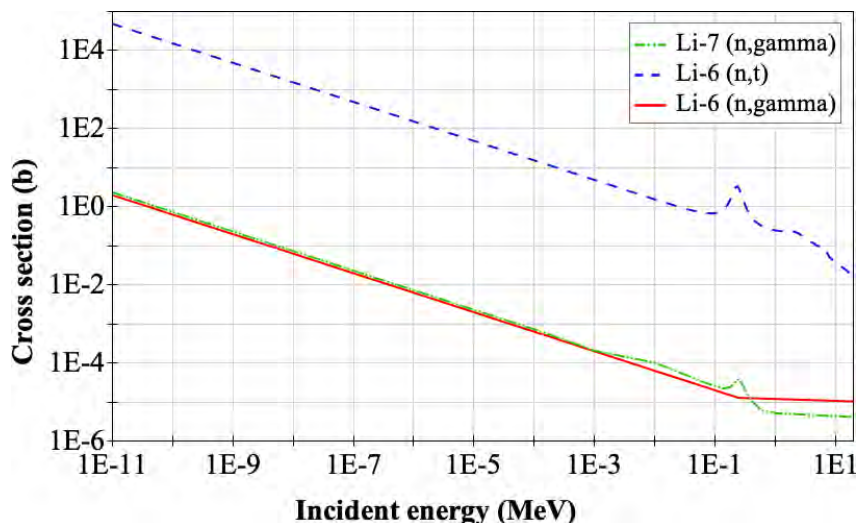
Figure 2-11 Relevant Lithium Cross Sections (ENDF/B-VII.1)

Inspection of the ^{6}Li (n,t) reaction cross section in different ENDF/B library releases reveals a visible difference in the thermal range: the ENDF/B-VII.0 data provide a cross section almost twice as large as that in ENDF/B-VII.1 in the thermal energy range below 0.01 eV (Figure 2-12). No studies on the potential impact of this difference have been found in the open literature. In contrast, the ^{6}Li (n,t) reaction cross sections are almost identical in ENDF/B-VII.1 and ENDF/B-VIII.0, with relative differences below 0.1% in the thermal energy range.
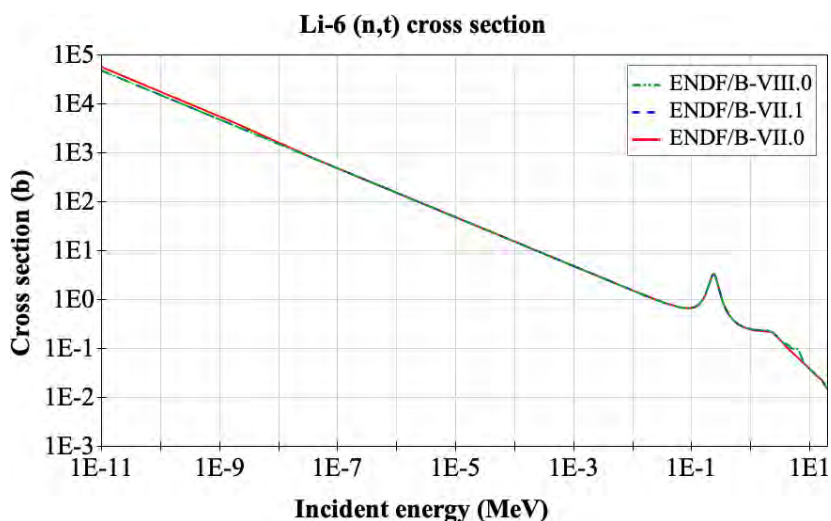
Figure 2-12 Comparison of ^{6}Li (n,t) Cross Section in ENDF/B Releases

As in the pebble-bed HTGR, additional relevant nuclide reactions for FHRs were identified through review of publications on uncertainty analysis using sensitivity coefficients. Fission, capture, and scattering of uranium (and plutonium nuclides in case of depleted fuel) were significant (Rochman et al., 2017; Shi et al., 2018; Powers et al., 2018). Furthermore, various capture and scattering reactions of Li, F, and Be nuclides were deemed relevant due to the high abundance of FLiBe salt in this reactor (Shi et al., 2018; Powers et al., 2018; Bostelmann et al., 2019a).

FHRs are intended to achieve significantly higher burnups than traditional LWRs. As in the high burnup fuel in the pebble-bed HTGR discussed above, the importance of the nuclear data for higher actinides may also be amplified for FHRs. The available nuclear data are often insufficiently compared with benchmarks for neutron reactions of minor actinides, especially for capture, fission, and inelastic scattering reactions (Bernstein et al., 2019; Salvatores, 2002).

2.2.1.3 Graphite-moderated MSR

For graphite-moderated MSRs, the same conclusions for the pebble-bed HTGR described in Section 2.2.1.1 also apply to carbon/graphite. Notably, as shown in the update of the carbon capture cross section from ENDF/B-VII.0 to ENDF/B-VII.1, the different graphite porosities in ENDF/B-VIII.0 can significantly impact reactivity.

As noted for the FHR concept in Section 2.2.1.2, thermal scattering data for the salt are not available. The impact on reactivity could be in the hundreds of pcm (Bostelmann et al., 2018; Zhang et al., 2020). Additionally, these systems also include a significant amount of lithium as part of the salt mixture. Thus, neutron capture in ^{6}Li and ^{7}Li is highly relevant for MSRs, as discussed for FHRs (Mei et al., 2013).

In contrast to the stationary fuel concept of an FHR, in graphite-moderated MSR concepts in which fuel salt circulates through the reactor during operation, the fuel salt includes the fission products that occur during fuel depletion. Several processes are proposed to strip fission products from the circulating salt, but not all of the products are removed. Radioactive fission products with short half lives are not usually relevant in a reactor with stationary fuel, but they become important in systems with moving fuel. ^{135m}Xe is one of these fission products. No data are available in the ENDF/B libraries for metastable ^{135m}Xe that decays to ^{135}Xe with a half-life of ~15 minutes. Consideration of ^{135m}Xe is important when calculating the steady-state xenon worth in thermal MSRs. A study based on a cross section estimate in the TALYS-Based Nuclear Data Library (TENDL)-2015 assumed that the neutron capture cross section of ^{135m}Xe was ~4 times greater than that for ^{135}Xe. With this assumption, a xenon worth for an MSR was calculated to be approximately 1.6 times higher than if ^{135m}Xe had not been considered in the analysis (Eades et al., 2016).

The review of various uncertainty analysis studies using sensitivity coefficients was especially useful for identifying nuclide reactions relevant to the reactivity of graphite-moderated MSRs. The relevant nuclide reactions for the fuel salt show a significant overlap with the reactions found to be relevant for FHRs (Bostelmann et al., 2019a; Bostelmann and Strydom, 2017; Powers et al., 2018; Rochman et al., 2017. Furthermore, relevant nickel cross sections were included for cases in which Ni-based alloys are used as structural materials (Shen et al., 2019).

2.2.1.4   Molten chloride fast spectrum reactor

For MSR systems in which chloride (Cl) is part of the salt, the ^{35}Cl (n,p) reaction is highly relevant when determining reactivity effects. New evaluations (not measurements) of this cross section resulted in a major change from ENDF/B-VII.0 to ENDF/B-VII.1 (Figure 2-13), and new measurements reported significant discrepancies in the data in the evaluated data libraries (Batchelder et al., 2019). Due to the large amount of chlorine in the fast MSR system, this change is highly relevant to reactivity and can cause differences of more than 1,000 pcm in the multiplication factor (Betzler et al., 2017a; Cisneros, 2021). With respect to chlorine as a salt component, scattering on ^{37}Cl becomes relevant. The concentration of ^{35}Cl in the salt is usually decreased by design (naturally 76% abundant) since neutron absorption in ^{35}Cl results in the generation of large amounts of the long-lived beta emitter ^{36}Cl, which must be minimized as much as possible due to its significant contribution to the total dose (Holcomb et al., 2011).
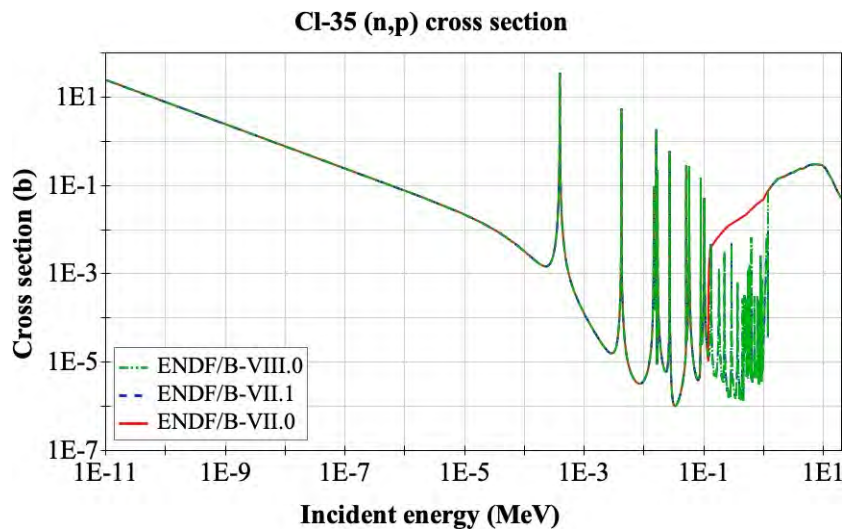
Figure 2-13 Comparison of ^{35}Cl (n,p) Cross Section in ENDF/B Releases

For MSRs in which fluoride is a component of the salt, the literature mentions a large inconsistency between JENDL-4.0 compared to ENDF/B-VII.1 and ENDF/B-VIII.0 data for inelastic scattering of ^{19}F. JENDL-4.0 appears to show better agreement with experimental data. In a reactivity comparison of fast spectrum MSR data from JENDL-4.0 and ENDF/B-VII.1, a difference of almost 2,000 pcm in reactivity was ascribed to the difference in only the inelastic scattering reaction of ^{19}F (Neudecker, 2020; van Rooijen et al., 2015).

Since molten chloride fast spectrum reactors have fuel salt circulating through the reactor during operation, missing ^{135m}Xe data are still relevant for determination of xenon worth as for the graphite-moderated MSR, as noted in Section 2.2.1.3.

Review of uncertainty analysis studies using sensitivity coefficients for this reactor type led to the identification of the neutron multiplicity, fission cross section, and capture cross section of various uranium and plutonium isotopes as being important for the analysis. Due to the large amount of the carrier salt NaCl in the reactor, the scattering and capture reactions of Na and Cl nuclides were also identified as relevant to reactivity (Bostelmann et al., 2019a). Updates of these Na and Cl cross sections, as well as uranium and plutonium cross sections between the

ENDF/B-VII.1 and ENDF/B-VIII.0 releases, can result in reactivity differences of a few hundred pcm (Bostelmann et al., 2019a; Bostelmann et al., 2019b).

2.2.1.5 Heat pipe reactor

Nuclide reactions of importance for the HPR reactivity were identified based on uncertainty analysis publications for similar reactors with fast neutron spectra. For the fuel material, the neutron multiplicity, fission, capture, and scattering of uranium and plutonium nuclides were deemed important for both fresh and depleted fuel. As mentioned for the previously discussed HTGR and FHR thermal reactor concepts, and as further discussed for fast systems in Section 2.2.1.6, there are major differences for various uranium and plutonium cross sections between ENDF/B-VII.1 and ENDF/B-VIII.0 that could cause changes in calculated reactivities. These differences are also seen for the HPR concept. Furthermore, the large amount of zirconium present in metal fuel increases the importance of scattering and capture reactions for several zirconium isotopes.

With respect to the coolant, the elastic and inelastic scattering reactions of Na and K were found relevant for this system. Nuclides present in the structural (Fe) or reflector (Al_2O_3, BeO) materials are also important. The scattering and capture reactions of Fe, Be, Al and O, as well as the thermal scattering data for BeO, were identified as relevant for this type of fast system (Bostelmann et al., 2019a; NEA, 2016). Although the neutron capture cross section in Be was found to have a small impact on reactivity, major differences were noted between its values in ENDF/B-VII.0 compared to the values in ENDF/B-VII.1 and ENDF/B-VIII.0, which are identical. These differences are observed for energies below 100 eV, in which the cross section is the greatest; the differences are approximately 14% (Figure 2-14).
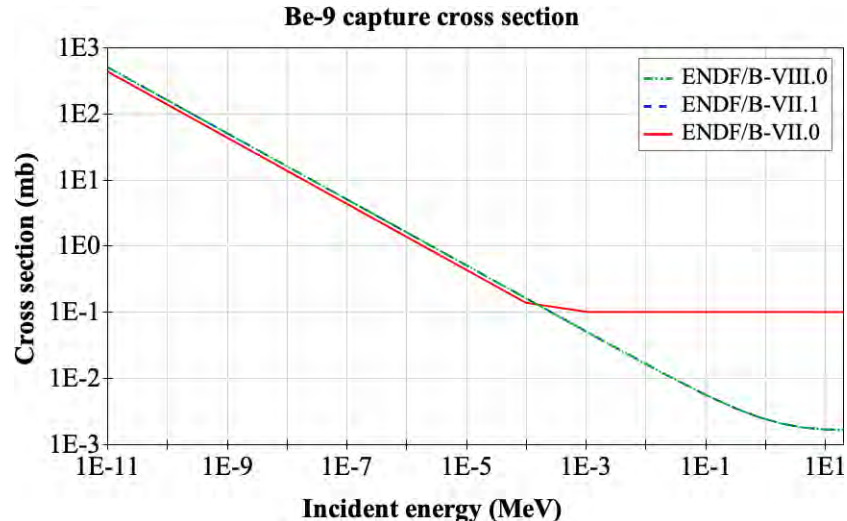
Figure 2-14 Comparison of ^{9}Be Radiative Neutron Capture in ENDF/B Releases

Relevant changes from ENDF/B-VII.1 to ENDF/B-VIII.0 were observed in the ^{16}O elastic scattering cross section, with a difference of approximately 2% in the energy range up to 10^5 eV, and even larger differences in the resonances within the fast energy range (Figure 2-15).
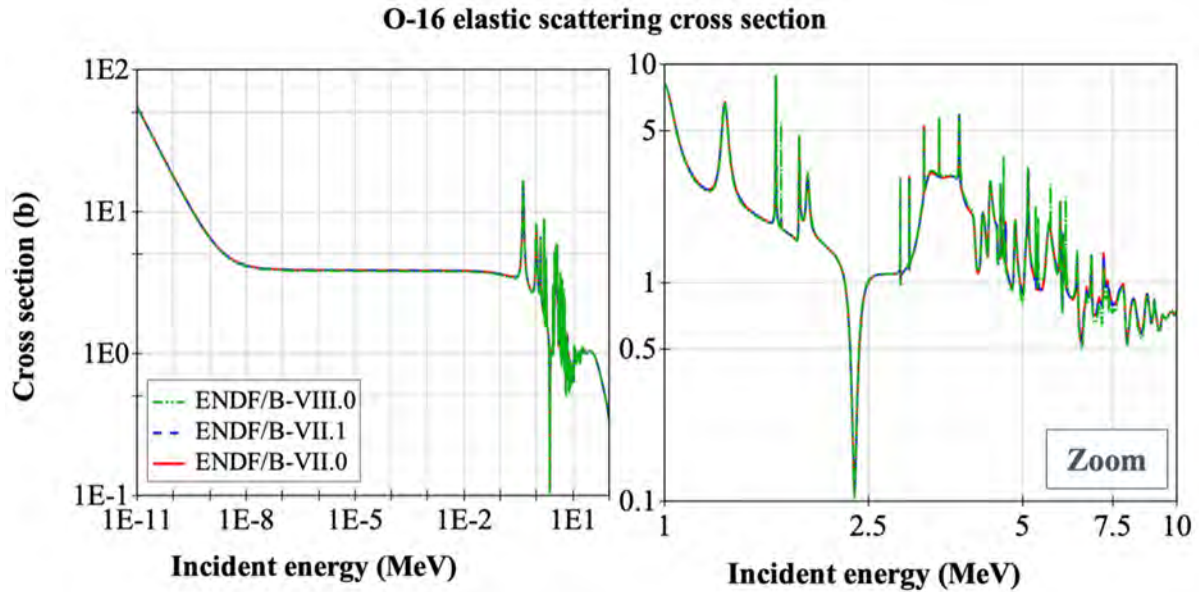
Figure 2-15 Comparison of ^{16}O Elastic Scattering Cross Section in ENDF/B Releases [2]

For analysis of fast spectrum systems with a high relevance of scattering reactions and neutron leakage, it is especially important to note the angular distributions of neutron scattering data. Differences of more than 100 pcm were found in highly enriched uranium and plutonium fast spectrum systems (Hill and Jeong, 2017). Notably, the (n,2n) reaction (Figure 2-16) has a greater importance in fast systems than in LWR systems (Yang, 2012).
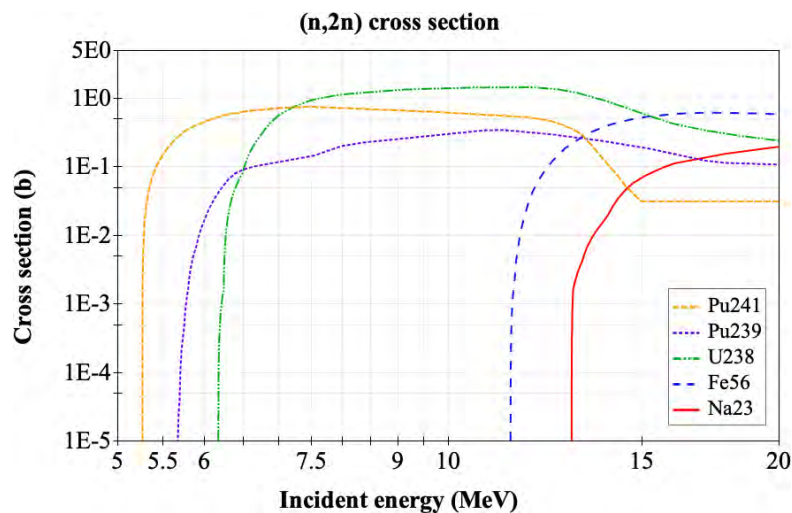
Figure 2-16 Relevant (n,2n) Cross Sections (ENDF/B-VII.1)

---

[2] See Figure 2-17 for the relative difference between the cross sections of the ENDF/B-VII.1 and ENDF/B-VIII.0 libraries

2.2.1.6   Sodium-cooled fast reactor

SFRs show important nuclide reactions for reactor physics analysis that are similar to those in the fast spectrum HPR discussed above. However, the initial SFR fuel composition is a mixture of U, Pu, and minor actinides, leading to an increased relevance of cross section data for minor actinides at the beginning of cycle.

A review of uncertainty analysis studies using sensitivity coefficients for SFRs revealed a large significance of scattering reactions of the coolant (Na) and structural materials (^{56}Fe, in particular) (Bostelmann, 2020; Bostelmann et al., 2019a; NEA, 2016). Furthermore, for fast spectrum systems, the (n,2n) reaction has a greater importance than in LWR systems (Yang, 2012). In the case of oxide fuel, elastic scattering of ^{16}O is relevant based on its resonances in the fast energy range (Bostelmann, 2020; Bostelmann et al., 2019a).

As with the other reactor concepts discussed herein, the updates between the ENDF/B-VII.1 and ENDF/B-VIII.0 releases of relevant cross sections cause differences in reactivity results for ^{16}O (Figure 2-17), ^{56}Fe (Figure 2-18), ^{238}U (Figure 2-9 above), and ^{239}Pu (Figure 2-19), for example. Reactivity differences of up to 200 pcm were observed in previous studies as a result of updates in ^{238}U data (Bostelmann et al., 2019a; Bostelmann et al., 2019b).
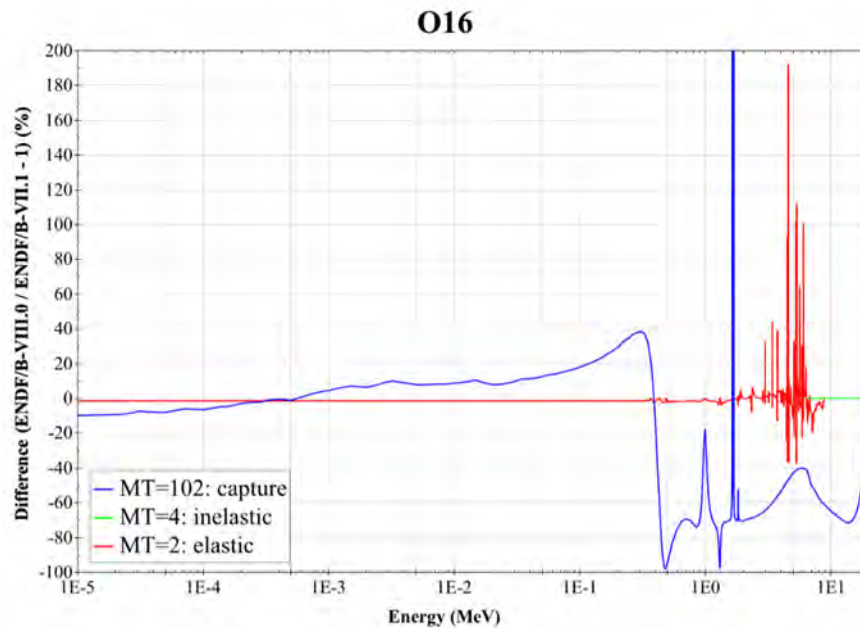
Figure 2-17 Relative Differences between ENDF/B-VII.1 and ENDF/B-VIII.0 for ^{16}O Cross Sections
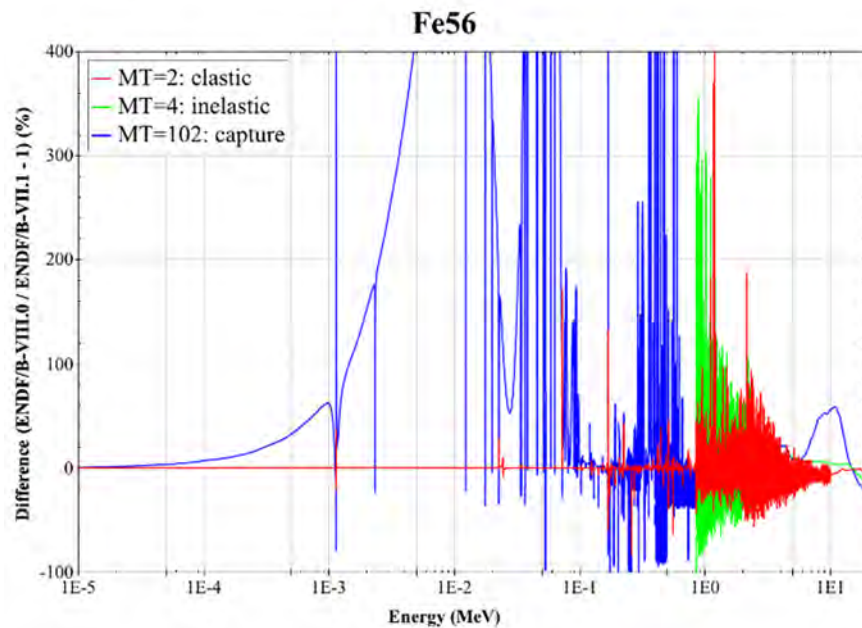
Figure 2-18 Relative Differences between ENDF/B-VII.1 and ENDF/B-VIII.0 for ^{56}Fe Cross Sections
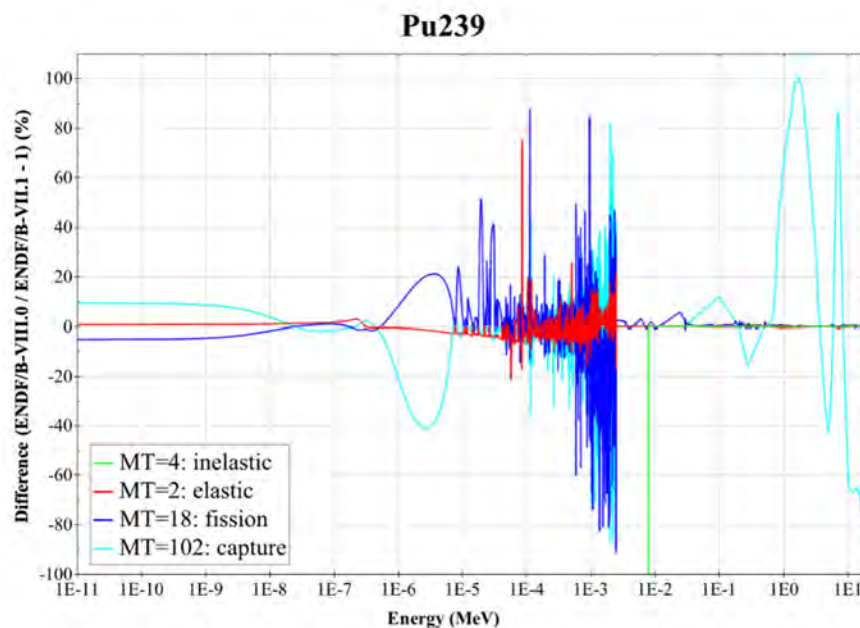
Figure 2-19 Relative Differences between ENDF/B-VII.1 and ENDF/B-VIII.0 for ^{239}Pu Cross Sections

2.2.1.7   Time-dependent analysis

As in the analysis of the time-dependent behavior of LWRs, the time-dependent behavior of conceptual advanced reactors requires more than just cross section data. Fission product yield data, decay constants, and branching fractions are also important factors in the buildup of fission products and higher actinides (Leray et al., 2017; Martinez et al., 2014; Rochman et al., 2017).

The fission product yields provided with ENDF/B-VII.0 and ENDF/B-VII.1 show only minor differences for ^{239}Pu, and the fission product yields provided with ENDF/B-VIII.0 are identical to those provided with ENDF/B-VII.1. However, calculated fission product concentrations using the branching fraction and independent yield data from the ENDF/B-VII.1 were found to be inconsistent with cumulative yield measurements (Pigni et al., 2015). This was traced to ENDF/B evaluators using an earlier version of the decay data to determine independent yields from measured cumulative yields. For SCALE 6.2, the independent yields of ^{235}U, ^{238}U, ^{239}Pu, and ^{241}Pu were adjusted from the values provided in ENDF/B-VII.1 to improve the internal consistency with the decay data, leading to improved agreement with cumulative fission yields measurements.

The ENDF/B nuclear data libraries provide fission product yields for up to four incident neutron energies (Table 2-1), suggesting the use of linear interpolation between these points. Since the average energy of neutrons causing fission for major fissionable nuclides is in the range of 10^4 and 10^5 eV (Table 2-2), the interpolated yields for both fast and thermal systems are primarily based on the 10^5 eV data point. It is unknown if the interpolation of these few data points is sufficient or if additional data points would cause significant differences in depletion calculations. As shown in Table 2-1, the yields of important fission products can easily vary by 10% because of incident fission neutron energy. For thermal systems, the use of these fission yields in depletion calculations generally leads to good agreement of fission product concentrations with measurements. However, for fast spectrum systems, the average energy of fission is higher, so the fission yields for the highest energy point play an increased role. Additional destructive assay data are needed to provide increased confidence using this data for fast spectrum reactors.

Table 2-1   ENDF/B-VII.1 Independent Fission Yields

Energy [eV]	^{235}U ^{96}Sr	^{235}U ^{135}Te	^{238}U ^{96}Sr	^{238}U ^{135}Te	^{239}Pu ^{96}Sr	^{239}Pu ^{135}Te	^{241}Pu ^{96}Sr	^{241}Pu ^{135}Te
2.53E-02	3.57E-02	3.22E-02			1.82E-02	2.19E-02	2.45E-02	3.73E-02
5.00E+05	4.38E-02	2.47E-02	4.13E-02	4.62E-02	1.95E-02	2.05E-02	2.73E-02	3.75E-02
2.00E+06					1.77E-02	1.68E-02		
1.40E+07	1.81E-02	1.04E-02	3.20E-02	2.66E-02	1.27E-02	8.11E-03		

Table 2-2   Average Energy of Neutrons Causing Fission for a Representative Thermal (LWR) and Fast (SFR) systems

Nuclide	Energy (eV)	
	Thermal (LWR)	Fast (SFR)
^{235}U	1.9E+04	3.4E+05
^{238}U	3.2E+06	2.9E+06
^{239}Pu	1.3E+04	4.5E+05
^{241}Pu	9.8E+03	3.3E+05

In transient analysis, the effective delayed neutron fraction is important (Kodeli, 2013), as are the fission spectra of individual actinides, with their dependence on the energy of the neutron causing fission. Furthermore, the decay constants are also of high importance (Aliberti et al., 2007). In all advanced reactor analysis, power normalization requires adequate knowledge of the recoverable fission and capture energy.

2.2.2   Key Uncertainty Data

This section summarizes key nuclear data uncertainties that affect advanced reactor physics analyses. These uncertainties were identified based on the review of publicly available literature. The section is structured according to the selected advanced reactor concepts included in Table 1 above; relevant conclusions are repeated as applicable.

The uncertainty plots shown here were generated using data from SCALE covariance libraries available in SCALE 6.1, 6.2, and 6.3 beta releases. These libraries are mainly based on ENDF/B-VII.0, ENDF/B-VII.1, and ENDF/B-VIII.0 evaluated data, respectively, with some ORNL additions or modifications (Wieselquist et al., 2020). Added or modified data are labeled using the SCALE release number instead of the corresponding ENDF/B release on which most of the covariance library data are based. SCALE 6.1 covariance data are presented in a 44-group structure, while SCALE 6.2 and 6.3 data are presented in a 56-group structure. Nominal data are presented with corresponding 2σ uncertainty bands. For context, the eigenvalue uncertainty for a typical thermal LWR assembly is between 0.5 and 0.8%, depending on the fuel composition (Rochman et al., 2017).

2.2.2.1   Pebble-bed high-temperature gas-cooled reactor

Studies on the impact of nuclear data uncertainties on HTGRs have mainly focused on reactivity impacts. Reported eigenvalue uncertainties for a fresh core of the Very High Temperature Reactor critical experiment (VHTRC) are between 0.5 and 0.7% (Bostelmann et al., 2019a; Bostelmann and Strydom, 2017); similar values were found for the HTR-10 reactor (Cheng et al., 2020b; Hao et al., 2018). Eigenvalue uncertainties for a core with depleted fuel are slightly larger than for a fresh fuel core due to the impact of higher actinides uncertainties such as in plutonium cross sections. The top contributing nuclide reactions to eigenvalue uncertainties are the neutron multiplicity ($\bar{\nu}$) of ^{235}U (Figure 2-20) for the VHTRC fresh fuel core and $\bar{\nu}$ of ^{239}Pu for a depleted fuel core (Figure 2-22). Other relevant contributors are fission and neutron capture in uranium and plutonium isotopes (Figure 2-20 and Figure 2-27), elastic scattering in ^{16}O as part of the fuel (Figure 2-31), and capture and scattering in graphite (Figure 2-28 and Figure 2-29).
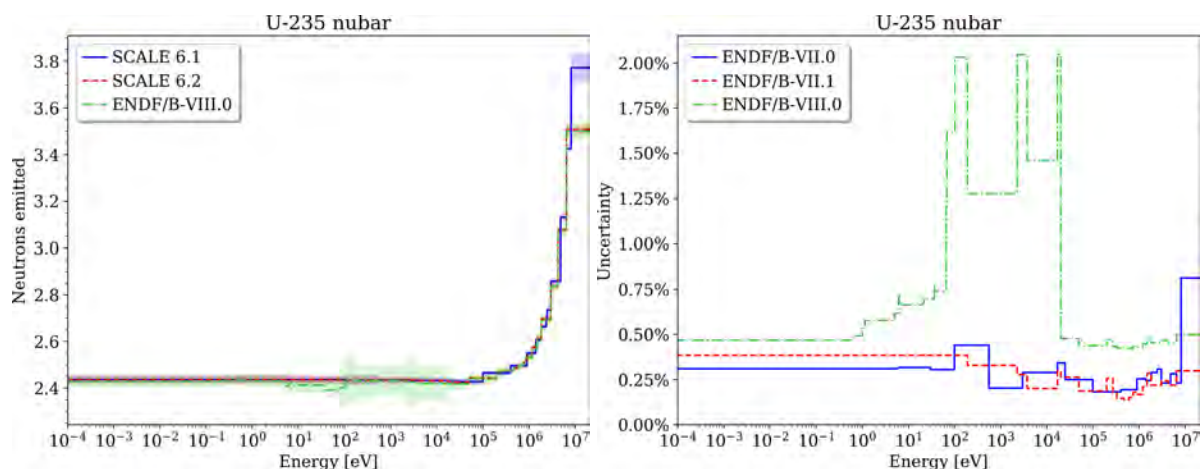
Figure 2-20 ^{235}U Fission Neutron Multiplicity Nominal Data and Uncertainty
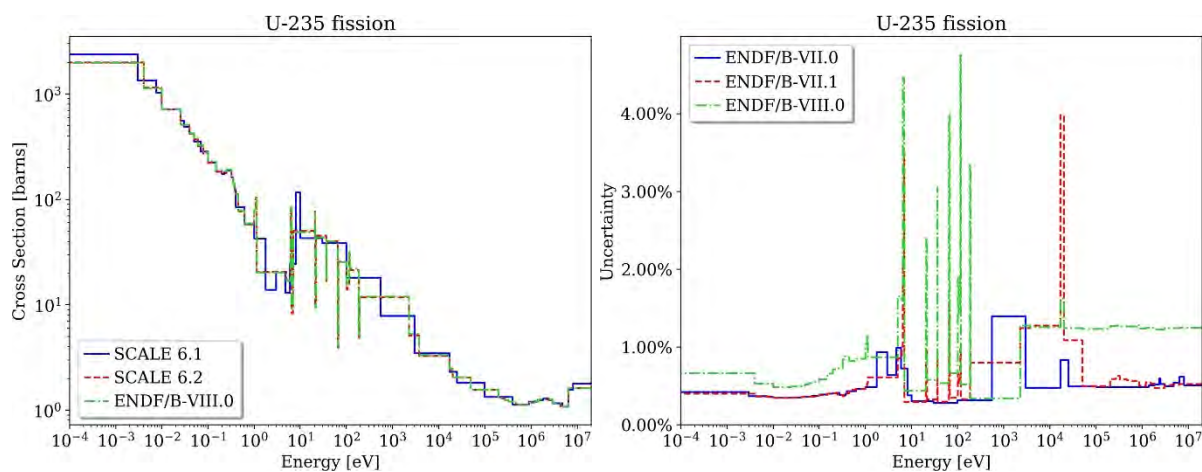
Figure 2-21 ^{235}U Fission Nominal Data and Uncertainty
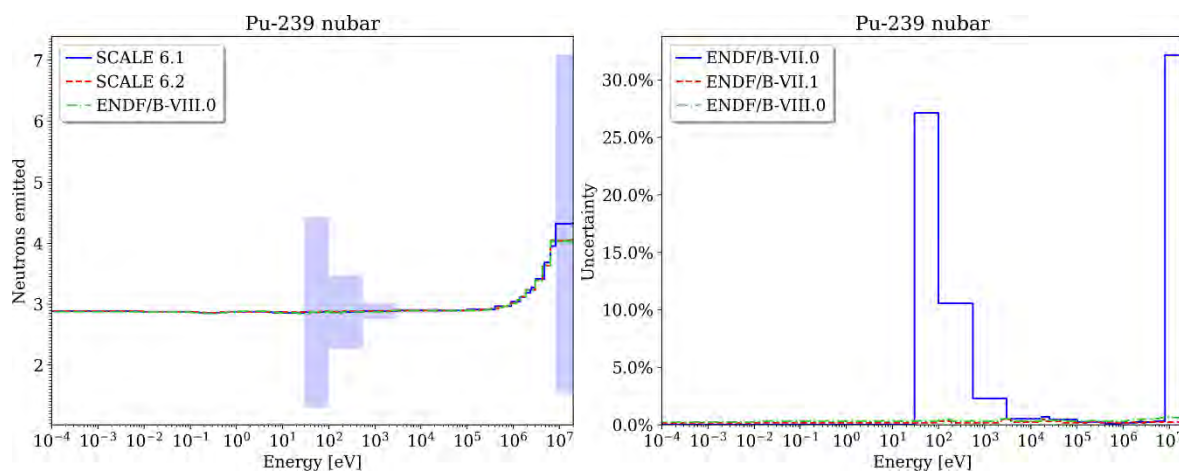
Figure 2-22 ^{239}Pu Fission Neutron Multiplicity Nominal Data and Uncertainty
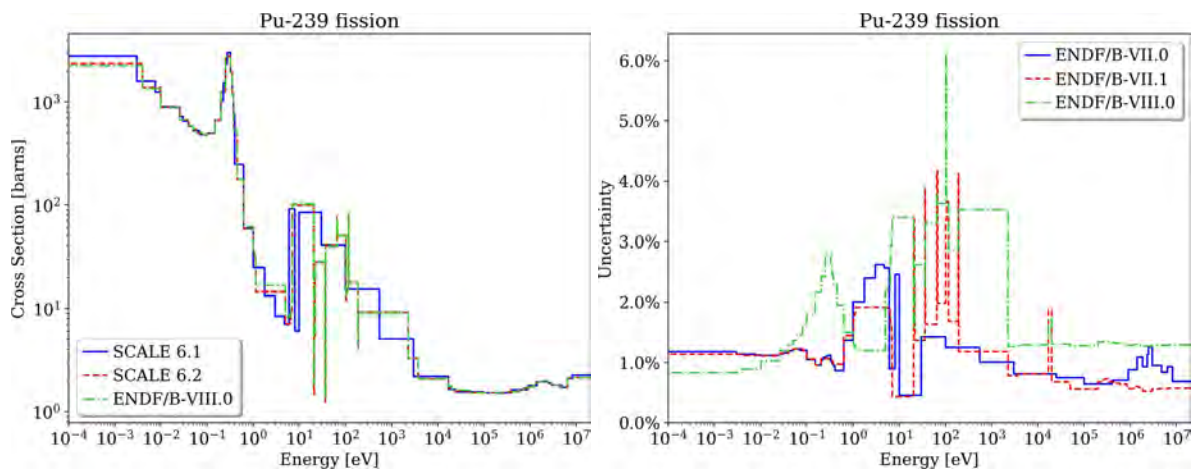
Figure 2-23 ^{239}Pu Fission Nominal Data and Uncertainty
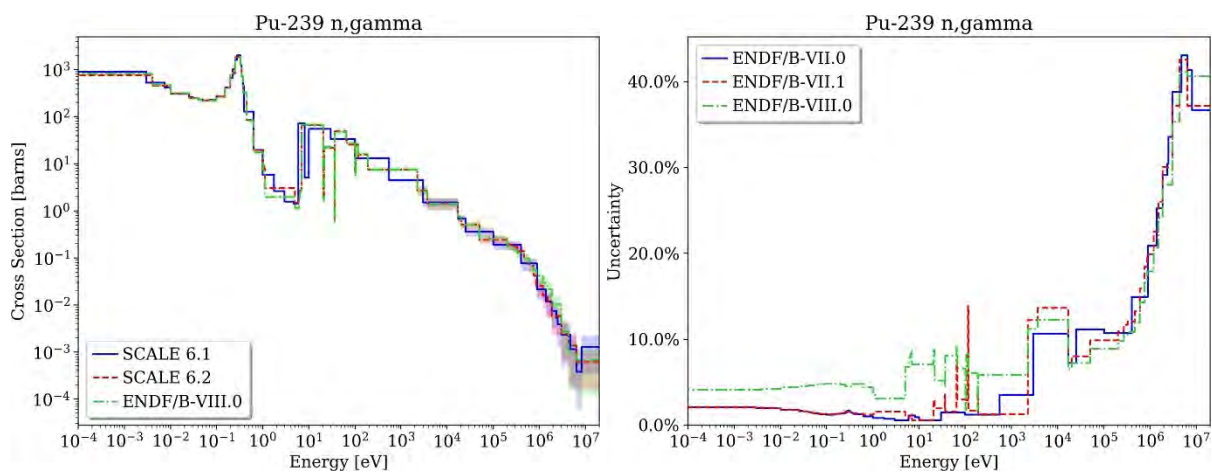
Figure 2-24 ^{239}Pu (n, γ) Nominal Data and Uncertainty
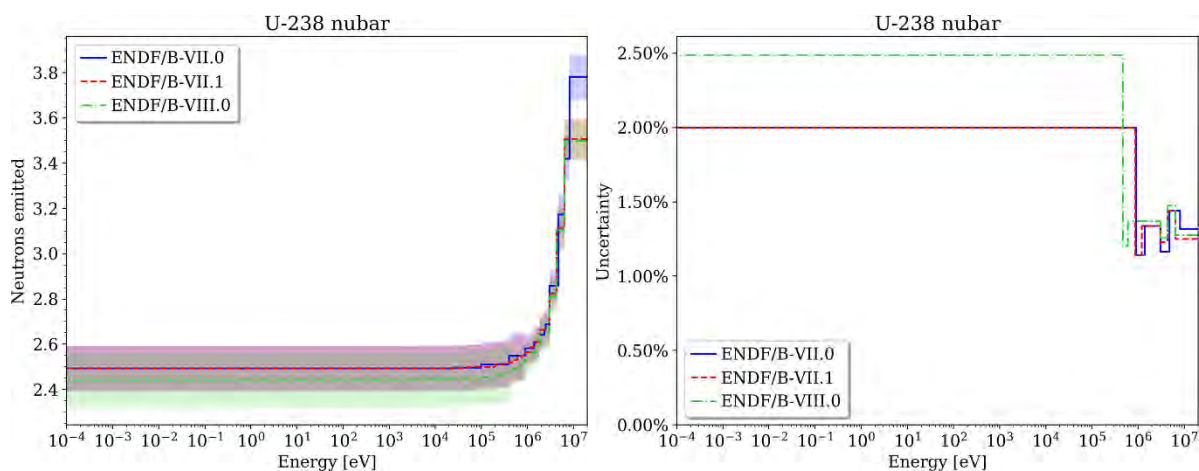
Figure 2-25 ^{238}U Fission Neutron Multiplicity Nominal Data and Uncertainty
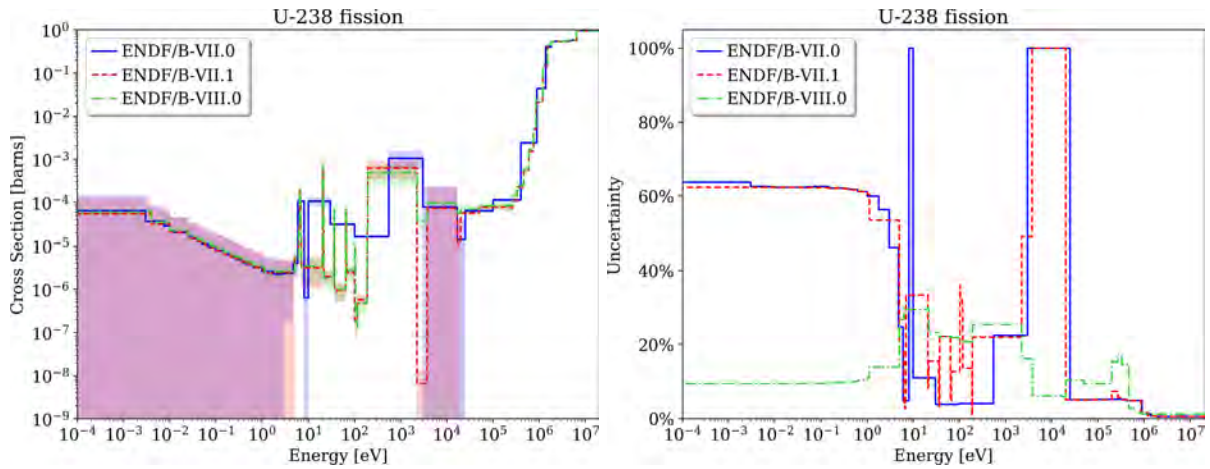
Figure 2-26 ^{238}U Fission Nominal Data and Uncertainty
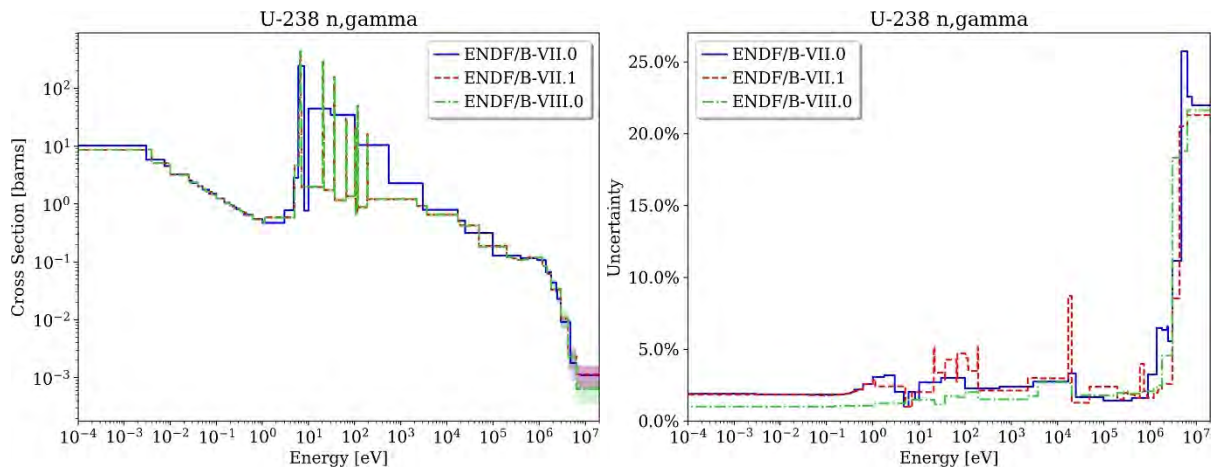
Figure 2-27 ^{238}U (n, γ) Nominal Data and Uncertainty
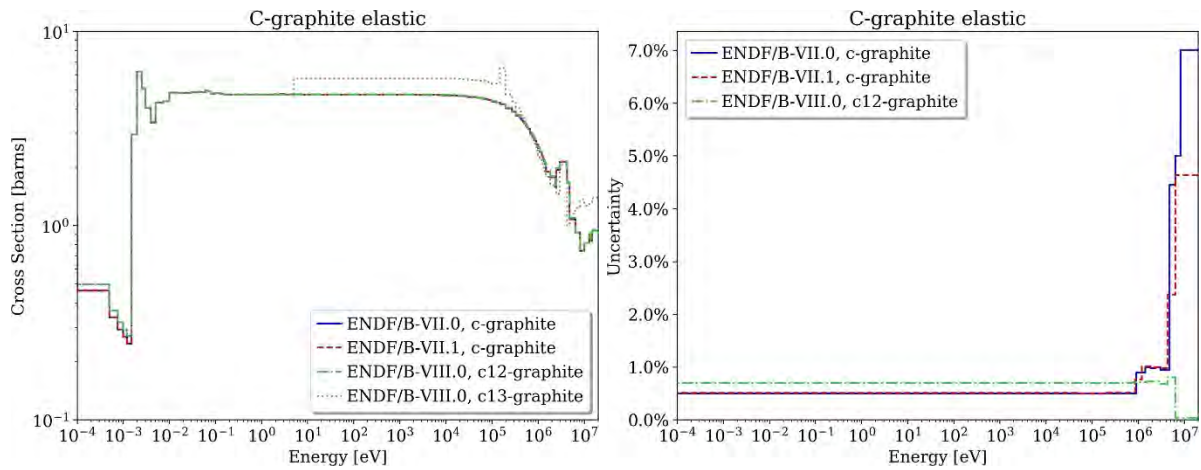
Figure 2-28 Graphite Elastic Scattering Nominal Data and Uncertainty
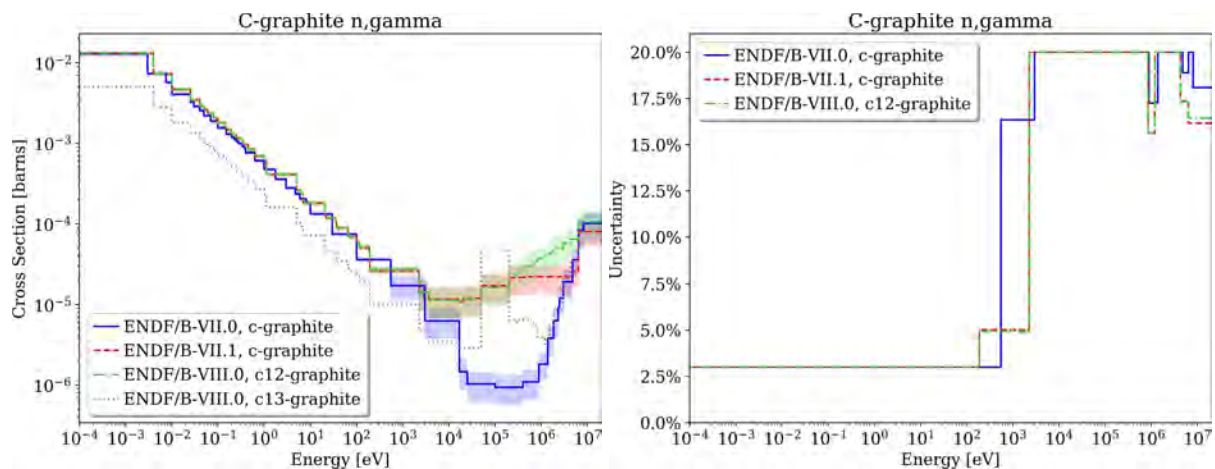
Figure 2-29 Graphite (n,γ) Nominal Data and Uncertainty
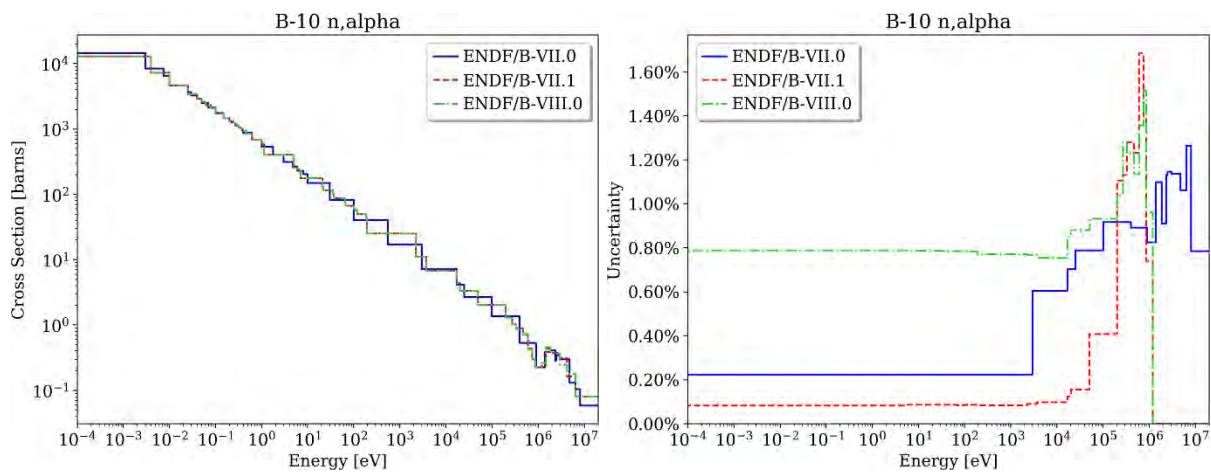
Figure 2-30 ¹⁰B (n,α) Nominal Data and Uncertainty
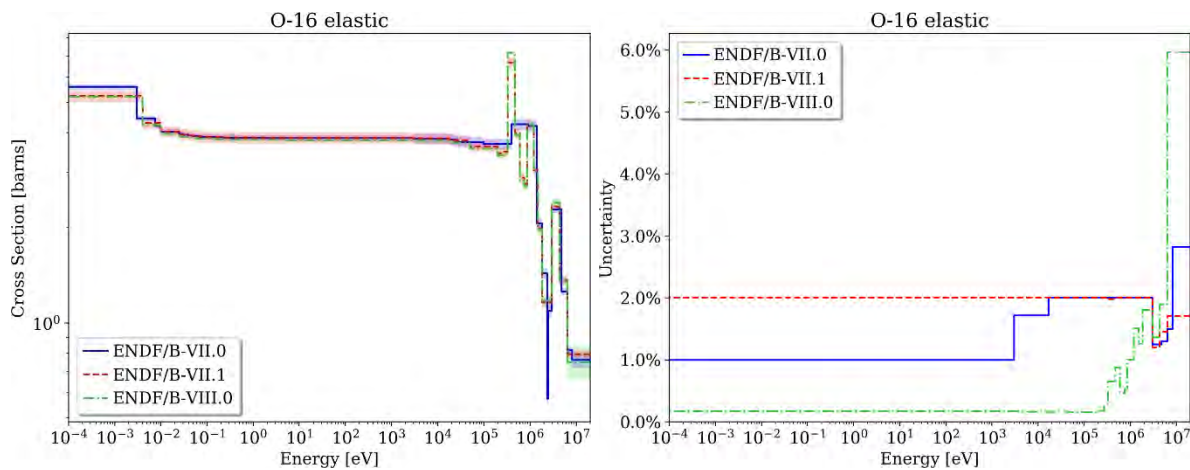
Figure 2-31 ¹⁶O Elastic Scattering Nominal Data and Uncertainty

Currently there are no published studies that address the impact of ENDF/B-VIII.0 uncertainties on the reactivity of HTGRs. However, differences in the ENDF/B-VII.0 and ENDF/B-VII.1 nuclear data uncertainties have been shown to cause relevant differences in calculated output uncertainties. In particular, updates in the released uncertainties for fission cross sections and $\bar{\nu}$ can cause significant changes in eigenvalue uncertainties. For example, for a small HTGR experiment, the eigenvalue uncertainty increased from 0.58% with SCALE 6.1 covariance data (mainly based on ENDF/B-VII.0) to 0.67% with SCALE 6.2 covariance data (mainly based on ENDF/B-VII.1) (Bostelmann and Strydom, 2017). Furthermore, the significant increase of the ^{10}B (n,α) cross section uncertainty in ENDF/B-VIII.0 (Figure 2-30) could increase the impact on the reactivity uncertainty of the equivalent boron content in the graphite reflector.

Consideration of uncertainties in graphite thermal scattering data could have an impact on the output uncertainties in pebble-bed HTGRs. Although such data are not currently available for use in uncertainty analysis, a rough estimate of the impact for a 100% uncertainty can be assessed by determining the difference between calculations that exclude or include thermal scattering data. Reactivity impacts of several hundred pcm were reported for graphite thermal scattering data in the reflector graphite of two HTGR systems (Bostelmann et al., 2018; Zhang et al., 2020) (Section 2.2.1.1).

2.2.2.2 *Fluoride salt-cooled high-temperature reactor*

Graphite-moderated systems such as FHRs that contain enriched ^{235}U fuel show reactivity uncertainties similar to those of pebble-bed HTGRs. A multiplication factor uncertainty of ~0.6%, with the $\bar{\nu}$ of ^{235}U (Figure 2-20) as top contributor to this uncertainty, was reported for an FHR fresh fuel core (Shi et al., 2018; Powers et al., 2018). In addition to the neutron capture reactions of ^{235}U and ^{238}U, other relevant reactions are scattering of ^{7}Li, the (n,t) reaction of ^{6}Li, and scattering of ^{19}F due to the large amount of FLiBe in the reactor (Figure 2-32 to Figure 2-36) (Shi et al., 2018; Fratoni, 2019; Powers et al., 2018). Neutron capture of ^{7}Li is especially relevant due to the large uncertainty of this reaction.

The consideration of uncertainties for graphite thermal scattering data and FLiBe thermal scattering data could have an impact on FHR output uncertainties. As discussed in Section 2.2.2.1, only an estimate for an assumed 100% uncertainty in this data can be made now because no uncertainty is available for these thermal scattering data in the evaluated released libraries. The consideration of FLiBe thermal scattering data was found to have an impact of 260–800 pcm on the multiplication factor in a molten salt system (Mei et al., 2013) (Section 2.2.1.3).
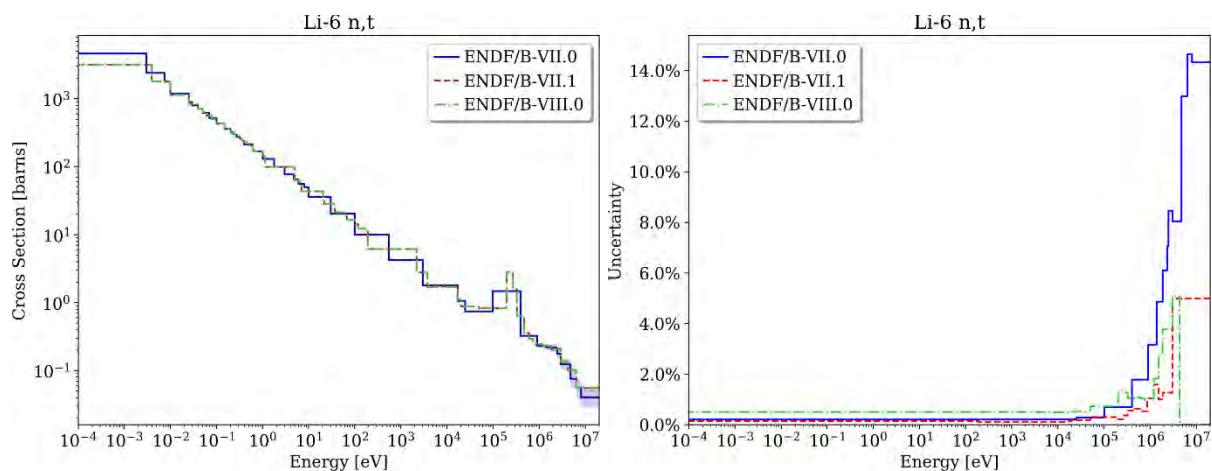
Figure 2-32 ^{6}Li (n,t) Nominal Data and Uncertainty
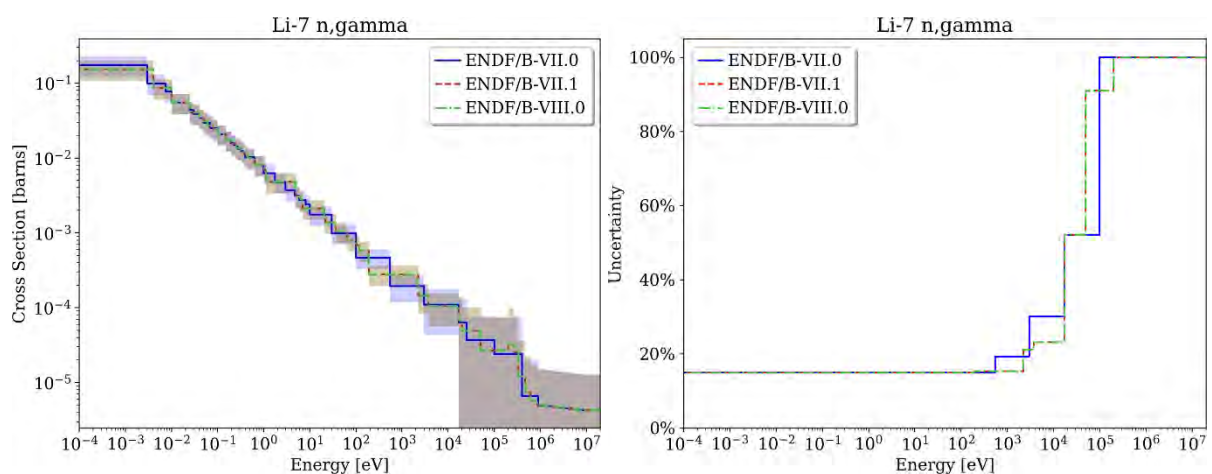
Figure 2-33 ^{7}Li (n,γ) Nominal Data and Uncertainty
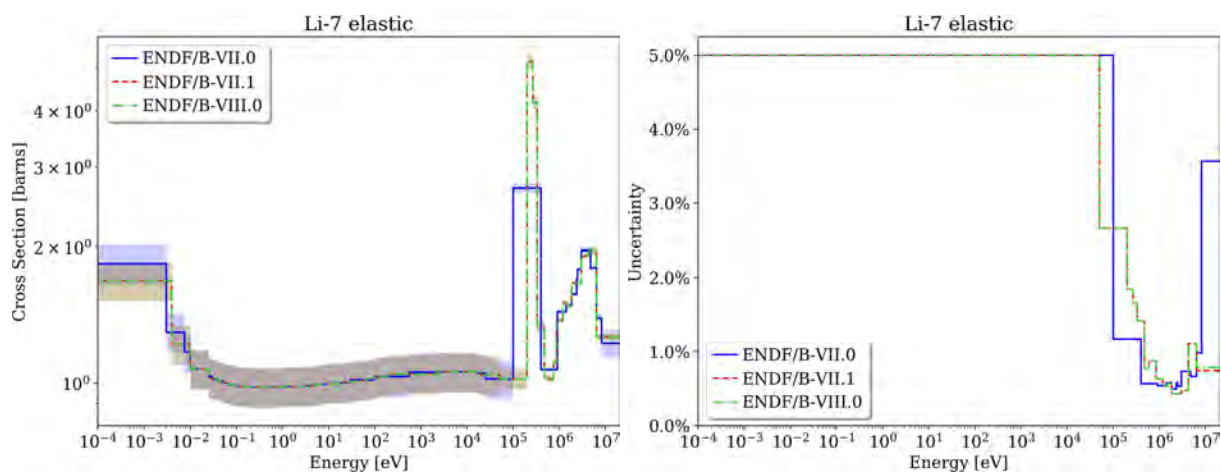
Figure 2-34 ^{7}Li Elastic Scattering Nominal Data and Uncertainty
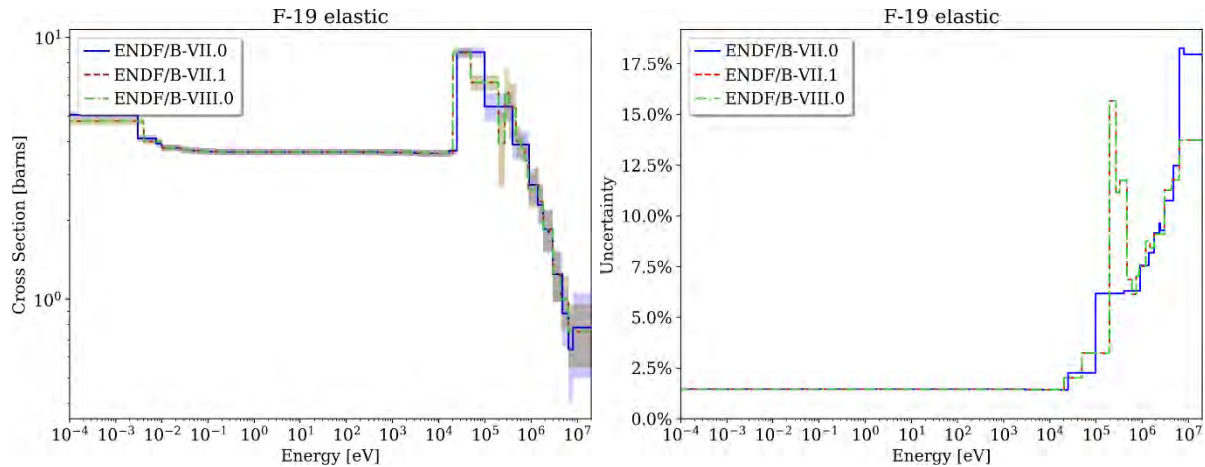
Figure 2-35 ^{19}F Elastic Scattering Nominal Data and Uncertainty
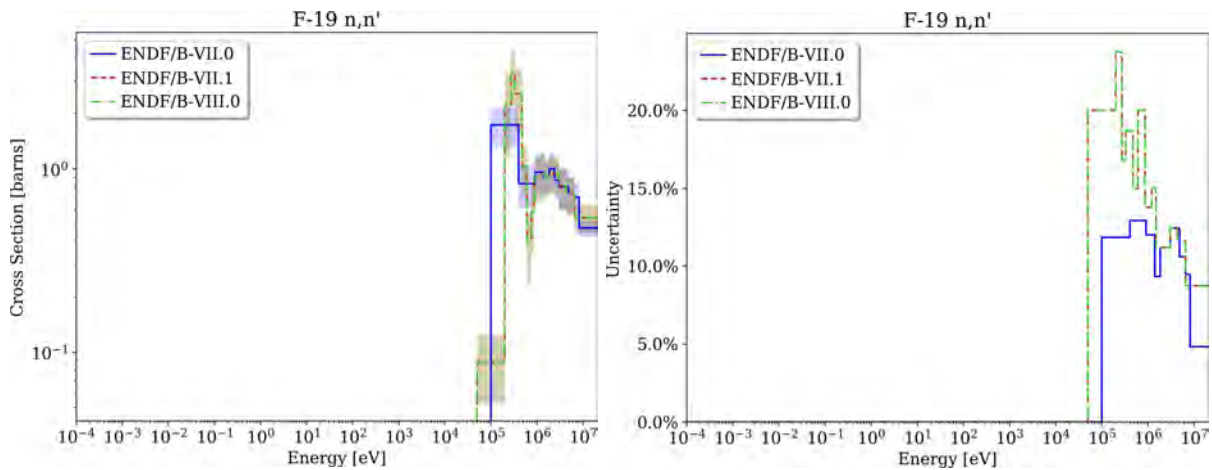
Figure 2-36 ^{19}F Inelastic Scattering Nominal Data and Uncertainty

2.2.2.3   *Graphite-moderated MSR*

Relevant nuclear data uncertainties for graphite-moderated MSRs are similar to those identified for FHRs (Section 2.2.2.2). The neutron multiplicity, fission, and capture cross section of ^{235}U, neutron capture of ^{238}U, and neutron capture and scattering of ^{7}Li, ^{19}F, and graphite play the most important roles for reactivity uncertainty analysis (Bostelmann et al., 2019a; Fratoni, 2019; Powers et al., 2018). As noted for the FHRs, the large uncertainty of neutron capture of ^{7}Li is also especially relevant (Figure 2-33) for graphite-moderated MSRs.

Uncertainties of graphite and FLiBe thermal scattering data could have a significant impact on the output uncertainties for graphite-moderated MSRs. Since these uncertainty data are missing in the released libraries, a specific quantification of the impact cannot be performed. The consideration of FLiBe thermal scattering data was found to have an impact of 260–800 pcm on the multiplication factor in a molten salt system (Mei et al., 2013).

2.2.2.4   *Molten chloride fast spectrum reactor*

The uncertainties of QOIs in fast spectrum MSR analyses result from nuclear data uncertainties are largely unknown compared to those in MSR thermal systems. Most previous studies and evaluations for nuclear data have focused on traditional thermal systems, whereas fewer have focused on fast spectrum systems. Therefore, many cross sections show a large uncertainty in the fast energy range for all ENDF/B releases. The eigenvalue uncertainty for fast spectrum systems can be up to 2–3 times larger than for LWRs. For example, an eigenvalue uncertainty in the 0.9–1.7% range with the major contributor [239]Pu fission (Figure 2-23) was reported for a molten chloride reactor when using ENDF/B-VIII.0 data (Cisneros, 2021). In addition to other [239]Pu reactions, including the neutron multiplicity and neutron capture, this study also found the [24]Mg elastic scattering (Figure 2-37) to be an important contributor to the eigenvalue uncertainty since the investigated reactor concept considered magnesium oxide as reflector material.
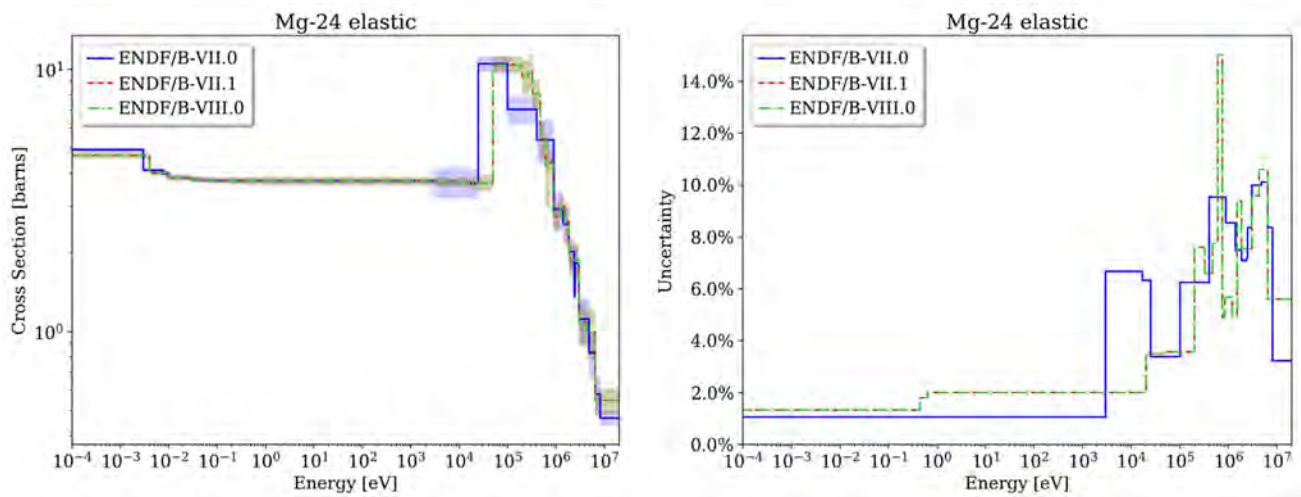
Figure 2-37 [24]Mg Elastic Scattering Nominal Data and Uncertainty
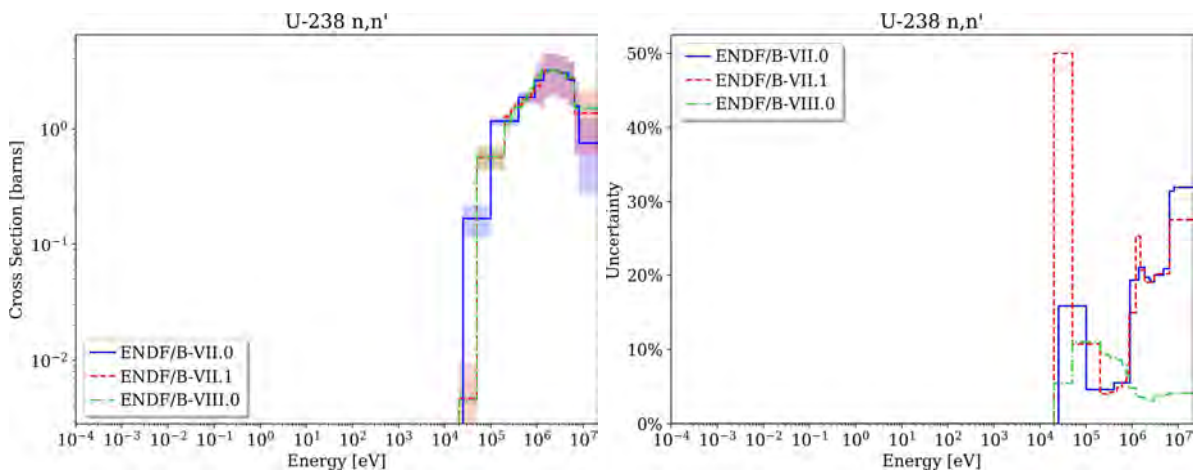
Figure 2-38 [238]U Inelastic Scattering Nominal Data and Uncertainty

A major contributor to the uncertainty in many fast spectrum systems with uranium fuel is the uncertainty of ^{238}U inelastic scattering. This uncertainty was decreased in the ENDF/B-VIII.0 release compared to the ENDF/B-VII.1 release (Figure 2-38). The uncertainties of other relevant reactions such as ^{239}Pu fission and ^{238}U neutron capture were also significantly changed in ENDF/B-VIII.0 compared to ENDF/B-VII.1; these changes can result in differences in output uncertainties and their top contributing nuclides.

The non-consideration of angular scattering distributions was shown to have an impact of several hundred pcm on the multiplication factor for highly enriched uranium and plutonium fast spectrum systems (Hill and Jeong, 2017). Note that the uncertainties available in ENDF/B for angular scattering data are limited.

2.2.2.5 *Heat pipe reactor*

Given the large uncertainties in relevant cross sections within the fast energy range, uncertainty for fast neutron spectrum systems such as HPRs are expected to be significant. The ^{235}U cross section data are well known in the thermal energy range due to extensive history of measurements and evaluations targeting traditional LWRs. However, in the fast energy range, the neutron capture cross section of ^{235}U shows a large uncertainty of over 30% in the ENDF/B-VII.0 and ENDF/B-VII.1 releases (Figure 2-39). Due to the importance for reactivity, this large uncertainty is expected to result in a large reactivity uncertainty. A significant reduction in reactivity uncertainty is expected when using ENDF/B-VIII.0 data because of the significantly reduced uncertainty for this reaction in the recent library release. Other relevant expected contributors to reactivity uncertainty are the various scattering reactions for selected nuclides in fuel and in structural and coolant materials as applicable for uncertainty analyses of other SFR systems previously studied (Bostelmann, 2020).
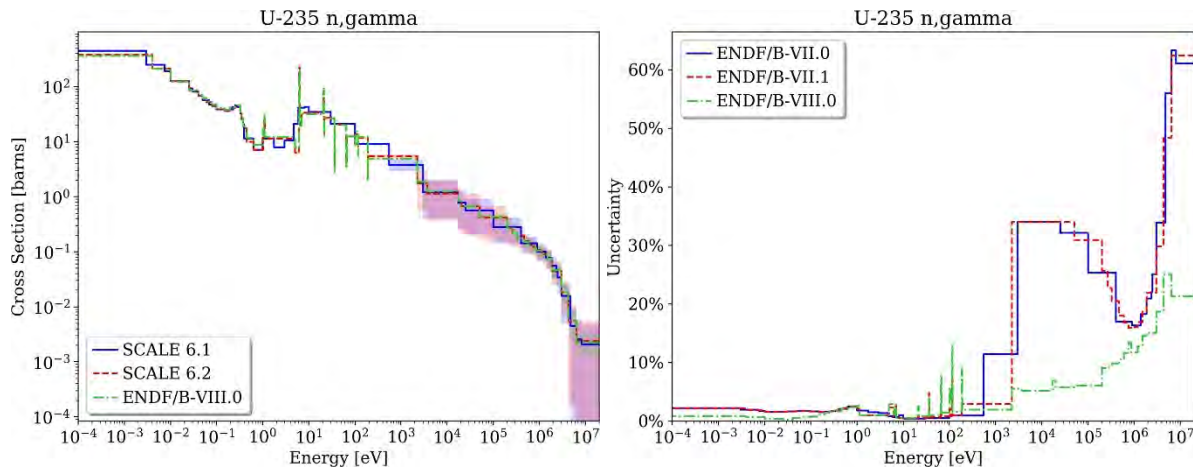
Figure 2-39 ^{235}U (n, γ) **Nominal Data and Uncertainty**

The impact of missing thermal scattering uncertainties for BeO is expected to be small for the HPR because it is a fast spectrum system. Since the neglect of angular scattering distributions was shown to have an impact of several hundred pcm on the multiplication factor of highly enriched uranium and the plutonium fast spectrum system (CSEWG 2019; Hill and Jeong, 2017), the impact of missing angular scattering uncertainties is expected to be in the same range for fast spectrum HPR systems. Note that the uncertainties available in ENDF/B for angular scattering data are limited.

2.2.2.6   Sodium-cooled fast reactor

As for fast spectrum MSR systems, the uncertainties of important quantities in SFR analyses due to nuclear data uncertainties can be significantly larger than those of thermal systems. This is due to the large uncertainties in relevant cross sections over the high energy range. The eigenvalue uncertainty for SFRs can be 2–3 times greater than for LWRs, depending on the libraries used. For example, the reactivity uncertainty for a typical SFR is in the range 1–1.5% when using ENDF/B-VII.1 data. The uncertainties of important reactivity coefficients such as the sodium void coefficient can be as high as 5%. The major contributor to the uncertainty of many reactivity coefficients is ^{238}U inelastic scattering due to its large uncertainty in the fast energy range (Figure 2-38). Other relevant contributors to reactivity coefficients uncertainties, as well as uncertainty in the power distribution, are the scattering reactions of ^{23}Na as the coolant and ^{56}Fe as the major component in structural materials (Bostelmann, 2020).

The uncertainty of ^{238}U inelastic scattering was shown to be a dominant contributor to output uncertainties in SFR uncertainty analyses using ENDF/B-VII.1 data. In the ENDF/B-VIII.0 release, the uncertainty of this cross section was decreased compared to the ENDF/B-VII.1 release (Figure 2-38). SFR uncertainty analyses based on the ENDF/B-VIII.0 release are therefore expected to show significant differences with respect to output uncertainties and their top contributing nuclide reactions when compared with ENDF/B-VII.1 calculations. The uncertainties of other relevant reactions such as ^{56}Fe scattering, ^{239}Pu fission, and ^{238}U neutron capture were also significantly changed in ENDF/B-VIII.0, so they will also contribute to these differences (Bostelmann et al., 2019b). The neglect of angular scattering distributions and their uncertainties was shown to have an impact of several hundred pcm on the multiplication factor of highly enriched uranium and plutonium fast spectrum systems (CSEWG, 2019; Hill and Jeong, 2017).
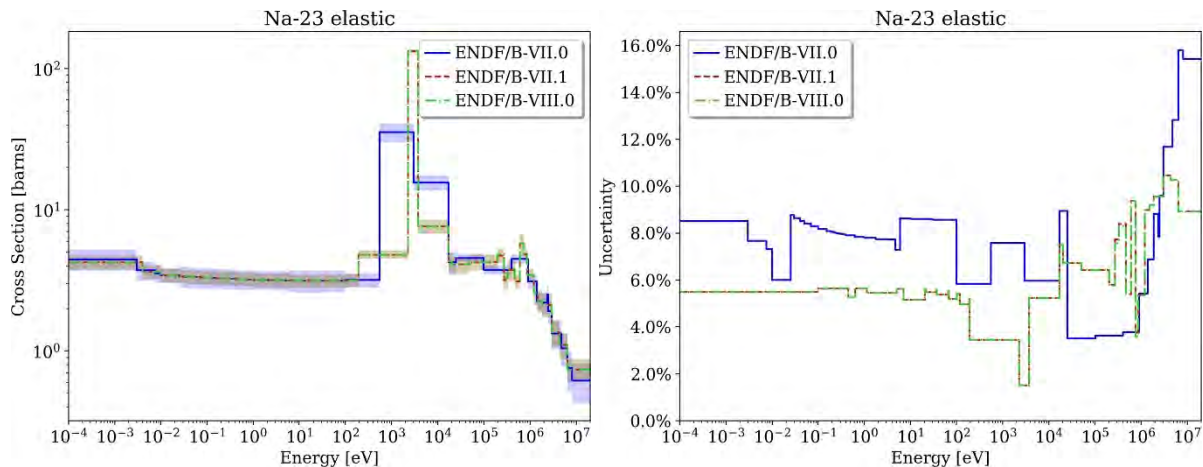
Figure 2-40 ^{23}Na Elastic Scattering Nominal Data and Uncertainty

2.2.2.7   Time-dependent analysis

The time-dependent behavior of advanced reactor concepts discussed in Section 2.2.1.7 requires data on fission yields, decay constants, branching ratios, recoverable energy for capture and fission, and effective delayed neutron fraction (β_{eff}) in the case of transient analysis. The current ENDF/B format does not allow correlations for fission product yields or decay data. However, correlations for fission product yields can be determined via constraints such as a

limited number of fission products per fission event. Such correlation matrices were generated for use in the SCALE code system (Pigni et al., 2015). Additionally, updates were implemented in SCALE for ^{235}U, ^{238}U, ^{239}Pu, and ^{241}Pu to ensure consistency between the measured cumulative fission yields and the independent fission yields taken from ENDF/B-VII.1. The consideration of fission yield uncertainties and details on their constraints can have a noticeable impact on the fission product evolution in depletion calculations, as has been shown for LWR systems (Aures et al., 2017a).

The literature review did not reveal the consideration or availability of branching ratio uncertainties by any computational tool or data library. If they were available and accounted for, then additional correlations would be introduced to the independent fission yields since they are always required to sum up to 2. No data for uncertainties in the recoverable fission and capture energy were found in the literature. In fact, the energy release per fission is often hard coded in many of the computational tools. If such uncertainties were available and considered, then they could affect the power distribution calculation.
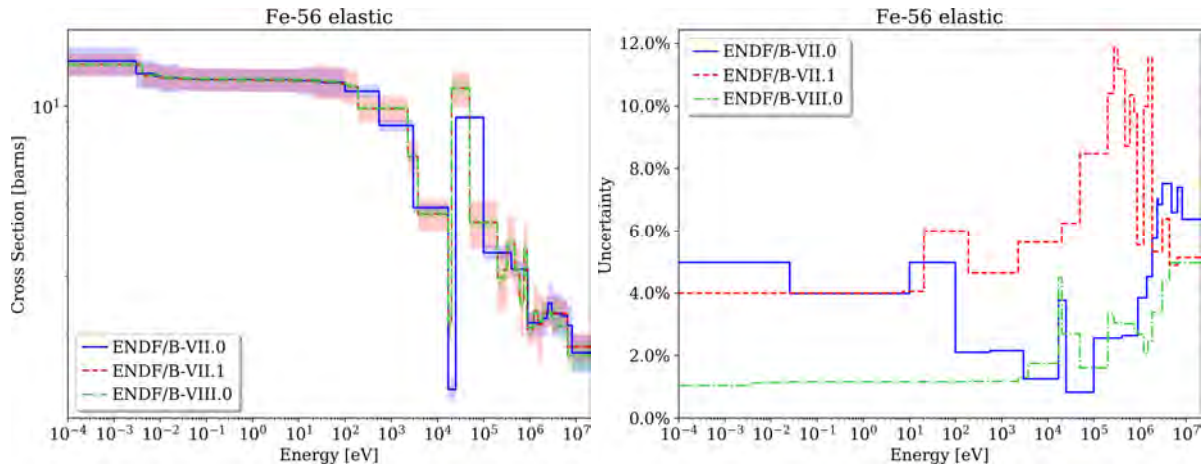
Figure 2-41 ^{56}Fe Elastic Scattering Nominal Data and Uncertainty
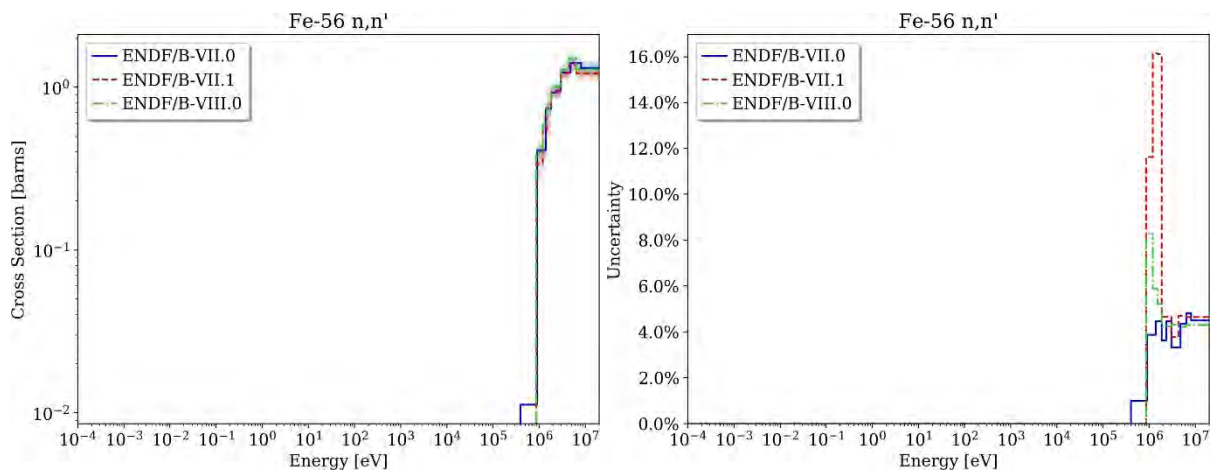
Figure 2-42 ^{56}Fe Inelastic Scattering Nominal Data and Uncertainty

The propagation of cross section uncertainties to β_{eff} in an LWR lattice calculation revealed significant β_{eff} uncertainties of approximately 7% for fresh fuel and approximately 15% for depleted fuel (Radaideh et al., 2019). Different studies found β_{eff} uncertainties of up to 4% for thermal and fast spectrum systems (Aures et al., 2017b; Kodeli, 2013). The ^{238}U scattering reactions were identified as major contributors to the uncertainty for fast spectrum systems, and the delayed neutron multiplicity of ^{235}U and ^{239}Pu for thermal systems.

Due to the buildup of Pu during depletion in an LWR, the value of β_{eff} decreases over time; consequently, the uncertainty in this value becomes even more relevant for safety analyses. Advanced reactor systems such as SFRs that are fueled with a mixture of U and Pu fuel show a smaller β_{eff} value than LWR systems; the impact of nuclear data uncertainties on β_{eff} in these systems is expected to be significant.

With respect to β_{eff}, some correlations are expected between correlated data such as fission cross section, neutron multiplicity, and fission spectrum. However, the correlations are assumed to be independent—not correlated—in ENDF/B. In fact, the current ENDF/B format cannot even store correlations between these reactions. In a recent ORNL study, the existing covariance library was augmented with such correlations (Sobes et al., 2019). It was demonstrated that the consideration of these additional correlations is relevant and that they have a visible impact on uncertainty analysis. Since all the above-mentioned data are used in the calculation of β_{eff}, a significant impact on the uncertainty of β_{eff} is expected when such correlations are included in the analysis.

2.2.3 Further Comments on the Availability and Use of Covariance Data

While ENDF/B provides a large number of uncertainty data, there are other nuclear data libraries containing uncertainty data that are not yet included in ENDF/B. For example, the SCALE covariance library not only contains ENDF/B data, but also data for missing fission spectrum uncertainties from JEFF. Furthermore, SCALE's libraries contain low-fidelity uncertainty data generated during the Low-Fidelity Covariance Project, which used simple procedures to estimate data uncertainties in the absence of high-fidelity covariance data (Little et al., 2008; Wieselquist et al., 2020). The available nuclear data libraries are still missing a significant number of uncertainties for various materials and reactions. For example, covariance data of inelastic scattering, (n,2n) and other neutron interactions are missing for relevant nuclides such as ^{197}Au (Bailey, 2020).

The covariance matrices in the ENDF/B libraries sometimes do not show their intrinsic attributes. For example, they may be not positive semi-definite (sometimes caused by limited precision when storing them in a particular format), they can show nonphysically large correlations, or they present correlations that seem incorrect because the data in certain energy ranges are independent (Wiarda et al., 2018). Depending on the application need (e.g., required matrix inversion), it may be necessary to modify the matrices to be able to perform the uncertainty calculations. Even if all relevant uncertainty data were available, the following three requirements must be met before the data can be used in sensitivity and uncertainty analyses:

1. The tools for nuclear data processing must be able to handle the provided data.

2. The data must be stored in a format suitable for subsequent use in uncertainty/sensitivity analysis tools.

3. The uncertainty/sensitivity analysis tools must be able to read and use the data.

Not all available nuclear data processing codes can process all data provided in the evaluated nuclear data files. Furthermore, the output format of processing codes might not allow storage of the data (e.g., consider the addition of a second dimension to the data). Modifications of the output format usually require modifications of the analysis tools that use the data.

The usability of existing nuclear data is impacted by the available computational capabilities that use these data. The perturbation theory–based approach relies on calculation of sensitivity coefficients for an output quantity with respect to the input data uncertainty. However, such sensitivity coefficients are not yet implemented for all available nuclear data in commonly used sensitivity analysis tools. In the random sampling approach, data provided in two dimensions (e.g., fission spectrum) cannot necessarily be sampled. Furthermore, many tools can only consider data in multigroup representation, but not in continuous-energy (CE) representation.

For example, the AMPX code system used to process nuclear data for SCALE cannot currently store available angular scattering uncertainties. Furthermore, it is not yet possible to consider the incident neutron energy dependence of the fission spectrum; uncertainties are currently included only for mean incident energies (Wiarda et al., 2016).

During the challenging process of developing ENDF/B libraries, nuclear data mean values are adjusted based on data from criticality experiments in the International Criticality Safety Benchmark Evaluation Project (ICSBEP) Handbook. As a result of this adjustment, the mean values allow for an accurate prediction of the multiplication factor values for such experiments. The covariance data development does not include or reflect this type of adjustment, which can sometimes lead to an inconsistent approach in predicting uncertainties for integral quantities such as the multiplication factor. The variation of calculated vs. experimental (C/E) multiplication factors for large sets of ICSBEP experiments was shown to be significantly smaller than that predicted using ENDF/B covariance data (Williams et al., 2017). However, methods are available to account for available information on the experiments in the generation of adjusted covariance data, enabling a more consistent approach in calculating C/E distributions (Salvatores et al., 2013). The nuclear data community is currently engaged in discussing an optimal approach to address the adjustment of the covariance data to better represent uncertainty in integral quantities (CSEWG, 2018; CSWEG, 2019).

3   ANALYSIS APPROACH

This section describes the approach for identifying and assessing key nuclear data impacting reactivity in the selected advanced reactor systems. The literature research presented in Section 2.2 is based on publications that include detailed descriptions of the reactor concepts of interest, the interrogation of available nuclear data libraries, published experience with LWRs, and publications providing results of sensitivity and uncertainty analyses with respect to nuclear data. The sensitivity and uncertainty analysis methods that were used in this study are described below, with a focus on those implemented in the SCALE code system for this project.

3.1   Geometry and Material Data

Publicly available literature was explored to identify representative geometrical and material definitions of the investigated advanced reactor technologies, as presented in Section 2.2. The relevant nuclides for these systems were identified by considering the material compositions and the volumetric abundance of these materials in the reactor. Particular consideration was given to major differences in the fuel, moderator (if applicable), coolant, and structure materials.

3.2   Interrogation of ENDF/B Libraries

Nuclear reactions important for the relevant nuclides as identified in the literature review were determined by studying the cross sections as provided in the ENDF/B libraries. In particular, the ENDF/B-VII.0, ENDF/B-VII.1, and ENDF/B-VIII.0 libraries were considered (Brown et al., 2018; Chadwick et al., 2006; Chadwick et al., 2011). The libraries' cross sections and uncertainties were compared to identify major differences that could result in a significant impact on reactor safety analyses.

SCALE's covariance libraries—which were used for the library interrogation—contain data mainly from the indicated ENDF/B release. They also contain (1) additional fission spectrum uncertainties from the JENDL 4.0 library (Shibata et al., 2012), (2) approximate uncertainties from the Low-Fidelity Covariance Project (Little et al., 2008), and (3) approximate covariance data from the Working Party on International Nuclear Data Evaluation Cooperation, Subgroup-26 (Salvatores and Jacqmin, 2008). More details on these libraries[1] can be found in the SCALE manual (Wieselquist et al., 2020).

Materials used in the selected advanced reactor technologies were assessed to identify gaps within the evaluated nuclear data libraries. In particular, the available data (e.g., individual reactions) of various nuclides within a nuclear data library were compared to identify missing nominal and uncertainty data.

3.3   Learning from LWR Experience

Because many of the considered advanced reactor systems use ^{235}U as the primary fission power nuclide, previous studies of LWR concepts were reviewed to discern the impact of nuclear data on the QOIs. Fuel characteristics and operating conditions such as power density, initial enrichment, and cycle length differ between LWRs and advanced reactor concepts. However, since ^{235}U is the major fissile nuclide at the beginning of life in LWRs and in many

---

[1] The ENDF/B-VII.0 and ENDF/B-VII.1 cross section and covariance libraries are available with the SCALE 6.2 release, and the ENDF/B-VIII.0 libraries will be available with SCALE 6.3.

advanced reactor concepts, some qualitative conclusions could be drawn to identify relevant fission products and actinides that build up in irradiated fuel during depletion. It must be noted that the spectral conditions differ between advanced reactor systems and traditional LWR systems; furthermore, advanced systems are expected to reach higher burnups than traditional LWRs.

3.4 Sensitivity Analysis

A common method for quantifying the importance of a nuclide reaction for an output QOI is the calculation of sensitivity coefficients via *linear perturbation theory* (Williams, 1986; Williams et al., 2001). In linear (or first-order) perturbation theory, the derivatives of the output quantity Y with respect to the input parameters—in this case, cross sections Σ—are obtained for all nuclides i of the model of interest with all reactions x in all energy groups g:

$$S_{Y,\Sigma_{x,g}^i=\cdot} = \left(\frac{\Sigma_{x,g}^i}{Y} \frac{dY}{d\Sigma_{x,g}^i} \right) \tag{1}$$

$S_{Y,\Sigma_{x,g}^i}$ are often called *sensitivity coefficients.* (Note: It is important not to confuse these sensitivity coefficients with the *sensitivity index* R^2 mentioned below in Section 3.5.2). $S_{Y,\Sigma_{x,g}^i}$, as defined above, describes the relative impact of a perturbation of cross section x of nuclide i in energy group g on the output quantity Y. In other words, a sensitivity coefficient defines how much an output quantity would change due to a change in a particular cross section. For example, the larger the sensitivity is for a particular cross section, the greater the impact of a change of this cross section will be due to an update from one evaluated library release to the next, or when considering this cross section's uncertainty.

It is important to note that the output quantity Y can be positive or negative. For example, sensitivities of reactivity differences are often analyzed, and these can be positive or negative. Using the convention of absolute values of Y in the denominator of Eq. (1), a negative sensitivity means that an increase in the cross section will cause a negative reactivity to become more negative, and it will cause a positive reactivity to become less positive. It is further important to note that Eq. (1) describes the *relative* sensitivity coefficient. In particular for reactivity differences, it can be useful for the interpretation to convert these relative sensitivity coefficients to absolute sensitivity coefficients.

This perturbation-based approach is implemented in SCALE's TSUNAMI code (Broadhead, 2004; Rearden et al., 2011). The multigroup (MG) version of TSUNAMI can be used in combination with various MG neutron transport kernels of SCALE, but it always requires forward and adjoint calculations. Since the release of SCALE 6.2, a CE version of TSUNAMI is available that only requires one forward calculation with Monte Carlo code KENO in CE mode. Both the *iterated fission probability* (IFP) method (Kiedrowski et al., 2011) and the *contribution-linked eigenvalue sensitivity/uncertainty estimation via track length importance characterization* (CLUTCH) method (Perfetti et al., 2016) can be used to determine the sensitivities. The IFP method computes adjoint solutions by recognizing that the importance of a neutron is proportional to the population of neutrons existing in some future generation resulting from the original neutron. After an initial neutron causes a fission event, the fission chain of this neutron is tracked for a number of generations (Kiedrowski et al., 2011). The CLUTCH method determines the importance by tracking how many fission neutrons are created by a neutron after the reaction of interest occurs (Perfetti et al., 2016). The application of CLUTCH requires appropriate settings to be determined to calculate the average importance generated per fission

neutron emitted (F*) in a spatial grid. Depending on the application (model size, spectral conditions), it can be challenging to determine settings for a well-converged F* mesh. For large full-core models with large reflector regions like the models considered in this project, it can be challenging to converge F* in outer reflector regions where few or no neutrons are born. While KENO-IFP is only available in serial mode, KENO-CLUTCH can be used in parallel with multiple processors to speed up the calculation. Therefore, the CE TSUNAMI results reported here were determined using KENO-CLUTCH, and KENO-IFP served for confirmatory analyses.

Direct perturbation calculations were also performed in conjunction with all CE TSUNAMI calculations to confirm the largest obtained sensitivities and thereby the adequacy of the settings chosen for the CE TSUNAMI calculations.

For output quantities involving reactivity differences, such as temperature feedback and CR worth, SCALE's module TSAR (Williams, 2007) was used to combine the sensitivity coefficients obtained from calculations at two different states for determining sensitivity coefficients for the reactivity difference.

There are other methods for sensitivity analysis, such as one-at-a-time perturbations of particular cross sections to understand the impact of a change of this cross section to a certain output quantity. However, the sensitivity analyses in this paper were performed only via perturbation theory and comparisons of calculations using different ENDF/B libraries.

3.5   Uncertainty Analysis

Uncertainty analyses were performed through linear perturbation theory and the random sampling approach.

3.5.1   Linear Perturbation Theory

The sensitivity coefficients determined through linear perturbation as described in Section 3.4 can be used to calculate the uncertainty of the investigated output due to nuclear data uncertainties.

The nuclear data uncertainties are given in energy-dependent covariance matrices for each nuclide reaction and for correlations between different nuclide reactions. Using these covariance matrices and the sensitivity coefficients, the application of first-order uncertainty propagation (the so-called *sandwich formula*) leads to the total output variance (Broadhead, 2004; Rearden et al., 2011):

$$\sigma_Y^2 = S_{Y,\Sigma}^T \, C \, S_{Y,\Sigma} \, . \tag{2}$$

Vector $S_{Y,\Sigma}$ includes the sensitivities of all the input cross sections Σ to the output quantity Y, and the covariance matrix C includes the covariance matrices of all the input cross sections. The square root of this total output variance provides the uncertainty of the output Y in terms of the standard deviation. This value is often labeled with unit "% ΔR/R" in TSUNAMI terminology, where R indicates a certain output response such as k_{eff} or a reactivity difference.

If Eq. (2) is applied to only the covariance matrix of one nuclear reaction, then the individual contribution of only this reaction to the output uncertainty is obtained. In addition to the total output uncertainty, TSUNAMI provides a list of the individual contributions of all relevant covariance matrices in terms of % ΔR/R. These contributions are ordered according to their

magnitude, therefore the top contributors to the output uncertainty can be easily identified. Since every available covariance matrix is considered independently, the list of contributors shows contributions from individual nuclide reactions as well as contributions from correlations between different nuclide reactions. In other words, listed contributions of individual nuclide reactions only consider uncertainties and correlations within the reaction (e.g., between the cross sections in the different energy groups), but not correlations to other reactions which could potentially reduce the overall contribution of a nuclide reaction. However, the impact of these correlations is usually small and does not significantly influence the ranking.

The connection of the individual contributions of individual covariance matrices to the overall output uncertainty is as follows: The relative standard deviation of a response can be computed from the individual contributions as the square root of a difference between two terms. The first term is the sum of the squares of the contributions with positive signs. The second term is the sum of the squares of the contributions with negative signs.

3.5.2 Random Sampling Approach

Another approach for determining the uncertainties in the output due to nuclear data uncertainties is the random sampling approach. This approach is especially useful for cases in which sensitivity coefficients cannot be easily determined using a perturbation theory approach for an output QOI such as power distribution.

For the random sampling approach, cross sections are randomly sampled based on the covariance matrices. The result of the random sampling is a library of perturbation factors for all cross sections in all energy groups that are generated considering the dependencies between the cross sections. The multiplication of the nominal cross sections by the corresponding perturbation factor leads to the perturbed cross sections.

The same reactor physics calculation is then repeated a number of times, always with a different set of perturbed cross sections. With a statistical analysis of the output, the resulting mean value and the uncertainty in terms of the standard deviation can be calculated for any output QOI.

For a sample size N, the sample mean $\bar{Y}$ and the standard deviation σ of the output values Y_1, ..., Y_N are calculated as follows:

$$\bar{Y} = \frac{1}{N} \sum_{i=1}^{N} Y_i, \qquad \sigma = \sqrt{\frac{1}{N-1} \sum_{i=1}^{N} (Y_i - \bar{Y})^2}. \tag{3}$$

This approach is followed by SCALE's Sampler sequence (Williams et al., 2013). Sampler is a super-sequence that can use any SCALE neutron transport kernel and reactor physics code for random sampling calculations. Input files for the calculations with perturbed cross sections are automatically set up, so a statistical analysis of the output QOIs can be requested. Sampler can currently be used with SCALE's MG modules; the extension to CE is in development.

While the identification of the top contributing nuclide reactions to the output uncertainty is a side product when using perturbation theory, it is challenging to implement a similar study for the random sampling approach because the reliability of sensitivity results depends on the large number of uncertain input parameters and the sample size. Sampler was recently extended to

allow the calculation of a sensitivity index R^2 (Bostelmann, 2020) which provides a measure of the importance of individual nuclear reactions to the observed output uncertainty.

R^2 is determined from correlations of the calculated output quantity Y (e.g., k_{eff}) with the sampled input cross sections Σ_A of nuclide reaction A (e.g., ^{235}U fission) in k groups (e.g., 56 energy groups if sampled from SCALE's 56-group covariance library) while accounting for correlations between the input cross sections:

$$R^2_{Y,A} = \boldsymbol{r}_{Y,A} \boldsymbol{C}^{-1}_{AA} \boldsymbol{r}^t_{Y,A}$$

with vector $\boldsymbol{r}_{Y,A}$ of size k containing the sample correlation coefficients r_N (calculated from sample size N) between the output Y and the input cross sections of nuclide reaction A:

$$\boldsymbol{r}_{Y,A} = \left(r_N(Y, \Sigma_1) \right), \cdots, r_N(Y, \Sigma_k)$$

and matrix $\boldsymbol{C}_{AA}$ of size $(k \times k)$ containing the sample correlation coefficients between the sampled input cross sections:

$$C_{AA} = \begin{pmatrix} r_N(\Sigma_1, \Sigma_1) & \cdots & r_N(\Sigma_1, \Sigma_k) \\ \vdots & \ddots & \vdots \\ r_N(\Sigma_k, \Sigma_1) & \cdots & r_N(\Sigma_k, \Sigma_k) \end{pmatrix}$$

It is important to emphasize that here the correlation matrix used in the calculation of R^2 is not the population correlation matrix that was initially used for the random sampling. Rather, it is the matrix containing the sample correlation coefficients between the sampled input cross sections. If the sample size approaches infinity, then the sample correlation matrix of nuclide reaction A converges toward the correlation matrix that is used for sampling of nuclide reaction A (i.e., the correlation matrix that is the normalized version of the covariance matrix as available from the ENDF/B covariance library).

R^2 is interpreted as the fraction of the output variance caused by the uncertainties of an individual nuclear reaction, including the fraction of uncertainties that this reaction has in common with other reactions due to correlations (Glaeser, 2012). R^2 has the following characteristics:

- The values range from 0 to 1,

- $R^2 = 0$ indicates that a reaction has no impact on the observed output uncertainty,

- $R^2 = 1$ indicates that the entire observed output uncertainty can be explained by only the uncertainty of this particular reaction.

R^2 can therefore be considered as an importance indicator for a certain nuclide reaction. If a large R^2 value is obtained for a certain nuclide reaction, the impact of the uncertainty of this reaction on the observed output uncertainty is large. If the obtained R^2 value is small, then the impact of this reaction on the output uncertainty is small.

If the calculation of R^2 is requested in Sampler for a certain output quantity, Sampler calculates R^2 for all reactions of all nuclides of the model. Sampler then provides a ranking of the determined R^2 values, simplifying the identification of the most relevant reactions. Each R^2 value is thereby accompanied with a 95% statistical confidence interval (the statistical uncertainty of

this value) and a 95% significance level. The R^2 value can be considered statistically relevant only if it is larger than the corresponding significance level; in this case, the result is not caused by statistical noise. The calculation of R^2 requires a sample size that is sufficiently large. A sample size of 1,000 can lead to the identification of 5–10 significant nuclear reactions. With smaller sample sizes, the statistical uncertainty of the determined R^2 values is often too large to identify any relevant reaction.

It is important to note that R^2 cannot directly be compared with the top contributors obtained with TSUNAMI. Both approaches can be used to identify relevant nuclide reactions for the observed output uncertainty, and the identified nuclide reactions have been shown to be mostly consistent. However, the obtained values are different due to the application of different approaches with different interpretations and the consideration of correlations between reactions in case of R^2.

4 SELECTED BENCHMARKS

Available benchmarks and fuel irradiation data that are applicable for evaluating the impact of advanced reactor safety analyses on uncertainties and gaps in nuclear data were identified and assessed. Benchmarks were identified by searching (1) the OECD/NEA ICSBEP handbook, (2) the OECD/NEA International Reactor Physics Experiment Evaluation Project (IRPhEP) handbook, (3) ongoing OECD/NEA benchmark activities, and (4) documentation in public literature. The ICSBEP handbook includes criticality safety benchmark specifications with a wide range of fissile materials, physical forms of fissile materials, and neutron spectra. The IRPhEP handbook contains specifications of a large number of experiments with various reported output quantities such as reactivity effects and power distributions.

Relevant benchmarks were identified by selecting reactors with geometry, materials, and neutron energy spectra that are similar to those of the advanced reactor technologies of interest. Given the limited availability of measured data for advanced reactor systems, only theoretical or simplified descriptions were found for some reactor technologies. However, as long as the models include representative geometric dimensions and representative materials, uncertainty analyses of these models can serve well to gain understanding of the impact of nuclear data uncertainties and to identify relevant nuclide reactions. Six relevant benchmarks were identified, of which three are experimental, and three are purely computational (Table 4-1). One experimental and one computational benchmark contain depleted fuel; all others are limited to fresh fuel. This section provides short descriptions of the selected benchmarks, along with the measured data available for comparison.

Table 4-1   Overview of Selected Advanced Reactor Technology Benchmarks[a]

Reactor type	Reactor technology	Selected benchmark	Type
Thermal spectrum, HTGR	Pebble-bed HTGR	HTR-10 (Terry et al., 2007)	Experiment
Thermal spectrum, MSR	FHR	UC Berkeley Mark1 PB-FHR (Andreades et al., 2014)	Computational benchmark
Thermal spectrum, MSR	Graphite-moderated MSR	MSRE (Shen et al., 2019)	Experiment
Fast spectrum, oxide and metal fueled stationary microreactor	HPR	INL Megapower Design A[b] (Sterbentz et al., 2018)	Computational benchmark
Fast spectrum, metal and oxide fueled, sodium-cooled reactor	SPR	EBR-II (Lum et al., 2018) ABR-1000 (Buiron et al., 2019)	Experiment Computational benchmark

[a] Although fast spectrum MSRs were identified as a relevant reactor concept (Table 1) and discussed in Section 2.2, such a concept was not included here because no description of such a concept with details sufficient for modeling could not be found in the open literature.

[b] The original design contains oxide fuel. However, for this project, metal fuel was assumed.

4.1 HTR-10, High-Temperature Gas-Cooled Reactor

The benchmark selected for the pebble-bed HTGR technology is the small 10-megawatt thermal (MWth) prototype pebble-bed reactor HTR-10 operated at Tsinghua University in China. With a core diameter of 1.8 m and a mean height of 1.97 m, it contains almost 10,000 fuel pebbles surrounded by graphite reflector structures. This reactor was designed to help in the development of pebble-bed technology in China and to test fuel, safety features, operational behavior, and other factors. Construction began in 1995, first criticality was achieved in December 2000, and the reactor operated at full power condition through January 2003.

The IRPhEP handbook contains high-fidelity specifications of the initial critical configuration (Terry et al., 2007). For this configuration, the conus and discharge tube were filled with pure graphite "dummy" pebbles. The key characteristics of the HTR-10 are presented in Table 4-2.

Table 4-2   Key Characteristics of the Initial Critical Configuration of the HTR-10 (Terry et al., 2007)

Description	Value
Reactor power (MWth)	10
Coolant ambient	Air
Number of pebbles in the core	
Fuel pebbles	9,627
Dummy pebbles	7,263
Pebble packing fraction	61%
UO_2 fuel kernel density (g/cm³)	10.4
Uranium enrichment (wt% 235U)	17.0
Fuel kernel radius (mm)	0.25
Fuel particle coating layer materials (starting from kernel)	Buffer/PyC/SiC/PyC
Fuel particle coating layer thickness (mm)	0.09/0.04/0.035/0.04
Fuel particle coating layer density (g/cm³)	1.1/1.9/3.18/1.9
Number of particles per fuel pebble	8,385
Radius of fuel pebble (cm)	3.0
Radius of fuel zone in pebble (cm)	2.5
Graphite matrix and fuel pebble outer shell density (g/cm³)	1.73
Graphite density of reflector structures (g/cm³)	~1.76
Graphite density of boronated carbon bricks (g/cm³)	~1.53
Temperature of all materials (K)	300

The cylindrical core consisted of a mixture of 9,627 fuel pebbles and 7,263 dummy pebbles at a packing fraction of 61%. Criticality was achieved at room temperature while all CRs in the outer graphite reflector were withdrawn. Instead of including helium coolant, void spaces were filled with ambient air.
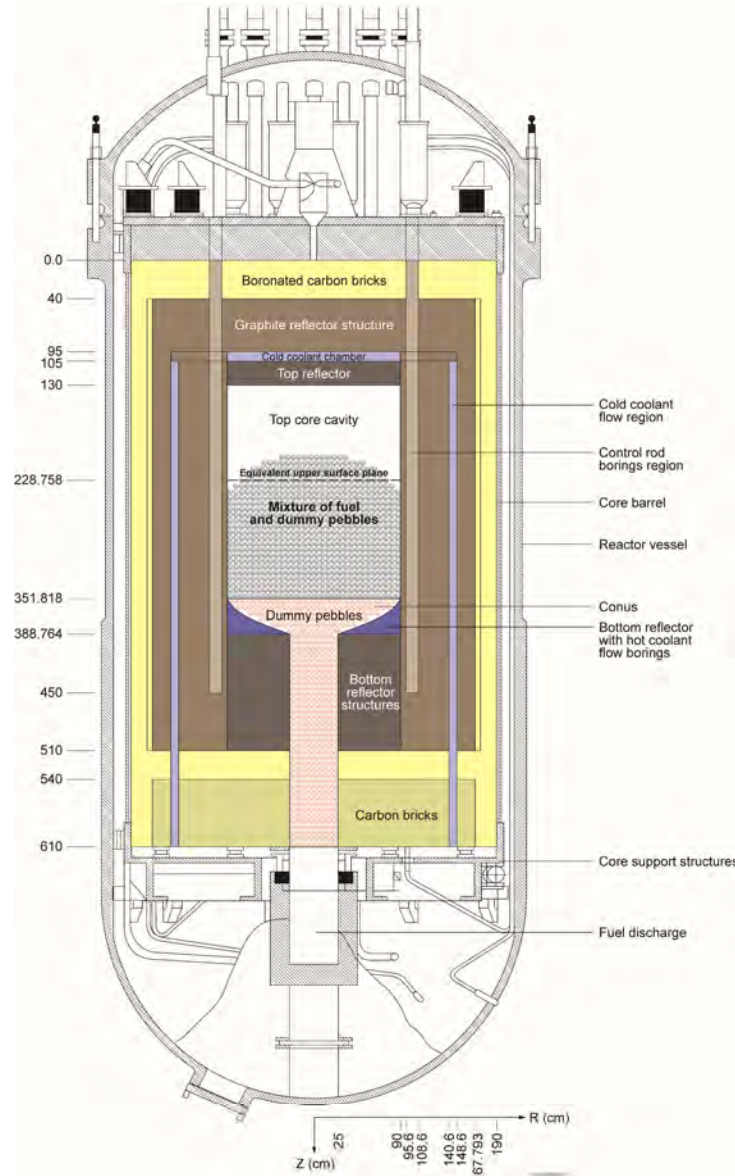
Figure 4-1 HTR-10 Initial Configuration (Terry et al., 2007).

The fuel pebble consisted of a fuel zone that was 5 cm in diameter and that contained over 8,000 TRISO fuel particles distributed randomly in a graphite matrix, surrounded by a 5 mm graphite layer, resulting in a pebble with a 6 cm outer diameter (Figure 4-3). The TRISO fuel particle was 0.91 mm in diameter and included a micro fuel kernel 0.5 mm in diameter that was composed of uranium oxide. The fuel kernel was enclosed by four concentric coatings: a porous graphite buffer, an inner PyC layer, a ceramic SiC layer, and an outer PyC layer (Figure 4-2). The ^{235}U enrichment of the fuel in this configuration of HTR-10 was 17 wt.%.
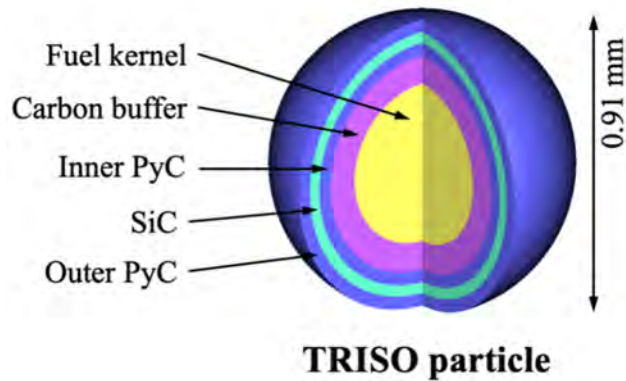
Figure 4-2 HTR-10 TRISO Fuel Particle
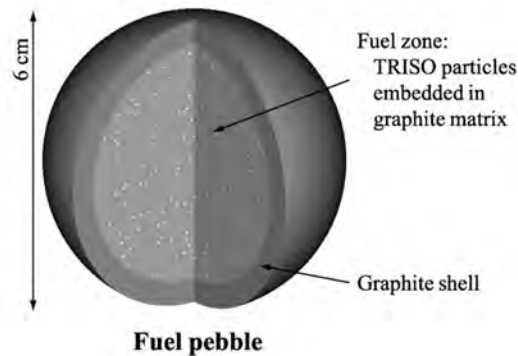
Figure 4-3 HTR-10 TRISO Fuel Pebble Model

The IRPhEP handbook provides an experimental eigenvalue, along with the corresponding experimental uncertainty for the first critical state of HTR-10.

SCALE/KENO-VI models of HTR-10 developed for ORNL studies (Ilas et al., 2012; Sunny and Ilas, 2010) were used for the computational analyses presented in this report. A comparison of eigenvalues calculated based on recent ENDF/B nuclear data libraries with the measured value and a first assessment of the impact of nuclear data uncertainties on the eigenvalue uncertainty for HTR-10 were documented in an earlier ORNL publication (Bostelmann et al., 2020).

4.2   PB-FHR-Mk1, Fluoride Salt-Cooled Pebble-Bed Reactor

The benchmark selected for the pebble-bed (PB) FHR technology is the preconceptual design for a small, modular 236 MWth reactor developed by the University of California, Berkeley. The Mark-1 (Mk1) PB-FHR design was developed within the scope of a US Department of Energy (DOE) project to establish the technical basis to design, license, and commercially deploy FHRs (Andreades et al., 2014). The key characteristics are presented in Table 4-3.

The PB-FHR-Mk1 design combines the HTGR fuel form with liquid fluoride salt coolant in a graphite-moderated environment. The annular core is filled with 470,000 fuel pebbles surrounded by 218,000 graphite moderator pebbles, and the core is contained in graphite

reflector structures (Figure 4-4). The pebbles travel from the bottom of the core to the top. On average, a fuel pebble completes 8 passes through the core before reaching its final discharge burnup of 180 GWd/HTIHM. As in an HTGR, the fuel pebbles contain TRISO particles distributed in a graphite matrix, but in this case they have an average of 4,730 TRISO particles per pebble, which corresponds to 1.5 g U per pebble. However, the fuel pebbles in the FHR are significantly smaller (3 cm diameter compared with 6 cm the HTR-10, for example). The fuel particles within the FHR pebble are distributed in a shell-like fuel region compared with a spherical fuel region in HTR-10. The fuel region in the FHR pebble is 1.5 mm thick, and the packing fraction of the TRISO particle in this shell is 40% (Figure 4-5).

The fuel material is $UC_{0.5}O_{1.5}$ with an enrichment of 19.9 wt% ^{235}U. The coolant salt is FLiBe, which is a mixture of LiF and BeF_2. Core inlet and outlet temperatures are approximately 600 and 700°C, respectively, and the fuel temperature ranges between 700 and 800°C. The average thermal power per fuel pebble is 500 W. Burnups reaching up to 180 GWd/MTHM are intended. Reactivity control is achieved using CRs and blades containing boron carbide (Andreades et al., 2014).

A SCALE model of this reactor has been developed using an MCNP model published by Cisneros (2013) as a starting point.
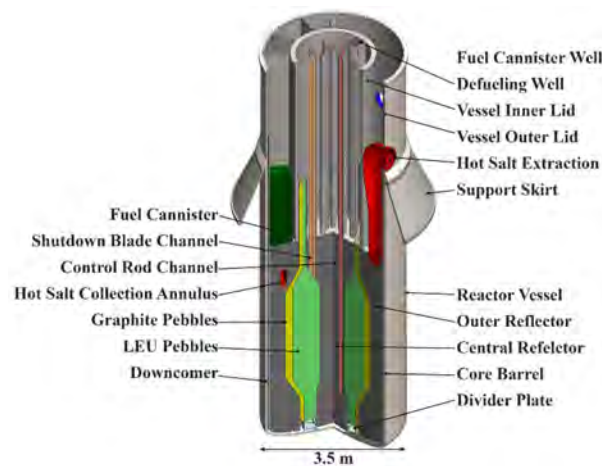
Figure 4-4 PB-FHR-Mk1 Full Core Model (Andreades et al., 2014)
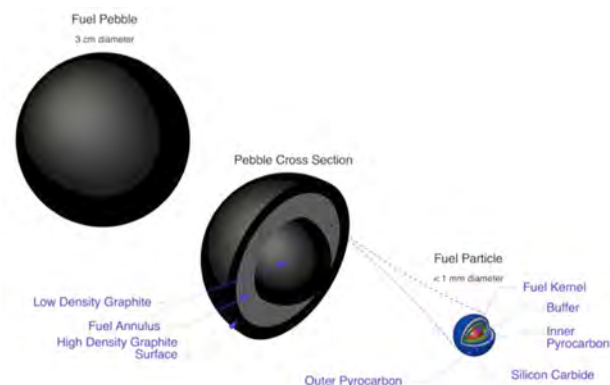
Figure 4-5 PB-FHR-Mk1 Fuel Pebble Model (Andreades et al., 2014)

Table 4-3   Key Characteristics of the PB-FHR-Mk1 (Andreades et al., 2014)

Description	Value
Reactor power (MWth)	236
Coolant	FLiBe salt
$UC_{0.5}O_{1.5}$ fuel kernel density (g/cm^3)	10.5
Uranium enrichment (wt% ^{235}U)	19.9
Fuel kernel radius (mm)	0.20
Fuel particle coating layer materials (starting from kernel)	Buffer/PyC/SiC/PyC
Fuel particle coating layer thickness (mm)	0.100/0.035/0.035/0.035
Number of particles in pebble	4,730
Particle packing fraction in fuel pebble	40%
Radius of fuel pebble (cm)	1.5
Radius of fuel zone in pebble (cm)	
Inner	1.25
Outer	1.40
Graphite matrix and fuel pebble outer shell density (g/cm^3)	1.73
Graphite density of reflector structures (g/cm^3)	~1.76
Graphite density of boronated carbon bricks (g/cm^3)	~1.53
Number of pebbles in the core	
Fuel pebbles	470,000
Dummy pebbles	218,000
Pebble packing fraction (%)	60
Core dimensions (cm)	
Inner reflector radius	35
Outer fuel pebble region	105
Outer graphite pebble region	125
Volume of active fuel region (m^3)	10.4
Average pebble thermal power (W)	500
Average pebble discharge burnup (GWd/MTHM)	180
Average pebble full-power lifetime (years)	1.40

4.3   MSRE, Molten Salt Reactor

The benchmark selected for the graphite-moderated MSR is the Molten Salt Reactor Experiment (MSRE). The MSRE was built at ORNL and operated between 1965 and 1969. Its purpose was to demonstrate key features of the molten-salt liquid-fuel reactor concept and to prove the practicality of the MSR technology. This was the first large-scale, long-term, high-temperature testing performed for a fluid fuel salt, graphite moderator, and new nickel-based alloys in a reactor environment. The circulating fuel was a mixture of lithium, beryllium, and zirconium fluoride salts that contained uranium fluorides. Reactor heat was transferred from the fuel salt to a coolant salt and was then dissipated to the atmosphere. The MSRE was designed to provide a thermal output of 10 MWth. The MSRE reached criticality for the first time in June

1965; the corresponding zero-power first critical experiment with ^{235}U was recently included in the IRPhEP handbook (Shen et al., 2019). Table 4-4 presents an overview of the key characteristics of the MSRE, and Figure 4-6 and Figure 4-7 are illustrations of the horizontal and vertical cross sections of the reactor core, respectively.

The MSRE core consisted of a graphite structure within a cylindrical reactor vessel. The fuel salt entered the flow distributor at the top of the vessel through the fuel inlet, was then distributed evenly around the circumference of the vessel, and then flowed downward through a ~2.54 cm annulus between the vessel wall and the core can. The salt was then pumped upward through the graphite structure. This graphite structure was a lattice of vertical stringers with a side length of 5.08 cm and an axial length of 170.03 cm. The salt could flow through more than 1,000 channels, each ~1 cm thick, that were formed by grooves in the sides of the stringers. In the center of the core, three graphite sample baskets were mounted to allow the behavior of the graphite moderator to be investigated in the reactor environment through periodic removals of graphite specimens. The salt served the dual purpose of carrying the fuel and serving as the primary coolant. It comprised (1) the carrier salt, containing the beryllium, zirconium, and most of the lithium fluorides, (2) depleted uranium eutectic (73LiF-27UF$_4$), and (3) highly enriched uranium eutectic (73LiF-27UF$_4$). The reactor vessel consisted of INOR-8, a nickel-based alloy. The core was surrounded by an insulator, simplified in the benchmark specification as a homogeneous mixture (O, Fe, Al, H, Si, Ca), and a steel thermal shield. The temperature specified for the thermal shield and insulation is 305 K; the temperature specified for all other materials in the benchmark is 911 K. The IRPhEP handbook provides an experimental eigenvalue, along with the corresponding experimental uncertainty. The benchmark also provides a calculated eigenvalue obtained using the Serpent code, and it documents a first assessment of the influence of nuclear data uncertainties on the eigenvalue, as also summarized in several conference papers (Fratoni et al., 2020; Shen et al., 2018; Shen et al. 2021).
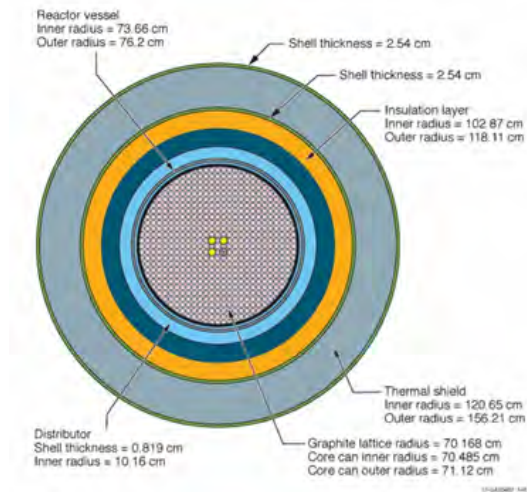
Figure 4-6 Horizontal Cross Section of the MSRE Benchmark (Shen et al., 2019)[1]
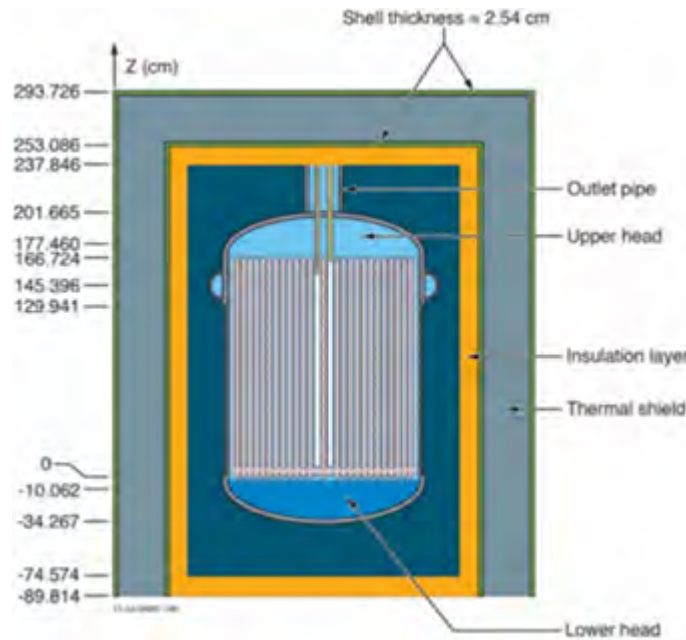
Figure 4-7 Vertical Cross Section of the MSRE Benchmark (Shen et al., 2019)[2]

---

[1] Molten salt is light blue, graphite lattice is pink, reactor vessel, INOR (Ni-based alloy) is gray, void is dark blue, insulation, homogeneous mixture (O, Fe, Al, H, Si, Ca) is orange, stainless steel shells are green, mainly steel thermal shield is gray.

[2] Molten salt is light blue, graphite lattice is pink, reactor vessel, INOR (Ni-based alloy) is gray, void is dark blue, insulation, homogeneous mixture (O, Fe, Al, H, Si, Ca) is orange, stainless steel shells are green, mainly steel thermal shield is gray.

Table 4-4   Key Characteristics of the MSRE (Shen et al., 2019)

Description	Value
Reactor power (MWth)	10
Fuel and coolant	64.88LiF-29.27BeF$_2$-5.06ZrF$_4$-0.79UF$_4$ (expressed as molar percent)
Fuel salt density (g/cm^3)	2.3275
Graphite density (g/cm^3)	1.8507
Graphite lattice radius (cm)	70.285
Core can radius (cm)	
Inner	71.097
Outer	71.737
Reactor vessel radius (cm)	
Inner	74.299
Outer (in active region)	75.741
Graphite stringer width (cm)	5.084
Fuel channel width (cm)	1.018
Fuel channel thickness (cm)	3.053
Graphite stringer height (cm)	170.311
Height of the core can (cm)	174.219
Total height of the vessel (from bottom of vessel to top of outlet pipe) (cm)	272.113

4.4   INL Design A-Met, Heat Pipe Reactor with Metal Fuel

Heat pipe–cooled reactors with limited power output were first developed at Los Alamos National Laboratory (LANL) during the 1960s. Originally designed for space applications, the Kilopower heat pipe concept was scaled up to the low megawatt electric (MWe) range and is now known as the Megapower reactor (Mcclure et al., 2015, Figure 4-8). This concept was further expanded upon by Idaho National Laboratory (INL), and two alternative core designs were proposed (Sterbentz et al., 2018). For this work, Design A was selected from these INL designs for the analysis of HPRs. INL Design A includes fuel elements with a solid fuel region and heat pipes containing a potassium (K) coolant. The heat carried away from the core via the heat pipe is converted to power using an open-air Brayton cycle. The core is surrounded with 12 radial CDs and has Al$_2$O$_3$ and BeO reflectors on all sides (Figure 4-9). While the original LANL design (Figure 4-7) is oriented horizontally, INL Design A is oriented vertically. Design A consists of hexagonal fuel elements that contain a heat pipe (Figure 4-10). The original INL Design A specifications include 19.75% [235]U enriched UO$_2$. However, in this study, a slightly modified version with metallic fuel consisting of 18.1% [235]U enriched uranium with a 10% weight fraction of zirconium (U-10Zr) was considered based on work presented in ANL-NSE-19/25 (Hu et al., 2019). Other key design characteristics are shown in Table 4-5. A limited number of neutronics analyses performed with MCNP and Serpent reported calculated values for eigenvalue, reactivities, and reactor power for all concepts (Hu et al., 2019; Lee et al., 2019; Sterbentz et al., 2018). However, since the design studied here deviates from the models in the referenced reports in terms of the fuel composition as mentioned above (metallic fuel instead of oxide fuel), only qualitative comparisons can be performed.
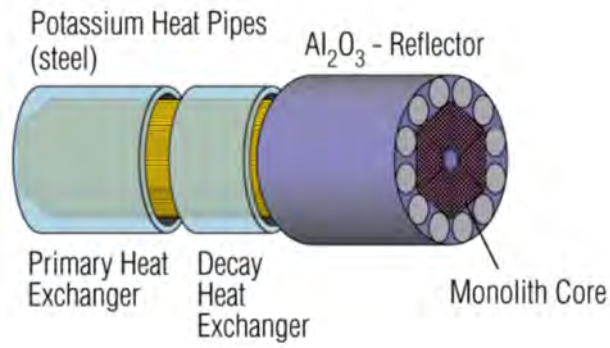
Figure 4-8 Megapower LANL Concept Illustration (Mcclure et al., 2015)
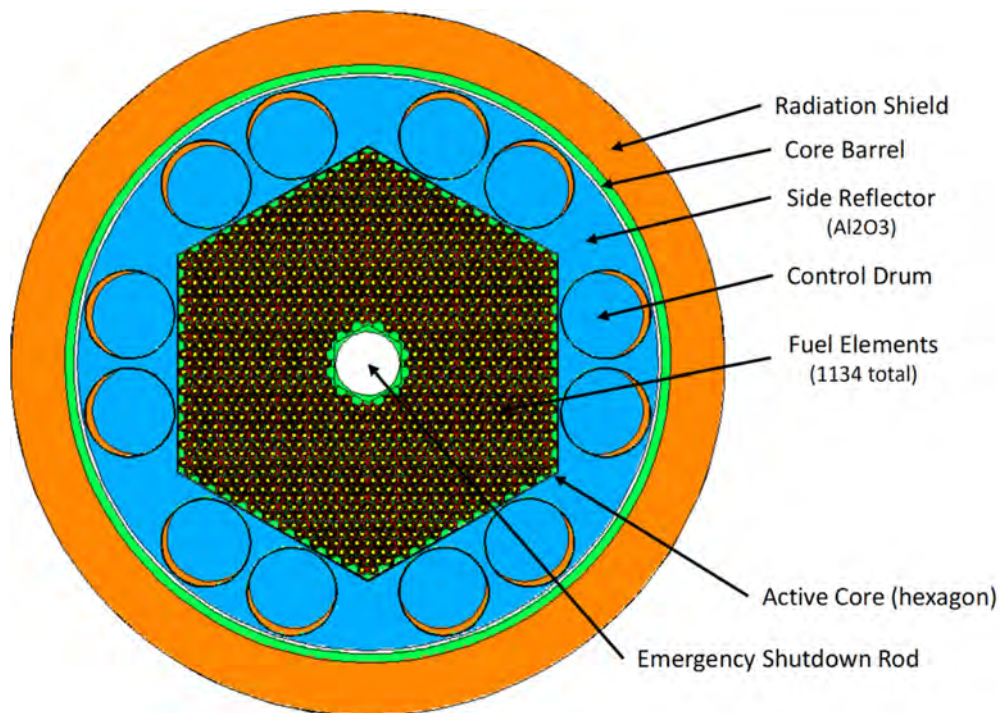
Figure 4-9 Cross Sectional View of INL Design A (Sterbentz et al., 2018)
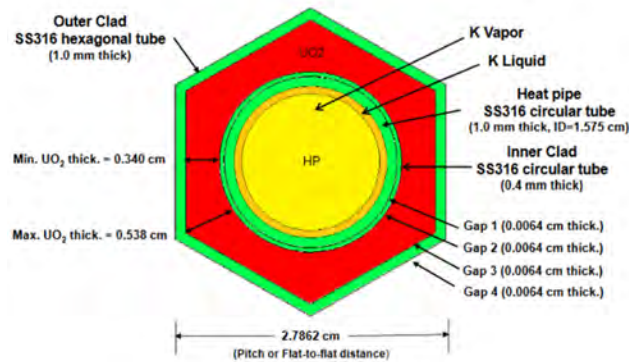
Figure 4-10 Material Composition and Dimensions for INL Design A Heat Pipe Fuel Element (Sterbentz et al., 2018)

Table 4-5   Key Characteristics of the INL Design A (Sterbentz et al., 2018)

Description	Value
Reactor power (MWth)	5
Fuel type	U-10Zr[*]
^{235}U enrichment (wt%)	18.1[*]
Fuel element geometry	Hexagonal with central hole
Number of heat pipes	1,134
Heat pipe working fluid	Potassium
Potassium mass (g/pipe)	100
Potassium temperature (°C)	675
Total heat pipe length (m)	4
Maximum air temperature (°C)	675
Number of fuel elements	1,134
Fuel pin or element pitch (cm)	2.78
Number of CDs	12
Core diameter (cm)	101.2
Mass of U in core (MTU)	4.57
Mass of ^{235}U in core (kg)	904
Beginning of life excess reactivity ($)	3.82

* Fuel specifications taken from (Hu et al., 2019).

4.5   EBR-II, Sodium-Cooled Fast Reactor

The benchmark experiment selected for the metal fuel SFR technology is the Experimental Breeder Reactor II (EBR-II). EBR-II was operated from 1964 through 1994 by Argonne National Laboratory on a site which now belongs to INL. The reactor had a maximum heat output of 62.5 MWth. Although it was initially designed to breed more fuel than it consumed, EBR-II was later reconfigured to operate as an irradiation facility, and a variety of fuels and structural materials were tested there. The evaluation of EBR-II run 138B, a test within the Shutdown Heat Removal

Tests series conducted on April 3, 1986, was recently included in the IRPhEP handbook (Lum et al., 2018). Table 4-6 presents an overview of the key characteristics of this EBR-II benchmark configuration.

The EBR-II core consisted of 637 hexagonal assemblies divided into three regions: the core, an inner blanket, and an outer blanket (Figure 4-11). The core region consisted of driver (full worth and half worth) assemblies, experimental/instrumentation assemblies, dummy assemblies, and movable assemblies that were used for reactivity control. The safety and control assemblies contained both a fuel and an absorber region. The core was surrounded by an inner blanket of stainless-steel reflector assemblies. The outer blanket region consisted almost entirely of depleted uranium assemblies for breeding and reflection.

The driver fuel assemblies contained a hexagonal lattice of 91 fuel rods (Figure 4-12 and Figure 4-13). Each fuel rod consisted of enriched uranium metal surrounded by a stainless-steel cladding. Each rod had a wire which wrapped helically up the length of the fuel rod. Due to the complexity of modeling a toroid, the benchmark specifications suggest that a single cylinder be modeled, corresponding to the wire wrap. They also suggest that the region above and below the fuel area—the upper extension, lower extension, and lower adapter—be simplified as homogenized regions of stainless steel and sodium.

All materials in the EBR-II benchmark are assumed to be at a temperature of 343°C.

The IRPhEP handbook provides an experimental eigenvalue, along with the corresponding experimental uncertainty. The results of a criticality calculation based on the benchmark model are also provided. No other calculations of this particular EBR-II benchmark have been found in the open literature.
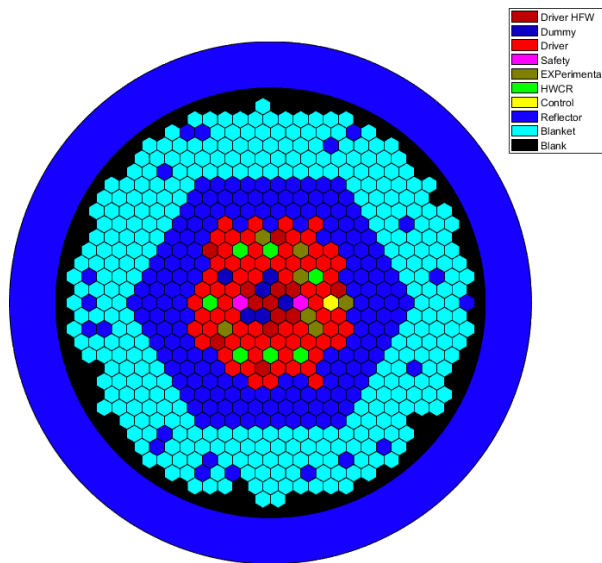
Figure 4-11 EBR-II Run 138B Core Configuration (Lum et al., 2018)
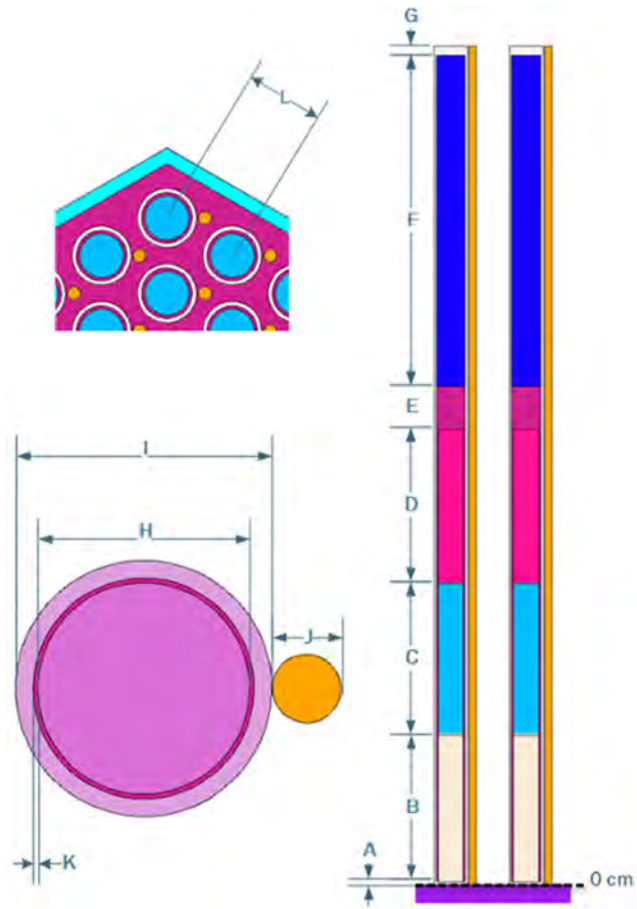
Figure 4-12 EBR-II Driver Rod (Lum et al., 2018)[3]

---

[3] The driver rod consisted of three fuel slugs (B, C, D), sodium bond (E), and gas plenum (F)
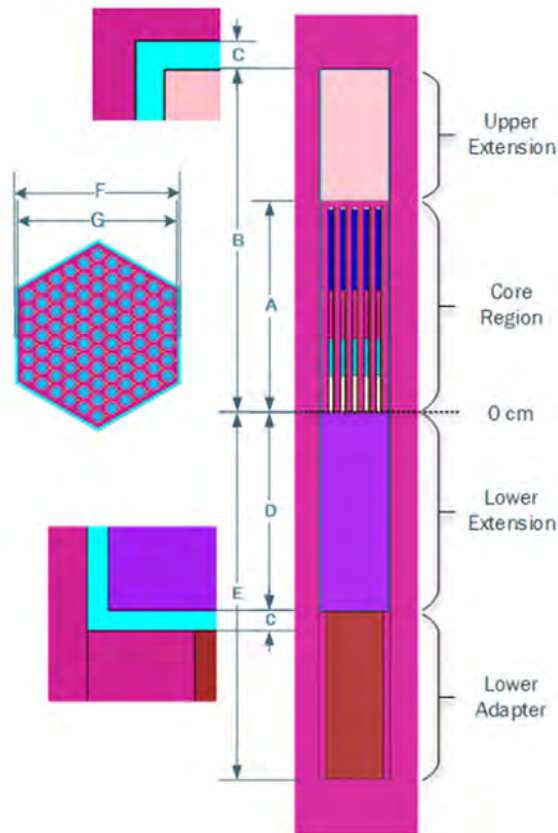
Figure 4-13 EBR-II Driver Assembly (Lum et al., 2018)

Table 4-6   Key Characteristics of EBR-II (Lum et al., 2018)

Description	Value
Reactor power (MWth)	62.5
Fuel material	Highly enriched uranium metal
Coolant material	Sodium
Major structural material	Steel
Temperature of all materials (K)	616
Number of fuel assemblies in the core:	
Full worth	70
Half worth	13
Number of fuel pins per assembly	91
Number of depleted uranium blanket assemblies	330
Assembly pitch (cm)	6.8877
Outer fuel radius (cm)	0.1651
Outer cladding radius (cm)	0.2210
Inner cladding radius (cm)	0.1905
Fuel pin pitch (cm)	0.566
Active core height (cm)	34.6075

4.6   ABR-1000, Sodium-Cooled Fast Reactor

The most relevant international activity with respect to nuclear data–related uncertainty analysis of SFRs is the OECD/NEA Benchmark for Uncertainty Analysis in Modeling for Design, Operation and Safety Analysis of SFRs (UAM-SFR) (Buiron et al., 2019). This benchmark is a successor of the OECD/NEA Sodium Fast Reactor core Feedback and Transient response (SFR-FT) task force (NEA, 2016). It was launched in 2015 to study reactivity feedback coefficients and their uncertainties with a medium-sized 1,000 MWth metallic core design based on the 1,000 MWth Advanced Burner Reactor (ABR) metallic core (Kim et al., 2009) and a large 3,600 MWth oxide core. The UAM-SFR benchmark includes full core neutronics and coupled neutronics/thermal-hydraulics calculations, and it focuses on analysis of the impact of nuclear data uncertainties on relevant output quantities.

For possible comparison with computational results of various participants, the UAM-SFR benchmark was considered for this study. Given the focus on SFR systems with metallic fuel in the United States, the 1,000 MWth metallic core (ABR1000) was chosen as a second SFR concept, along with EBR-II, for investigation in this study. The key characteristics of the ABR1000 are presented in Table 4-7.

The ABR1000 core consists of a grid of hexagonal assemblies (Figure 4-14). The fuel zone is divided into an inner and outer fuel zone, and each zone has a slightly different fuel composition. The fuel zone is surrounded by reflector assemblies and an absorbing shield. Reactivity control is maintained by moving control and safety assemblies into locations not occupied by fuel assemblies. The assembly pitch is 16.2471 cm, and the active core height is 85.82 cm.

The hexagonal fuel assemblies consist of a tight hexagonal lattice of fuel pins surrounded by a HT-9 steel wrapper. From bottom to top, the fuel pins consist of a lower reflector, an active zone with mixed uranium-transuranic-zirconium (U-TRU-Zr) metal alloy fuel, bond sodium (sodium within the fuel rod), and a helium gas plenum that is always encased in HT-9 steel cladding (Figure 4-15). The metal fuel temperature is 534°C, and the temperature of all structural materials and the coolant is 432.5°C.

The UAM-SFR benchmark exercise required the calculation of nominal values and uncertainties of the following

- eigenvalue,

- CR worth (fully inserted and 5 cm inserted),

- Doppler constant for fuel temperature increase,

- sodium void worth,

- reactivity changes due to 1% density changes in the fuel, coolant, cladding, and wrapper (always only in the fuel assembly),

- reactivity change due to 1% grid expansion while preserving fuel and structural masses,

- reactivity change due to 1% fuel density change with simultaneous increase of axial fuel length by 1%,

- the axially integrated fuel assembly power (radial power distribution), and

- the axial power distribution of one specified assembly.

A first comparison of calculated nominal values, along with an assessment of the impact of nuclear data uncertainties on some of the specified quantities, were previously published (Bostelmann, 2020; Stauff et al., 2017). While the specifications of the UAM-SFR benchmark are only accessible to benchmark participants including ORNL, the ABR1000 concept is described in detail in the publicly accessible SFR-FT task force report (NEA, 2016). The only difference between the two benchmark specifications is the fuel composition. While the SFR-FT task force model included beginning-of-equilibrium-cycle (BOEC) fuel, the UAM-SFR benchmark specifies end-of-equilibrium-cycle (EOEC) fuel.
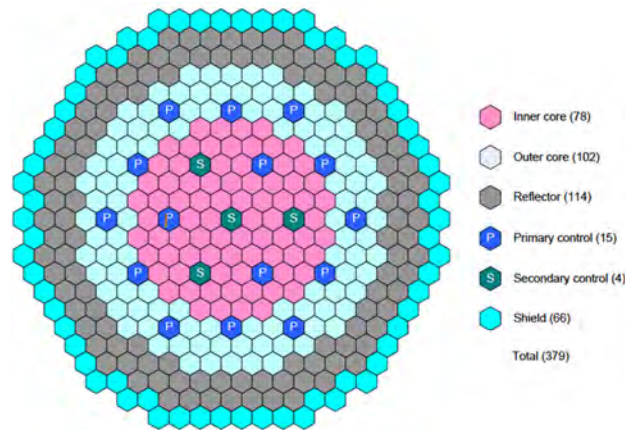
Figure 4-14 Sodium-Cooled Fast Reactor Model Cross Section View (Buiron, et al., 2019)
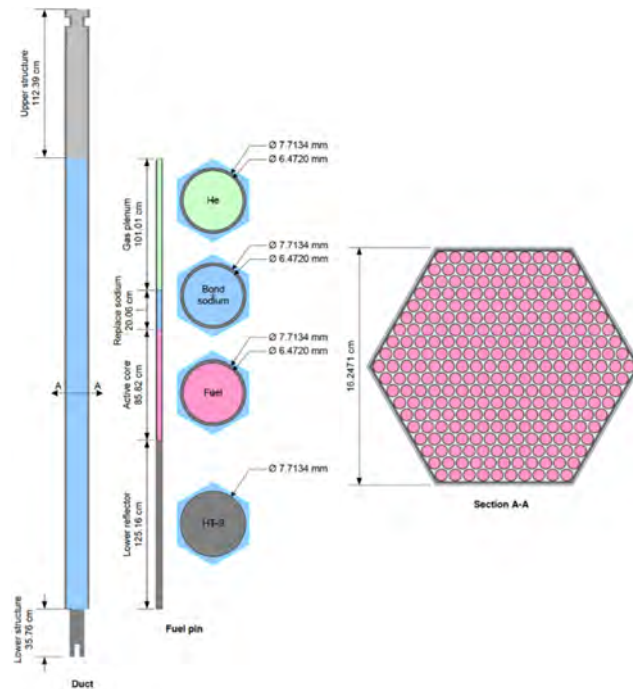
Figure 4-15 Fuel Assembly Model of a Sodium-Cooled Fast Reactor (Buiron, et al., 2019)

Table 4-7   Key Characteristics of the ABR-1000 (Buiron, et al., 2019)

Description	Value
Reactor power (MWth)	1,000
Fuel material	U-TRU-Zr metal alloy
Coolant material	Sodium
Major structural material	HT-9
Fuel temperature (°C)	534
Structure and coolant temperature (°C)	432.5
Assembly pitch (cm)	16.2471
Outer fuel radius (cm)	0.3236
Outer cladding radius (cm)	0.3857
Fuel pin pitch (cm)	0.8966
Active core height (cm)	85.82
Number of fuel assemblies:	
Inner fuel zone	78
Outer fuel zone	102
Number of fuel pins per assembly	271

5   KEY NUCLEAR DATA

This section presents the results of the sensitivity and uncertainty analyses for the selected advanced reactor benchmarks discussed in Section 4. All calculations were performed using a development version of SCALE 6.3 (Wieselquist et al., 2020). Depending on the considered benchmark, different libraries, modules, and approaches for the uncertainty analyses were applied. The neutron transport calculations were performed with SCALE's KENO-VI Monte Carlo code based on developed three-dimensional (3D) full reactor core models. KENO-VI calculations in CE mode are labeled as KENO-CE, and KENO-VI calculations in MG mode are labeled as KENO-MG. In some cases, nominal calculations were performed with SCALE's new Monte Carlo code Shift, which was shown to provide consistent results with KENO-VI while offering improved parallel performance (Pandya et al., 2016).

Note the following for the analyses documented in this section:

- Reactivity effects (e.g., temperature or density reactivities) were determined by calculating the reactivity difference between a nominal eigenvalue k_{nom} and the eigenvalue of a modified state k_{mod}:

$$\Delta\rho = \frac{1}{k_{nom}} - \frac{1}{k_{mod}} \ . \tag{4}$$

- Eigenvalue and reactivity differences are provided in pcm, where 1 pcm = 0.00001.

- Uncertainties of output quantities (eigenvalue and reactivity differences) due to nuclear data are provided in %, where 1% = 1,000 pcm.

- Provided errors (e.g., 1.01365 ± 0.00014 for k_{eff} in Table 5-1) correspond to the 1σ statistical error from the Monte Carlo calculation unless noted otherwise.

- Sensitivity coefficients are reported for results using the ENDF/B-VII.1 library. Sensitivity coefficients were also obtained using the ENDF/B-VII.0 and ENDF-/B-VIII.0 libraries. The obtained values are close to the ones obtained using ENDF/B-VII.1, but not included in this report.

- Unless otherwise stated, uncertainty analyses were performed using ENDF/B-VII.0, ENDF/B-VII.1, and ENDF-/B-VIII.0.

- Temperature reactivity coefficients do not account for thermal expansion (i.e., they only account for the effects on nuclear data).

- The sensitivities determined with TSUNAMI are relative sensitivities. For example, a sensitivity of ~0.5 to a certain cross section shows that a 1% change in this cross section would result in a ~0.5% change of the output quantity for which the sensitivity was determined.

- As part of the comparison of results obtained with TSUNAMI using the different ENDF/B libraries, comparisons between top contributing nuclear reactions to an output uncertainty are performed. This comparison is performed *for the union* of the top 10 contributors from the individual calculations: the top 10 reactions of one calculation do

not necessarily match the top 10 reactions of another calculation. Consequently, the comparisons are extended to include all top 10 reactions, so they often list more than 10 values.

- If a combination of two reactions is listed in the tables of top contributors to the output uncertainty determined with TSUNAMI, then this record is referring to the contribution of a covariance matrix between these two reactions. If only one reaction is listed, then the record refers to the contribution of the covariance matrix of this reaction, without considering correlations to other reactions.

- Some reactivity effects were investigated by applying large input perturbations to geometry, density, or temperature that may not be characteristic of the actual reactor operation. Although the nominal reactivity effect might not be representative for realistic conditions that the reactor system might experience, these large perturbations are necessary in some cases to clearly distinguish the contribution due to nuclear data perturbation from statistical calculation uncertainty (noise).

- Top contributors to the uncertainty determined using Sampler are presented in terms of the sensitivity index R^2. R^2 values are only presented if the R^2 value is larger than the corresponding statistical significance level (see Section 3). In this case, the obtained R^2 value is considered statistically relevant.

- The analysis of R^2 with Sampler is only enabled for calculations based on either ENDF/B-VII.1 or ENDF/B-VIII.0 data. The calculation of R^2 requires details of the perturbation of the nuclear data as applied in the individual sample calculations. Only the perturbations based on ENDF/B-VII.1 and ENDF/B-VIII.0 data were generated with the current version of SCALE, so ENDF/B-VII.0 results for R^2 are not presented.

- Energy-dependent flux distributions in different regions or reactor models are displayed to support discussion of the results. These fluxes were obtained by overlaying a 3D mesh on the full core geometry. The displayed fluxes present the flux per unit lethargy normalized to 1.

5.1 HTR-10, High-Temperature Gas-Cooled Reactor

A SCALE/KENO-VI model of the HTR-10, which was developed based on the IRPhEP benchmark specification (Terry et al., 2007) for earlier ORNL studies (Ilas et al., 2012; Sunny and Ilas, 2010), was used for the computational analyses. A comparison of calculated eigenvalues based on recent ENDF/B nuclear data libraries with the measured value and a first assessment of the impact of nuclear data uncertainties on the eigenvalue uncertainty for HTR-10 were documented in an earlier ORNL study (Bostelmann et al., 2020).

The SCALE full core model is displayed in Figure5-1. The TRISO particle and fuel pebble models are displayed in Figure 4-2 and Figure 4-3, respectively. The TRISO particles were explicitly modeled in the CE KENO-VI model. They are explicitly placed in a square lattice to avoid particle clipping by the outer spherical boundary. The neutron flux spectrum in different regions of the core is displayed in Figure 5-2.
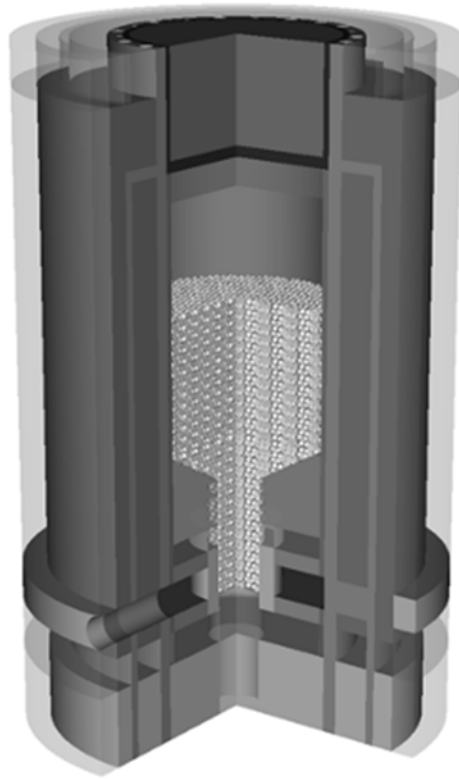
Figure 5-1 HTR-10: SCALE Model
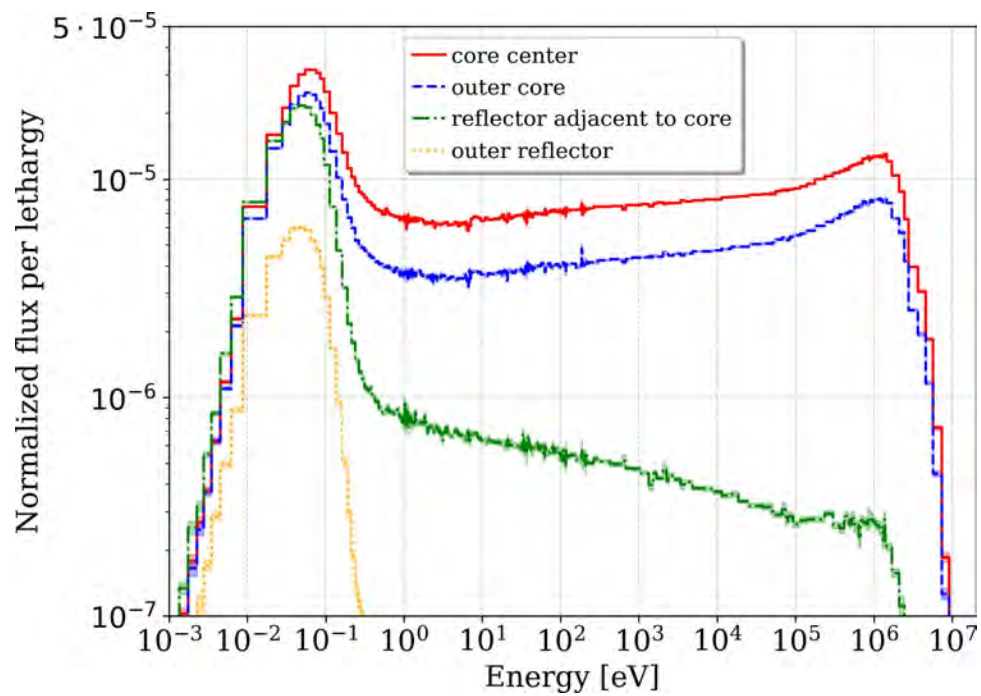
Figure 5-2 HTR-10: Normalized Neutron Flux in a 252-Group Representation at the Core Axial Midline at Different Radial Positions Determined with KENO-CE

The sensitivity and uncertainty analyses were performed with the CE TSUNAMI code using the CLUTCH method. Results were obtained with all three considered ENDF/B library releases.

As mentioned in Section 2.2.1.1, the ENDF/B-VIII.0 library includes data for graphite evaluations assuming 10 and 30% porosity, in addition to the evaluation for graphite a as perfect crystal lattice, which was already available with ENDF/B-VII.0 and ENDF/B-VII.1 (Hawari and Gillete, 2014). The HTR-10 benchmark specifications do not provide information about the porosity of the different graphite materials used. Therefore, additional criticality calculations with all graphite evaluations were performed to assess the impact of different porosities. This study only estimates the impact of porosity in the thermal scattering data. Thus, in these calculations, only the graphite thermal scattering data changed, but the graphite density (i.e., the nuclide density in atoms/b-cm) did not change. The porosity is assumed to indirectly affect the graphite density by decreasing the value, which is already accounted for by the specification provided.

Although the benchmark specifications only provide an eigenvalue (k_{eff}), the sensitivity and uncertainty analyses for the HTR-10 in this study include additional metrics and were performed for the following QOIs:

1. k_{eff}

2. fuel temperature reactivity: fuel temperature increased by 100 K

3. pebble graphite density reactivity: graphite density in all pebbles multiplied by 1.03

4. pebble graphite impurities reactivity: graphite impurity densities in all pebbles multiplied by 2

5. pebble graphite temperatures reactivity: graphite temperature in all pebbles increased by 100 K

6. structural graphite density reactivity: graphite density in all structural materials multiplied by 1.03

7. structural graphite impurities reactivity: graphite impurity densities in all structural materials multiplied by 2

8. structural graphite temperatures reactivity: graphite temperature in all structural materials increased by 100 K

5.1.1   Nominal Results

Table 5-1 compares the eigenvalue (k_{eff}) results obtained with KENO-VI to the experimental benchmark value. The (1σ) benchmark uncertainty is given as 370 pcm and considers uncertainties in the geometry and material data. The graphite density in the fuel pebble, the uranium fuel loading, the boron content in the graphite reflector, the pebble packing fraction, and the geometry of the upper surface cone of pebbles are the main contributors to this uncertainty (Terry et al., 2007). Considering this uncertainty, very good agreement is observed between the result calculated with ENDF/B-VII.1 data and the benchmark. The ENDF/B-VII.0 result overestimates the benchmark value due to the lower carbon neutron capture cross section, as discussed in Section 2.2.1.1. The ENDF/B-VIII.0 result is slightly larger than the

ENDF/B-VII.1 result due to updates in the ^{235}U and ^{238}U cross section data (Bostelmann et al., 2020).

Table 5-1   HTR-10: KENO-CE k_{eff} Results Compared to the Benchmark Besults[1]

Case	k_{eff}	Benchmark Δk [pcm]	Library Δk [pcm]
ENDF/B-VII.0	1.01365 ± 0.00014	1365 ± 370	(ref)
ENDF/B-VII.1	1.00280 ± 0.00016	280 ± 370	-1085 ± 21
ENDF/B-VIII.0	1.00601 ± 0.00015	601 ± 370	-764 ± 21
Benchmark	1.00000 ± 0.00370	(ref)	

TableTable 5-2 shows the impact of using graphite thermal scattering data with different porosities (0, 10, and 30%) or carbon without thermal scattering data with ENDF/B-VIII.0. The graphite thermal scattering data with porosities led to an increase in calculated k_{eff} and therefore to larger differences compared to the corresponding benchmark value.

Table 5-2   HTR-10: Effects of Graphite Porosity Evaluations on Calculated KENO-CE k_{eff} Results using ENDF/B-VIII.0 Graphite Data[2]

	Cold, all materials		Hot[*], all materials	
Cross section data	k_{eff}	Δk [pcm]	k_{eff}	Δk [pcm]
Graphite, 0% porosity	1.00601 ± 0.00015	(ref)	0.90746 ± 0.00021	(ref)
Graphite, 10% porosity	1.00963 ± 0.00013	362 ± 20	0.90706 ± 0.00025	-40 ± 33
Graphite, 30% porosity	1.01212 ± 0.00016	611 ± 22	0.90607 ± 0.00021	-139 ± 30
Carbon	1.02089 ± 0.00018	1488 ± 23	0.90805 ± 0.00024	59 ± 32
	Cold, structure		Cold, pebbles	
Cross section data	k_{eff}	Δk [pcm]	k_{eff}	Δk [pcm]
Graphite, 0% porosity	1.00601 ± 0.00015	(ref)	1.00601 ± 0.00015	(ref)
Graphite, 10% porosity	1.00532 ± 0.00023	-69 ± 27	1.01028 ± 0.00023	427 ± 27
Graphite, 30% porosity	1.00458 ± 0.00022	-143 ± 27	1.01366 ± 0.00018	765 ± 23
Carbon	1.00295 ± 0.00022	-306 ± 27	1.02371 ± 0.00025	1770 ± 29

*The fuel temperature was increased to 1,200 K, and all other temperatures were increased to 1,000 K.

---

[1] All results were obtained using the graphite evaluations as perfect crystal; that is, assuming 0% porosity.

[2] The graphite evaluation is changed either in all graphite materials, only in the graphite structure, or only in the pebbles. In addition to the benchmark condition at room temperature (cold), a case with elevated temperatures is considered (hot).

Note that the HTR-10 benchmark was simulated at room temperature as specified in the benchmark specifications. However, simulations at different higher temperatures were performed in this study to gain more understanding of potential temperature effects. When increasing the fuel temperature to 1,200 K and all other temperatures to 1,000 K, the impact of the different applied graphite thermal scattering data was significantly decreased. Furthermore, the graphite data were changed either in all graphite materials, in the graphite structure components only, or in the pebbles only, to allow for investigation of the impact of the graphite data on calculated k_{eff}. The main driver of the changes in k_{eff} for the 10 and 30% porosities, as well as for the carbon-evaluated data, is the graphite evaluated data in the pebbles. The effect of graphite in the structural components is smaller than that of graphite in pebbles, and the effect has a different direction, leading to a k_{eff} decrease instead of the k_{eff} increase when replacing the graphite data in the pebbles.

Section 2.2.1.1 mentions the availability of thermal scattering data for SiC in ENDF/B-VIII.0. Since SiC is one of the materials used in the TRISO particles, a calculation was performed applying this new data. However, no difference in k_{eff} was found for the HTR-10.

Table 5-3 compares the nominal values of the investigated reactivity QOIs between ENDF/B libraries. All reactivity uncertainties appear consistent except for the graphite temperature reactivity, which changes significantly in ENDF/B-VIII.0. The structural graphite impurity reactivity changes by more than the 2σ statistical uncertainty if ENDF/B-VII.0 and ENDF/B-VIII.0 are compared, but between successive releases, the difference is slightly less than 2σ.

5.1.2 Sensitivity Analysis

Relevant mixture-, region-, and energy-integrated sensitivities of all considered QOIs as determined with CE TSUNAMI are presented in Table 5-4 to Table 5-11. Each sensitivity coefficient shown in these tables represents the sensitivity of a specific QOI to a single specific reaction, and each can be used to understand relevant sensitivities for a given QOI.

The largest k_{eff} sensitivity is the sensitivity to the average number of neutrons produced per fission event ($\bar{v}$) of ^{235}U. This is the largest sensitivity due to the immediate contribution to the reactivity of the system (Table 5-4). The sensitivity coefficient of $\sim$1 shows that a $\sim$1% change in ^{235}U $\bar{v}$) data would result in a 1% change of k_{eff}. Other large sensitivities are observed for graphite elastic scattering, graphite radiative neutron capture (n,γ), and ^{235}U fission and (n,γ). A significant sensitivity was also observed for the ^{10}B (n,α) reaction, the dominant neutron-absorbing reaction in boron, a common graphite impurity.

For the reactivity effects, the sensitivities to ^{235}U $\bar{v}$ and fission are among the top 3 sensitivities for all QOIs due to their immediate contribution to the reactivity of the system. Note that they are positive for negative reactivity effects and negative for positive reactivity effects (see Table 5-3). The (n,γ) cross sections play a major role for ^{235}U, ^{238}U, and graphite. The ^{10}B (n,α) reaction is also important. Other relevant reactions are elastic scattering of ^{16}O, ^{28}Si, ^{235}U, and ^{238}U, ^{28}Si (n,γ) reaction, and ^{238}U fission.

Table 5-3 HTR-10: Nominal Values of all QOIs Determined with KENO-CE (in pcm)

QOIs	ENDF/B-VII.0	ENDF/B-VII.1	ENDF/B-VIII.0	$\frac{VII.1}{VII.0} - 1$	$\frac{VIII.0}{VII.1} - 1$
Fuel temperature	-243 ± 22	-241 ± 25	-222 ± 25	3 ± 33	19 ± 36
Pebble gr. density	1182 ± 23	1175 ± 23	1201 ± 27	-8 ± 32	26 ± 35
Pebble gr. impurities	-602 ± 23	-623 ± 23	-588 ± 25	-21 ± 32	35 ± 34
Pebble gr. temperature	-1948 ± 23	-1960 ± 22	-1701 ± 25	-11 ± 32	259 ± 33
Structural gr. density	546 ± 25	504 ± 22	543 ± 24	-43 ± 33	40 ± 32
Structural gr. impurities	-3947 ± 26	-3877 ± 25	-3807 ± 25	70 ± 36	70 ± 35
Structural gr. temperature	780 ± 24	783 ± 22	798 ± 24	4 ± 33	14 ± 33

Due to insufficient convergence, graphite elastic scattering sensitivities are not included in the reactivity effect tables, with the exception of Table 5-4. Since the sensitivities to graphite elastic scattering are very similar in the nominal state and the state with perturbed temperature or composition, the difference between the states is affected by large statistical uncertainties, despite tighter convergence criteria in the calculation. However, when considering the definition and interpretation of these *relative* sensitivities (Section 3), the impact of large sensitivities with large statistical uncertainties on reactivity differences $\Delta\rho$ is small. Let us assume a very large sensitivity of $\Delta\rho$ to graphite elastic scattering of $S = 2$, a statistical error of this sensitivity as $\sigma = 100$, and reactivity difference $\Delta\rho = 500$ pcm. Then the relative sensitivity interval $[s - 2\sigma, S + 2\sigma] = [0,4]$ translates into an absolute change of $\Delta\rho$ between 0 and 20 pcm in the case that the graphite elastic scattering cross section change by 1%. A change of 20 pcm in $\Delta\rho$ is about the same range as the statistical error from the Monte Carlo calculation reported here (Table 5-3).

Table 5-4 HTR-10: Top k_{eff} Sensitivities (Top 10 Positive and Top 10 Negative Mixture-, region-, and Energy-Integrated Sensitivities[3]

Nuclide	Reaction	Sensitivity (increasing k_{eff})	Nuclide	Reaction	Sensitivity (decreasing k_{eff})
u-235	$\bar{\nu}$	9.986e-01 ± 8.919e-06	u-235	n,γ	-1.179e-01 ± 1.548e-05
graphite	elastic	6.832e-01 ± 5.080e-02	graphite	n,γ	-8.463e-02 ± 2.062e-05
u-235	fission	3.672e-01 ± 8.087e-05	b-10	n,α	-5.150e-02 ± 1.973e-05
u-238	elastic	4.170e-03 ± 1.237e-04	u-238	n, γ	-4.455e-02 ± 2.370e-05
graphite	n,n′	3.194e-03 ± 3.263e-05	n-14	n,p	-8.933e-03 ± 2.734e-06
u-238	$\bar{\nu}$	1.440e-03 ± 8.919e-06	si-28	n,γ	-2.509e-03 ± 3.750e-07
u-238	fission	9.390e-04 ± 8.918e-06	graphite	n,α	-8.854e-04 ± 2.624e-06
c	elastic	6.029e-04 ± 1.246e-04	n-14	n,γ	-3.651e-04 ± 1.121e-07
n-14	elastic	3.469e-04 ± 7.876e-05	c	n,γ	-5.714e-05 ± 8.454e-09
u-238	n,n′	2.807e-04 ± 2.208e-05	n-14	n,α	-4.437e-05 ± 2.687e-08

---

[3] Determined with TSUNAMI using ENDF/B-VII.1 data.

Table 5-5   HTR-10: Top Fuel Temperature Reactivity Sensitivities[4]

Nuclide	Reaction	Sensitivity (reducing negative Δρ)	Nuclide	Reaction	Sensitivity (increasing negative Δρ)
u-235	$\bar{\nu}$	9.920e-01 ± 5.959e-03	u-238	n,γ	-5.200e-01 ± 1.512e-02
u-235	fission	4.422e-01 ± 4.806e-02	graphite	n,γ	-1.277e-01 ± 1.275e-02
u-238	elastic	1.759e-01 ± 7.273e-02	u-235	n,γ	-1.008e-01 ± 9.047e-03
o-16	elastic	9.022e-02 ± 6.969e-02	b-10	n,α	-1.008e-01 ± 1.219e-02
n-14	elastic	3.622e-02 ± 4.756e-02	c	elastic	-6.221e-02 ± 7.500e-02
si-28	elastic	3.230e-02 ± 5.065e-02	u-235	elastic	-2.601e-02 ± 2.536e-02
u-238	$\bar{\nu}$	8.045e-03 ± 5.959e-03	n-14	n,p	-1.250e-02 ± 1.595e-03
u-238	fission	7.647e-03 ± 5.963e-03	si-28	n,n′	-2.567e-03 ± 3.958e-03
u-238	n,n′	1.986e-03 ± 1.284e-02	si-28	n,γ	-2.309e-03 ± 2.188e-04
u-235	n,n′	1.035e-03 ± 4.784e-03	b-11	elastic	-8.709e-04 ± 2.924e-03

Table 5-6   HTR-10: Top Pebble Graphite Density Reactivity Sensitivities[5]

Nuclide	Reaction	Sensitivity (increasing Δρ)	Nuclide	Reaction	Sensitivity (reducing Δρ)
b-10	n,α	1.874e-01 ± 2.471e-03	u-235	$\bar{\nu}$	-9.952e-01 ± 1.104e-03
u-235	n,γ	1.131e-01 ± 1.843e-03	u-235	fission	-4.606e-01 ± 9.713e-03
graphite	n,γ	9.747e-02 ± 2.557e-03	u-235	elastic	-1.047e-02 ± 5.353e-03
u-238	n,γ	6.698e-02 ± 2.855e-03	c	elastic	-6.382e-03 ± 1.541e-02
o-16	elastic	2.604e-02 ± 1.432e-02	u-238	$\bar{\nu}$	-4.786e-03 ± 1.104e-03
n-14	n,p	2.068e-02 ± 3.191e-04	u-238	fission	-3.718e-03 ± 1.103e-03
u-238	elastic	1.679e-02 ± 1.448e-02	ar-40	elastic	-3.512e-04 ± 2.376e-04
si-28	elastic	7.714e-03 ± 1.063e-02	o-16	n,n′	-9.431e-05 ± 1.063e-04
n-14	elastic	6.044e-03 ± 9.284e-03	h-1	elastic	-4.571e-05 ± 2.618e-03
si-28	n,γ	2.129e-03 ± 4.383e-05	b-10	elastic	-1.805e-05 ± 1.757e-04

---

[4] Fuel temperature increased by 100 K, Δρ = -241 ± 25 pcm; mixture-, region-, and energy-integrated sensitivities, determined with TSUNAMI using ENDF/B-VII.1 data.

[5] Density multiplied by 1.03, Δρ = 1175 ± 23 pcm; mixture-, region-, and energy-integrated sensitivities, determined with TSUNAMI using ENDF/B-VII.1 data.

Table 5-7   HTR-10: Top Pebble Graphite Impurity Reactivity Sensitivities[6]

Nuclide	Reaction	Sensitivity (reducing negative $\Delta\rho$)	Nuclide	Reaction	Sensitivity (increasing negative $\Delta\rho$)
u-235	$\bar{\nu}$	9.992e-01 ± 2.112e-03	b-10	n,α	-1.044e+00 ± 4.721e-03
u-235	fission	9.749e-01 ± 1.923e-02	u-238	n,γ	-3.292e-02 ± 5.464e-03
o-16	elastic	5.058e-02 ± 2.693e-02	graphite	n, γ	-2.767e-02 ± 4.901e-03
n-14	elastic	2.155e-02 ± 1.818e-02	u-235	n, γ	-1.235e-02 ± 3.629e-03
si-28	elastic	2.123e-02 ± 2.077e-02	u-235	elastic	-6.059e-03 ± 1.014e-02
u-238	elastic	1.848e-02 ± 2.821e-02	n-14	n,p	-1.671e-03 ± 5.950e-04
c	elastic	1.834e-02 ± 3.034e-02	b-11	elastic	-1.133e-03 ± 1.165e-03
h-1	elastic	9.311e-03 ± 4.953e-03	graphite	n,α	-8.771e-04 ± 6.554e-04
u-238	$\bar{\nu}$	7.882e-04 ± 2.112e-03	ar-40	elastic	-8.661e-04 ± 4.750e-04
u-235	n,n′	4.031e-04 ± 4.975e-03	o-16	n,n′	-1.834e-04 ± 1.910e-04

Table 5-8   HTR-10: Top Pebble Graphite Temperature Reactivity Sensitivities[7]

Nuclide	Reaction	Sensitivity (reducing negative $\Delta\rho$)	Nuclide	Reaction	Sensitivity (increasing negative $\Delta\rho$)
u-235	fission	1.196e+00 ± 6.070e-03	b-10	n,α	-9.273e-02 ± 1.440e-03
u-235	$\bar{\nu}$	9.976e-01 ± 6.552e-04	u-238	n,γ	-3.655e-02 ± 1.764e-03
si-28	elastic	9.796e-03 ± 6.801e-03	n-14	n,p	-5.147e-03 ± 1.908e-04
c	elastic	9.083e-03 ± 9.656e-03	u-235	elastic	-3.560e-03 ± 3.272e-03
u-238	elastic	8.487e-03 ± 9.148e-03	si-28	n,γ	-4.577e-04 ± 2.769e-05
o-16	elastic	6.737e-03 ± 8.590e-03	graphite	n,α	-8.149e-04 ± 2.176e-04
u-235	n,γ	6.585e-03 ± 1.145e-03	si-28	n,n′	-3.930e-04 ± 4.912e-04
n-14	elastic	6.281e-03 ± 6.051e-03	n-14	n,γ	-2.084e-04 ± 7.821e-06
graphite	n,n′	4.702e-03 ± 2.311e-03	ar-40	elastic	-1.988e-04 ± 1.457e-04
u-238	nu-fission	2.402e-03 ± 6.552e-04	n-14	n,α	-4.236e-05 ± 1.867e-06

---

[6] Impurity densities multiplied by 2, $\Delta\rho$ = -623 ± 23 pcm; mixture-, region-, and energy-integrated sensitivities, determined with TSUNAMI using ENDF/B-VII.1 data.

[7] Temperature increased by 100 K, $\Delta\rho$ = -1960 ± 22 pcm; mixture-, region-, and energy-integrated sensitivities, determined with TSUNAMI using ENDF/B-VII.1 data.

Table 5-9   HTR-10: Top Structural Graphite Density Reactivity Sensitivities[8]

Nuclide	Reaction	Sensitivity (increasing $\Delta\rho$)	Nuclide	Reaction	Sensitivity (reducing $\Delta\rho$)
u-235	n,γ	9.312e-02 ± 4.348e-03	u-235	$\bar{\nu}$	-9.938e-01 ± 2.495e-03
u-238	n,γ	5.957e-02 ± 6.989e-03	u-235	fission	-5.395e-01 ± 2.318e-02
o-16	elastic	3.011e-02 ± 3.248e-02	graphite	n,γ	-2.072e-01 ± 6.083e-03
c	elastic	2.995e-02 ± 3.461e-02	si-28	elastic	-2.753e-02 ± 2.437e-02
b-10	n,α	1.904e-02 ± 5.777e-03	u-235	elastic	-2.091e-02 ± 1.241e-02
u-238	elastic	1.424e-02 ± 3.333e-02	graphite	n,n′	-6.987e-03 ± 9.358e-03
h-1	elastic	2.870e-03 ± 6.052e-03	u-238	$\bar{\nu}$	-6.240e-03 ± 2.495e-03
si-28	n,γ	1.782e-03 ± 1.072e-04	u-238	fission	-5.771e-03 ± 2.496e-03
u-238	n,n′	1.463e-03 ± 2.329e-03	n-14	elastic	-4.607e-03 ± 2.336e-02
graphite	n,α	1.435e-03 ± 7.841e-04	n-14	n,p	-4.276e-03 ± 7.467e-04

Table 5-10   HTR-10: Top Structural Graphite Impurity Reactivity Sensitivities[9]

Nuclide	Reaction	Sensitivity (reducing negative $\Delta\rho$)	Nuclide	Reaction	Sensitivity (increasing negative $\Delta\rho$)
u-235	$\bar{\nu}$	9.973e-01 ± 3.572e-04	b-10	n,α	-6.100e-01 ± 1.041e-03
u-235	fission	5.910e-01 ± 3.233e-03	u-235	n,γ	-8.675e-02 ± 6.051e-04
graphite	n,γ	2.165e-01 ± 7.345e-04	u-238	n,γ	-5.799e-02 ± 9.209e-04
n-14	n,p	1.435e-02 ± 9.645e-05	si-28	n,γ	-1.638e-03 ± 1.402e-05
o-16	elastic	1.340e-02 ± 4.367e-03	u-235	elastic	-6.130e-04 ± 1.760e-03
u-238	elastic	1.247e-02 ± 4.597e-03	graphite	n,α	-4.663e-04 ± 1.041e-04
graphite	n,n′	7.149e-03 ± 1.296e-03	b-11	elastic	-2.667e-04 ± 2.139e-04
c	elastic	5.503e-03 ± 4.755e-03	h-1	n,γ	-1.321e-04 ± 5.207e-07
si-28	elastic	4.979e-03 ± 3.397e-03	b-10	n,γ	-7.937e-05 ± 1.354e-07
u-238	$\bar{\nu}$	2.682e-03 ± 3.572e-04	ar-40	n,γ	-7.158e-05 ± 2.828e-07

---

[8] Density multiplied by 1.03, $\Delta\rho$ = 504 ± 22 pcm; mixture-, region-, and energy-integrated sensitivities, determined with TSUNAMI using ENDF/B-VII.1 data.

[9] Impurity densities multiplied by 2, $\Delta\rho$ -3877 ± 25 pcm; mixture-, region-, and energy-integrated sensitivities, determined with TSUNAMI using ENDF/B-VII.1 data.

Table 5-11   HTR-10: Top Structural Graphite Temperature Reactivity Sensitivities[10]

Nuclide	Reaction	Sensitivity (increasing $\Delta\rho$)	Nuclide	Reaction	Sensitivity (reducing $\Delta\rho$)
graphite	n,γ	2.497e-01 ± 3.787e-03	u-235	$\bar{\nu}$	-9.956e-01 ± 1.706e-03
b-10	n,α	2.286e-01 ± 3.732e-03	u-235	fission	-4.999e-01 ± 1.457e-02
u-235	n,γ	1.052e-01 ± 2.762e-03	Graphite	n,n′	-7.931e-03 ± 5.957e-03
u-238	n,γ	4.752e-02 ± 4.434e-03	u-238	$\bar{\nu}$	-4.418e-03 ± 1.706e-03
o-16	elastic	3.733e-02 ± 2.044e-02	u-235	elastic	-4.230e-03 ± 7.406e-03
n-14	elastic	3.056e-02 ± 1.442e-02	u-238	fission	-3.964e-03 ± 1.709e-03
u-238	elastic	2.500e-02 ± 2.236e-02	si-28	elastic	-1.622e-03 ± 1.585e-02
c	elastic	2.297e-02 ± 2.272e-02	b-11	elastic	-6.280e-04 ± 9.127e-04
n-14	n,p	2.176e-02 ± 4.600e-04	ar-40	elastic	-4.943e-04 ± 3.646e-04
u-238	n,n′	2.698e-03 ± 4.046e-03	o-16	n,n'	-2.647e-04 ± 1.511e-04

5.1.3   Uncertainty Analysis

Uncertainty calculations of all QOIs were performed for the three considered ENDF/B libraries based on the sensitivity coefficients determined with CE TSUNAMI. Table 5-12 compares these calculated uncertainties and shows the differences in the uncertainty values calculated with

The k_{eff} uncertainty is between 0.6 and 0.7%, depending on which ENDF/B library is used in calculation. The uncertainty obtained with ENDF/B-VIII.0 is slightly larger than the other two results obtained with ENDF/B-VII.0 and ENDF/B-VII.1 because of an increased uncertainty of ^{235}U $\bar{\nu}$ and fission in ENDF/B-VIII.0 (Figure 2-20 and Figure 2-21), as well as an increased uncertainty in the thermal and intermediate energy range for graphite elastic scattering (Figure 2-28). The uncertainties of the other considered quantities vary within the range of 0.6 to 1.2%, depending on the QOI or the library used for calculation. Significant differences between the ENDF/B libraries occur for the graphite impurity reactivity uncertainty in the pebble; this uncertainty increases by ~70% when using ENDF/B-VIII.0 compared to ENDF/B-VII.0 and ENDF/B-VII.1 because the uncertainty of ^{10}B (n,α) is significantly larger in the thermal region in ENDF/B-VIII.0 (Figure 2-30). Another QOI with significant difference in uncertainty when using different libraries is the graphite temperature reactivity; the ENDF/B-VIII.0 calculation results in a 40% larger uncertainty compared to the ENDF/B-VII.0 library because of increased uncertainties in relevant ^{235}U cross sections, including fission, and (n,γ) (Figure 5-5).

The top uncertainty contributors generally correspond to the nuclear reactions identified as top sensitivities of these QOIs in Section 5.1.2. In particular, $\bar{\nu}$ and the fission cross section of ^{235}U are listed as top contributors to some of these uncertainties due to their large sensitivity and non-negligible uncertainty. Additionally, the fission spectrum (χ) of ^{235}U is listed among the top contributors (Figure 1-3 and Figure 5-5). Graphite scattering and (n,γ) also play an important role due to the large amount of graphite moderator (Figure 2-28 and Figure 2-29).

Although some output uncertainties agree well between the calculations with different ENDF/B libraries, significant differences in the contributions of some individual reactions can be

---

[10]   Temperature increased by 100 K, $\Delta\rho$ = 783 ± 22 pcm; mixture-, region-, and energy-integrated sensitivities, determined with TSUNAMI using ENDF/B-VII.1 data.

observed that cancel each other out in the calculation of the total output uncertainty. In addition to the relevant changes of nuclear data already mentioned, clearly decreased contributions in ENDF/B-VIII.0 calculations were observed for ^{235}U (n,γ) and χ, and graphite inelastic scattering (n,n′).

Table 5-12   HTR-10: Uncertainties of QOIs Determined with TSUNAMI

QOIs	ENDF/B-VII.0	ENDF/B-VII.1	ENDF/B-VIII.0	$\frac{VII.1}{VII.0}-1$	$\frac{VIII.0}{VII.1}-1$
k_{eff}	0.607%	0.668%	0.690%	10.1%	3.3%
Fuel temperature	1.124%	1.192%	1.030%	6.1%	-13.6%
Pebble gr. density	0.667%	0.848%	0.618%	27.1%	-27.1%
Pebble gr. impurities	0.639%	0.749%	1.126%	17.2%	50.3%
Pebble gr. temperature	0.694%	0.753%	0.972%	8.4%	29.1%
Structural gr. density	0.873%	0.952%	0.820%	9.1%	-13.9%
Structural gr. impurities	0.921%	1.109%	0.990%	20.3%	-10.7%
Structural gr. temperature	0.998%	1.135%	0.920%	13.7%	-18.9%
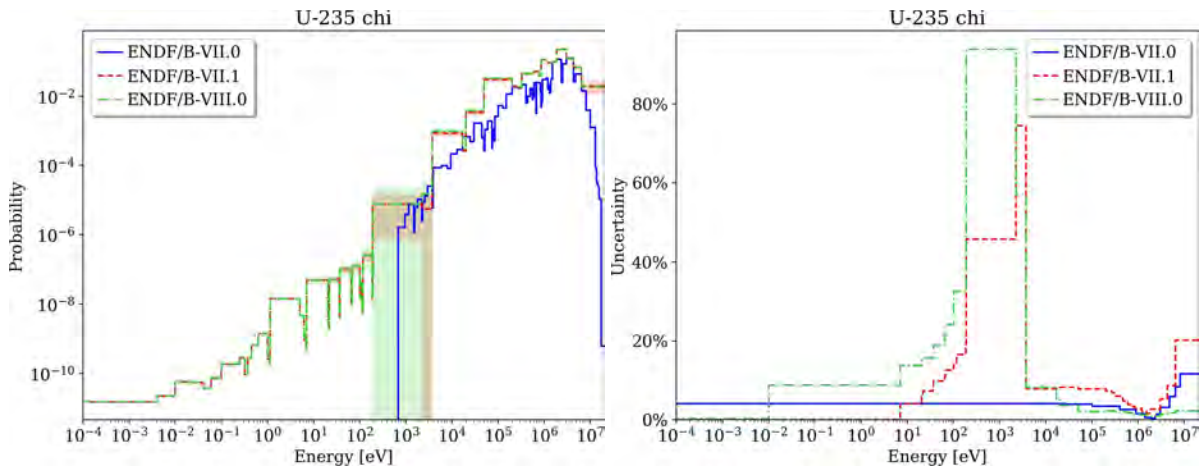
Figure 5-3 ^{235}U Fission Spectrum (χ) Nominal Data and Uncertainty[11]

---

[11] Note that the large uncertainty between 10^2 and 10^4 eV is caused by division by small numbers. The major differences between the ENDF/B evaluations that are significant for the analyses here are between 10^6 and 10^7 eV.
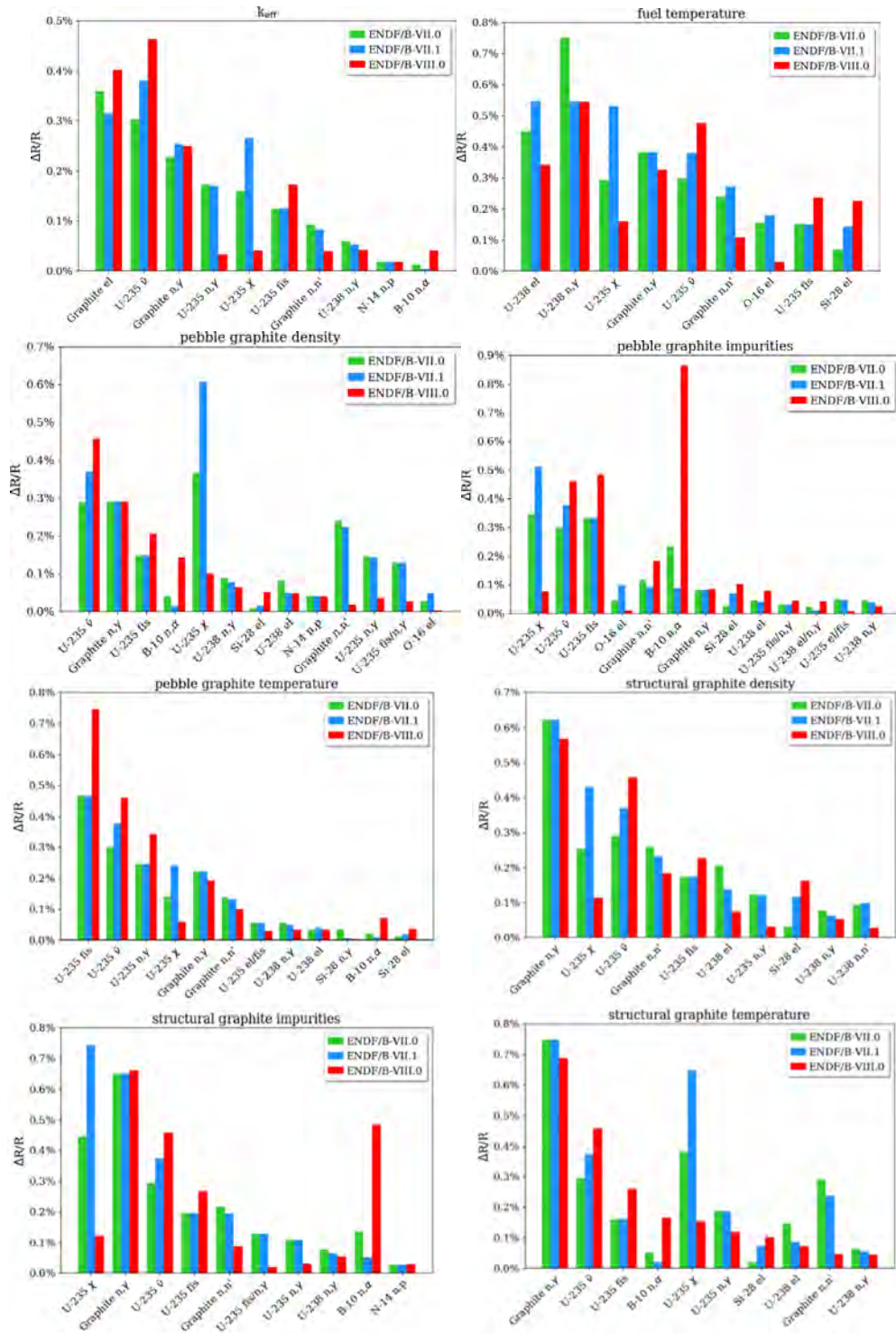
Figure 5-4 HTR-10: Contributions to the Output Uncertainties[12]

---

[12] Obtained using TSUNAMI

5.2   PB-FHR-Mk1, Fluoride Salt-Cooled Pebble Bed-Reactor

A SCALE/KENO-VI model of the PB-FHR-Mk1 was developed based on the technical description of the PB-FHR-Mk1 (Andreades et al., 2014) using an MCNP model published by Cisneros (Cisneros, 2013) as a starting point. The SCALE full core model is displayed in Figure5-5. A fuel pebble with explicitly modeled TRISO particles for a KENO CE calculation is displayed in Figure 5-6. For the application of KENO in MG mode, SCALE's *doublehet* approach for resonance self-shielding treatment in double-heterogeneous systems was used (Bostelmann et al., 2020; Wieselquist et al., 2020). The neutron flux spectrum in different regions of the core is shown in Figure 5-7.
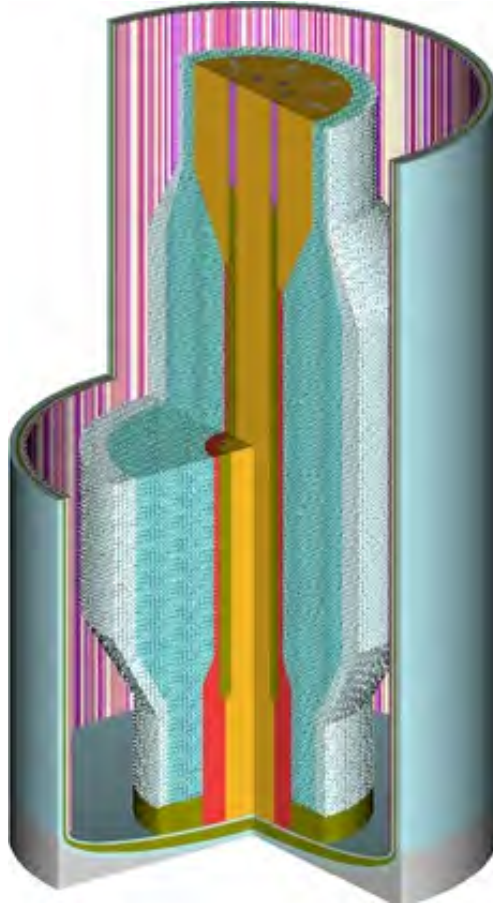
Figure 5-5 PB-FHR-Mk1: SCALE Full Core Model[13].

To investigate the effects for more realistic operating states of this reactor, a fuel composition quasi-representative of a non-fresh fuel core was developed. Fuel compositions corresponding to different burnups were determined through depletion calculations of a two-dimensional (2D) slice model of the reactor with reflective axial boundary conditions and vacuum radial boundary conditions. Although a simplified depletion model with only a few fuel pebbles was depleted, the approach provides greater fidelity than a depletion model that considers a pebble in an infinite

---

[13]   The annular core contains fuel pebbles (cyan) surrounded by a layer of dummy pebbles (light blue). The other part of the core is mainly composed of graphite (partially removed to allow a better view of the core).

lattice of pebbles. The pebbles in the 2D slice model were exposed to representative conditions in the reactor through a more realistic moderator-to-fuel ratio and therefore a more realistic neutron flux spectrum environment. Further details on this approach are provided in Appendix A.2.1.
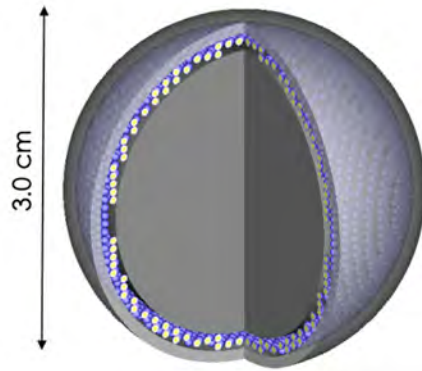
Figure 5-6 PB-FHR-Mk1: SCALE Model of a Fuel Pebble with TRISO Particles Explicitly Modeled by Placing Them in a Square Pattice, Avoiding Clipping by the Inner or Outer Shells

The 3D full core model was divided into 10 axial regions of equal volume. Average fuel compositions for each of these axial regions were estimated based on the burnup-dependent fuel compositions obtained with the 2D depletion model and by considering the final pebble discharge burnup of 180 GWd/tHM, the pebble flow from the bottom of the core to the top, and the average number of passes (8) of a pebble through the reactor. Although such a coarse model with these estimated fuel compositions is only a very rough approximation of realistic operations, this approach was considered sufficient for the nuclear data assessment studies since all relevant isotopes in the depleted fuel are included.

The sensitivity and uncertainty analyses for the PB-FHR-Mk1 were performed for the following QOIs:

1. k_{eff}

2. Fuel temperature reactivity: fuel temperature increased by 500 K

3. Coolant salt temperature reactivity: salt temperature increased by 300 K

4. Coolant salt density reactivity: salt density multiplied by 1.5

5. Axial power profile

The magnitude of perturbations was chosen to obtain reactivity differences large enough to clearly distinguish the statistical effects of the Monte Carlo calculations from the impact of nuclear data uncertainties on the results.

The initial sensitivity and uncertainty analyses were performed with the CE TSUNAMI code using the CLUTCH method. However, it was found that the statistical error of the sensitivity to certain scattering reactions in the salt (e.g., ^{19}F, ^9Be, and ^7Li elastic scattering) and in the

graphite (graphite elastic scattering) was significant, despite several repetitions with tighter convergence criteria. While the k_{eff} sensitivities could be confirmed with direct perturbation calculations and allowed a thorough analysis of k_{eff} based on the CE TSUNAMI results, the same analysis was challenging for reactivity differences between two states. The sensitivities to these scattering reactions were very similar between the two states. Therefore, the difference between those similar sensitivities is very sensitive to large statistical errors, causing statistical errors of the integrated sensitivities larger than 100%.

Although many relevant well-converged sensitivities could still be studied from the CE TSUNAMI calculations, the corresponding output uncertainties were not considered reliable since they were biased by the mentioned nonconverged sensitivities. To obtain reliable uncertainties, Sampler calculations were performed based on KENO MG calculations using SCALE's 252-group library. A sample size of 1,000 was used to allow for calculations of the sensitivity index R^2 to determine the top contributors to the observed uncertainties.

Figure 5-7 PB-FHR-Mk1: Normalized Neutron Flux in a 252-Group Representation at the Core Axial Midline at Different Radial Positions as Determined with KENO-CE

Since TSUNAMI does not permit the direct calculation of power sensitivities, Sampler was also used to study the uncertainties of the axial power profile and the axial peak power. The calculation of the power profile can be significantly influenced by the statistical uncertainty inherent to the Monte Carlo method. The statistical uncertainty can be significant, especially in the outer regions of the reactor with reduced neutron flux. To estimate which portion of the uncertainty determined with Sampler is caused by inherent statistics and which portion is caused by nuclear data uncertainties, the statistical uncertainty was calculated as the standard deviation for a set of power calculations with different random seeds. Sampler calculations were performed using the ENDF/B-VII.1 and ENDF/B-VIII.0 data; calculations with ENDF-B/VII.0 were not included since sensitivity analysis cannot be conducted with ENDF/B-VII.0, as mentioned in the introduction to this section.

5.2.1 Nominal Results

Table 5-13 compares the nominal QOIs calculated with KENO-CE using the different ENDF/B libraries. The k_{eff} value obtained with ENDF/B-VII.0 is lower than the values obtained with ENDF/B-VII.1 and VIII.0 due to the lower carbon neutron capture cross section in ENDF/B-VII.0, as discussed in Section 2.2.1.1 and as also observed for the HTR-10 (Section 5.1) eigenvalue. The differences of k_{eff} in the ENDF/B-VII.1 and ENDF/B-VIII.0 results are likely caused by updates in the ^{235}U, ^{238}U, and ^{239}Pu cross section data, as indicated by the k_{eff} sensitivities (Table 5-15) and be a study previously performed for the HTR-10 (Bostelmann et al., 2020). The results of other investigated quantities show consistent results within ~2σ statistical uncertainties.

Table 5-14 shows the impact on k_{eff} of using graphite thermal scattering data with different porosities (0, 10, and 30%) or carbon without thermal scattering data in ENDF/B-VIII.0. While the impact of the different graphite porosities is small (within 1σ statistical standard deviations), neglecting thermal scattering data leads to a k_{eff} increase of ~100 pcm. The smaller impact of the porosity compared to the impact observed for the HGR-10 is likely due to the PB-FHR-Mk1's elevated temperature (temperature of all mixtures above 800 K) since it was shown that the increased temperatures show a decreased effect of the choice of graphite thermal scattering data (Table 5-2).

The nominal axial power distribution is displayed in Figure5-8 (left side). The power distribution was normalized to achieve an average core value of 1.0. The dotted lines indicate the straight cylindrical region of the reactor as opposed to the (de)fueling chutes above and below. The statistical error (see right side of Figure 5-9) was determined based on repeated nominal calculations with different random seeds using the same sample size, as in the nuclear data perturbation calculations (1,000). The power shows its maximum in a region located slightly below the axial midline of the core; there is an asymmetry in the burnup distribution as the pebbles travel through the reactor from the bottom to the top and therefore have on average a smaller burnup in the lower regions than in the higher elevation regions. The statistical error is larger in the uppermost and bottom regions of the reactor since the neutron flux is lower in these regions. The ENDF/B-VII.1 and the ENDF/B-VIII.0 KENO-MG calculations resulted in an axial power peaking factor of 1.409 and 1.410, respectively, with a statistical uncertainty of ~0.14%. (The statistical error was only calculated with ENDF/B-VII.1 and is assumed to be similar for the ENDF/B-VIII.0 result since the statistical error is mainly dependent on factors such as the number of simulated neutron histories and the axial discretization of the model.)

Table 5-13   PB-FHR-Mk1: Nominal Results Determined with KENO-CE

QOI	ENDF/B-VII.0	ENDF/B-VII.1	ENDF/B-VIII.0	$\Delta\rho^{VII.1/VII.0}$ [pcm]	$\Delta\rho^{VIII.0/VII.1}$ [pcm]
k_{eff}	0.94607 ± 0.00022	0.94091 ± 0.00008	0.94368 ± 0.00021	-579 ± 26	312 ± 25
Fuel temp.	-720 ± 34	-776 ± 12	-745 ± 34	-56 ± 36	30 ± 36
Salt temp.	-286 ± 33	-363 ± 11	-373 ± 36	-77 ± 34	-10 ± 38
Salt density	-1023 ± 38	-1071 ± 12	-1015 ± 44	-48 ± 40	56 ± 45

Table 5-14   PB-FHR-Mk1: Effects of Graphite Porosity Evaluations on Calculated KENO k_{eff} Results using ENDF/B-VIII.0 Graphite Data[14]

Graphite/carbon evaluation	k_{eff}	Δk [pcm]
Graphite, 0% porosity	0.94368 ± 0.00021	(ref)
Graphite, 10% porosity	0.94372 ± 0.00020	4 ± 29
Graphite, 30% porosity	0.94362 ± 0.00020	-6 ± 29
Carbon	0.94464 ± 0.00023	96 ± 31

5.2.2 Sensitivity Analysis

Relevant mixture-, region-, and energy-integrated sensitivities of all QOIs as determined with CE TSUNAMI are presented in Table 5-15 through Table 5-18. Each sensitivity coefficient shown in these tables represents the sensitivity of a specific QOI to a single specific reaction and can be used to understand relevant sensitivities for a given QOI.

The largest k_{eff} sensitivity is the sensitivity to the average number of neutrons produced per fission event ($\bar{\nu}$) of ^{235}U resulting from the immediate contribution to the system's reactivity (Table 5-15). Other large sensitivities are observed for ^{239}Pu $\bar{\nu}$, fission and (n,γ), graphite elastic scattering, graphite radiative neutron capture (n,γ), ^{235}U fission and (n,γ), and ^{238}U (n,γ). A significant sensitivity was also observed for ^{7}Li (n,γ) reaction since Li is a major component of the coolant salt.

For the reactivity effects, it was found that $\bar{\nu}$ and the fission cross section of the major fissile nuclides—^{235}U, ^{239}Pu, and ^{241}Pu—are among the top sensitivities due to their immediate contribution to the reactivity of the system. Radiative capture (n,γ) cross sections of ^{235}U, ^{238}U, ^{239}Pu, and ^{240}Pu are relevant for all QOIs. Other relevant reactions are reactions of salt components: (n,γ) for ^{7}Li, ^{9}Be, and ^{19}F; ^{6}Li; (n,α) for ^{9}Be and ^{19}F; elastic scattering for ^{7}Li, ^{9}Be and ^{19}F; and ^{9}Be (n,2n). Furthermore, since the fuel is a mixture of fuel at different burnups, fission and decay products play a role, such as ^{135}Xe and several Sm isotopes.

While the displayed k_{eff} sensitivities show the largest obtained sensitivities, sensitivities to scattering reactions of fuel component, including ^{7}Li, ^{9}Be, and ^{19}F, were removed from the sensitivity ranking of the other QOIs. As mentioned above, it was not possible to sufficiently converge these sensitivities with TSUNAMI; the statistical uncertainties of these reactions were above 100%, despite tighter convergence criteria and tallies in few energy groups. Since each sensitivity coefficient represents the sensitivity of a QOI to only this specific reaction and is not

---

[14] Changes in k_{eff} are relative to the 0% porosity graphite evaluation.

influenced by other potentially nonconverged sensitivities, the listed values remain valid and can be used to understand relevant sensitivities of the QOIs.
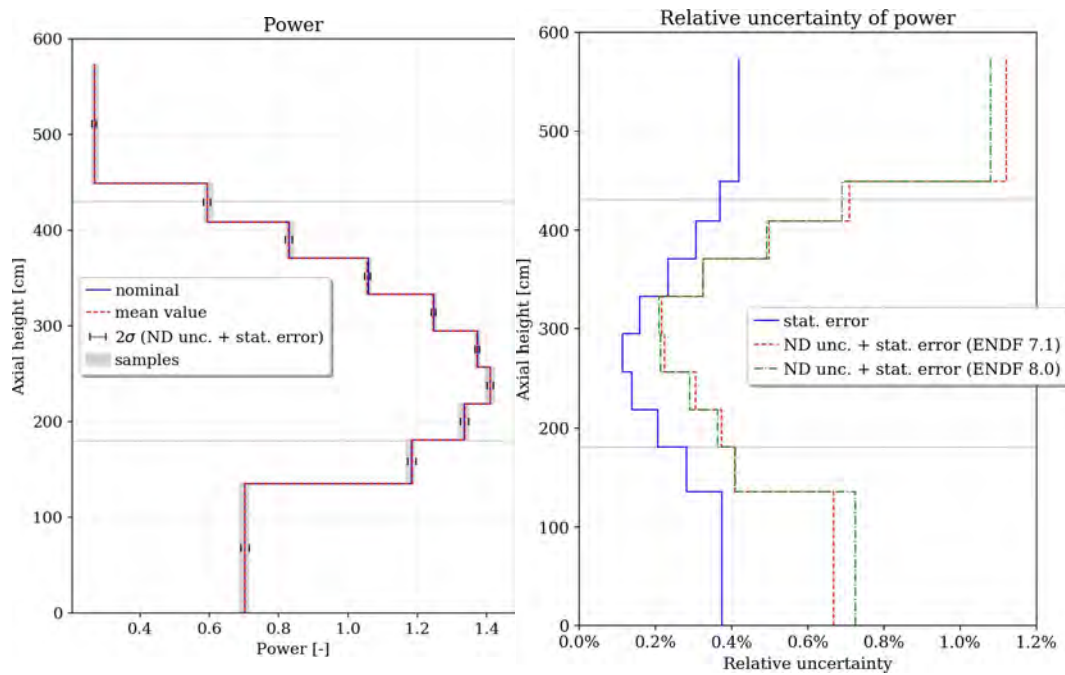
Figure 5-8 Sampler∕KENO-MG Mean Value and Uncertainty Results of the Axial Power Distribution of the PB-FHR-Mk1[15]

---

[15] The left axial power plot shows results determined with ENDF/B-VII.1 data. Differences between ENDF/B-VII.1 and ENDF/B-VIII.0 results would not be visible in this plot. The samples refer to the individual calculations with perturbed nuclear data.

Table 5-15   PB-FHR-Mk1: Top k_eff Sensitivities[16]

Nuclide	Reaction	Sensitivity (increasing k_{eff})	Nuclide	Reaction	Sensitivity (decreasing k_{eff})
u-235	$\bar{\nu}$	7.756e-01 ± 9.335e-05	u-238	n,γ	-9.834e-02 ± 3.780e-05
u-235	fission	3.790e-01 ± 1.066e-04	li-7	n,γ	-8.118e-02 ± 1.109e-05
graphite	elastic	2.842e-01 ± 3.343e-02	u-235	n,γ	-7.937e-02 ± 9.396e-06
pu-239	$\bar{\nu}$	1.789e-01 ± 8.609e-05	pu-239	n,γ	-4.682e-02 ± 6.211e-06
pu-239	fission	1.005e-01 ± 8.629e-05	graphite	n,γ	-4.287e-02 ± 7.562e-06
f-19	elastic	6.652e-02 ± 8.836e-03	f-19	n,γ	-3.612e-02 ± 4.859e-06
pu-241	$\bar{\nu}$	4.414e-02 ± 4.771e-05	pu-240	n,γ	-3.273e-02 ± 1.068e-05
be-9	elastic	3.482e-02 ± 3.613e-03	xe-135	n,γ	-3.255e-02 ± 4.204e-06
pu-241	fission	2.544e-02 ± 4.775e-05	li-6	n,t	-2.061e-02 ± 2.816e-06
li-7	elastic	1.762e-02 ± 1.294e-03	nd-143	n,γ	-9.885e-03 ± 1.202e-06

Table 5-16   PB-FHR-Mk1: Fuel Temperature Reactivity Sensitivities[17]

Nuclide	Reaction	Sensitivity (reducing negative $\Delta\rho$)	Nuclide	Reaction	Sensitivity (increasing negative $\Delta\rho$)
u-235	$\bar{\nu}$	6.404e-01 ± 1.308e-02	u-238	n,γ	-1.108e+00 ± 5.159e-03
u-235	fission	3.381e-01 ± 1.444e-02	pu-239	n,γ	-9.163e-02 ± 8.206e-04
pu-239	$\bar{\nu}$	3.110e-01 ± 1.196e-02	li-7	n,γ	-8.405e-02 ± 1.517e-03
pu-239	fission	1.718e-01 ± 1.210e-02	u-238	elastic	-8.261e-02 ± 1.479e-02
pu-241	$\bar{\nu}$	4.664e-02 ± 6.811e-03	pu-240	n,γ	-7.281e-02 ± 1.368e-03
pu-241	fission	2.466e-02 ± 6.815e-03	u-235	n,γ	-6.315e-02 ± 1.257e-03
be-9	n,2n	1.508e-02 ± 2.978e-03	f-19	n,γ	-3.730e-02 ± 6.628e-04
si-29	elastic	3.406e-03 ± 2.678e-03	li-6	n,t	-2.134e-02 ± 3.850e-04
ce-142	elastic	2.381e-03 ± 1.391e-03	u-236	n,γ	-1.029e-02 ± 3.728e-04
sm-153	elastic	1.948e-03 ± 1.277e-03	pu-241	n,γ	-9.850e-03 ± 1.191e-04

---

[16] Top 10 positive and top 10 negative mixture-, region-, and energy-integrated sensitivities, determined with SCALE/TSUNAMI using ENDF/B-VII.1 data.

[17] Temperature increased by 500 K, $\Delta\rho$ = -776 ± 12 pcm; mixture-, region-, and energy-integrated sensitivities, determined with SCALE/TSUNAMI using ENDF/B-VII.1 data.

Table 5-17   PB-FHR-Mk1: Salt Temperature Reactivity Sensitivities[18]

Nuclide	Reaction	Sensitivity (reducing negative $\Delta\rho$)	Nuclide	Reaction	Sensitivity (increasing negative $\Delta\rho$)
pu-239	$\bar{\nu}$	3.265e+00 ± 2.480e-02	u-235	$\bar{\nu}$	-2.534e+00 ± 2.724e-02
pu-239	fission	1.878e+00 ± 2.514e-02	pu-239	n,γ	-1.009e+00 ± 1.806e-03
xe-135	n,γ	5.249e-01 ± 1.160e-03	u-235	fission	-8.792e-01 ± 2.973e-02
pu-241	$\bar{\nu}$	2.678e-01 ± 1.435e-02	pu-240	elastic	-3.118e-01 ± 3.037e-03
pu-241	fission	1.689e-01 ± 1.437e-02	pu-241	n,γ	-6.586e-02 ± 2.544e-04
u-235	n,γ	1.526e-01 ± 2.602e-03	u-238	n,γ	-4.409e-02 ± 1.088e-02
sm-149	n,γ	9.843e-02 ± 2.703e-04	eu-155	n,γ	-3.640e-02 ± 5.630e-05
li-7	n,γ	8.545e-02 ± 3.162e-03	np-237	n,γ	-3.076e-02 ± 6.326e-05
sm-151	n,γ	5.536e-02 ± 1.207e-04	rh-103	n,γ	-2.871e-02 ± 2.462e-04
u-238	elastic	4.906e-02 ± 3.246e-02	f-19	n,α	-7.455e-03 ± 9.678e-04

Table 5-18   PB-FHR-Mk1: Salt Density Reactivity Sensitivities[19]

Nuclide	Reaction	Sensitivity (reducing negative $\Delta\rho$)	Nuclide	Reaction	Sensitivity (increasing negative $\Delta\rho$)
u-235	fission	2.002e+00 ± 1.043e-02	li-7	n,γ	-2.264e+00 ± 1.207e-03
u-235	$\bar{\nu}$	8.650e-01 ± 9.368e-03	f-19	n,γ	-9.905e-01 ± 5.280e-04
u-238	n,γ	4.303e-01 ± 3.566e-03	li-6	n,t	-5.747e-01 ± 3.062e-04
pu-239	fission	3.753e-01 ± 8.552e-03	be-9	n,γ	-2.503e-01 ± 1.333e-04
u-235	n,γ	2.619e-01 ± 8.730e-04	o-16	elastic	-9.242e-02 ± 5.322e-02
be-9	n,2n	2.533e-01 ± 2.283e-03	f-19	n,α	-8.808e-02 ± 3.654e-04
pu-240	n,γ	1.816e-01 ± 9.513e-04	be-9	n,α	-7.679e-02 ± 1.402e-04
pu-239	n,γ	1.603e-01 ± 5.702e-04	f-19	n,n'	-6.617e-02 ± 2.831e-02
pu-239	$\bar{\nu}$	1.149e-01 ± 8.495e-03	u-238	elastic	-3.942e-02 ± 1.052e-02
pu-241	fission	9.554e-02 ± 4.848e-03	c	elastic	-2.001e-02 ± 1.345e-02

5.2.3   Uncertainty Analysis

Table 5-19 presents the uncertainties of the different QOIs due to nuclear data as calculated with Sampler/KENO-MG using different covariance libraries. Despite the large sample size of 1,000, the sensitivity analysis revealed only a few top contributors to these uncertainties in terms of R^2 (Figure 5-9). Individual contributions to the uncertainty are further determined using the sensitivities obtained with TSUNAMI, only for the sensitivities that were well converged. These contributions are compared in Figure 5-9.

---

[18]   Temperature increased by 300 K, $\Delta\rho$ = -363 ± 11 pcm; mixture-, region-, and energy-integrated sensitivities, determined with SCALE/TSUNAMI using ENDF/B-VII.1 data.

[19]   Density multiplied by 1.5, $\Delta\rho$ = -1071 ± 12 pcm; mixture-, region-, and energy-integrated sensitivities, determined with SCALE/TSUNAMI using ENDF/B-VII.1 data.

The behavior of the mean values and standard deviations of the Sampler/KENO-MG calculation was investigated as a function of the sample size to confirm that a sufficient sample size was used and to rule out any unexpected behavior. It was further confirmed that the output comes from a normal distribution, so that the calculated *standard deviation* can indeed be interpreted as *uncertainty* similar to the output obtained with TSUNAMI. An example of such analysis is provided in Appendix A.2.2 for the axial peak power.

Table 5-19   PB-FHR-Mk1: Sampler/KENO-MG Uncertainties of QOIs

QOI	ENDF/B-VII.1	ENDF/B-VIII.0	$\frac{VIII.0}{VII.1} - 1$
k_{eff}	1.382%	1.432%	3.60%
Fuel temperature	3.111%		
Salt temperature	5.538%		
Salt density	35.647%		
Axial peak power[*]	0.305%	0.280%	-4.89%

[*] All uncertainties determined with Sampler include the statistical and nuclear data uncertainties. Figure 5-7 shows that the axial power experiences a statistical error of ~0.14%. To obtain the uncertainty only from nuclear data, this uncertainty can be subtracted from the values (arriving at 0.165% and 0.140% for ENDF/B-VII.1 and ENDF/B-VIII.0, respectively).

The dominating contributor to the k_{eff} uncertainty and a relevant contributor to the other QOI uncertainties is ^{7}Li (n,γ). The uncertainty of this reaction (Figure 2-33) did not change in the latest ENDF/B releases. Due to the Doppler broadening of the resonance with temperature, next to ^{7}Li (n,γ), the uncertainty of ^{238}U (n,γ) (Figure 2-27) is the most relevant contributor to the fuel temperature reactivity uncertainty. The salt temperature reactivity uncertainty is driven by the uncertainties of ^{239}Pu $\bar{\nu}$ (Figure 2-22), fission (Figure 2-23) and (n,γ) (Figure 2-24), and by the uncertainty of ^{135}Xe (n,γ) (Figure 5-14). Differences in the output uncertainty in ENDF/B-VIII.0 are caused by updates of the mentioned ^{239}Pu cross section uncertainties. It is further noted that the uncertainty of ^{155}Eu (n,γ) increased from ENDF/B-VII.0 to ENDF/B-VII.1, providing a relevant contribution to the salt temperature reactivity uncertainty with ENDF/B-VII.1 and ENDF/B-VIII.0. The salt density reactivity uncertainty is mainly influenced by neutron capture in the main salt components ^{7}Li, ^{9}Be, and ^{19}F (Figure 2-33, Figure 5-12, Figure 5-13).

Relevant differences of the individual contributions between the calculations with different ENDF/B libraries is mainly observed for reactions of ^{235}U, ^{238}U, and ^{239}Pu. In particular, the uncertainties of the relevant reactions in the salt did not change at all, or they changed only slightly.
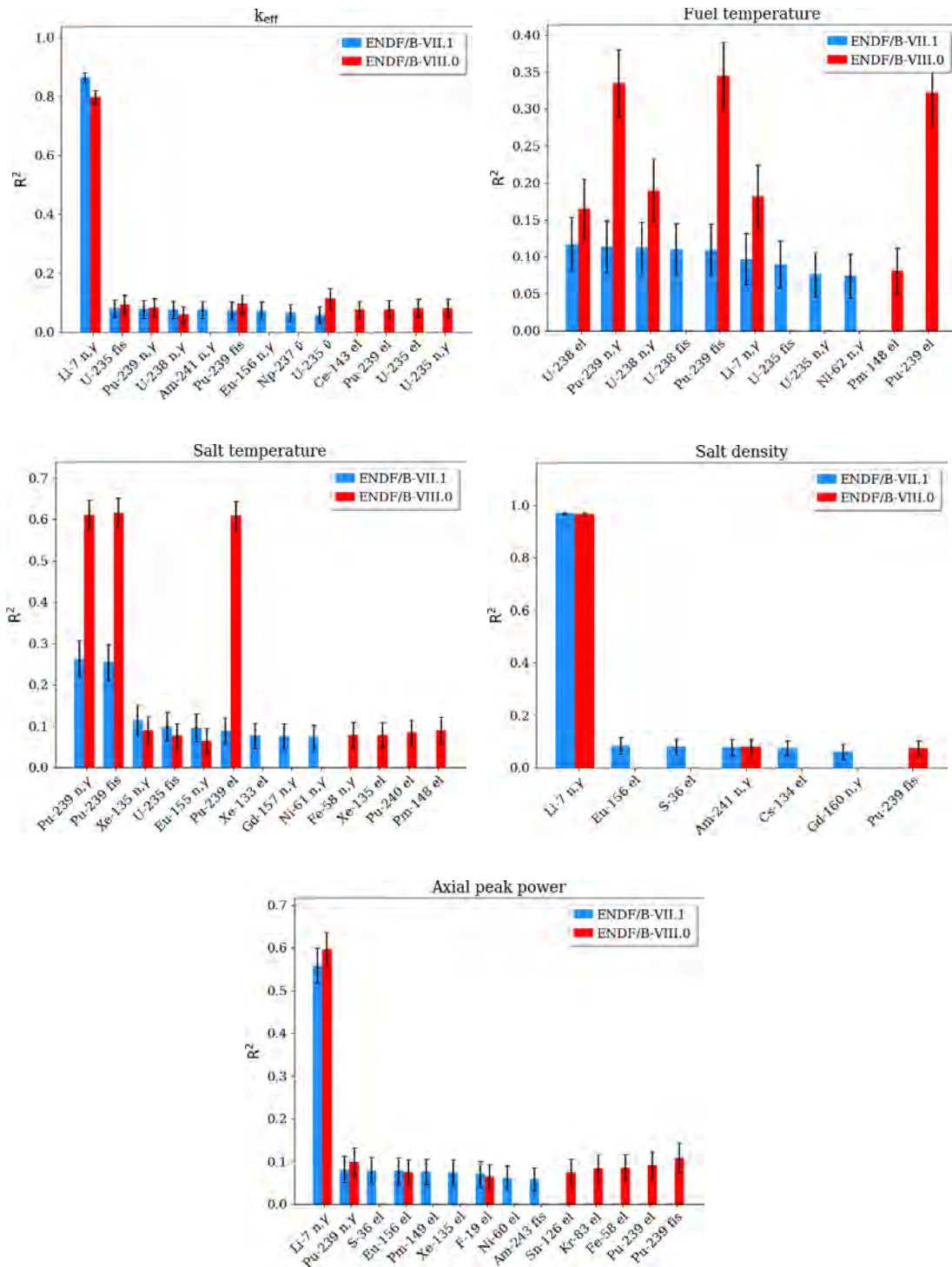
Figure 5-9 PB-FHR-Mk1: Sampler/KENO-MG Top Contributor to the Output Uncertainties in Terms of R²
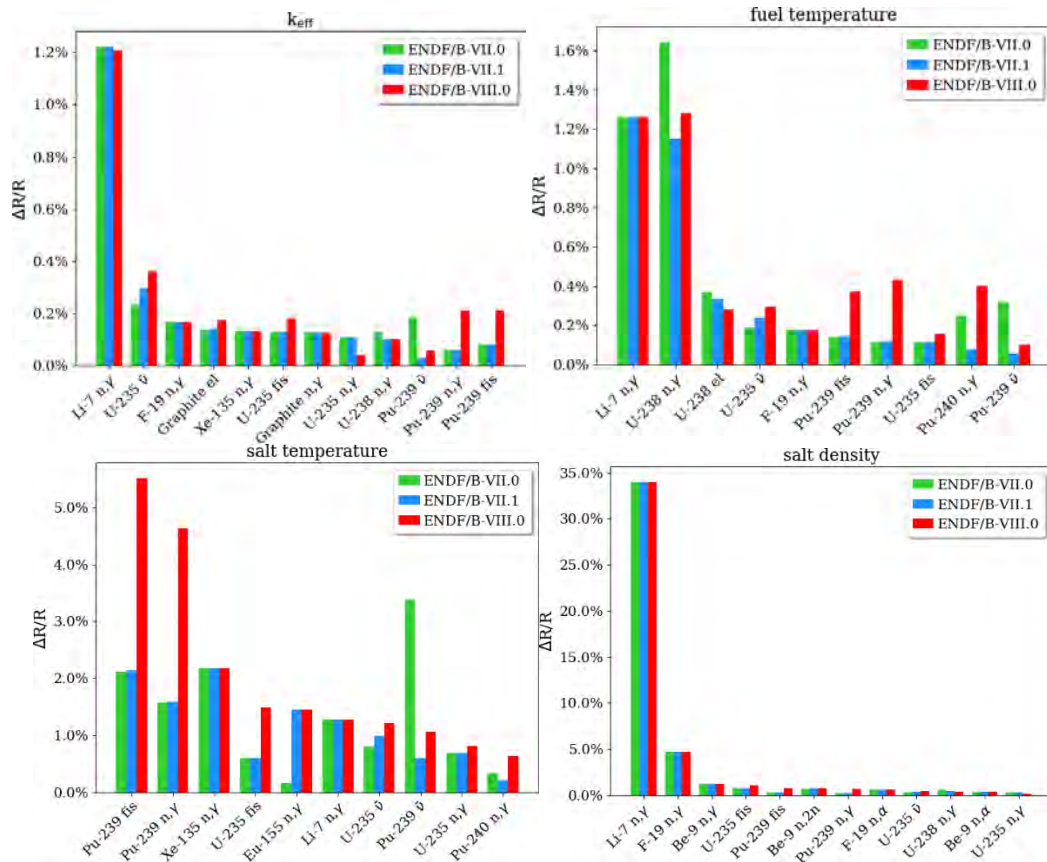
Figure 5-10 PB-FHR-Mk1: Contributions to the Output Uncertainties[20]
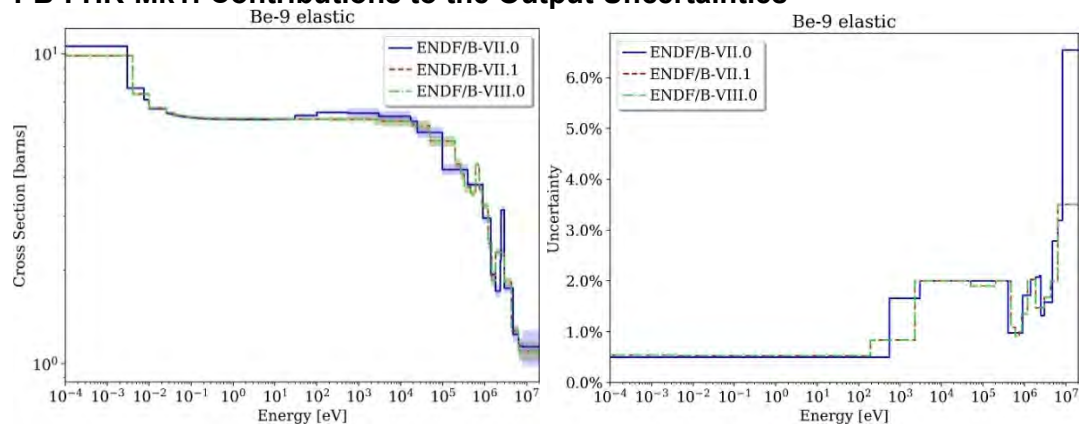
Figure 5-11 ⁹Be Elastic Scattering Nominal Data and Uncertainty

---

[20] Obtained with TSUNAMI, in ΔR/R, R response
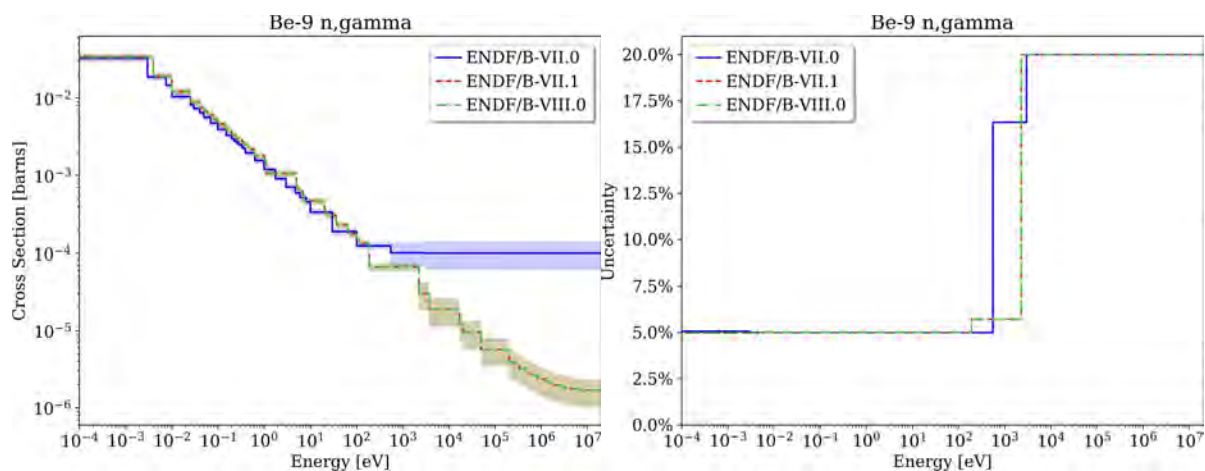
Figure 5-12 ⁹Be (n,γ) Nominal Data and Uncertainty
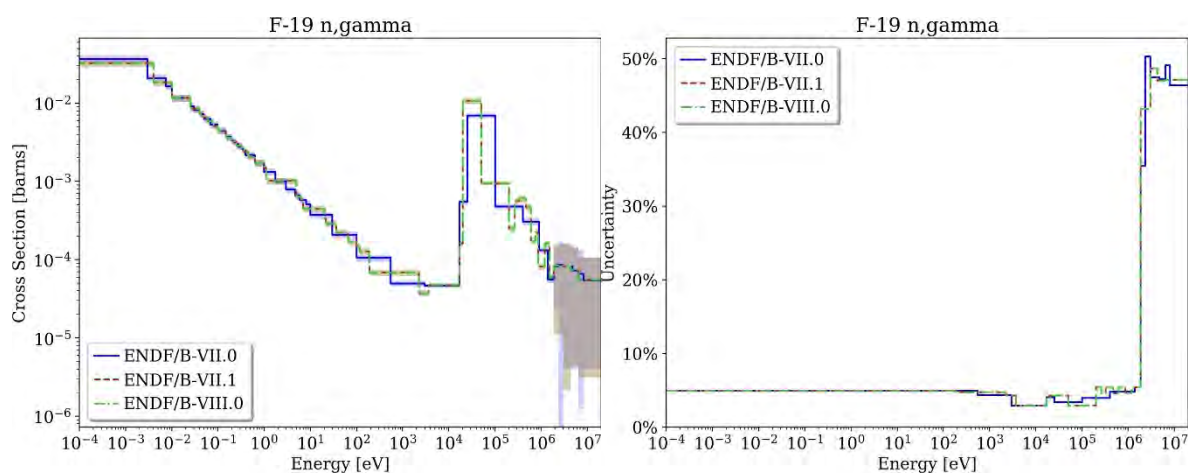
Figure 5-13 ¹⁹F (n,γ) Nominal Data and Uncertainty
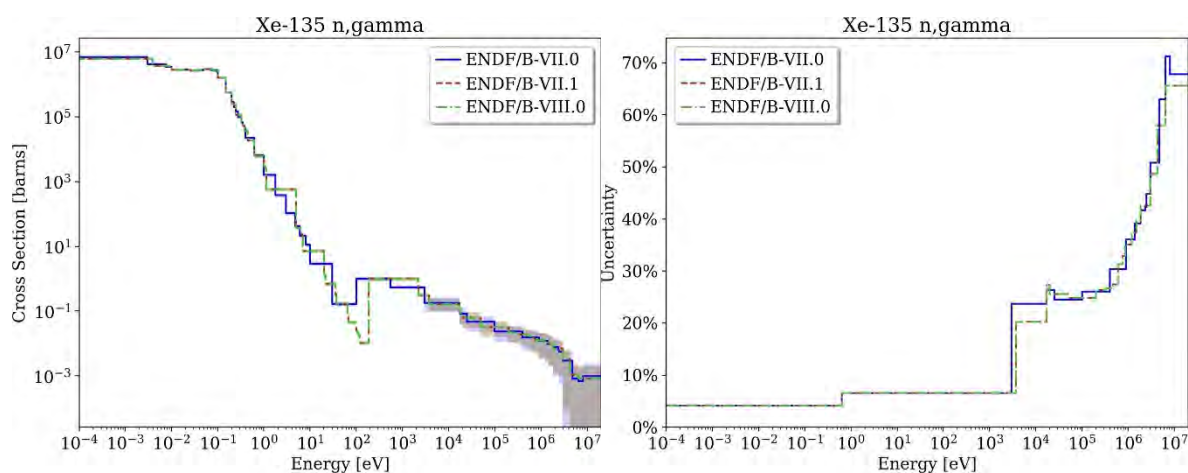
Figure 5-14 ¹³⁵Xe (n,γ) Nominal Data and Uncertainty
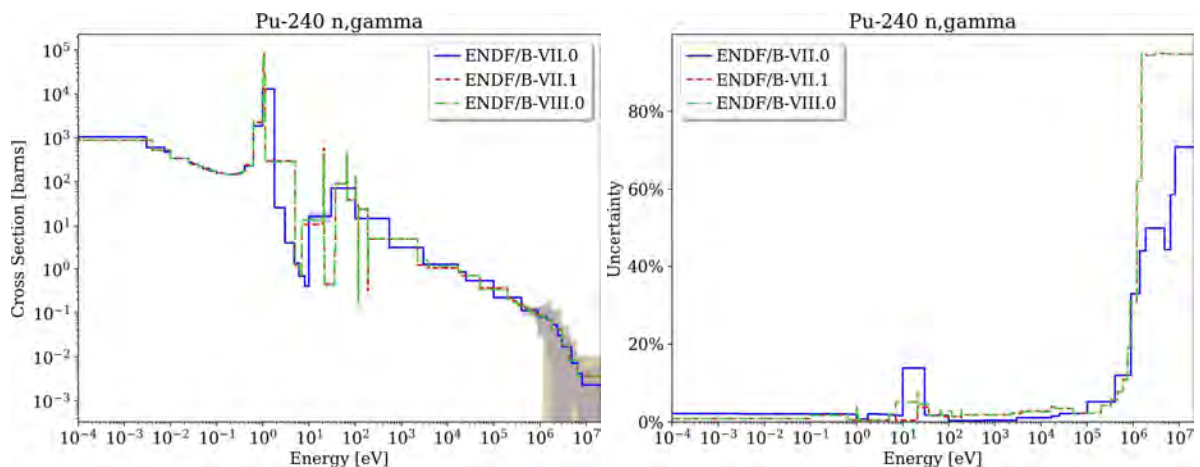
Figure 5-15 ^{240}Pu (n,γ) Nominal Data and Uncertainty
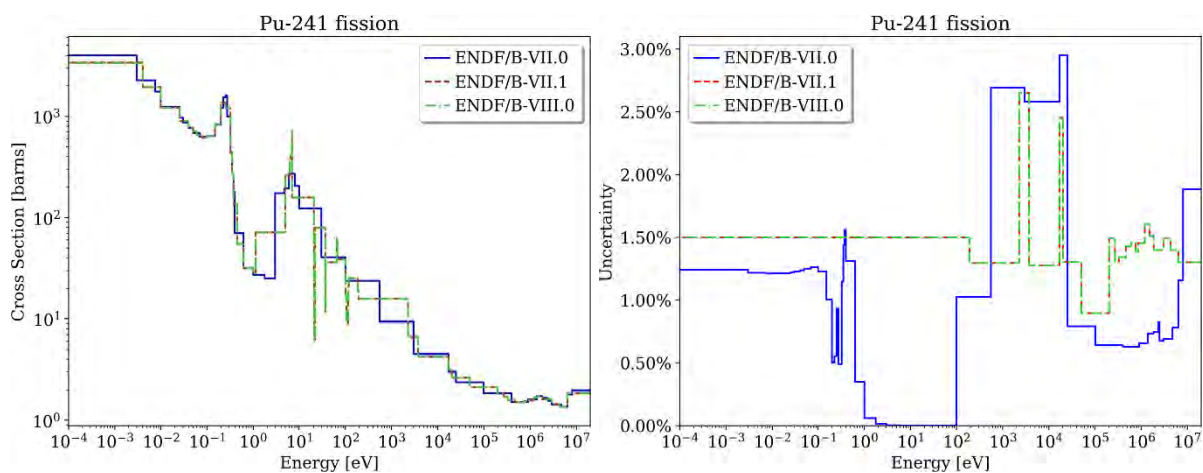
Figure 5-16 ^{241}Pu Fission Nominal Data and Uncertainty
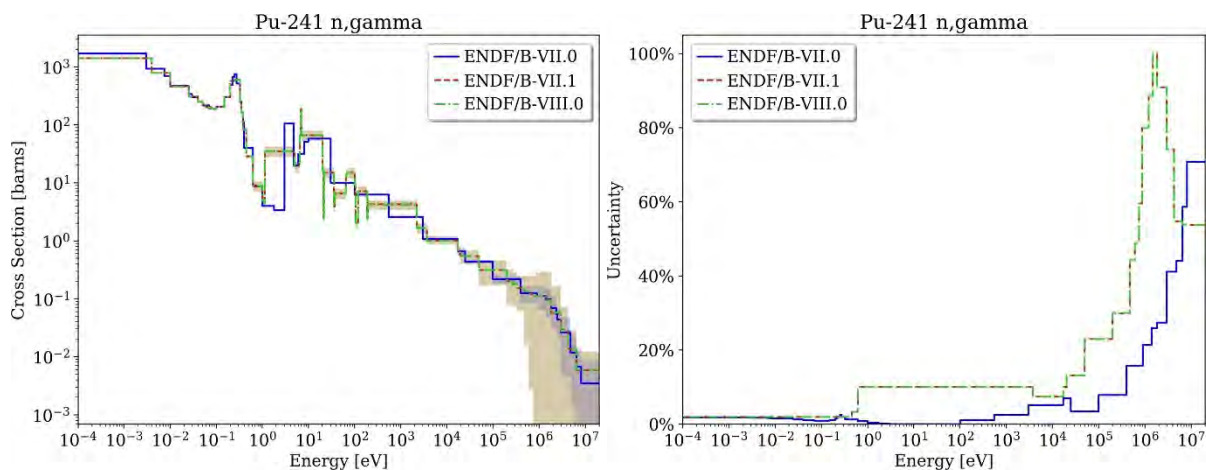
Figure 5-17 ^{241}Pu (n,γ) Nominal Data and Uncertainty
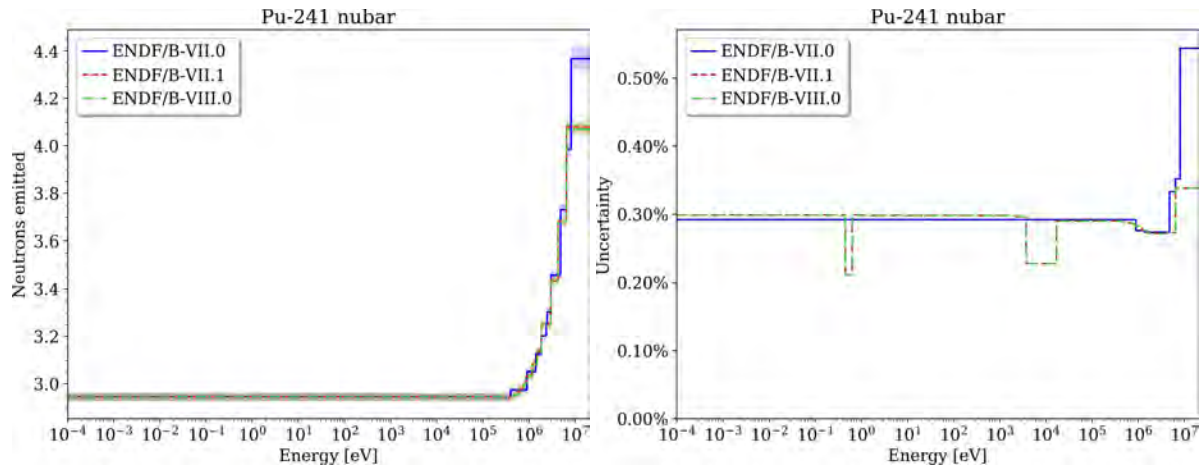
Figure 5-18 ²⁴¹Pu Fission Neutron Multiplicity Nominal Data and Uncertainty

5.3   MSRE, Molten Salt Reactor

The SCALE model of the MSRE was developed based on the benchmark specifications in the IRPhEP handbook (Shen et al., 2019). Figure 5-19 and Figure 5-20 show plots of the full core model. The neutron flux spectrum in different regions of the core is displayed in Figure 5-21.
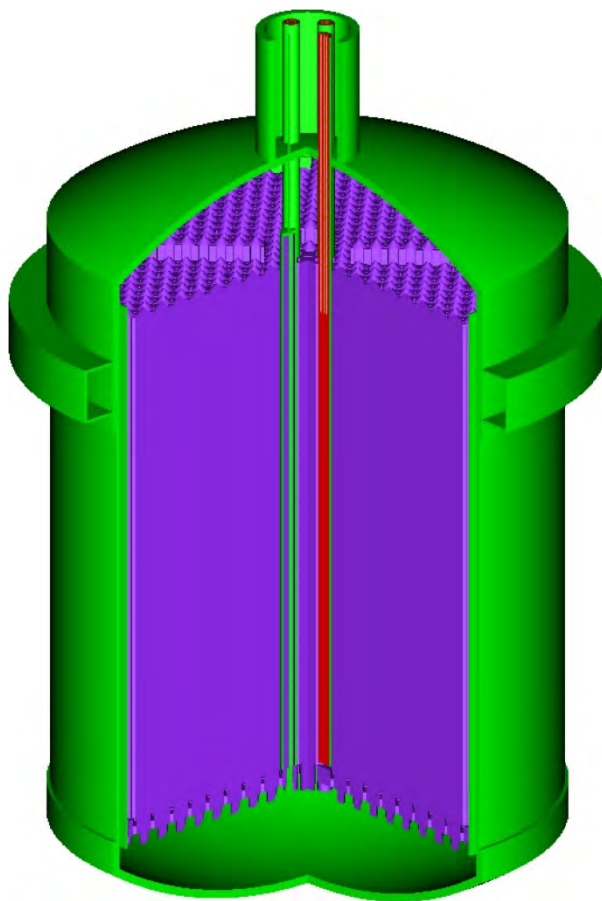
Figure 5-19 MSRE: SCALE Model of the Reactor Vessel (Outer Structure not Displayed)[21] The sensitivity and uncertainty analyses for the MSRE were performed for the following QOIs:

1. k_{eff}

2. CR worth: reactivity difference between the nominal state and all CRs fully inserted

3. graphite impurity reactivity: graphite impurity densities multiplied by 3 (all impurities but boron)

4. graphite temperature reactivity: graphite temperature increased by 500 K

5. graphite density reactivity: graphite density multiplied by 1.05

6. fuel salt temperature reactivity: fuel salt temperature increased by 500 K

7. fuel salt density reactivity: fuel salt density multiplied by 1.05

---

[21] The INOR-8 structure is visible in green, and the graphite structure is in purple. The red tube shows one of the three CR channels (CR almost fully withdrawn). The other visible tube is occupied by the sample basket. The fuel salt was removed from this plot to provide a better view of the different elements.

8. ^{6}Li content reactivity: ^{6}Li densities in fuel salt multiplied by 2

9. boron content reactivity: boron densities in graphite multiplied by 5
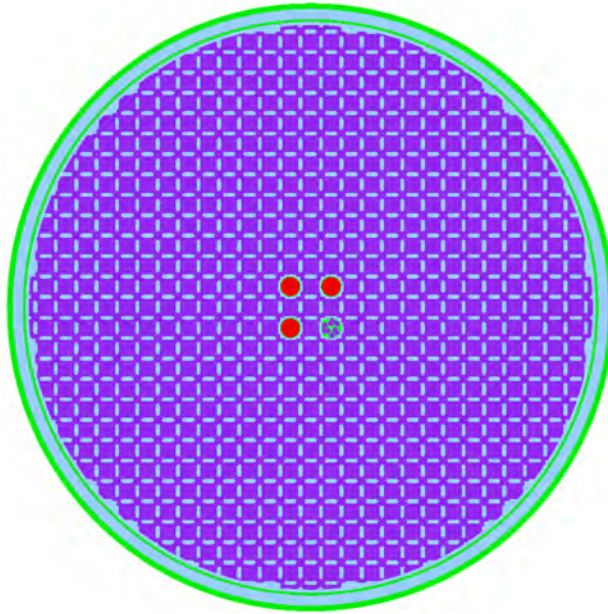
Figure 5-20 MSRE: Horizontal Cut of the SCALE Full Core Model (Outer Structure not Displayed)[22] This case had challenges similar to those for the PB-FHR-Mk1 CE TSUNAMI calculations with respect to convergence of several sensitivities to scattering reactions, mainly from salt components (^{7}Li, ^{9}Be, ^{19}F). As in the PB-FHR-Mk1, calculations with Sampler in combination with KENO in MG mode using SCALE's 252-group library were performed to study the uncertainties caused by nuclear data uncertainties on the listed QOIs. A sample size of 1,000 in Sampler allowed for analysis of the top contributing cross section uncertainties to the observed output uncertainties.

Nominal k_{eff} results with different ENDF/B libraries and different graphite porosities for ENDF/B-VIII.0 were obtained using the Shift Monte Carlo code. All other neutron transport calculations were performed with the KENO Monte Carlo code. An ORNL study of nominal results and uncertainty and sensitivity results of k_{eff} with Shift for the full MSRE core, as well as simplified MSRE models, are published in the literature (Bostelmann et al., 2021).

5.3.1 Nominal Results

Table 5-20 compares the k_{eff} values calculated using different ENDF/B evaluations to the reported benchmark value and the calculated benchmark result (Shen et al., 2019) as determined by the University of California, Berkeley (UCB) using the Serpent Monte Carlo code (Leppänen 2007).

---

[22] The magnitude of perturbations was chosen to result in reactivity differences large enough to clearly distinguish statistical effects from the Monte Carlo calculations based on the impact of nuclear data uncertainties on the results
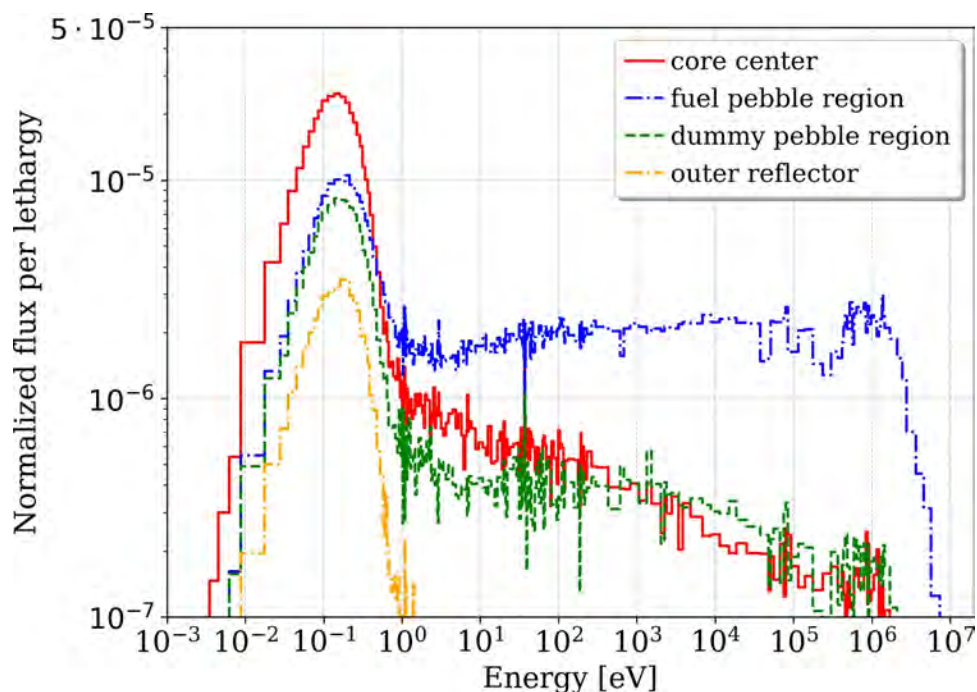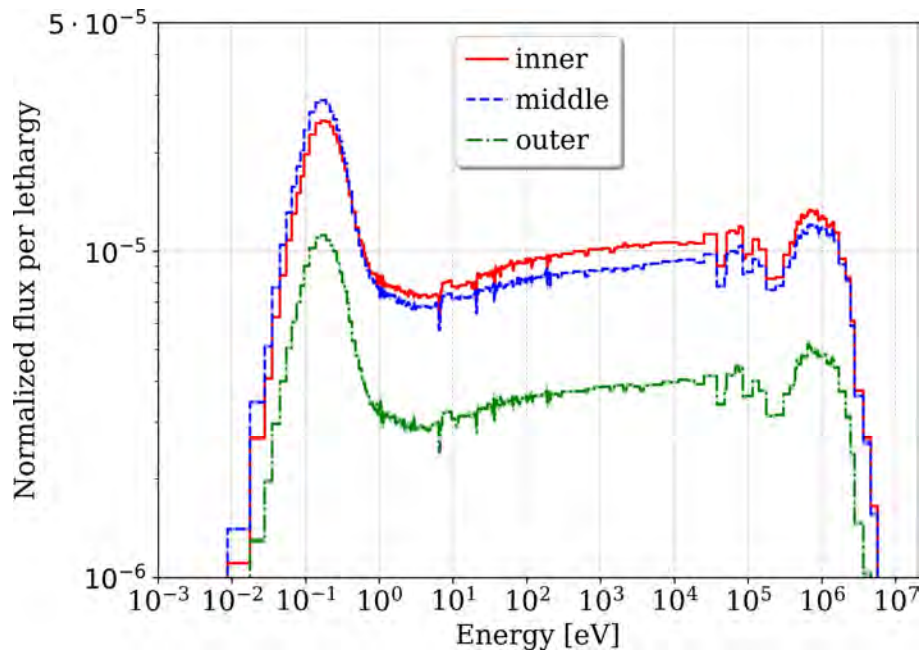
Figure 5-21 MSRE: Normalized Neutron Flux in a 252-Group Representation at the Core Axial Midline, at Different Radial Positions as Determined with SCALE/Shift

A difference of 230 pcm is observed between the eigenvalues calculated with ENDF/B-VII.1 using Shift and Serpent. This difference is likely due to differences in the code processing of the respective applied cross section libraries, the cross section temperature interpolation method, and other code modeling differences. Shen et al. demonstrated that applying the graphite thermal scattering data at 800 or 1,000 K instead of applying interpolated data to MSRE's uniform temperature of 911 K can cause a difference in eigenvalue of several hundred pcm (Shen et al., 2021). This indicated that differences in temperature interpolation can cause a difference in eigenvalue. Modeling differences can arise from simplifying modeling assumptions; the Serpent model of the benchmark was initially developed to include many details that were later simplified for the final benchmark specifications included in the IRPhEP handbook. Although the benchmark was well described in general, some minor information was missing, such as details on the end pieces of the CRs or other small elements.

The k_{eff} values calculated with ENDF/B-VII.0 and ENDF/B-VII.1 are consistent, despite the differences in the carbon capture cross section in the thermal energy range (Figure 2-29) and the ^{6}Li (n,t) reaction (Figure 2-32) between the two libraries. Large differences due to the carbon capture cross section update, which were observed for the HTR-10 (Table 5-1Table), were not seen here. The impact of this cross section is reduced in the MSRE case because of the different moderator-to-fuel ratio and the different fuel and moderator arrangement. The MSRE has a slightly harder neutron spectrum than the HTR-10 (compare Figure 5-21 to Figure 5-2), and therefore decreases the sensitivity of MSRE to nuclear data changes in the thermal energy range. Consistently, the sensitivity analysis presented in Section 5.3.2 shows that the k_{eff} sensitivity to both ^{6}Li (n,t) and carbon capture is small for MSRE. For example, the k_{eff} sensitivity to graphite (n,γ) is -0.017 for MSRE (Table 5-24) and -0.085 (i.e., 5 times higher) for HTR-10 (Table 5-4).

A 265 pcm difference in k_{eff} was obtained between the ENDF/B-VII.1 and ENDF/B-VIII.0 calculations. Since only fresh fuel is considered here, it is likely that updates in ^{235}U and ^{238}U cross sections are the major cause of the observed differences based on previous studies (Bostelmann et al., 2020) and based on the sensitivity analysis presented in Section 5.3.2. For example, ^{235}U $\bar{\nu}$ and (n,γ) show significant differences between two ENDF/B evaluations and have the largest positive and negative sensitivities, respectively. The values for all other investigated QOIs agree between the calculations with different ENDF/B library versions (Table 5-22).

Table 5-21 shows the impact on k_{eff} of using graphite thermal scattering data with different porosities (0, 10, and 30%) or carbon without thermal scattering data in ENDF/B-VIII.0. While the impact of the different graphite porosities is small (within 2σ statistical standard deviations), neglecting thermal scattering data leads to a k_{eff} increase of ~300 pcm. The smaller impact of the porosity compared to the impact observed for the HTR-10 is likely due to MSRE's elevated temperature (911 K), as well as geometrical differences in the system with respect to the fuel and moderator, which cause a slightly harder neutron spectrum in the MSRE as compared to the HTR-10 and therefore decreases the sensitivity of MSRE to changes in the thermal energy range, Consistently, the k_{eff}. sensitivity to graphite elastic scattering is smaller for MSRE as compared to HTR-10. Table 5-23 shows a value of 0.528 for MSRE as compared to a value of 0.683 (i.e., ~30% higher) for HTR-10 (Table 5-4).

All calculations that were performed with SCALE or Serpent show large differences in the 2,000 pcm range compared to the experimental benchmark k_{eff}. The (1σ) experimental k_{eff} uncertainty is given as 420 pcm and considers uncertainties in the geometry and material data. The graphite density, fuel salt density, and ^6Li enrichment in the fuel salt are the main contributors to this uncertainty (Shen et al., 2021). However, these uncertainties alone cannot explain the large difference between the calculations and the measurement. The authors of the benchmark specifications report several challenges when determining the dimensions and material compositions of this benchmark and when performing the initial Monte Carlo criticality calculations with Serpent. For example, discrepancies with respect to the fuel salt compositions were identified which could cause a k_{eff} bias of up to 450 pcm (Shen et al., 2021). With respect to nuclear data, the non-consideration of the salt's thermal scattering could lead to a bias of a few hundred pcm as demonstrated by Mei et al. (Mei et al., 2013). The impact of nuclear data uncertainties on k_{eff} is in the range of 600–700 pcm, as shown in the next sections.

Table 5-20   MSRE: Shift-CE k_{eff} Results Compared to the Benchmark and the Reported Serpent Results

Case	Library	k_{eff}	Benchmark Δk [pcm]
SCALE/Shift	ENDF/B-VII.0	1.01936 ± 0.00019	1958 ± 420
	ENDF/B-VII.1	1.01903 ± 0.00021	1925 ± 421
	ENDF/B-VIII.0	1.02168 ± 0.00019	2190 ± 420
UCB, Serpent (Shen et al., 2019)	ENDF/B-VII.1	1.02132 ± 0.00003	2154 ± 420
Benchmark		0.99978 ± 0.00420	(ref)

Table 5-21 MSRE: Effects of Graphite Porosity Evaluations on Calculated Shift k_{eff} Results using ENDF/B-VIII.0 Graphite Data[23]

Graphite/carbon evaluation	k_{eff}	Δk [pcm]
Graphite, 0% porosity	1.02168 ± 0.00019	(ref)
Graphite, 10% porosity	1.02113 ± 0.00021	-55 ± 28
Graphite, 30% porosity	1.02194 ± 0.00018	26 ± 26
Carbon	1.02460 ± 0.00018	292 ± 26

5.3.2 Sensitivity Analysis

Relevant mixture-, region-, and energy-integrated sensitivities for k_{eff} and the CR worth as determined with CE TSUNAMI are presented in Table 5-23 and Table 5-24. Each sensitivity coefficient shown in these tables represents the sensitivity of a specific QOI to a single specific reaction and can be used to understand relevant sensitivities for a given QOI.

Table 5-22 MSRE: Nominal Values of all QOIs Determined with KENO-CE

QOI	ENDF/B-VII.0	ENDF/B-VII.1	ENDF/B-VIII.0	$\Delta\rho^{VII.1/VII.0}$ [pcm]	$\Delta\rho^{VIII.0/VII.1}$ [pcm]
k_{eff}	1.01989 ± 0.00035	1.01932 ± 0.00029	1.02208 ± 0.00023	-55 ± 45	265 ± 37
CR worth	-6262 ± 54	-6283 ± 40	-6238 ± 36	-20 ± 67	45 ± 53
Graphite impurities	-1555 ± 41	-1517 ± 39	-1538 ± 40	38 ± 57	-21 ± 56
Graphite temperature	-2490 ± 41	-2521 ± 38	-2541 ± 31	-31 ± 56	-19 ± 49
Graphite density	2430 ± 40	2412 ± 36	2438 ± 31	-18 ± 54	26 ± 48
Fuel salt temperature	-1315 ± 44	-1259 ± 37	-1206 ± 34	56 ± 57	53 ± 50
Fuel salt density	1104 ± 43	1167 ± 48	1092 ± 35	63 ± 64	-75 ± 59
^{6}Li content in fuel salt	-1433 ± 46	-1425 ± 38	-1413 ± 35	8 ± 60	12 ± 51
Boron content in graphite	-1202 ± 44	-1117 ± 39	-1154 ± 32	84 ± 59	-36 ± 50

As observed for the HTR-10 and the PB-FHR-Mk1, the largest k_{eff} sensitivity is the sensitivity to the average number of neutrons produced per fission event ($\bar{\nu}$) of ^{235}U due to the immediate contribution to the reactivity of the system (Table 5-23). Other large sensitivities were observed for graphite elastic scattering, graphite radiative neutron capture (n,γ), ^{235}U fission and (n,γ), and ^{238}U (n,γ). Significant sensitivities were also observed for ^{7}Li (n,γ) and elastic scattering, ^{19}F elastic and inelastic scattering, and ^{6}Li (n,t) since Li and F are major components of the fuel salt. Sensitivities to Ni elastic scattering and (n,γ) are observed since Ni is the major component of the MSRE's structural material INOR-8. The CR worth of MSRE shows similar sensitivities as k_{eff}, but with different magnitudes. Additionally, the CR worth shows a large sensitivity to (n,γ) reactions of the Gd neutron absorber.

---

[23] Changes in k_{eff} are relative to the 0% porosity graphite evaluation.

Sensitivities are not shown for the other QOIs because many of the listed top sensitivities, in particular elastic scattering of the salt and structural components, show large statistical uncertainties. As mentioned above, it was not possible to sufficiently converge these sensitivities with TSUNAMI; the statistical uncertainties of many reactions are often above 100%, despite tighter convergence criteria and tallies in few energy groups.

Table 5-23 MSRE: Top k_{eff} Sensitivities[24]

Nuclide	Reaction	Sensitivity (increasing k_{eff})	Nuclide	Reaction	Sensitivity (decreasing k_{eff})
u-235	$\bar{\nu}$	9.990e-01 ± 7.088e-06	u-235	n,γ	-1.405e-01 ± 1.600e-05
graphite	elastic	5.283e-01 ± 2.272e-02	u-238	n,γ	-9.196e-02 ± 3.689e-05
u-235	fission	3.726e-01 ± 7.297e-05	Ni-58	n,γ	-2.239e-02 ± 1.102e-05
f-19	elastic	7.693e-02 ± 3.164e-03	graphite	n,γ	-1.689e-02 ± 2.223e-06
be-9	elastic	3.065e-02 ± 1.052e-03	li-6	n,t	-1.428e-02 ± 1.675e-06
ni-58	elastic	2.174e-02 ± 4.849e-04	li-7	n,γ	-1.383e-02 ± 1.622e-06
li-7	elastic	1.863e-02 ± 5.115e-04	f-19	n,γ	-7.724e-03 ± 8.815e-07
f-19	n,n′	1.519e-02 ± 2.291e-04	zr-91	n,γ	-6.799e-03 ± 2.311e-06
be-9	n,2n	7.058e-03 ± 1.718e-05	b-10	n,α	-6.747e-03 ± 1.922e-06
u-238	elastic	5.896e-03 ± 1.057e-04	mo-95	n,γ	-5.766e-03 ± 5.402e-06

Table 5-24 MSRE: Top CR Worth Sensitivities[25]

Nuclide	Reaction	Sensitivity (reducing negative $\Delta\rho$)	Nuclide	Reaction	Sensitivity (increasing negative $\Delta\rho$)
u-235	$\bar{\nu}$	9.977e-01 ± 1.659e-04	u-238	n,γ	-8.170e-02 ± 8.742e-04
graphite	elastic	5.283e-01 ± 2.272e-02	gd-155	n,γ	-8.043e-02 ± 1.669e-04
u-235	fission	7.447e-01 ± 1.767e-03	u-235	n,γ	-7.313e-02 ± 3.852e-04
f-19	elastic	2.582e-01 ± 7.317e-02	graphite	n,γ	-1.689e-02 ± 2.223e-06
ni-58	elastic	1.205e-01 ± 1.082e-02	gd-157	n,γ	-6.119e-02 ± 1.596e-04
ni-58	n,γ	8.372e-02 ± 2.244e-04	gd-156	n,γ	-9.353e-03 ± 4.456e-05
be-9	Elastic	7.627e-02 ± 2.424e-02	li-6	n,t	-5.496e-03 ± 4.044e-05
li-7	Elastic	4.665e-02 ± 1.201e-02	li-7	n,γ	-5.317e-03 ± 3.917e-05
f-19	n,n′	2.433e-02 ± 5.179e-03	h-1	elastic	-5.241e-03 ± 1.465e-03
fe-56	elastic	1.941e-02 ± 2.710e-03	zr-91	n,γ	-5.216e-03 ± 5.359e-05

5.3.3 Uncertainty Analysis

Table 5-25 presents the uncertainties of the different QOIs due to nuclear data as calculated with Sampler/KENO-MG using different covariance libraries. The top contributors to these uncertainties in terms of R^2 are displayed in Figure 5-22. The contributions of reactions for which the sensitivities were not converged are not displayed. Therefore, these tables present

---

[24] Top 10 positive and top 10 negative mixture-, region-, and energy-integrated sensitivities, determined with TSUNAMI using ENDF/B-VII.1 data.

[25] All CRs fully inserted, $\Delta\rho$ = -6303 +/- 18 pcm; top 10 positive and top 10 negative mixture-, region-, and energy-integrated sensitivities, determined with TSUNAMI using ENDF/B-VII.1 data.

comparisons between relevant individual contributions to the output uncertainty. However, they should not be confused with a ranking of relevant contributions, which can be obtained only via Sampler's sensitivity analysis for this case.

The k_{eff} uncertainty is between 0.6 and 0.7%, and the control worth uncertainty is between 1.2 and 1.3%. Small differences in the total uncertainty are observed when using the different ENDF/B libraries due to the increase of the ^{235}U $\bar{\nu}$ and graphite elastic scattering uncertainties in ENDF/B-VIII.0 (Figure 5-22 and Figure 5-23). The uncertainties of the other QOIs also vary slightly between the calculations with the different libraries, but all differences are below 10%. In addition to the reactions described above, relevant differences are observed due to the increased uncertainties of ^{235}U χ and fission and ^{238}U (n,γ) in ENDF/B-VIII.0 compared to the other two libraries. The uncertainty of ^{58}Ni (n,γ) decreased from ENDF/B-VII.0 and VII.1 to VIII.0, and therefore its contribution to the considered output uncertainty decreased (Figure5-25). In contrast, the uncertainty of ^{62}Ni (n,γ) increased (Figure 5-26). For the ^{6}Li content reactivity, the ^{6}Li (n,t) reaction is a relevant contributor to the uncertainty, and an increased contribution is observed in the ENDF/B-VIII.0 calculation due to the increased uncertainty of this reaction in ENDF/B-VIII.0 in the thermal energy range (Figure 2-32). For the boron content reactivity, the contribution of ^{10}B (n,α) is significant, and the increased impact due to an increased uncertainty of this reaction in ENDF/B-VIII.0 is clearly visible in Figure 5-24.

Table 5-25   MSRE: Sampler/KENO-MG Uncertainties of QOIs

QOI	ENDF/B-VII.1	ENDF/B-VIII.0	$\frac{VIII.0}{VII.1} - 1$
k_{eff}	0.655%	0.693%	5.9%
CR worth	1.234%	1.313%	6.4%
Graphite impurities	2.595%	2.590%	-0.2%
Graphite temperature	1.947%	2.056%	5.6%
Graphite density	2.019%	1.945%	-3.7%
Fuel salt density	3.531%	3.516%	-0.4%
^{6}Li content in fuel salt	2.660%	2.825%	6.2%
Boron content in graphite	3.291%	3.420%	3.9%
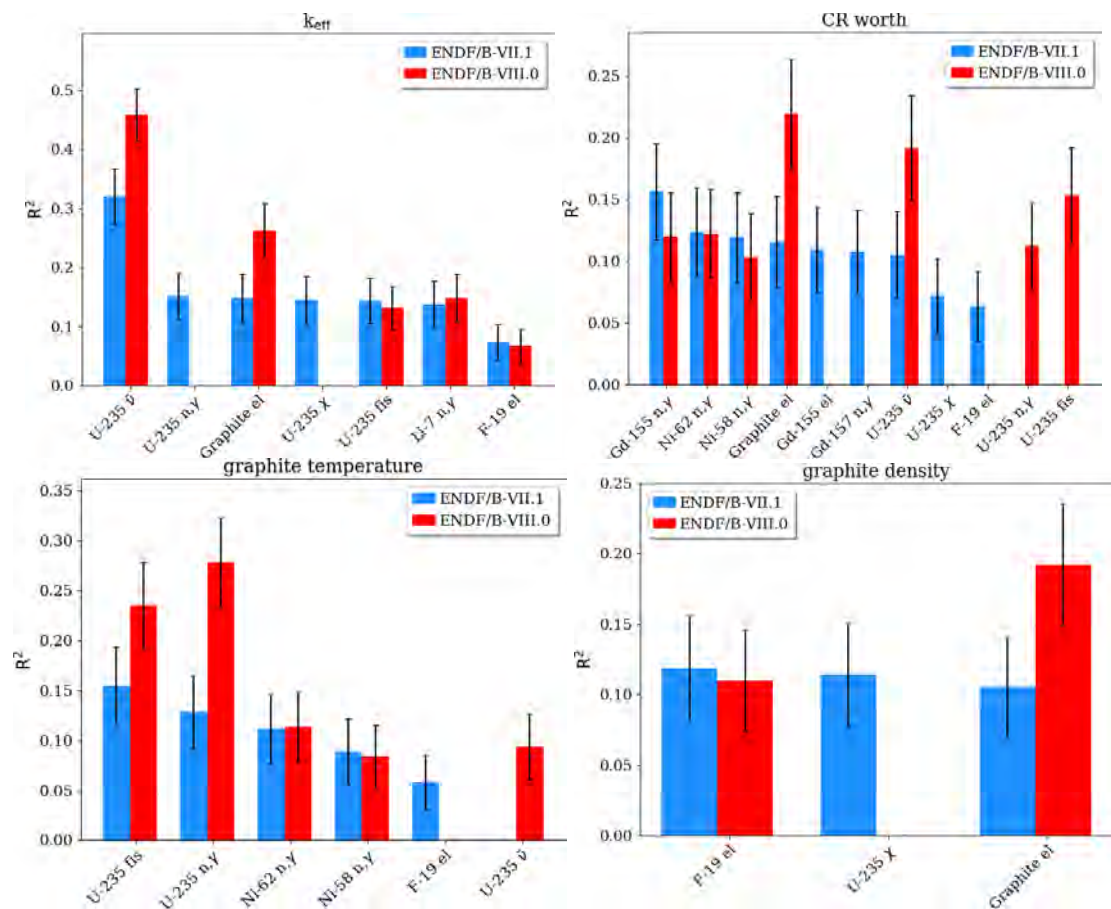
Figure 5-22 MSRE: Sampler/KENO-MG Top Contributor to the Output Uncertainties in Terms of R²
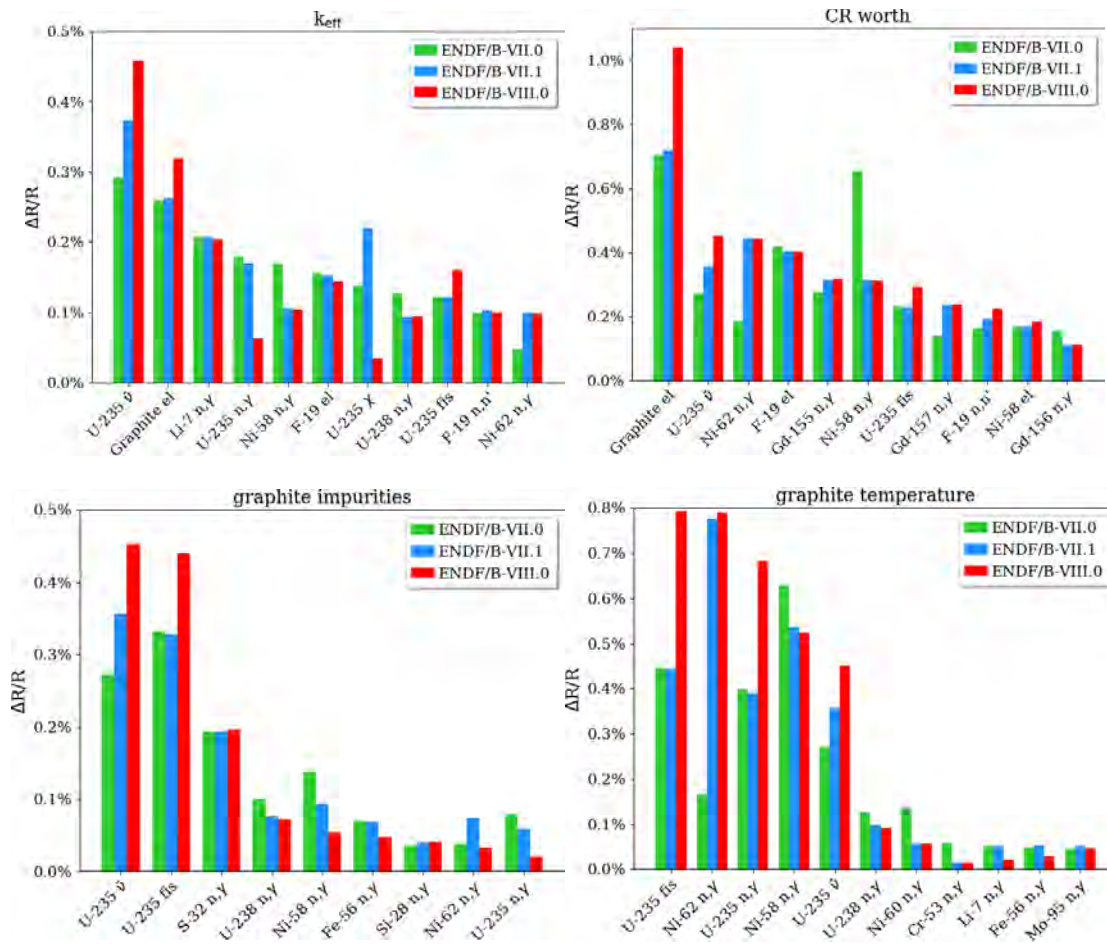
Figure 5-23 MSRE: Contributions to the Output Uncertainties (1 of 2)[26]

---

[26] Obtained with TSUNAMI in ΔR/R
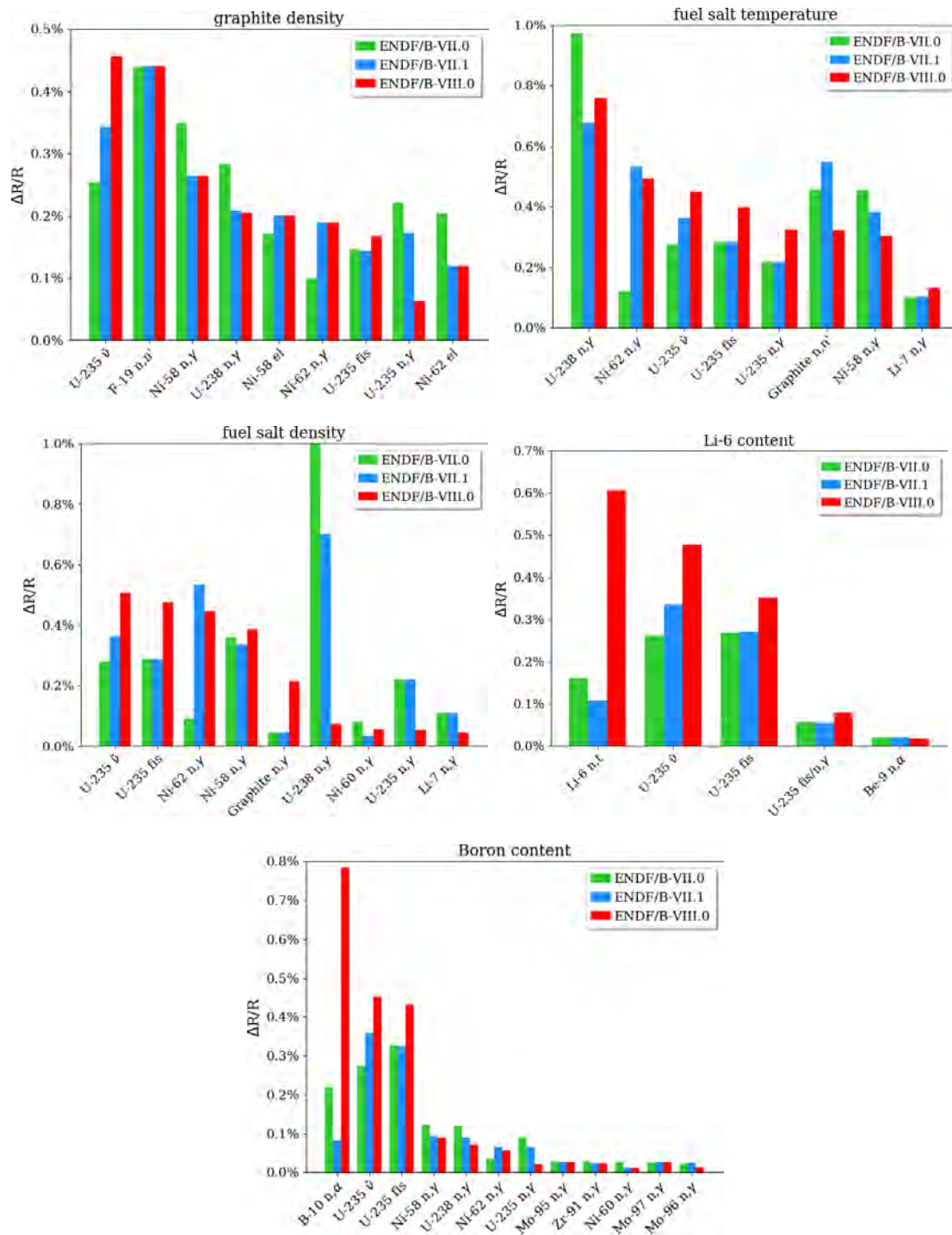
Figure 5-24 MSRE: Contributions to the Output Uncertainties (2 of 2)[27]

---

[27] Obtained with TSUNAMI in ΔR/R
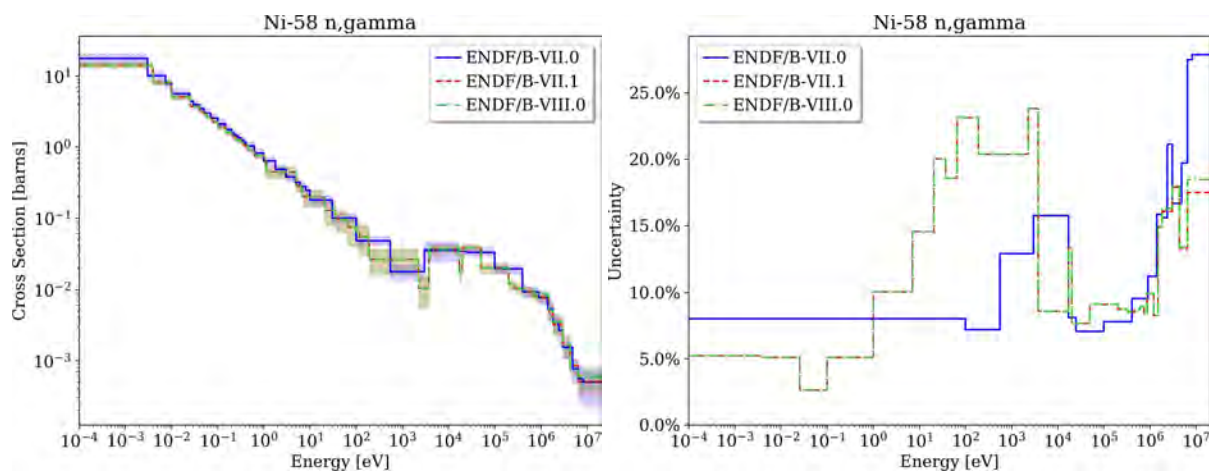
Figure 5-25 ^{58}Ni n,γ Nominal Data and Uncertainty
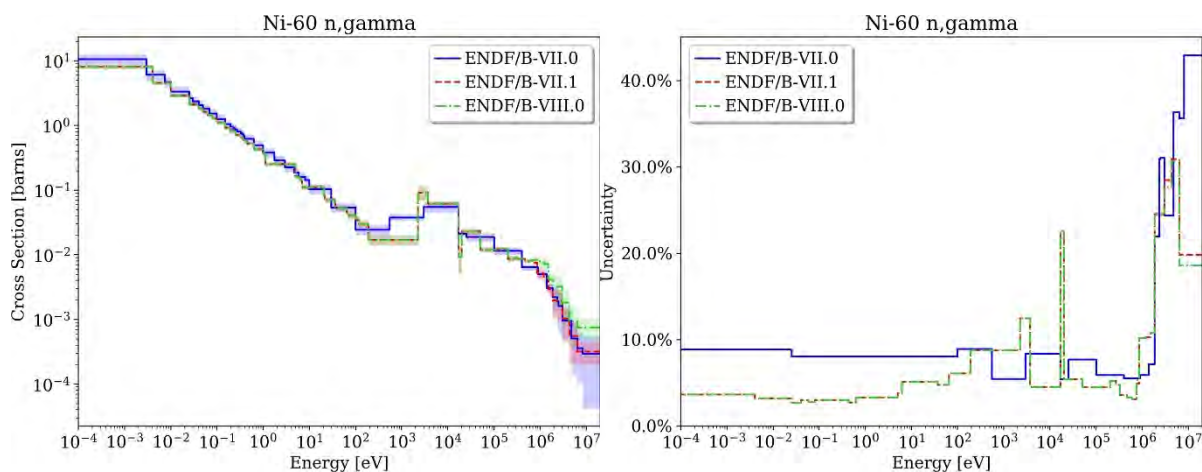
Figure 5-26 ^{60}Ni n,γ Nominal Data and Uncertainty
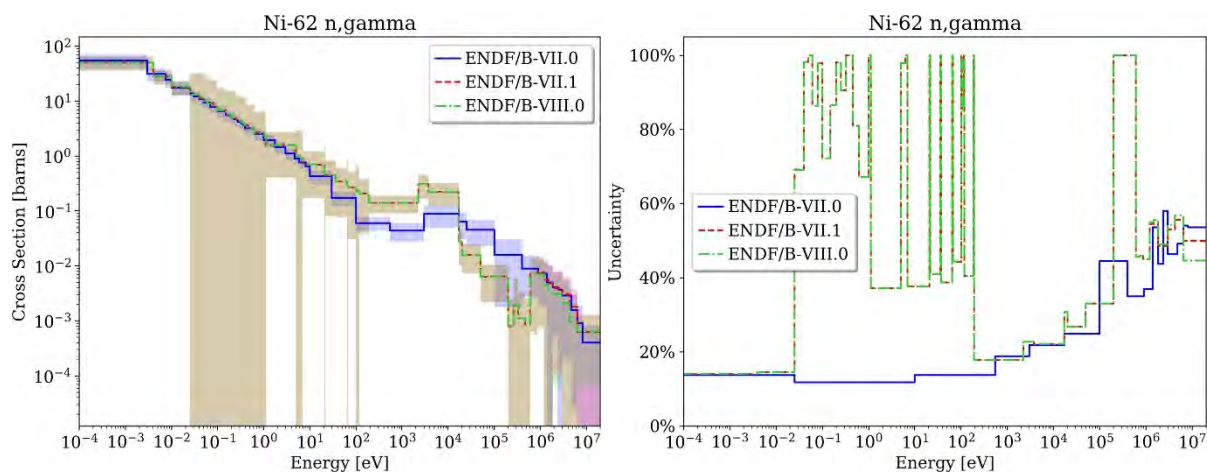
Figure 5-27 ^{62}Ni n,γ Nominal Data and Uncertainty

5.4   INL Design A-Met, Heat Pipe Reactor with Metal Fuel

The SCALE/KENO-VI model of the modified HPR based on INL's Design A was developed based on the descriptions in the literature (Sterbentz et al., 2018), except for the metal fuel composition, which was taken from Hu et al. (Hu et al., 2019). Figure 5-28 shows the 3D full core SCALE model, and Figure5-29 shows a fuel unit cell. The neutron flux spectrum in different regions of the core is displayed in Figure 5-29.
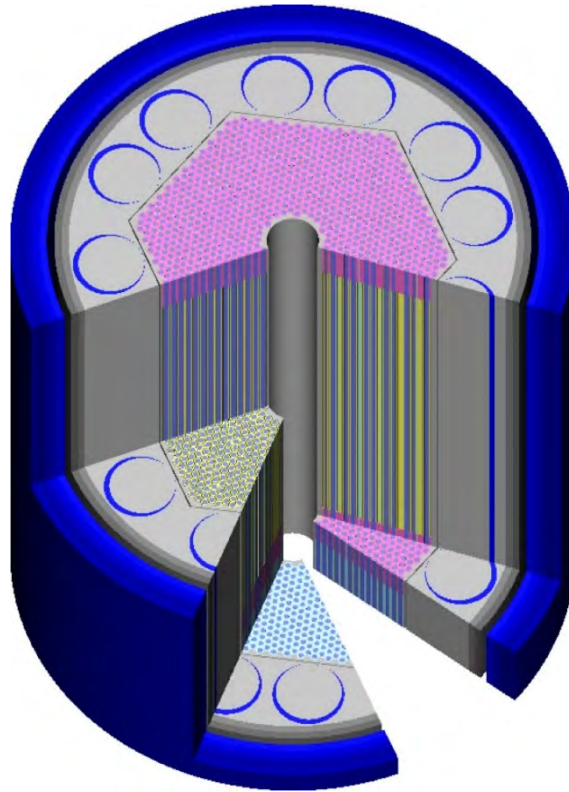
Figure 5-28 INL Design A - MET: SCALE Full Core Model[28]

The sensitivity and uncertainty analyses for the INL Design A - MET reactor were performed for the following QOIs:

1. k_{eff}

2. CD worth: CDs rotated by 180°

3. CR worth: CR fully inserted into the central hole

4. Fuel temperature reactivity: fuel temperature increased by 500 K

---

[28] B_4C absorber in CDs and outer shell (blue), BeO axial reflector (pink), fuel (yellow), radial Al_2O_3 reflector (light gray), K vapor and liquid (lilac), structure (gray), helium gas (light blue)

5. Grid radial expansion: expansion of the fuel element grid 0.08% into the surrounding gap (pink gaps between the fuel region and the CRs in Figure 5-28)

6. Fuel axial expansion: axial expansion of the fuel by 0.5% into the lower gas plenum

7. Axial power profile (i.e., considering radially integrated power in the individual axial layers)
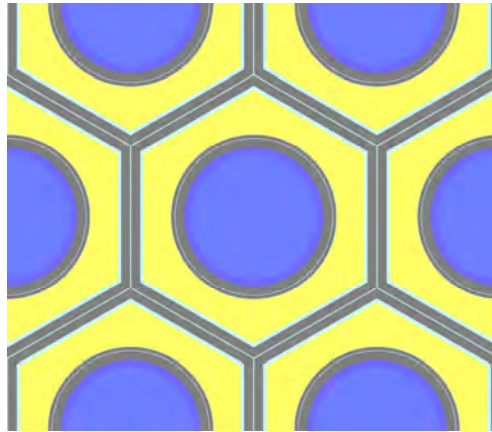
Figure 5-29 INL Design A - MET: SCALE Fuel Unit Cell Lattice[29]

The sensitivity and uncertainty calculations of the reactivities were performed with CE TSUNAMI using ENDF/B-VII.0, ENDF/B-VII.1, and ENDF/B-VIII.0 data. Since TSUNAMI does not permit the direct calculation of power sensitivities, Sampler was used in combination with KENO in MG mode using SCALE's 302-group fast reactor library to study the impact of nuclear data uncertainties on the axial power profile. Since the 302-group library is only available based on ENDF/B-VII.1 and ENDF/B-VIII.0 data, the power uncertainty analysis was performed with only these two libraries. A sample size of 500 in Sampler allowed a limited analysis of the top contributing cross section uncertainties to the observed peak power uncertainties. As applicable for the analysis of the axial power profile of PB-FHR-Mk1 (Section 5.2), the statistical error of the axial power profile was estimated through the standard deviation derived for 500 repeated calculations that used different random seeds.

5.4.1   Nominal Results

Table 5-26 compares the nominal QOIs calculated with KENO-CE using the different ENDF/B libraries. The differences between the ENDF/B-VII.1 and ENDF/B-VII.0 results are negligible. The ENDF/B-VIII.0 results differ only for k_{eff} and the CD worth. The differences are small, under 200 pcm. Given that the considered output quantities show the largest sensitivities to reactions of ^{235}U and ^{238}U, it can be assumed that these small differences are mainly caused by updates of these two nuclide evaluations.

The nominal axial power distribution is displayed in Figure 5-31 (left side). The statistical error was determined through repeated nominal calculation with different random seeds and is displayed in the right side of Figure 5-31. As expected, the power is peaking in the center of the

---

[29] Fuel (yellow), K vapor and liquid (lilac), structure (gray), helium gap (light blue)

core. The upper and lower peaks—which were only resolved after refining the axial discretization in these regions—are caused by the upper and lower BeO reflectors in the core. The statistical error is larger in the upper and lower regions since the neutron flux is lower in these regions and since the axial zones are smaller.

The ENDF/B-VII.1 calculation resulted in an axial power peaking factor of 1.4099 ± 0.0015 (0.11%). The ENDF/B-VIII.0 calculation resulted in a peaking factor of 1.4077, which is within the 2σ statistical uncertainty of the ENDF/B-VII.1 result. (The statistical error was only calculated with ENDF/B-VII.1 and is assumed to be identical for the ENDF/B-VIII.0 result since the statistical error is mainly dependent on factors such as the number of neutron histories simulated and the axial discretization of the model.)

Figure 5-30 INL Design A – MET: Normalized Neutron Flux in a 302-Group Representation at the Core Axial Midline, at Different Radial Positions as Determined with KENO-CE

5.4.2 Sensitivity Analysis

Table 5-27 to Table 5-32 list the top integrated sensitivities of the different QOIs as determined with CE TSUNAMI. Each sensitivity coefficient shown in these tables represents the sensitivity of a specific QOI to a single specific reaction and can be used to understand relevant sensitivities for a given QOI.

As expected for fresh uranium fuel, the largest sensitivities are found for ^{235}U and ^{238}U. Scattering of various zirconium isotopes are listed as important for many QOIs; note the 10% fraction of zirconium in the metal fuel. Scattering reactions and the (n,γ) reaction of ^{56}Fe and ^{52}Cr play a non-negligible role since these isotopes are the major parts of the cladding materials. Due to the large amount of Al_2O_3 that is radially surrounding the core, elastic

scattering of ^{16}O and elastic and inelastic scattering of ^{27}Al are listed among the largest sensitivities. These sensitivities are especially large for the CD worth since the CDs are located in the radial reflector. Some of the considered QOIs are sensitive to the (n,α) reaction of ^{10}B because ^{10}B is part of the CD absorber material. Due to the fast neutron flux, the neutrons are traveling far in the reflector, so they "see" much of the CDs. ^{10}B (n,α) is listed as one of the largest sensitivities for the radial expansion coefficient since the distance between the fuel and the drums is reduced through the expansion.

It is worth pointing out that, with one exception, the K nuclides are not listed among the top sensitivities of any QOI, despite their abundance in the heat pipes.

Table 5-26 INL Design A – MET: Nominal Results of all QOIs Determined with KENO-CE

QOI	ENDF/B-VII.0	ENDF/B-VII.1	ENDF/B-VIII.0	$\Delta\rho^{VII.1/VII.0}$ [pcm]	$\Delta\rho^{VIII.0/VII.1}$ [pcm]
k$_{eff}$	1.05462 ± 0.00007	1.05465 ± 0.00007	1.05250 ± 0.00007	4 ± 10	-216 ± 10
CD worth [pcm]	-4130 ± 11	-4179 ± 10	-4251 ± 12	-48 ± 14	-73 ± 15
CR worth [pcm]	-9308 ± 9	-9314 ± 10	-9389 ± 10	-6 ± 14	-75 ± 14
Fuel temp. [pcm]	-99 ± 11	-110 ± 11	-110 ± 10	-11 ± 15	-1 ± 15
Grid radial exp. [pcm]	-1614 ± 9	-1634 ± 10	-1635 ± 10	-21 ± 14	-1 ± 14
Fuel axial exp. [pcm]	-243 ± 10	-249 ± 10	-265 ± 11	-6 ± 14	-16 ± 14
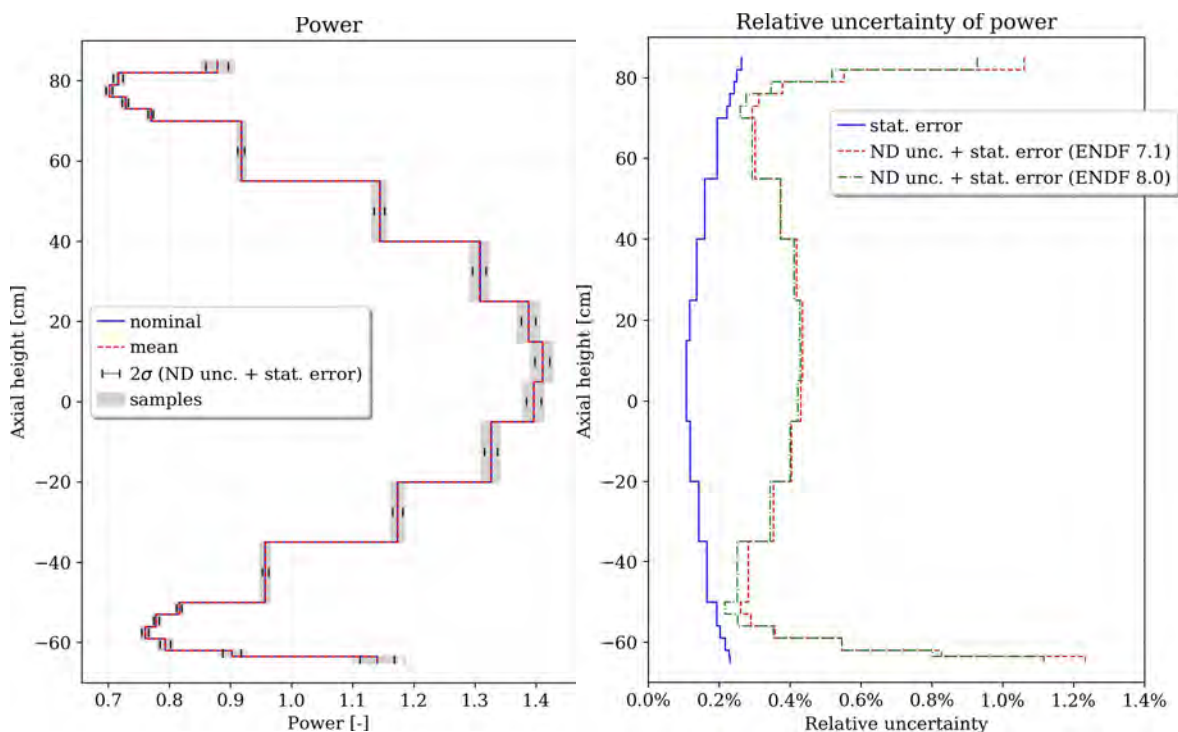
Figure 5-31 INL Design A – MET: Sampler∕KENO-MG Mean Value and Uncertainty Results of the Axial Power Distribution[30]

Table 5-27   INL Design A – MET: Top k$_{eff}$ Sensitivities[31]

Nuclide	Reaction	Sensitivity (increasing k$_{eff}$)	Nuclide	Reaction	Sensitivity (decreasing k$_{eff}$)
u-235	$\bar{\nu}$	8.591e-01 ± 4.795e-05	u-238	n,γ	-1.720e-01 ± 2.346e-05
u-235	fission	5.289e-01 ± 5.843e-05	u-235	n,γ	-7.299e-02 ± 1.063e-05
u-238	$\bar{\nu}$	1.382e-01 ± 4.734e-05	u-238	n,n′	-2.369e-02 ± 1.503e-04
u-238	fission	8.265e-02 ± 4.900e-05	b-10	n,α	-1.464e-02 ± 1.006e-05
o-16	elastic	3.286e-02 ± 3.295e-04	fe-56	n,n′	-9.483e-03 ± 4.635e-05
u-238	elastic	3.012e-02 ± 6.308e-04	fe-56	n,γ	-6.386e-03 ± 1.620e-06
al-27	elastic	1.965e-02 ± 1.900e-04	u-235	n,n′	-4.109e-03 ± 4.918e-05
fe-56	elastic	1.099e-02 ± 3.425e-04	cr-52	n,n′	-2.594e-03 ± 1.774e-05
be-beo	elastic	6.532e-03 ± 2.230e-04	ni-58	n,p	-2.385e-03 ± 6.879e-07
zr-90	elastic	5.977e-03 ± 1.602e-04	ni-58	n,γ	-2.212e-03 ± 4.547e-07

---

[30] The left axial power plot shows results determined with ENDF/B-VII.1 data; differences between ENDF/B-VII.1 and ENDF/B-VIII.0 results would not be visible in this plot. The samples refer to the calculations with perturbed nuclear data.

[31] Top 10 positive and top 10 negative mixture-, region-, and energy-integrated sensitivities, determined with TSUNAMI using ENDF/B-VII.1 data.

Table 5-28 INL Design A – MET: Top CD Worth Sensitivities[32]

Nuclide	Reaction	Sensitivity (reducing negative $\Delta\rho$)	Nuclide	Reaction	Sensitivity (increasing negative $\Delta\rho$)
u-235	fission	7.112e-01 ± 1.956e-03	o-16	elastic	-4.776e-02 ± 8.859e-03
u-235	$\bar{\nu}$	7.037e-01 ± 1.567e-03	al-27	elastic	-3.451e-02 ± 5.478e-03
u-238	elastic	3.332e-01 ± 2.102e-02	fe-56	n,n′	-8.120e-03 ± 1.560e-03
u-238	$\bar{\nu}$	2.910e-01 ± 1.553e-03	al-27	n,n′	-7.124e-03 ± 4.383e-04
u-238	fission	2.327e-01 ± 1.605e-03	cr-52	n,n′	-4.212e-03 ± 5.996e-04
fe-56	elastic	1.702e-01 ± 1.100e-02	zr-90	n,n′	-3.397e-03 ± 4.984e-04
u-238	n,n′	9.258e-02 ± 4.935e-03	ni-58	n,p	-2.619e-03 ± 2.269e-05
zr-90	elastic	7.167e-02 ± 5.307e-03	fe-56	n,γ	-1.659e-03 ± 5.379e-05
u-235	elastic	6.893e-02 ± 4.163e-03	ni-60	n,n′	-1.523e-03 ± 2.765e-04
u-238	n,γ	6.555e-02 ± 7.765e-04	zr-92	n,n′	-1.490e-03 ± 4.113e-04

Table 5-29 INL Design A – MET: Top CR Worth Sensitivities[33]

Nuclide	Reaction	Sensitivity (reducing negative $\Delta\rho$)	Nuclide	Reaction	Sensitivity (increasing negative $\Delta\rho$)
u-235	fission	7.742e-01 ± 8.962e-04	b-10	n,α	-2.051e-01 ± 2.272e-04
u-235	$\bar{\nu}$	7.402e-01 ± 7.553e-04	u-238	n,n′	-4.213e-02 ± 2.227e-03
u-238	$\bar{\nu}$	2.553e-01 ± 7.466e-04	fe-56	n,n′	-2.337e-02 ± 6.909e-04
u-238	fission	2.077e-01 ± 7.608e-04	cr-52	n,n′	-5.739e-03 ± 2.668e-04
o-16	elastic	1.915e-01 ± 5.634e-03	zr-90	n,n′	-4.032e-03 ± 2.160e-04
al-276	elastic	1.130e-01 ± 3.001e-03	zr-92	n,n′	-2.810e-03 ± 1.914e-04
u-238	n,γ	5.216e-02 ± 3.418e-04	zr-94	n,n′	-2.538e-03 ± 1.832e-04
b-10	elastic	2.273e-02 ± 3.746e-04	ni-58	n,n′	-2.330e-03 ± 1.626e-04
u-235	n,γ	2.266e-02 ± 1.575e-04	u-235	n,n′	-2.229e-03 ± 7.321e-04
c	elastic	1.137e-02 ± 1.939e-04	ni-58	n,p	-2.158e-03 ± 1.062e-05

---

[32] CDs rotated by 180°, $\Delta\rho$ = -4179 ± 10; top 10 positive and top 10 negative mixture-, region-, and energy-integrated sensitivities, determined with TSUNAMI using ENDF/B-VII.1 data.

[33] CR fully inserted, $\Delta\rho$ = -9314 ± 10; top 10 positive and top 10 negative mixture-, region-, and energy-integrated sensitivities, determined with TSUNAMI using ENDF/B-VII.1 data.

Table 5-30   INL Design A – MET: Top Fuel Temperature Reactivity Sensitivities[34]

Nuclide	Reaction	Sensitivity (reducing negative $\Delta\rho$)	Nuclide	Reaction	Sensitivity (increasing negative $\Delta\rho$)
u-235	fission	1.276e+00 ± 2.567e-01	u-238	elastic	-3.425e+00 ± 2.799e+00
u-235	elastic	1.171e+00 ± 5.832e-01	u-238	n,n′	-1.885e+00 ± 6.832e-01
u-235	$\bar{\nu}$	9.906e-01 ± 2.096e-01	al-27	elastic	-1.366e+00 ± 8.387e-01
si-28	elastic	2.829e-01 ± 1.701e-01	cr-52	elastic	-6.186e-01 ± 5.284e-01
fe-57	n,n′	1.771e-01 ± 7.580e-02	u-238	n,γ	-5.722e-01 ± 1.025e-01
u-235	n,γ	1.766e-01 ± 4.633e-02	zr-91	elastic	-5.537e-01 ± 2.842e-01
k-41	elastic	9.559e-02 ± 4.983e-02	fe-54	elastic	-3.995e-01 ± 3.413e-01
mo-95	elastic	9.540e-02 ± 8.456e-02	cr-50	elastic	-3.037e-01 ± 1.506e-01
b-10	n,α	6.281e-02 ± 4.365e-02	u-235	n,n′	-3.010e-01 ± 2.129e-01
al-27	n,n′	6.236e-02 ± 6.369e-02	ni-62	elastic	-2.177e-01 ± 1.290e-01

Table 5-31   INL Design A – MET: Top Grid Radial Expansion Sensitivities[35]

Nuclide	Reaction	Sensitivity (reducing negative $\Delta\rho$)	Nuclide	Reaction	Sensitivity (increasing negative $\Delta\rho$)
u-235	$\bar{\nu}$	8.534e-01 ± 2.633e-02	cr-52	elastic	-1.594e-01 ± 6.320e-02
u-235	fission	7.508e-01 ± 3.205e-02	b-10	n,α	-1.451e-01 ± 5.465e-03
o-16	elastic	2.209e-01 ± 1.820e-01	u-238	n,γ	-1.393e-01 ± 1.277e-02
u-238	$\bar{\nu}$	1.544e-01 ± 2.611e-02	zr-94	elastic	-8.878e-02 ± 4.486e-02
u-238	fission	1.446e-01 ± 2.683e-02	u-235	n,γ	-8.642e-02 ± 5.758e-03
u-235	n,n′	3.925e-02 ± 2.684e-02	zr-91	elastic	-5.848e-02 ± 3.480e-02
si-28	elastic	3.004e-02 ± 2.203e-02	cr-50	elastic	-2.244e-02 ± 1.823e-02
mo-98	elastic	1.896e-02 ± 1.357e-02	u-236	elastic	-2.098e-02 ± 5.217e-03
fe-57	n,n′	1.604e-02 ± 9.438e-03	zr-96	elastic	-1.925e-02 ± 1.577e-02

---

[34] Temperature increased by 500 K, $\Delta\rho$ = -110 ± 11; top 10 positive and top 10 negative mixture-, region-, and energy-integrated sensitivities, determined with TSUNAMI using ENDF/B-VII.1 data.

[35] Expansion by 0.08%, $\Delta\rho$ = -1634 ± 10; top 10 positive and top 10 negative mixture-, region-, and energy-integrated sensitivities, determined with TSUNAMI using ENDF/B-VII.1 data.

Table 5-32   INL Design A – MET: Top Fuel Axial Expansion Sensitivities[36]

Nuclide	Reaction	Sensitivity (reducing negative $\Delta\rho$)	Nuclide	Reaction	Sensitivity (increasing negative $\Delta\rho$)
u-235	$\bar{\nu}$	8.870e-01 ± 4.100e-03	u-238	n,γ	-8.870e-02 ± 1.932e-03
u-235	fission	7.970e-01 ± 4.884e-03	b-10	n,α	-7.569e-02 ± 8.415e-04
o-16	elastic	1.729e-01 ± 2.791e-02	u-235	n,γ	-4.789e-02 ± 8.615e-04
u-238	fission	1.235e-01 ± 4.163e-03	fe-56	n,γ	-1.917e-02 ± 1.420e-04
u-238	$\bar{\nu}$	1.110e-01 ± 4.047e-03	fe-56	n,n′	-1.539e-02 ± 4.033e-03
al-27	elastic	1.036e-01 ± 1.679e-02	ni-58	n,γ	-6.982e-03 ± 3.988e-05
u-238	n,n′	5.451e-02 ± 1.243e-02	cr-52	n,n′	-6.308e-03 ± 1.489e-03
zr-90	elastic	1.831e-02 ± 1.359e-02	ni-58	n,p	-6.071e-03 ± 5.869e-05
u-235	n,n′	1.525e-02 ± 4.048e-03	mo-95	n,γ	-3.675e-03 ± 3.044e-05
si-28	elastic	5.404e-03 ± 3.300e-03	cr-52	n,γ	-3.578e-03 ± 3.331e-05

5.4.3   Uncertainty Analysis

Uncertainty calculations of the considered QOIs were performed for all three considered ENDF/B libraries based on the sensitivity coefficients determined with CE TSUNAMI. Table 5-33 compares the obtained output uncertainties. The causes of the observed differences can be explained when studying the individual contributions of the top contributing nuclear reactions (covariance matrices of the individual reactions) to the uncertainties presented for each individual QOI in Table A-17 to

Table A-22 and in Figure 5-32.

The most relevant update between the different ENDF/B libraries for all observed output uncertainties for INL Design A is the uncertainty of ^{235}U (n,γ). The uncertainty of this reaction is greater than 30% in the fast energy range in ENDF/B-VII.0 and ENDF/B-VII.1 (Figure 2-39). It is responsible for the major portion of the k_{eff} and fuel temperature reactivity uncertainty and is a significant contributor to the uncertainty of all other QOIs. Another significant contributor to all output uncertainties is inelastic scattering (n,n′) of ^{238}U, which shows a large uncertainty in ENDF/B-VII.0 and ENDF/B-VII.1 (Figure 2-38). The uncertainty of both of these reactions was decreased in ENDF/B-VIII.0, leading to a significant decrease in the total output uncertainty of k_{eff}, the fuel temperature reactivity, and the fuel axial expansion reactivity. Other relevant updates influencing the uncertainty of several QOIs are mostly observed for ENDF/B-VIII.0 as compared to the other library releases: a reduced uncertainty of ^{16}O elastic scattering (Figure 2-31), an increased uncertainty of ^{27}Al elastic scattering (Figure 5-35), increased uncertainties of fission and $\bar{\nu}$ of ^{235}U (Figure 2-20 and Figure 2-21), and a decreased uncertainty of ^{235}U χ (Figure 5-3).

Axial peak power uncertainty of 0.435 and 0.430% with ENDF/B-VII.1 and ENDF/B-VIII.0 data, respectively, was obtained with Sampler/KENO-MG. The corresponding statistical uncertainty due to the Monte Carlo approach is about 0.110% (Figure 5-31, right side). Therefore, the uncertainty due to nuclear data is estimated as approximately 0.325 and 0.320% for ENDF/B-VII.1 and ENDF/B-VIII.0, respectively. The top contributors to the peak power uncertainty are reactions that have already been found relevant for the other investigated QOIs. In the case of

---

[36] Expansion by 0.5%, $\Delta\rho$ = -249 ± 10; top 10 positive and top 10 negative mixture-, region-, and energy-integrated sensitivities, determined with TSUNAMI using ENDF/B-VII.1 data.

the ENDF/B-VII.1 calculation, the ^{235}U (n,γ) is the most relevant contributor, followed by scattering of ^{60}Ni, ^{62}Ni, and ^{56}Fe, and inelastic scattering of ^{238}U (Figure 5-33). In the case of the ENDF/B-VIII.0 calculation, the increased uncertainty of ^{235}U fission as compared to ENDF/BVII.1 causes an increased contribution of this uncertainty to the axial peak power uncertainty. Since the ^{235}U (n,γ) uncertainty decreased in ENDF/B-VIII.0, this reaction is no longer listed in the ranking of top contributors, and the importance of other reactions such as ^{60}Ni (n,γ) for the output uncertainty is increased. The uncertainty of the axial power distribution is displayed in Figure 5-31 (right side). The ENDF/B-VII.1 and ENDF/B-VIII.0 results are almost consistent. As expected, the uncertainty is the largest in the upper and lower regions, where the power shows significant increases due to the upper and lower reflector. The contribution of the statistical error to the overall uncertainty is larger in the upper and lower regions since the neutron flux is lower in these regions and the axial zones are smaller. The slight increase at the core midline is the result of the power normalization. Each individual power profile is normalized to yield an average of 1. The smallest variation in power due to perturbations (i.e., the smallest uncertainty) is therefore generally expected in regions where the power profile is approximately 1, and larger uncertainties are expected in all other regions. The uncertainty of the INL Design A - MET power profile is loosely following this trend. Small axial deviations of this trend and differences in the magnitude of the power outside the low uncertainty regions are caused by differences in the volume of the individual zones, as well as the power in these zones. Note that the trend observed for PB-FHR-Mk1 in Figure 5-8 differed because the core has smaller fuel regions in the upper and lower zones due to the (de)fueling chutes and cones, resulting in a different power profile and different axial discretizations.

Table 5-33   INL Design A - MET. Uncertainties of QOIs

QOI	ENDF/B-VII.0	ENDF/B-VII.1	ENDF/B-VIII.0	$\frac{VII.1}{VII.0} - 1$	$\frac{VIII.0}{VII.1} - 1$
k_{eff}	2.01%	2.08%	0.98%	3.4%	-53.0%
CD worth	1.99%	1.97%	2.12%	-1.0%	7.2%
CR worth	1.73%	1.98%	1.44%	14.9%	-27.4%
Fuel temp.	8.77%	6.59%	4.34 %	-24.9%	-34.1%
Grid radial exp.	1.40%	1.68%	1.49%	19.9%	-11.3%
Fuel axial exp.	2.92%	2.69%	2.00%	-8.0%	-25.7%
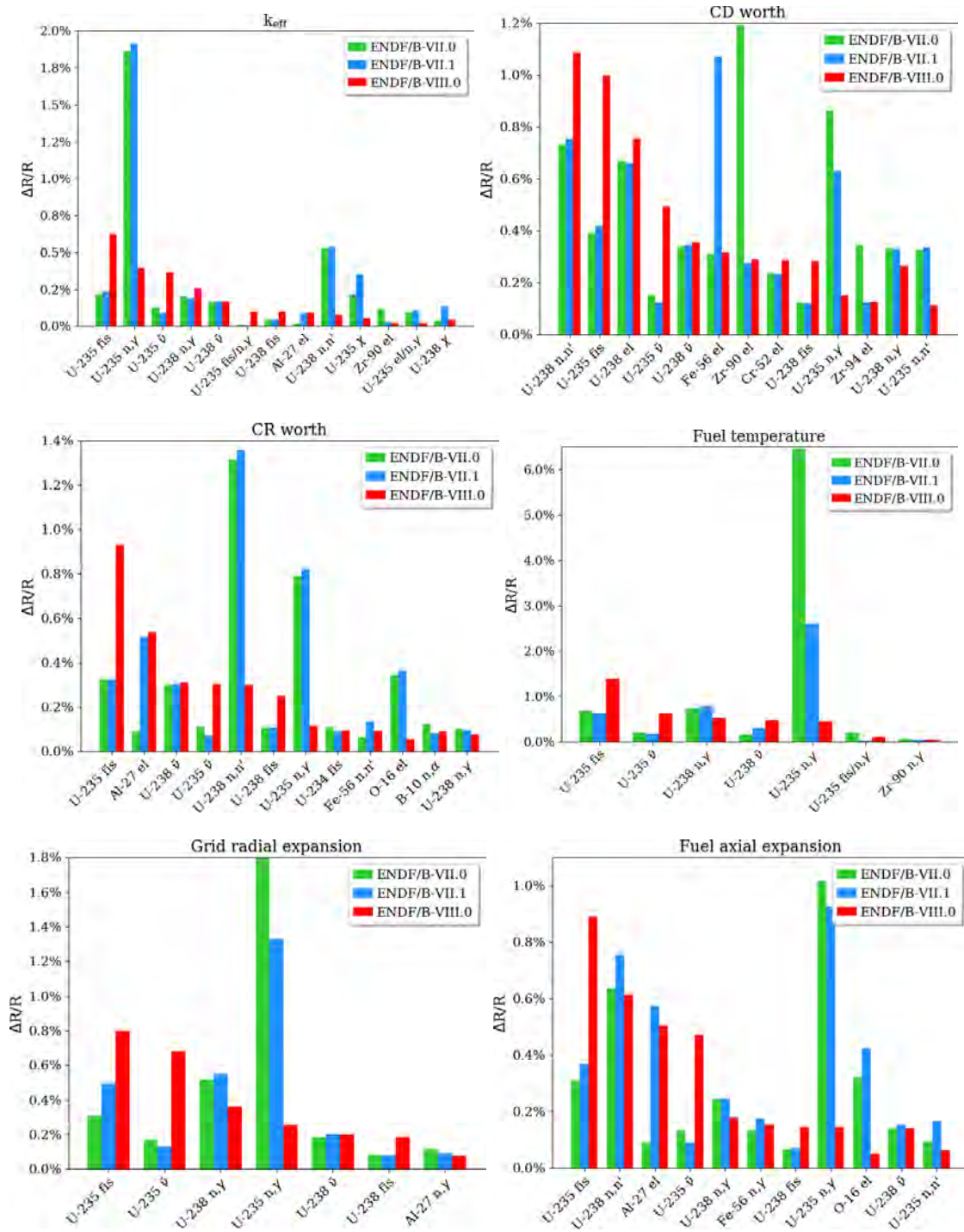
Figure 5-32 INL Design A – MET: Contributions to the Output Uncertainties[37]

---
[37] Obtained using TSUNAMI in DR/R
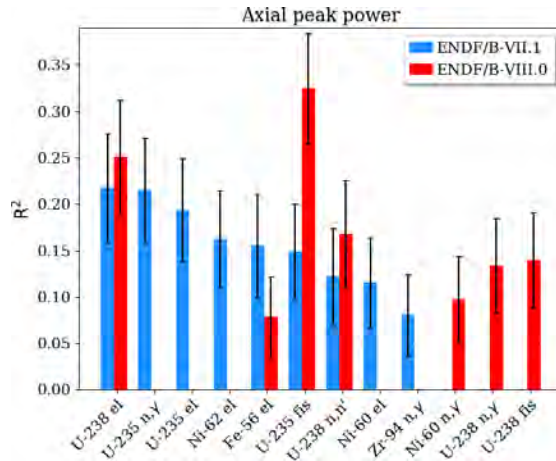
Figure 5-33 INL Design A - MET: Sampler/KENO-MG Top Contributor to the Peak Power Uncertainty in Terms of R2
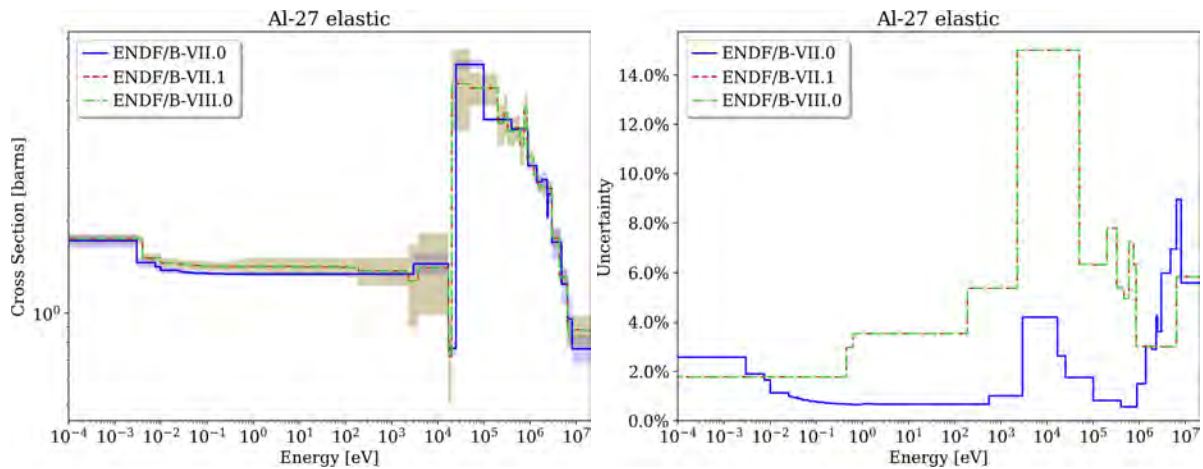
Figure 5-34 ^{27}Al Elastic Scattering Nominal Data and Uncertainty

5.5   EBR-II, Sodium-Cooled Fast Reactor

The SCALE/KENO-VI model of the EBR-II was developed based on the benchmark specifications in the IRPhEP handbook (Lum et al., 2018). Figure 5-35 shows a plot of the full core model, and Figure 5-36 shows a plot of a half worth driver assembly. The neutron flux spectrum in different regions of the core is displayed in Figure 5-37.
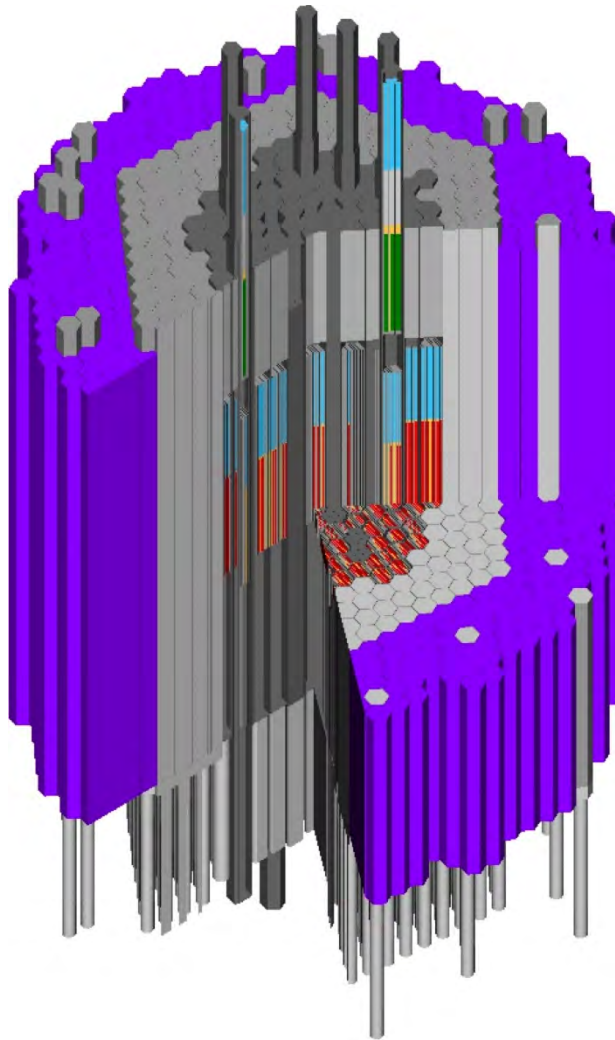
Figure 5-35 EBR-II: SCALE Full Core Model[38]

The sensitivity and uncertainty analyses for the EBR-II were performed for the following QOIs:

1. k_{eff}

2. CR worth: reactivity difference between all control assemblies out and all control assemblies in

3. Sodium void worth: all sodium removed from the model

4. Radial power profile

---

[38] The inner driver core region (driver fuel in red, bond sodium in yellow, gas plenum in blue) is surrounded by a steel reflector (gray) which is surrounded by the blanket assemblies (purple). The green region shows absorber material in one of the control assemblies.
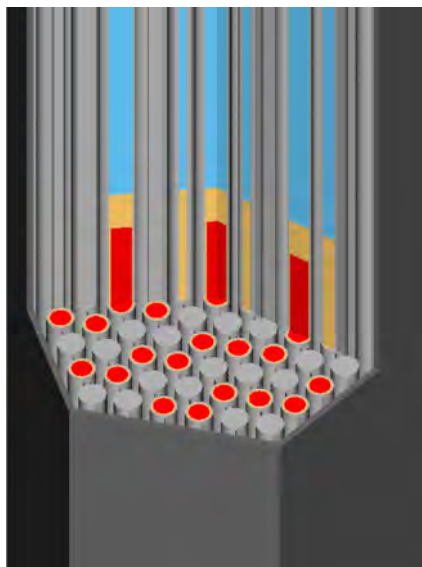
Figure 5-36 EBR-II: SCALE Half Worth Driver Assembly Model[39]

The sensitivity and uncertainty calculations of the reactivities were performed with CE TSUNAMI using ENDF/B-VII.1 and ENDF/B-VIII.0 data. Neutron transport calculations were not performed with ENDF/B-VII data because of an issue with the generation of probability tables for SCALE's CE libraries that was recently fixed. SCALE's ENDF/B-VII.1 and ENDF/B-VIII.0 libraries were updated, but the ENDF/B-VII.0 library was not updated since it will no longer be included in the next SCALE releases. The correction of the probability tables has been found to impact reactivity calculations of fast spectrum systems which include irradiated fuel (Kim et al., 2019).

Since TSUNAMI does not permit the direct calculation of power sensitivities, Sampler was used, in combination with KENO in MG mode using SCALE's 302-group fast reactor library, to study uncertainties due to nuclear data of the radial power profile. As in the TSUNAMI calculations, these calculations are also limited to ENDF/B-VII.1 and ENDF/B-VIII.0 data. A sample size of 500 allowed a limited analysis of the top contributing cross section uncertainties to the observed peak power uncertainties. Just as for the analysis of the axial power profile of the PB-FHR-Mk1 (Section 5.2), the statistical error of the axial power profile was estimated by calculating the standard deviation of calculations using different random seeds.

The initial plan was to investigate the Doppler reactivity of the EBR-II's fuel, but only a small reactivity difference of less than 100 pcm was obtained, even when the fuel temperature increased from 616 to 1,800 K. Because of the hard neutron flux spectrum in the EBR-II, Doppler broadening in the resonance range with increasing temperature only has a minor effect on the reactivity. With such a small reactivity difference, sensitivities of this quantity cannot be determined with sufficient statistical convergence. Therefore, the analysis was omitted in this study. Choi et al. determined EBR-II's fuel Doppler reactivity as -0.04268$ when doubling the fuel temperature (Choi and Ha, 2016); given an effective delayed neutron fraction between 200

---

[39]   The fuel (red) is located in every second rod, the other rods (gray) being solid steel cylinders. Bond sodium in the fuel rods is displayed in yellow, and the gas plenum in blue.

and 700 pcm, -0.04268$ corresponds to a reactivity between 8 and 30 pcm, thus confirming the small Doppler reactivity.

5.5.1 Nominal Results

Table 5-34 compares the k_{eff} results obtained with KENO-CE to the experimental benchmark value and the reported MCNP calculation. The (1σ) benchmark uncertainty is given as 618 pcm and allows for uncertainties in the geometry and material data. The driver fuel mass and the ^{235}U concentration are the main contributors to this uncertainty (Lum et al., 2018). Considering this uncertainty, very good agreement is observed between all calculated results.

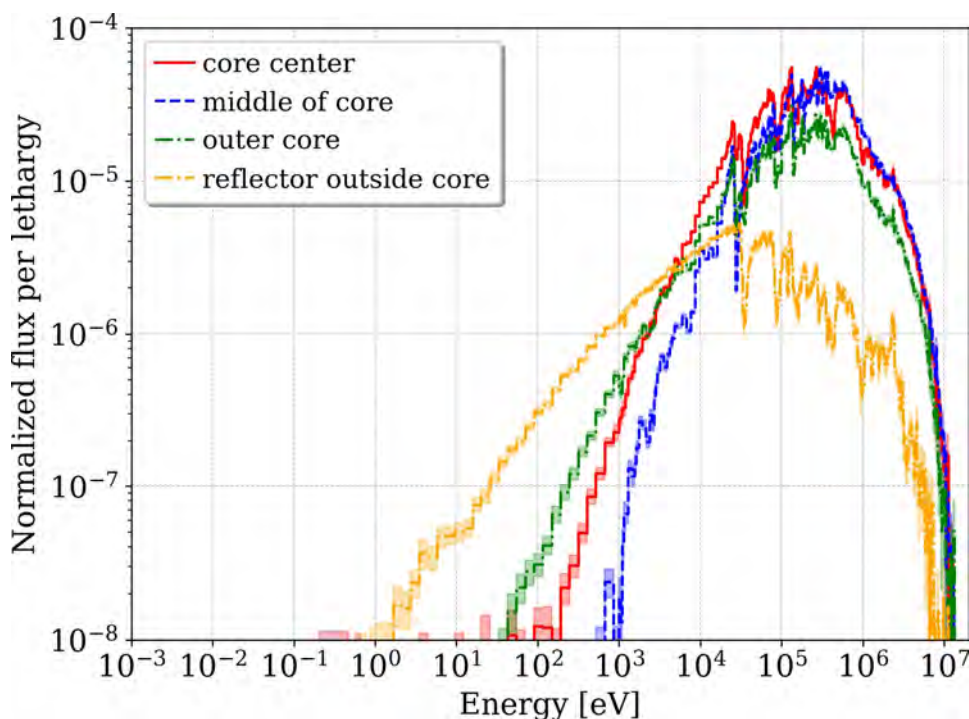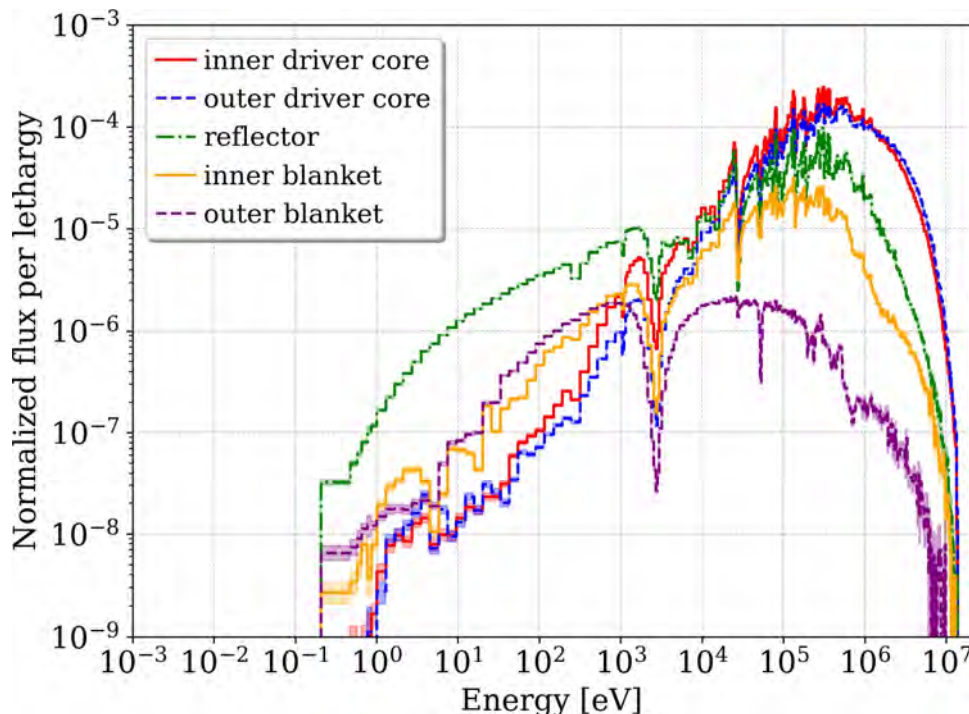**Figure 5-37 EBR-II: Normalized Neutron Flux in a 302-Group Representation at the Core Axial Midline, at Different Radial Positions Determined with KENO-CE**

Due to the update of probability tables mentioned above, a direct comparison between the reported MCNP result and the KENO result with ENDF/B-VII.0 data could not be performed. However, the benchmark specification provided the MCNP input. In a side study, MCNP was applied with this input using both the ENDF/B-VII.0 and ENDF/B-VII.1 libraries. The eigenvalue decreased by ~400 pcm when using ENDF/B-VII.1 compared to ENDF/B-VII.0. The ORNL MCNP ENDF/B-VII.1 result and the KENO ENDF/B-VII.1 result show a difference of ~250 pcm; after the provided MCNP model was studied in more detail, it was concluded that this small difference is caused by slight geometric inconsistencies between the models.

Table 5-35 compares the nominal QOIs based on the different ENDF/B libraries. The differences between the ENDF/B-VIII.1 and ENDF/B-VII.1 results are negligible.

Table 5-34 EBR-II: KENO EBR-II k_{eff} Results Compared to the Benchmark and the Reported MCNP Result

Case	Library	k_{eff}	Benchmark Δk [pcm]
SCALE/KENO	ENDF/B-VII.1	1.00703 ± 0.00016	-224 ± 618
	ENDF/B-VIII.0	1.00704 ± 0.00019	-223 ± 618
MCNP (Lum et al., 2018)	ENDF/B-VII.0	1.01169 ± 0.00005	242 ± 618
Benchmark		1.00927 ± 0.00618	(ref)

Table 5-35 EBR-II: Nominal Values of QOIs Determined with KENO

QOI	ENDF/B-VII.1	ENDF/B-VIII.0	$\Delta\rho$ [pcm]
k_{eff}	1.00703 ± 0.00016	1.00704 ± 0.00019	1 ± 25
CR worth	4728 ± 26	4728 ± 25	0 ± 36
Na void	-4651 ± 18	-4681 ± 29	-29 ± 34

Figure 5-38 shows the radial power distribution—meaning the axially integrated assembly powers—normalized to achieve an average of 1.0. Since the power was obtained in all materials containing fuel, the high power in the inner core with driver fuel assemblies is visible, as well as the low power outer blanket. The minimum of the power distribution is 0.003/0.003 in the outer blanket region, and the maximum is 5.653/5.590 in a half worth driver assembly in the center of the inner core for ENDF/B-VII.1 / ENDF/B-VIII.0, respectively. If only the inner core is considered, then the minimum and maximum values are 0.653/0.597 and 1.297/1.282 for ENDF/B-VII.1 / ENDF/B-VIII.0, respectively.

5.5.2 Sensitivity Analysis

Table 5-36 to Table 5-38 list the top integrated sensitivities of the different QOIs as determined with CE TSUNAMI. Each of these sensitivity coefficients represents the sensitivity of a specific QOI to a single specific reaction and can be used to understand relevant sensitivities for a given QOI.

As expected for fresh uranium fuel, the largest sensitivities are found for ^{235}U and ^{238}U. Scattering reactions and the (n,γ) reaction of ^{56}Fe, ^{52}Cr, and ^{58}Ni play a significant role since these isotopes are the major parts of the cladding materials. The CR worth is very sensitive towards the ^{10}B (n,α) since boron is the absorbing material in the CRs. The sodium void reactivity is naturally very sensitive to the elastic and inelastic scattering of ^{23}Na.

Table 5-36   EBR-II: Top k$_{eff}$ Sensitivities[40]

Nuclide	Reaction	Sensitivity (increasing k$_{eff}$)	Nuclide	Reaction	Sensitivity (decreasing k$_{eff}$)
u-235	$\bar{\nu}$	9.537e-01 ± 5.591e-05	u-235	n,γ	-8.695e-02 ± 3.010e-05
u-235	fission	5.486e-01 ± 1.086e-04	u-238	n,γ	-3.966e-02 ± 2.076e-05
fe-56	elastic	6.762e-02 ± 2.669e-03	fe-56	n,γ'	-1.685e-02 ± 1.265e-05
na-23	elastic	5.407e-02 ± 1.208e-03	b-10	n,α	-9.555e-03 ± 1.340e-05
cr-52	elastic	3.480e-02 ± 6.083e-04	ni-58	n,γ	-5.420e-03 ± 3.072e-06
u-238	$\bar{\nu}$	3.469e-02 ± 5.355e-05	cr-52	n,γ	-3.634e-03 ± 4.483e-06
u-238	elastic	2.210e-02 ± 5.359e-05	ni-58	n,p	-2.952e-03 ± 1.940e-06
ni-58	elastic	1.837e-02 ± 6.585e-04	mn-55	n,γ	-2.717e-03 ± 2.584e-06
u-238	elastic	1.653e-02 ± 5.665e-04	fe-54	n,γ	-2.176e-03 ± 1.330e-06
fe-56	n,n'	1.309e-02 ± 1.491e-04	cr-53	n,γ	-2.135e-03 ± 1.919e-06

Table 5-37   EBR-II: Top CR Worth Sensitivities[41]

Nuclide	Reaction	Sensitivity (increasing k$_{eff}$)	Nuclide	Reaction	Sensitivity (reducing k$_{eff}$)
b-10	n,α	4.262e-01 ± 4.564e-04	u-235	$\bar{\nu}$	-9.493e-01 ± 1.680e-03
u-235	n,γ	5.357e-02 ± 8.876e-04	u-235	fission	-9.320e-01 ± 3.148e-03
fe-56	n,γ	5.356e-02 ± 3.804e-04	fe-56	elastic	-9.565e-02 ± 8.242e-02
u-238	n,γ	3.144e-02 ± 6.463e-04	cr-52	elastic	-3.683e-02 ± 1.718e-02
u-235	n,n'	2.857e-02 ± 3.657e-03	ni-58	elastic	-3.680e-02 ± 2.229e-02
u-238	n,n'	2.204e-02 ± 4.350e-03	u-238	elastic	-3.379e-02 ± 1.720e-02
mn-55	n,γ	1.442e-02 ± 9.126e-05	u-238	elastic	-2.808e-02 ± 1.532e-03
ni-58	n,γ	1.321e-02 ± 7.568e-05	b-11	elastic	-2.653e-02 ± 2.908e-03
cr-52	n,γ	1.102e-02 ± 1.262e-04	u-238	$\bar{\nu}$	-2.603e-02 ± 1.519e-03
cr-53	n,γ	8.054e-03 ± 5.581e-05	pu-239	$\bar{\nu}$	-2.314e-02 ± 7.302e-04

*EBR-II's control assemblies include fuel and therefore cause a positive reactivity when fully inserted.

---

[40] Top 10 positive and top 10 negative mixture-, region-, and energy-integrated sensitivities, determined with SCALE/TSUNAMI using ENDF/B-VII.1 data.

[41] Reactivity difference between all controls fully inserted and all controls fully withdrawn, $\Delta\rho$ = 4728 ± 25 pcm; top 10 positive and top 10 negative mixture-, region-, and energy-integrated sensitivities, determined with SCALE/TSUNAMI using ENDF/B-VII.1 data.

Table 5-38   EBR-II: Top Sodium Void Worth Sensitivities[42]

Nuclide	Reaction	Sensitivity (reducing negative $\Delta\rho$)	Nuclide	Reaction	Sensitivity (increasing negative $\Delta\rho$)
u-235	fission	9.829e-01 ± 2.171e-03	na-23	elastic	-7.047e-01 ± 2.672e-02
u-235	$\bar{\nu}$	8.492e-01 ± 1.241e-03	na-23	n,n'	-6.572e-02 ± 2.099e-03
fe-56	elastic	2.336e-01 ± 6.374e-02	fe-56	n,γ	-1.655e-02 ± 2.909e-04
u-238	$\bar{\nu}$	1.143e-01 ± 1.106e-03	u-238	n,γ	-9.823e-03 ± 4.789e-04
u-235	n,γ	1.128e-01 ± 6.320e-04	ni-58	n,p	-9.340e-03 ± 4.690e-05
cr-52	elastic	9.926e-02 ± 1.268e-02	ni-58	n,γ	-4.537e-03 ± 5.656e-05
u-238	elastic	8.745e-02 ± 1.279e-02	fe-54	n,p	-3.900e-03 ± 2.127e-05
u-238	fission	8.563e-02 ± 1.108e-03	cr-52	n,γ	-3.288e-03 ± 9.066e-05
ni-58	elastic	8.351e-02 ± 1.781e-02	fe-54	n,γ	-2.901e-03 ± 2.811e-05
fe-54	elastic	5.294e-02 ± 8.601e-03	ni-60	n,γ	-1.665e-03 ± 2.070e-05
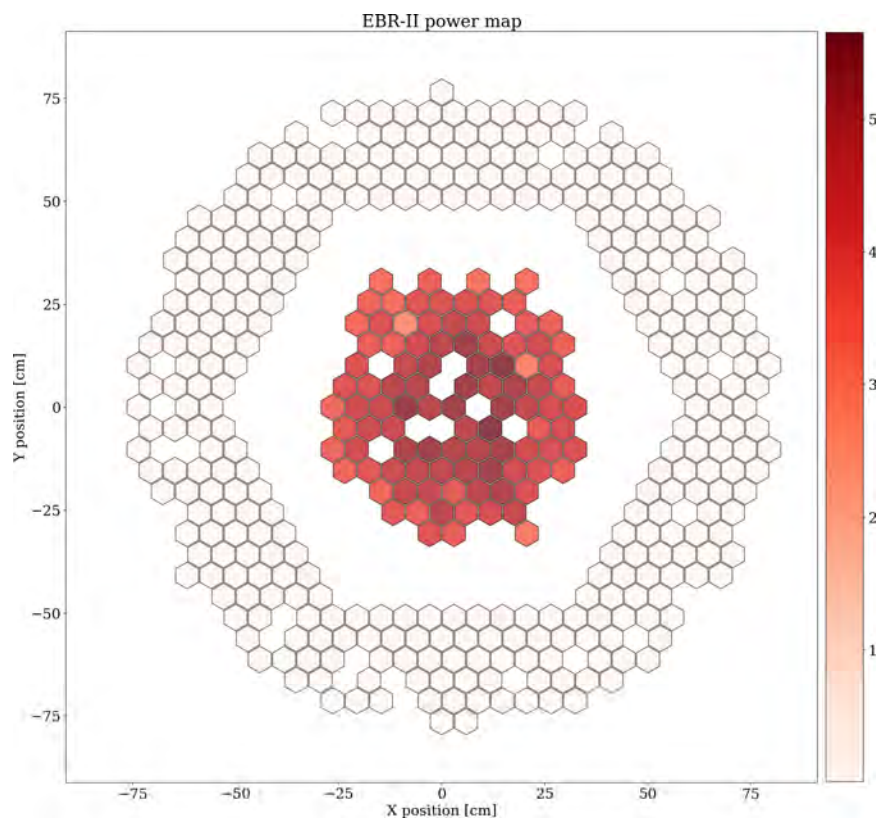
Figure 5-38 EBR-II: KENO Radial Power Distribution (Axially Integrated Assembly Powers) using ENDF/B-VII.1 Data[43]

---

[42] All sodium removed, $\Delta\rho$ = -4681 ± 29 pcm; top 10 positive and top 10 negative mixture-, region-, and energy-integrated sensitivities, determined with SCALE/TSUNAMI using ENDF/B-VII.1 data.

[43] High power is visible in the central driver core region, whereas only very low power is observed in the outer blanket region.

5.5.3 Uncertainty Analysis

Uncertainty calculations of all QOIs were performed for all considered ENDF/B libraries based on the sensitivity coefficients determined with CE TSUNAMI. Table 5-39 compares the obtained output uncertainties. The causes of the observed differences can be explained when comparing the individual contributions of the top contributing nuclear reactions (covariance matrices of the individual reactions) to the uncertainties presented for each individual QOIs in Table A-23 to Table A-25 and in Figure 5-39.

As noted above for the HPR in Section 5.4, the k_{eff} uncertainty was calculated as ~2% when using ENDF/B-VII.0 and ENDF/B-VII.1 data, but the uncertainty is significantly smaller with ~1% when using ENDF/B-VIII.0 data. The major contributor to this uncertainty in the ENDF/B-VII.0 and ENDF/B-VII.1 calculations is ^{235}U (n,γ). The uncertainty of this reaction in these libraries is above 30% in the fast energy range (Figure 2-39). The decrease of this uncertainty in ENDF/B-VIII.0 leads to the significant decrease of the k_{eff} uncertainty. Although the individual contribution of ^{235}U (n,γ) is also significantly decreased for the sodium void worth in ENDF/B-VIII.0, the effect is partially compensated through increased uncertainties of ^{235}U fission and $\bar{\nu}$ (Figure 2-20 and Figure 2-21) and elastic scattering reactions of structural materials such as ^{52}Cr and ^{58}Ni. The CR worth uncertainty is significantly influenced by changes in ^{235}U (n,γ), ^{235}U $\bar{\nu}$, inelastic scattering of ^{235}U and ^{238}U, and ^{10}B (n,α) as absorbing material in the CRs.

Table 5-39   EBR-II: TSUNAMI Uncertainties of QOIs Determined with TSUNAMI

QOI	ENDF/B-VII.0	ENDF/B-VII.1	ENDF/B-VIII.0	$\frac{VII.1}{VII.0} - 1$	$\frac{VIII.0}{VII.1} - 1$
k_{eff}	Na void	2.16%	1.01%	3.3%	-53.0%
CR worth	1.02%	3.3%	1.26%	15.5%	6.8%
Na void	4.07%	5.15%	4.21%	26.5%	-18.3%

The uncertainty of the EBR-II's radial power distribution as determined with Sampler/KENO-MG is displayed in Figure 5-40 and Figure 5-41. The uncertainty of the power in the inner driver assemblies is much smaller than the power uncertainty of the outer blanket assemblies (Table 5-40). The ENDF/B-VII.1 calculation yields larger uncertainties as compared to the ENDF/B-VIII.0 calculation.

Although only slightly visible in Figure 5-40, the uncertainties of three assemblies in the inner driver core stand out. These assemblies are high worth CR assemblies and their uncertainties are larger than those of all other assemblies in the inner driver core. The uncertainty of the peak assembly power is 0.343% and 0.335% as determined with ENDF/B-VII.1 and ENDF/B-VIII.0, respectively. Figure 5-42 shows that the most significant contributor to the uncertainty was found to be ^{23}Na elastic scattering (Figure 2-40). As for other QOIs of the EBR-II, the (n,γ) uncertainty of ^{235}U (Figure 2-39) provides a significant contribution to the power uncertainty. This contribution is no longer identified in the ENDF/B-VIII.0 calculation due to the decrease of this uncertainty in this library. In contrast, the ENDF/B-VIII.0 calculation shows a significant contribution of the ^{235}U and ^{239}Pu fission uncertainties due to the increased uncertainty of these reactions in ENDF/B-VIII.0 (Figure 2-21 and Figure 2-23). The contribution of the ^{23}Na (n,γ) uncertainty is increased in the ENDF/B-VIII.0 calculation as compared to the ENDF/B-VII.1. This is caused not by an increase of the uncertainty in the latest ENDF/B release (Figure 5-43 shows that the uncertainty did not change between the latest two ENDF/B releases), but by an

increased relevance of this reaction due to the smaller relevance of other cross section uncertainties.
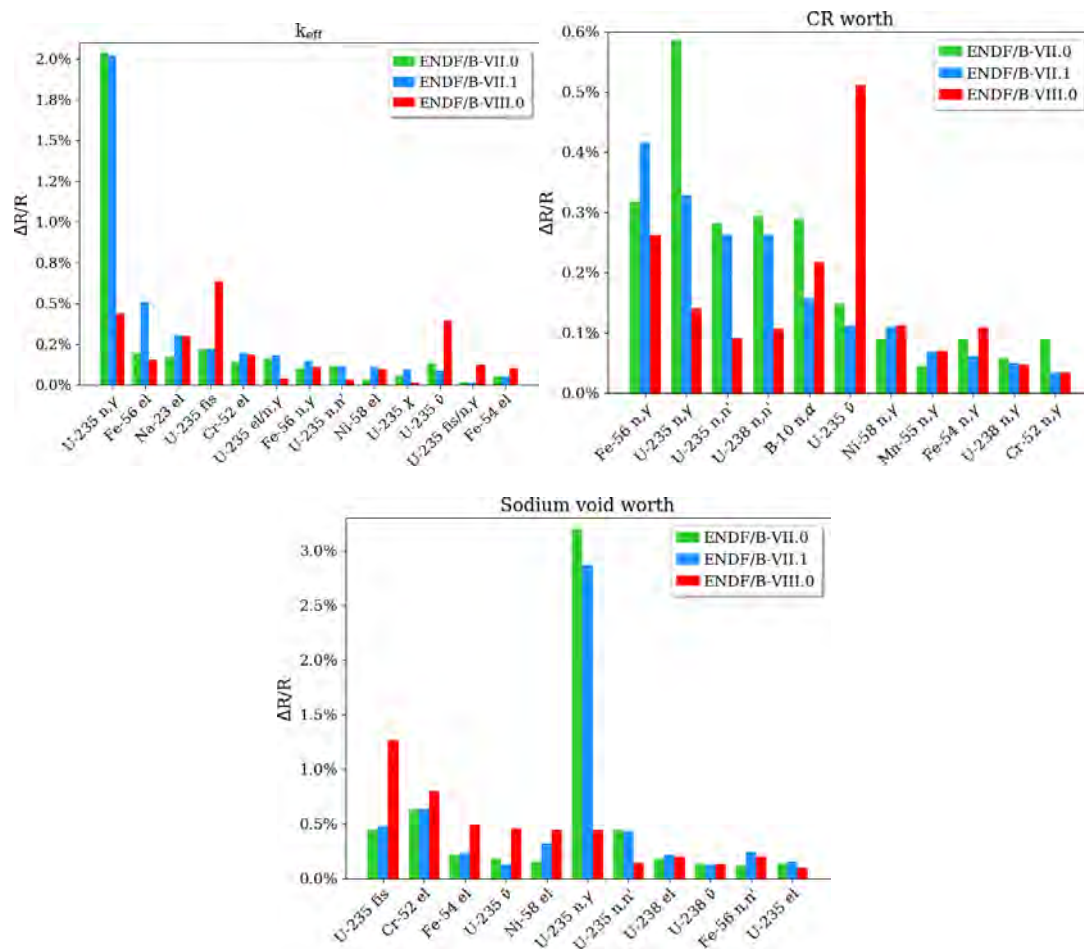
Figure 5-39 EBR-II: Contributions to the Output Uncertainties[44]

---

[44] Obtained using TSUNAMI in ΔR/R

Table 5-40   EBR-II: Power Uncertainties Determined with Sampler/KENO-MG

QOI	ENDF/B-VII.1	ENDF/B-VIII.0
Power uncertainty in outer blanket zone	3.293–7.049%	1.739–5.255%
Power uncertainty in inner driver zone	0.147–1.496%	0.128–0.976%
Radial peak power uncertainty	0.343%	0.335%
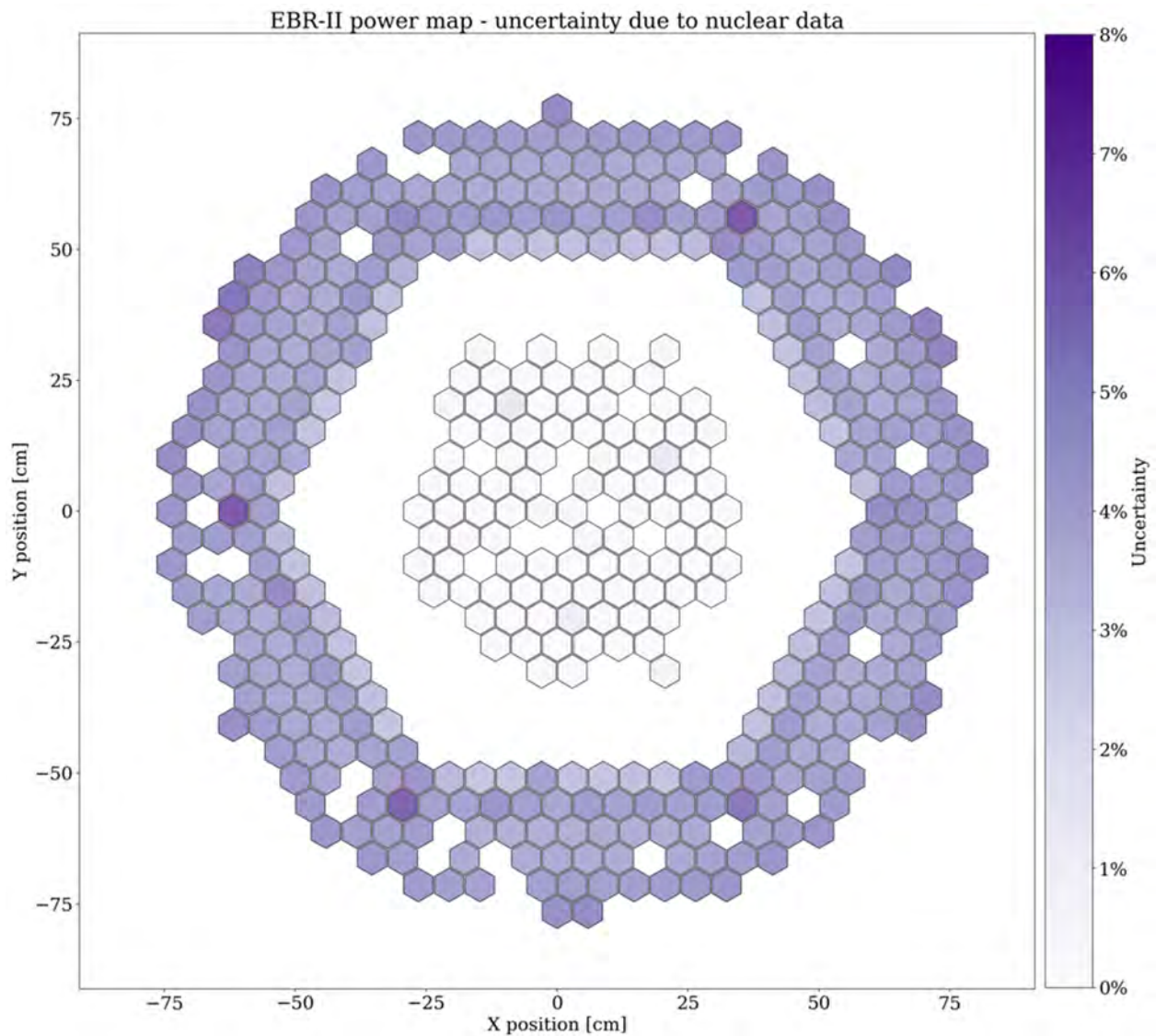
Figure 5-40 EBR-II: Sampler/KENO-MG Uncertainty of Axially Integrated Assembly Powers Using ENDF/B-VII.1 Data
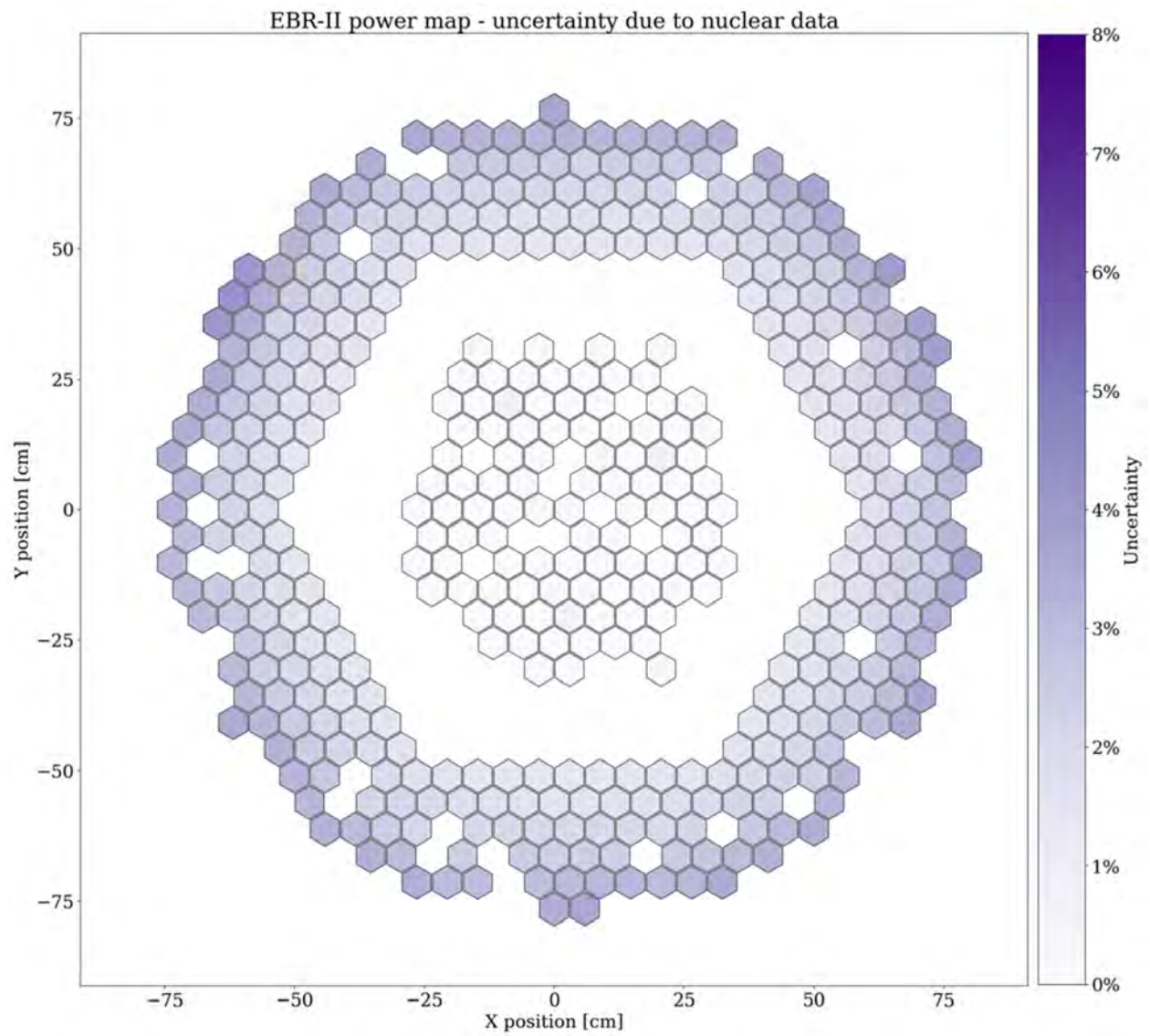
Figure 5-41 EBR-II: Sampler/KENO-MG Uncertainty of Axially Integrated Assembly Powers Using ENDF/B-VIII.0 Data
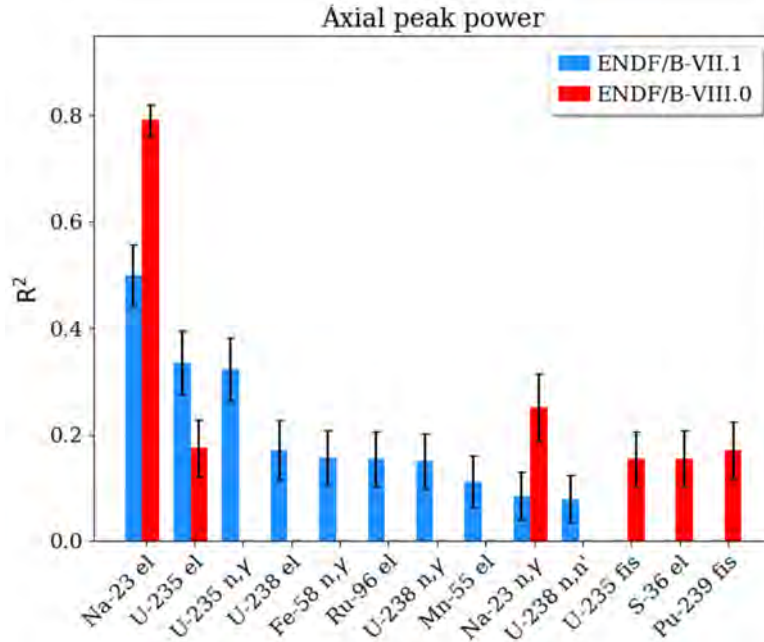
Figure 5-42 EBR-II: Sampler/KENO-MG Top Contributor to the Peak Power Uncertainty in Terms of R^2
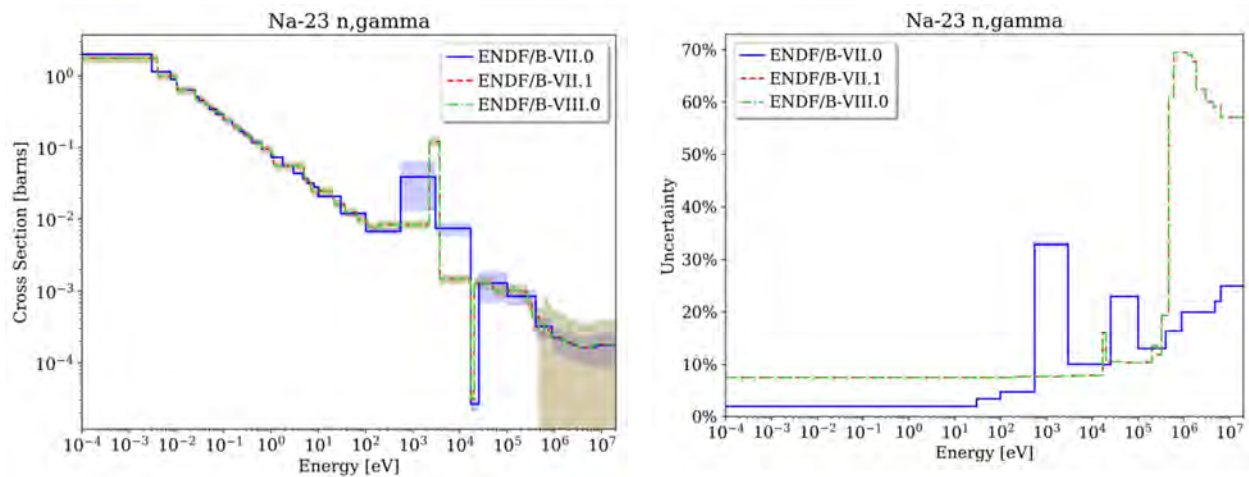
Figure 5-43 ^{23}Na (n,γ) Nominal Data and Uncertainty

5.6   ABR-1000, Sodium-Cooled Fast Reactor

The SCALE/KENO-VI model of the ABR-1000 was developed based on the UAM-SFR benchmark specifications (Buiron et al., 2019). Figure shows the full core model, and Figure 5-45 shows a driver fuel assembly. The neutron flux spectrum in different regions of the core is displayed in Figure-46.
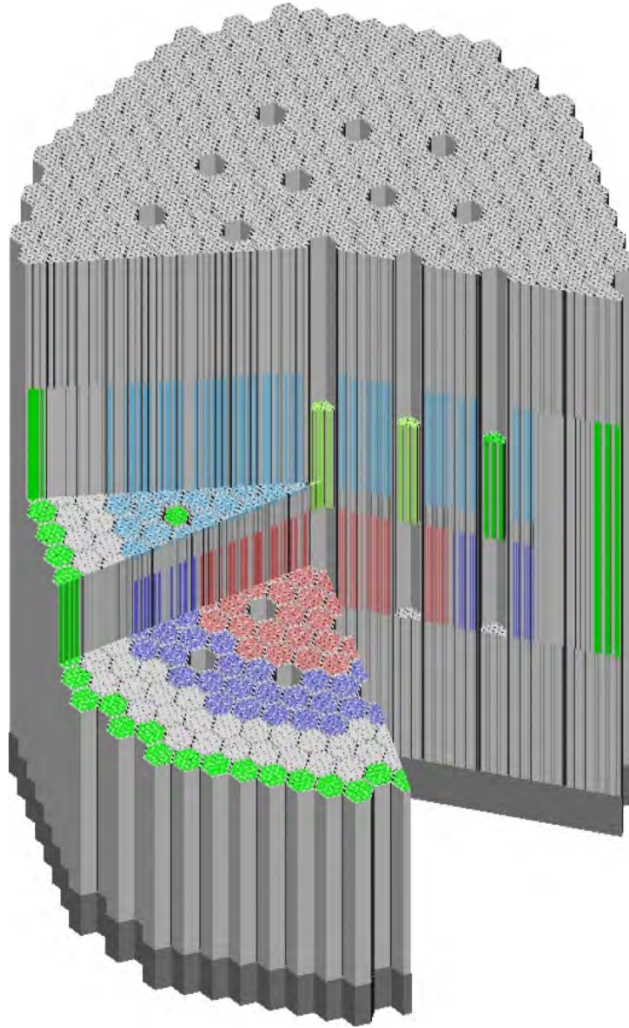
Figure 5-44 ABR-1000: SCALE Full Core Model[45]

The sensitivity and uncertainty analyses for the ABR1000 were performed for the following QOIs:

1. k_{eff}

2. Reactivity effect due to 10% density change in the coolant (only in the fuel assembly)

3. Reactivity effect due to 10% density change in the wrapper (only in the fuel assembly)

4. Reactivity effect due to 10% density change in the cladding (only in the fuel assembly)

5. Reactivity effect due to 1% density change in the fuel

---

[45] Structure in gray, inner fuel in red, outer fuel in blue, absorber in green, helium within fuel rod in blue. The sodium coolant was removed for this plot.

6. Reactivity effect due to 1% grid expansion while preserving fuel and structural masses

7. Reactivity effect due to 1% fuel density change with simultaneous increase of axial fuel length by 1%

8. CR worth: (fully inserted and 5 cm inserted)

9. Fuel Doppler constant: fuel temperature is doubled

10. Sodium void worth: sodium removed in all fuel assemblies

11. Axially integrated fuel assembly power (radial power distribution)

12. Axial power distribution of one specified assembly
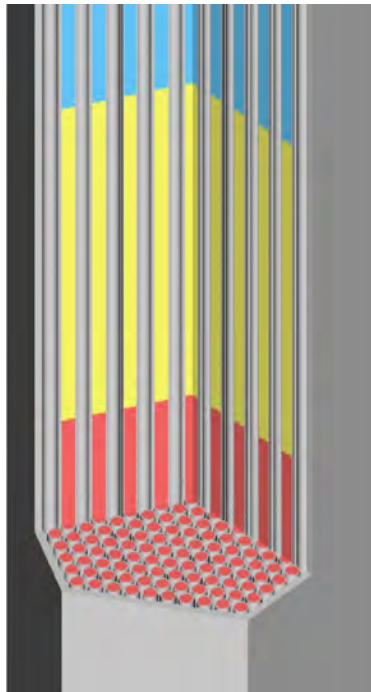
Figure 5-45 ABR-1000: SCALE Fuel Assembly Model[46]

---

[46] Structure in gray, fuel in red, bond sodium in yellow, helium in blue. The sodium coolant was removed for this plot.

The sensitivity and uncertainty calculations of the reactivities were performed with MG TSUNAMI using KENO-MG in combination with SCALE's 302-group ENDF/B-VII.1 and ENDF/B-VIII.0 fast reactor libraries. Neutron transport calculations were not performed with ENDF/B-VII.0 data because of an issue with the generation of probability tables for SCALE's CE libraries that also affects the MG library generation; this issue was recently resolved. SCALE's ENDF/B-VII.1 and ENDF/B-VIII.0 libraries were updated, but the ENDF/B-VII.0 library was not updated since it will no longer be included in future SCALE releases. Correction of the probability tables has been found to impact the reactivity calculations of fast spectrum systems that include irradiated fuel (Kim et al., 2019).
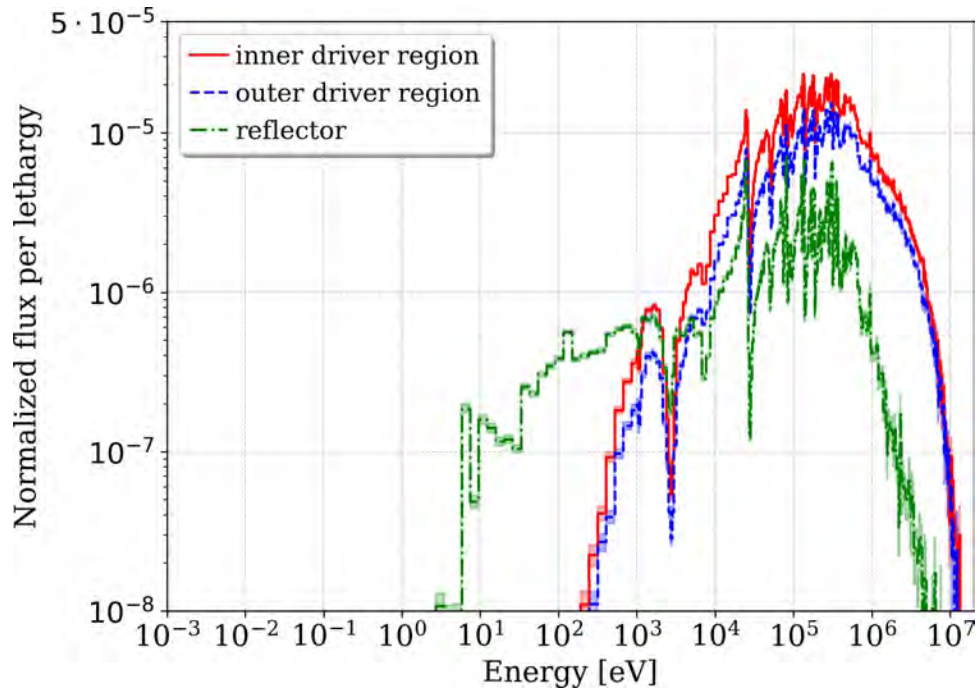
Figure 5-46 ABR-1000: Normalized Neutron Flux in a 302-Group Representation at the Core Axial Midline at Different Radial Positions, as Determined with KENO-CE

Note that the Doppler constant was calculated as suggested by the OECD/NEA benchmark specifications:

$$K_D = \frac{\frac{1}{k_{nom} - \frac{1}{k_{mod}}}}{ln\left(\frac{T_{mod}}{T_{nom}}\right)} \tag{5}$$

Furthermore, the density and expansion reactivity effects were calculated by dividing the reactivity difference by the temperature difference that corresponds with the applied density change or expansion.

Results on the radial and axial power distribution are provided in a previous publication which presents a study of these quantities' uncertainties (Bostelmann, 2020).

5.6.1 Nominal Results

Table 5-41 compares the nominal QOIs calculated with KENO-MG using the different ENDF/B libraries. The ENDF/B-VIII.0 results show small differences of less than 100 pcm for k_{eff}. Notable differences are observed for the sodium density, wrapper density, and sodium void worth, which have relative differences of 5% and above. However, analysis of the reactivity differences between the perturbed calculations using the different libraries shows that the differences range between 60 and 110 pcm for all considered reactivity effects. The difference is slightly larger for the sodium void worth. This coefficient shows the largest sensitivity to ^{238}U (n,γ) from all considered effects (Figure 5-3). Since the cross section of this reaction changed significantly between ENDF/B-VII.1 and ENDF/B-VIII.0 (Figure 2-27), the slightly larger difference could be caused by this update. The other observed small differences result from the combination of updates in several relevant ^{238}U and ^{239}Pu cross sections, including $\bar{\nu}$, fission, and (n,γ).

Table 5-41 ABR1000: Nominal Values of all QOIs Determined with KENO-MG

QOI	ENDF/B-VII.1	ENDF/B-VIII.0	Difference
k_{eff}	1.02175 ± 0.00003	1.02266 ± 0.00003	92 pcm ± 4 pcm
10% sodium [pcm/K]	0.384 ± 0.007	0.450 ± 0.008	17.1% ± 3.0%
10% wrapper [pcm/K]	0.019 ± 0.001	0.021 ± 0.001	10.8% ± 2.8%
10% cladding [pcm/K]	0.046 ± 0.001	0.049 ± 0.001	5.7% ± 1.1%
1% fuel [pcm/K]	-0.556 ± 0.004	-0.560 ± 0.004	0.7% ± 1.0%
1% fuel + axial [pcm/K]	-0.270 ± 0.004	-0.275 ± 0.004	2.0% ± 2.1%
1% grid [pcm/K]	-1.087 ± 0.005	-1.081 ± 0.005	-0.6% ± 0.6%
CSD+DSD worth (fully inserted) [pcm]	-9758 ± 3	-9784 ± 3	0.3% ± 0.0%
CSD+DSD worth (5 cm from top) [pcm]	-234 ± 3	-230 ± 3	-1.7% ± 1.7%
Delayed neutron fraction [pcm]	-398 ± 3	-397 ± 3	-0.3% ± 1.0%
Doppler [pcm]	-418 ± 4	-399 ± 4	-4.5% ± 1.4%
Na void worth [pcm]	1181 ± 3	1292 ± 3	9.4% ± 0.4%

5.6.2 Sensitivity Analysis

Table 5-42 through Table 5-53 list the top integrated sensitivities of the different QOIs as determined with MG TSUNAMI. Each of these sensitivity coefficients represents the sensitivity of a specific QOI to a single specific reaction and can be used to understand relevant sensitivities for a given QOI.

As expected for a system with irradiated fuel, the largest sensitivities are found for several reactions of ^{238}U and ^{239}Pu. The average number of neutrons produced per fission event ($\bar{\nu}$) and the fission cross section of ^{239}Pu are among the top 4 sensitivities for all QOIs due to their immediate contribution to the reactivity of the system; the same reactions of ^{238}U are also consistently listed as having significant sensitivity. Other relevant reactions of ^{238}U and several plutonium isotopes to all QOIs are (n,γ) and inelastic scattering (n,n').

Scattering reactions and the (n,γ) reaction of ^{56}Fe and ^{52}Cr play a significant role—especially for the cladding and wrapper effects—since these isotopes are the major parts of the cladding

materials. The scattering reactions of ^{23}Na show large sensitivities to most studied reactivity effects, especially the sodium void worth. The CR worth is very sensitive to the ^{10}B (n,α) since boron is the absorbing material in the CRs. The sodium void reactivity is very sensitive to elastic and inelastic scattering of ^{23}Na. In thermal spectrum systems, the fuel temperature reactivity is most sensitive to the ^{238}U (n,γ) reaction, but this is not the case for this fast spectrum system, since Doppler broadening in the resonance range with increasing temperature only has a minor effect on the reactivity. Instead, scattering reactions of ^{23}Na, ^{238}U, and ^{56}Fe are listed as top sensitivities.

Table 5-42   ABR1000: Top k$_{eff}$ Sensitivities[47]

Nuclide	Reaction	Sensitivity (increasing k$_{eff}$)	Nuclide	Reaction	Sensitivity (decreasing k$_{eff}$)
pu-239	$\bar{\nu}$	6.379e-01 ± 3.762e-05	u-238	n,γ	-1.506e-01 ± 1.378e-05
pu-239	fission	4.693e-01 ± 3.888e-05	u-238	n,n'	-6.477e-02 ± 7.508e-05
u-238	$\bar{\nu}$	1.143e-01 ± 2.504e-05	pu-239	n,γ	-3.028e-02 ± 4.367e-06
pu-240	$\bar{\nu}$	9.156e-02 ± 2.246e-05	fe-56	n,n'	-2.732e-02 ± 3.831e-05
pu-241	$\bar{\nu}$	7.610e-02 ± 2.040e-05	pu-240	n,γ	-2.067e-02 ± 2.388e-06
u-238	fission	6.877e-02 ± 2.557e-05	fe-56	n,γ	-1.431e-02 ± 3.079e-06
pu-240	fission	6.366e-02 ± 2.252e-05	na-23	n,n'	-1.052e-02 ± 2.645e-05
pu-241	fission	5.674e-02 ± 2.045e-05	am-241	n,γ	-6.989e-03 ± 7.183e-07
pu-238	$\bar{\nu}$	2.296e-02 ± 1.169e-05	am-243	n,γ	-5.241e-03 ± 5.959e-07
fe-56	elastic	1.705e-02 ± 7.320e-04	pu-239	n,n'	-4.485e-03 ± 1.749e-05

Table 5-43   ABR1000: Top Sodium Density Reactivity Sensitivities[48]

Nuclide	Reaction	Sensitivity (increasing $\Delta\rho$)	Nuclide	Reaction	Sensitivity (reducing $\Delta\rho$)
u-238	n,γ	1.182e+00 ± 6.385e-03	pu-239	$\bar{\nu}$	-1.310e+00 ± 6.585e-04
na-23	elastic	1.004e+00 ± 1.195e-01	pu-239	fission	-1.073e+00 ± 6.531e-03
na-23	n,n'	4.710e-01 ± 8.094e-03	fe-56	elastic	-4.508e-01 ± 1.281e-01
pu-239	n,γ	4.588e-01 ± 1.667e-03	u-238	n,n'	-4.329e-01 ± 5.399e-02
pu-240	$\bar{\nu}$	3.176e-01 ± 1.407e-04	pu-241	$\bar{\nu}$	-3.455e-01 ± 7.799e-05
u-238	$\bar{\nu}$	2.544e-01 ± 2.429e-04	pu-241	fission	-2.665e-01 ± 7.556e-04
pu-240	n,γ	2.100e-01 ± 9.644e-04	fe-56	n,n'	-2.029e-01 ± 1.289e-02
pu-240	fission	1.904e-01 ± 1.684e-03	u-238	elastic	-1.618e-01 ± 8.440e-02
u-238	fission	9.714e-02 ± 3.931e-03	fe-56	n,γ	-8.012e-02 ± 8.055e-04
pu-242	$\bar{\nu}$	6.620e-02 ± 2.711e-05	cr-52	elastic	-6.666e-02 ± 2.058e-02

---

[47]   Top 10 positive and top 10 negative mixture-, region-, and energy-integrated sensitivities, determined with TSUNAMI using ENDF/B-VII.1 data.

[48]   Density increased by 10%, $\Delta\rho$ = 0.450 ± 0.008 pcm/K; top 10 positive and top 10 negative mixture-, region-, and energy-integrated sensitivities, determined with TSUNAMI using ENDF/B-VII.1 data.

Table 5-44   ABR1000: Top Wrapper Density Reactivity Sensitivities[49]

Nuclide	Reaction	Sensitivity (increasing $\triangle\rho$)	Nuclide	Reaction	Sensitivity (reducing $\triangle\rho$)
u-238	n,γ	4.654e-01 ± 6.072e-03	fe-56	n,n′	-3.823e+00 ± 1.325e-02
u-238	$\bar{\nu}$	3.202e-01 ± 2.284e-04	fe-56	elastic	-2.592e+00 ± 1.314e-01
pu-239	n,γ	1.645e-01 ± 1.596e-03	pu-239	$\bar{\nu}$	-1.165e+00 ± 6.180e-04
u-238	fission	1.295e-01 ± 3.733e-03	pu-239	fission	-9.949e-01 ± 6.178e-03
pu-240	n,γ	7.256e-02 ± 9.209e-04	cr-52	n,n′	-4.616e-01 ± 1.340e-03
pu-240	$\bar{\nu}$	6.329e-02 ± 1.318e-04	fe-56	n,γ	-4.353e-01 ± 7.613e-04
mn-55	n,γ	4.060e-02 ± 1.326e-04	cr-52	elastic	-4.044e-01 ± 2.119e-02
na-23	elastic	2.451e-02 ± 1.159e-01	u-238	n,n′	-2.822e-01 ± 5.090e-02
am-241	n,γ	2.189e-02 ± 2.755e-04	pu-241	$\bar{\nu}$	-1.995e-01 ± 7.337e-05
am-243	n,γ	1.909e-02 ± 2.436e-04	fe-54	n,p	-1.746e-01 ± 1.173e-04

Table 5-45   ABR1000: Top Cladding Density Reactivity Sensitivities[50]

Nuclide	Reaction	Sensitivity (increasing $\triangle\rho$)	Nuclide	Reaction	Sensitivity (reducing $\triangle\rho$)
u-238	n,γ	4.265e-01 ± 2.550e-03	pu-239	$\bar{\nu}$	-1.087e+00 ± 2.635e-04
fe-56	n,n′	3.907e-01 ± 4.910e-03	pu-239	fission	-9.467e-01 ± 2.596e-03
fe-56	elastic	3.166e-01 ± 4.899e-02	u-238	n,n′	-2.512e-01 ± 2.141e-02
u-238	$\bar{\nu}$	2.682e-01 ± 9.774e-05	pu-241	$\bar{\nu}$	-1.720e-01 ± 3.126e-05
fe-56	n,γ	1.590e-01 ± 3.115e-04	pu-241	fission	-1.458e-01 ± 3.013e-04
pu-239	n,γ	1.143e-01 ± 6.695e-04	na-23	n,n′	-4.810e-02 ± 3.318e-03
u-238	fission	1.016e-01 ± 1.572e-03	pu-239	fission	-1.977e-02 ± 1.103e-04
pu-240	n,γ	5.865e-02 ± 3.863e-04	pu-239	$\bar{\nu}$	-1.957e-02 ± 1.040e-05
cr-52	elastic	4.633e-02 ± 7.853e-03	zr-90	n,n′	-1.859e-02 ± 5.765e-04
cr-52	n,γ	4.595e-02 ± 4.980e-04	cm-245	$\bar{\nu}$	-1.703e-02 ± 3.255e-06

---

[49] Density increased by 10%, $\triangle\rho$ = 0.021 ± 0.001 pcm/K; top 10 positive and top 10 negative mixture-, region-, and energy-integrated sensitivities, determined with TSUNAMI using ENDF/B-VII.1 data.

[50] Density increased by 10%, $\triangle\rho$ = 0.049 ± 0.001 pcm/K; top 10 positive and top 10 negative mixture-, region-, and energy-integrated sensitivities, determined with TSUNAMI using ENDF/B-VII.1 data.

Table 5-46   ABR1000: Top Fuel Density Reactivity Sensitivities[51]

Nuclide	Reaction	Sensitivity (reducing negative $\Delta\rho$)	Nuclide	Reaction	Sensitivity (increasing negative $\Delta\rho$)
pu-239	$\bar{v}$	6.655e-01 ± 2.466e-04	u-238	n,γ	-9.637e-02 ± 2.341e-03
pu-239	fission	6.304e-01 ± 2.374e-03	fe-56	n,n'	-5.360e-02 ± 4.703e-03
u-238	fission	9.983e-02 ± 1.429e-03	pu-239	n,γ	-4.612e-02 ± 6.177e-04
pu-241	$\bar{v}$	9.195e-02 ± 2.932e-05	fe-56	n,γ	-3.336e-02 ± 2.952e-04
u-238	$\bar{v}$	9.109e-02 ± 9.086e-05	na-23	n,n'	-2.384e-02 ± 3.036e-03
pu-241	fission	8.346e-02 ± 2.760e-04	pu-240	n,γ	-1.865e-02 ± 3.558e-04
pu-240	fission	8.012e-02 ± 6.095e-04	b-10	n,α	-1.032e-02 ± 2.496e-04
pu-240	$\bar{v}$	7.606e-02 ± 5.248e-05	cr-52	n,n'	-6.531e-03 ± 4.765e-04
u-238	n,n'	3.474e-02 ± 1.951e-02	am-241	n,γ	-5.746e-03 ± 1.063e-04
u-238	elastic	2.786e-02 ± 3.069e-02	mo-95	n,γ	-5.615e-03 ± 8.009e-05

Table 5-47   ABR1000: Top Fuel Density and Axial Expansion Reactivity Sensitivities[52]

Nuclide	Reaction	Sensitivity (reducing negative $\Delta\rho$)	Nuclide	Reaction	Sensitivity (increasing negative $\Delta\rho$)
pu-239	$\bar{v}$	7.794e-01 ± 4.884e-04	u-238	n,γ	-2.481e-01 ± 4.839e-03
pu-239	fission	6.978e-01 ± 4.904e-03	fe-56	n,n'	-1.037e-01 ± 9.709e-03
pu-241	$\bar{v}$	1.219e-01 ± 5.808e-05	pu-239	n,γ	-8.719e-02 ± 1.275e-03
u-238	n,n'	1.089e-01 ± 4.031e-02	fe-56	elastic	-6.447e-02 ± 9.658e-02
pu-241	fission	1.033e-01 ± 5.699e-04	fe-56	n,γ	-6.396e-02 ± 6.073e-04
pu-240	fission	5.140e-02 ± 1.259e-03	pu-240	n,γ'	-4.063e-02 ± 7.341e-04
u-238	fission	5.051e-02 ± 2.948e-03	na-23	n,n'	-3.595e-02 ± 6.263e-03
pu-240	$\bar{v}$	3.291e-02 ± 1.039e-04	cr-52	n,n'	-1.281e-02 ± 9.830e-04
u-238	fission	1.879e-02 ± 2.079e-04	am-241	n,γ	-1.207e-02 ± 2.194e-04
u-238	$\bar{v}$	1.811e-02 ± 1.923e-05	mo-95	n,γ	-1.193e-02 ± 1.642e-04

---

[51] Density increased by 1%, $\Delta\rho$ = -0.560 ± 0.004 pcm/K; top 10 positive and top 10 negative mixture-, region-, and energy-integrated sensitivities, determined with TSUNAMI using ENDF/B-VII.1 data.

[52] Density and height increased by 1%, $\Delta\rho$ = -0.275 ± 0.004 pcm/K; top 10 positive and top 10 negative mixture-, region-, and energy-integrated sensitivities, determined with TSUNAMI using ENDF/B-VII.1 data.

Table 5-48   ABR1000: Top Grid Expansion Reactivity Sensitivities[53]

Nuclide	Reaction	Sensitivity (reducing negative $\Delta\rho$)	Nuclide	Reaction	Sensitivity (increasing negative $\Delta\rho$)
pu-239	$\bar{\nu}$	6.419e-01 ± 1.588e-04	u-238	n,γ	-1.341e-01 ± 1.514e-03
pu-239	fission	5.913e-01 ± 1.532e-03	pu-239	n,γ	-8.656e-02 ± 4.031e-04
u-238	$\bar{\nu}$	1.163e-01 ± 5.858e-05	fe-56	n,n′	-4.133e-02 ± 3.039e-03
u-238	fission	1.136e-01 ± 9.214e-04	fe-56	n,γ	-3.854e-02 ± 1.926e-04
pu-241	$\bar{\nu}$	1.093e-01 ± 1.892e-05	pu-240	n,γ	-3.464e-02 ± 2.313e-04
pu-241	fission	9.308e-02 ± 1.787e-04	na-23	n,n′	-2.521e-02 ± 1.953e-03
pu-240	fission	6.877e-02 ± 3.928e-04	b-10	n,α	-1.511e-02 ± 1.633e-04
pu-240	$\bar{\nu}$	5.994e-02 ± 3.379e-05	am-241	n,γ	-1.128e-02 ± 6.907e-05
u-238	n,n′	5.236e-02 ± 1.254e-02	am-243	n,γ	-9.640e-03 ± 6.117e-05
u-238	elastic	3.621e-02 ± 1.976e-02	na-23	n,γ	-9.477e-03 ± 1.705e-05

Table 5-49   ABR1000: Top CR Worth (5 cm Insertion) Sensitivities[54]

Nuclide	Reaction	Sensitivity (reducing negative $\Delta\rho$)	Nuclide	Reaction	Sensitivity (increasing negative $\Delta\rho$)
pu-239	fission	5.472e-01 ± 4.104e-03	b-10	n,α	-2.442e-01 ± 4.653e-04
pu-239	$\bar{\nu}$	4.630e-01 ± 4.293e-04	u-238	n,n′	-1.362e-01 ± 3.377e-02
u-238	n,γ	2.474e-01 ± 4.035e-03	b-11	elastic	-7.595e-02 ± 2.179e-03
u-238	$\bar{\nu}$	2.082e-01 ± 1.583e-04	fe-56	n,n′	-4.773e-02 ± 8.101e-03
pu-240	$\bar{\nu}$	1.695e-01 ± 9.151e-05	b-10	elastic	-2.855e-02 ± 7.163e-04
u-238	fission	1.640e-01 ± 2.472e-03	c	elastic	-2.545e-02 ± 7.060e-04
pu-240	fission	1.464e-01 ± 1.056e-03	pu-239	n,n′	-9.956e-03 ± 2.637e-03
pu-239	n,γ	7.173e-02 ± 1.061e-03	pu-240	n,n′	-8.270e-03 ± 2.033e-03
pu-241	fission	5.538e-02 ± 4.765e-04	zr-90	n,n′	-6.839e-03 ± 9.052e-04
pu-241	n,γ	4.281e-02 ± 5.099e-05	cr-52	n,n′	-6.040e-03 ± 8.204e-04

---

[53] Grid expanded by 1%, $\Delta\rho$ = -1.081 ± 0.04 pcm/K; top 10 positive and top 10 negative mixture-, region-, and energy-integrated sensitivities, determined with TSUNAMI using ENDF/B-VII.1 data.

[54] $\Delta\rho$ = -9784 ± 3 pcm; top 10 positive and top 10 negative mixture-, region-, and energy-integrated sensitivities, determined with TSUNAMI using ENDF/B-VII.1 data.

Table 5-50   ABR1000 – Top CR Worth (Full Insertion) Sensitivities[55]

Nuclide	Reaction	Sensitivity (reducing negative Δρ)	Nuclide	Reaction	Sensitivity (increasing negative Δρ)
pu-239	fission	5.423e-01 ± 1.007e-04	b-10	n,α	-4.303e-01 ± 6.143e-05
pu-239	$\bar{\nu}$	4.837e-01 ± 1.019e-05	b-11	elastic	-1.529e-01 ± 4.416e-04
u-238	$\bar{\nu}$	1.938e-01 ± 3.889e-06	u-238	n,n'	-1.179e-01 ± 8.249e-04
u-238	n,γ	1.686e-01 ± 9.265e-05	fe-56	n,n'	-6.486e-02 ± 2.046e-04
u-238	fission	1.577e-01 ± 6.206e-05	b-10	elastic	-5.173e-02 ± 1.397e-04
pu-240	$\bar{\nu}$	1.551e-01 ± 2.306e-06	c	elastic	-4.968e-02 ± 1.454e-04
pu-240	fission	1.378e-01 ± 2.699e-05	fe-56	elastic	-1.858e-02 ± 1.955e-03
pu-241	fission	6.016e-02 ± 1.172e-05	fe-56	n,γ	-1.335e-02 ± 1.348e-05
pu-241	$\bar{\nu}$	5.291e-02 ± 1.204e-06	na-23	n,n'	-1.302e-02 ± 1.178e-04
pu-239	n,γ	3.003e-02 ± 2.522e-05	pu-239	n,n'	-8.254e-03 ± 6.499e-05

Table 5-51   ABR1000 – Top Delayed Neutron Fraction Sensitivities[56]

Nuclide	Reaction	Sensitivity (reducing negative Δρ)	Nuclide	Reaction	Sensitivity (increasing negative Δρ)
pu-239	$\bar{\nu}$	6.333e-01 ± 2.362e-04	u-238	n,γ	-4.045e-02 ± 2.379e-03
pu-239	fission	5.863e-01 ± 2.415e-03	pu-239	n,γ	-1.180e-02 ± 6.265e-04
u-238	fission	1.204e-01 ± 1.451e-03	pu-240	n,γ	-7.160e-03 ± 3.610e-04
u-238	$\bar{\nu}$	1.133e-01 ± 8.703e-05	fe-56	n,γ	-4.835e-03 ± 2.974e-04
pu-240	$\bar{\nu}$	9.317e-02 ± 5.028e-05	am-241	n,γ	-2.880e-03 ± 1.079e-04
pu-240	fission	8.882e-02 ± 6.198e-04	b-10	n,α	-1.949e-03 ± 2.527e-04
pu-241	$\bar{\nu}$	7.855e-02 ± 2.807e-05	am-243	n,γ	-1.853e-03 ± 9.530e-05
pu-241	fission	7.216e-02 ± 2.806e-04	pu-242	n,γ	-1.407e-03 ± 7.286e-05
u-238	n,n'	6.884e-02 ± 1.986e-02	np-237	n,γ	-1.276e-03 ± 4.943e-05
fe-56	n,n'	3.616e-02 ± 4.758e-03	mo-95	n,γ	-1.269e-03 ± 8.107e-05

---

[55] Δρ = -230 ± 3 pcm; top 10 positive and top 10 negative mixture-, region-, and energy-integrated sensitivities, determined with TSUNAMI using ENDF/B-VII.1 data.

[56] Δρ = -397 ± 3 pcm; top 10 positive and top 10 negative mixture-, region-, and energy-integrated sensitivities, determined with TSUNAMI using ENDF/B-VII.1 data.

Table 5-52   ABR1000: Top Fuel Doppler Reactivity Sensitivities[57]

Nuclide	Reaction	Sensitivity (reducing negative Δρ)	Nuclide	Reaction	Sensitivity (increasing negative Δρ)
pu-239	fission	9.357e-01 ± 3.327e-03	na-23	elastic	-4.718e-01 ± 6.250e-02
pu-239	$\bar{\nu}$	5.176e-01 ± 3.309e-04	u-238	n,n′	-3.529e-01 ± 2.746e-02
pu-239	n,γ	2.760e-01 ± 8.521e-04	u-238	elastic	-1.744e-01 ± 4.311e-02
u-238	$\bar{\nu}$	2.234e-01 ± 1.221e-04	fe-56	elastic	-1.496e-01 ± 6.527e-02
pu-240	$\bar{\nu}$	1.853e-01 ± 7.053e-05	u-238	n,γ	-9.451e-02 ± 3.303e-03
u-238	fission	1.685e-01 ± 2.005e-03	fe-56	n,n′	-8.857e-02 ± 6.575e-03
pu-240	fission	1.663e-01 ± 8.573e-04	fe-54	elastic	-4.640e-02 ± 9.049e-03
pu-240	n,γ	8.142e-02 ± 4.958e-04	na-23	n,n′	-3.855e-02 ± 4.245e-03
pu-241	fission	5.912e-02 ± 3.851e-04	zr-90	elastic	-3.607e-02 ± 1.771e-02
fe-56	n,γ	5.485e-02 ± 4.029e-04	pu-239	n,n′	-3.521e-02 ± 2.143e-03

Table 5-53   ABR1000: Top Sodium Void Worth Sensitivities[58]

Nuclide	Reaction	Sensitivity (increasing Δρ)	Nuclide	Reaction	Sensitivity (reducing Δρ)
na-23	elastic	1.650e+00 ± 1.306e-02	pu-239	$\bar{\nu}$	-1.611e+00 ± 8.286e-05
u-238	n,γ	1.511e+00 ± 7.683e-04	pu-239	fission	-1.365e+00 ± 8.577e-04
na-23	n,n′	7.128e-01 ± 8.842e-04	u-238	n,n′	-5.532e-01 ± 7.416e-03
pu-239	n,γ	5.466e-01 ± 1.901e-04	pu-241	$\bar{\nu}$	-4.453e-01 ± 9.477e-06
pu-240	$\bar{\nu}$	5.098e-01 ± 1.854e-05	fe-56	elastic	-4.006e-01 ± 1.648e-02
u-238	$\bar{\nu}$	3.813e-01 ± 3.086e-05	pu-241	fission	-3.493e-01 ± 9.532e-05
pu-240	fission	3.153e-01 ± 2.304e-04	fe-56	n,n′	-2.313e-01 ± 1.686e-03
pu-240	n,γ	2.669e-01 ± 1.128e-04	u-238	elastic	-1.458e-01 ± 1.080e-02
u-238	fission	1.693e-01 ± 5.086e-04	b-10	n,α	-8.720e-02 ± 9.462e-05
pu-242	$\bar{\nu}$	1.054e-01 ± 3.546e-06	cr-52	elastic	-6.666e-02 ± 2.667e-03

5.6.3   Uncertainty Analysis

Uncertainty calculations of all QOIs were performed for all considered ENDF/B libraries based on the sensitivity coefficients determined with CE TSUNAMI. Table 5-54 compares the output uncertainties obtained. The causes of the observed differences can be explained by comparing the individual contributions of the top contributing nuclear reactions (covariance matrices of the individual reactions) to the uncertainties presented for each QOI listed in Table A-26 through

Table A-37 and in Figure 5-47 and Figure 5-48.

---

[57]   Fuel temperature doubled, K_D = -399 ± 4 pcm; top 10 positive and top 10 negative mixture-, region-, and energy-integrated sensitivities, determined with TSUNAMI using ENDF/B-VII.1 data.

[58]   Sodium removed in fuel assemblies, Δρ = 1292 ± 3 pcm; top 10 positive and top 10 negative mixture-, region-, and energy-integrated sensitivities, determined with TSUNAMI using ENDF/B-VII.1 data.

The k_{eff} uncertainty as determined with ENDF/B-VII.0 data is ~1.4%, decreased to ~1.2% with ENDF/B-VII.1, and to ~0.9% with ENDF/B-VIII.0. The major cause for the uncertainty decrease from ENDF/B-VII.0 to ENDF/B-VII.1 is a decreased ^{239}Pu $\bar{\nu}$ uncertainty (Figure 2-22), as well as $\bar{\nu}$ and fission data for a few other actinides. The major cause of the decrease from ENDF/B-VII.1 to ENDF/B-VIII.0 is the decreased uncertainty of ^{238}U inelastic scattering (Figure 2-38). On the other hand, the uncertainty of the ^{239}Pu fission cross section increased in ENDF/B-VIII.0 (Figure 2-23), and it causes a more significant contribution to the overall output uncertainty than before.

The uncertainties of the other studied reactivity effects are influenced by the same updates as k_{eff}. In the case of the wrapper and cladding density, updates in uncertainties of the elastic and inelastic scattering reactions of ^{56}Fe (Figure 2-41 and Figure 2-42) between the three library releases are also contributing significantly to the difference in total output uncertainty. Furthermore, the fuel temperature reactivity and sodium void worth uncertainties are significantly influenced by updates in the uncertainty of elastic and inelastic scattering of ^{23}Na (Figure 2-40 and Figure 1-3).

Table 5-54   ABR1000: Uncertainties of QOIs Determined with TSUNAMI

QOI	ENDF/B-VII.0	ENDF/B-VII.1	ENDF/B-VIII.0	VII.1/VII.0	VIII.0/VII.1
k_{eff}	1.397%	1.186%	0.900%	-15.1%	-24.1%
10% sodium [pcm/K]	9.540%	11.067%	8.397%	16.0%	-24.1%
10% wrapper [pcm/K]	15.478%	35.103%	19.747%	126.8%	-43.7%
10% cladding [pcm/K]	5.811%	6.896%	3.026%	18.7%	-56.1%
1% fuel [pcm/K]	1.074%	0.844%	1.162%	-21.5%	37.7%
1% fuel + Axial [pcm/K]	1.589%	1.869%	1.529%	17.6%	-18.1%
1% grid [pcm/K]	1.258%	1.045%	1.477%	-16.9%	41.4%
CSD+DSD worth (fully inserted) [pcm]	3.159%	2.582%	1.561%	-18.3%	-39.5%
CSD+DSD worth (5 cm from top) [pcm]	2.687%	2.471%	1.363%	-8.0%	-44.8%
Delayed neutron fraction [pcm]	1.480%	1.555%	1.002%	5.0%	-35.5%
Doppler [pcm]	5.063%	5.434%	4.731%	7.3%	-12.9%
Na void worth [pcm]	12.965%	15.679%	13.483%	20.9%	-14.0%
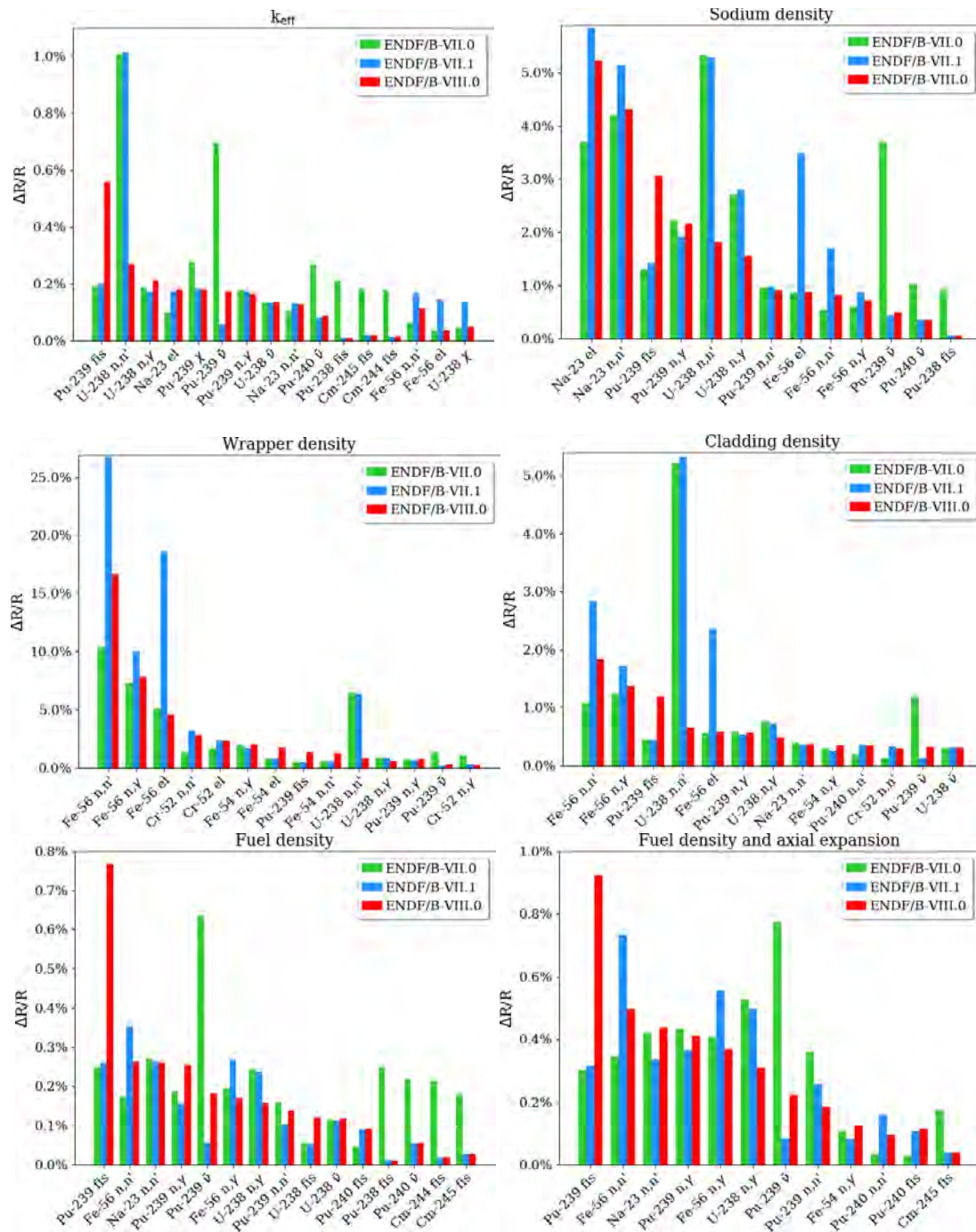
Figure 5-47 ABR1000: Contributions to the Output Uncertainties (1 of 2)[59]

---

[59] Obtained using TSUNAMI in ΔR/R
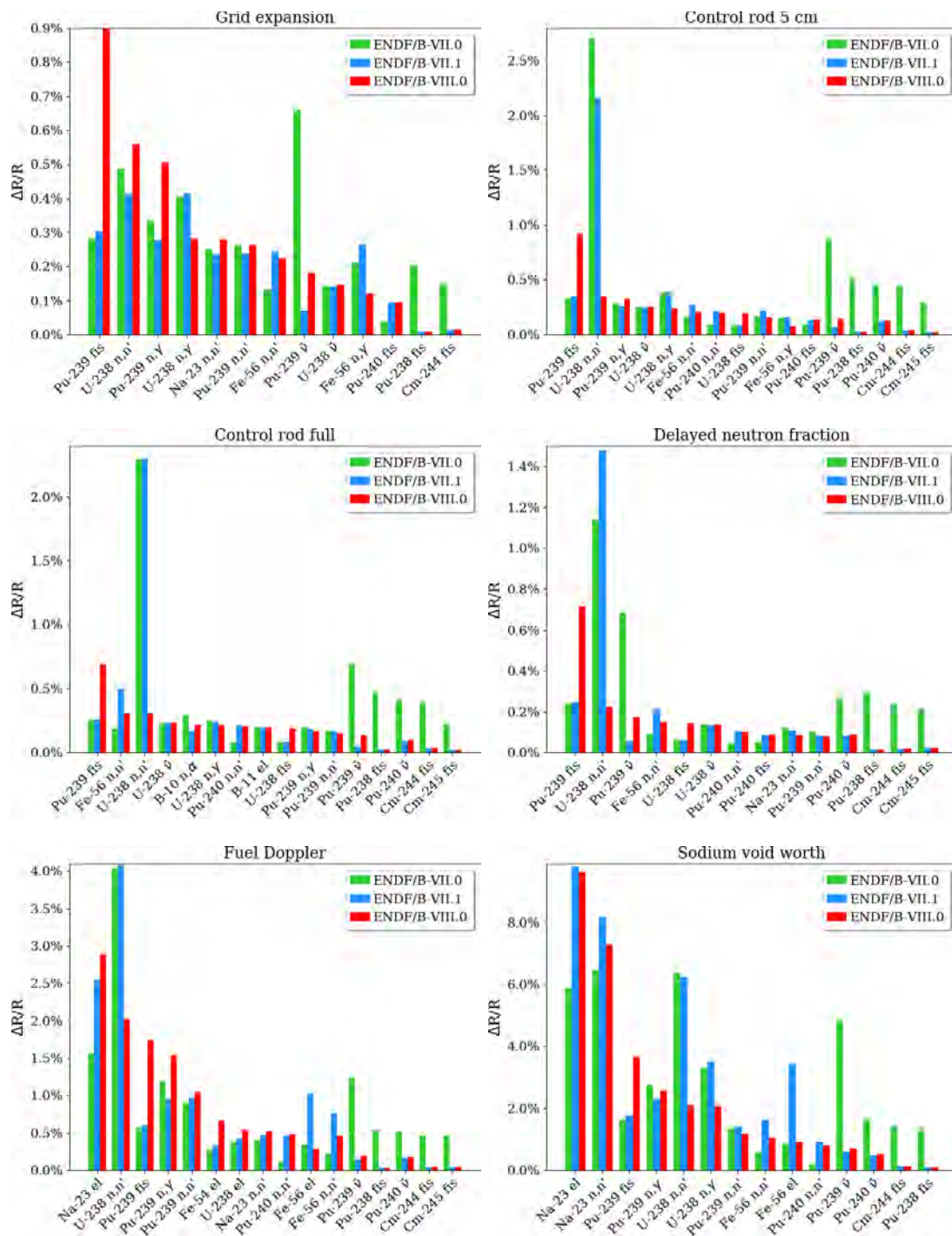
Figure 5-48 ABR1000: Contributions to the Output Uncertainties (2 of 2)

6   CONCLUSIONS

Key nuclear data that are relevant for reactor safety analysis in selected advanced reactor technologies were identified, and their impact on important key figures of merit was assessed based on a review of available advanced reactor specifications, analysis of previous studies performed at ORNL and other research institutions, and examination of available evaluated nuclear data libraries. Sensitivity and uncertainty analyses were performed for six selected benchmarks—three experimental and three computational—to quantify the impact of the identified key nuclear data on several key metrics.

In general, the most important reactions of relevance for reactivity analyses have been found to be the neutron multiplicity ($\bar{\nu}$), fission, the (n,γ) reaction of the fissile nuclides of the fuel, and the (n,γ) reaction of the fertile nuclides of the fuel. Depending on the spectral conditions and fuel composition, these nuclides are several U and Pu isotopes. In the case of depleted fuel, the neutron capture reactions of relevant fission products are important. Depending on the reactivity control mechanism, neutron capture reactions, including (n,γ) and (n,α) of the absorbing material (e.g., Gd or B isotopes), are important. In the case of lighter nuclides with large abundance in the reactor due to their use as moderators, coolants or structural materials, the scattering reactions and (n,γ) reactions are relevant. For MSRs in particular, additional neutron capture reactions such as (n,p) and (n,t) for components of the salt (e.g., Li and Cl) are important.

The most important findings are summarized herein for each of the considered advanced reactor technologies. Table 6-1 provides an overview of the most relevant nominal nuclear reactions, and Table 6-2 provides an overview of the most relevant nuclear data uncertainties.

This report includes many comments regarding relevant differences between important nuclear data as provided with the different ENDF/B library releases; however, given the limited amount of experimental measurement data, no conclusion regarding the better performance of either library can be drawn. The presented sensitivity analyses provide information about the nuclear data, for which a change could have a significant impact on the calculated metric of interest. The uncertainty analyses, in particular the ranking of contributions to the output uncertainties, can be used to guide future measurement and evaluation efforts to reduce the significant nuclear data uncertainties, thereby significantly reducing the overall observed uncertainties.

6.1   High-Temperature Gas Cooled Reactor

For graphite-rich pebble-bed HTGRs, the update of the carbon neutron capture cross section from the ENDF/B-VII.0 to the ENDF/B-VII.1 release led to reactivity differences greater than 1,000 pcm. Calculated k_{eff} results showed better agreement with experimental measurements when using ENDF/B-VII.1 or ENDF/B-VIII.0 data as compared to calculations with ENDF/B-VII.0 data. With the release of ENDF/B-VIII.0, graphite can be considered at different porosities, and the use of these available different options can lead to differences in predicted reactivities, depending on the graphite component in which the data are applied, and depending on the applied temperature. The application of SiC thermal scattering data as provided for the first time with ENDF/B-VIII.0, did not lead to significant changes in reactivity for the HTGR system considered in this study.

Apart from the capture and scattering reactions for graphite, including neutron capture reactions of graphite impurities—[10]B (n,α) being the most significant—the identified key nuclide reactions

impacting reactivity in HTGRs are the neutron multiplicity, fission reaction, and neutron capture reaction for ^{235}U and ^{238}U. A significant gap was identified in terms of the unavailability of uncertainty for graphite thermal scattering data.

Special attention should be paid to cross section and uncertainty differences between different evaluated nuclear data library releases because significant differences in nuclear data were found that can lead to major differences in reactivity calculation, even for well-known nuclides. For example, differences in ^{235}U and ^{238}U nominal and uncertainty data—fission (n,γ), $\bar{\nu}$— between the ENDF/B-VII.1 and ENDF/B-VIII.0 nuclear data releases, are the major cause of difference between calculations of models using fresh fuel compositions performed with these libraries. Furthermore, a larger uncertainty of ^{10}B (n,α) in ENDF/B-VIII.0 as compared to the previous considered releases can have a significant impact on the uncertainty of graphite impurity–related quantities.

6.2   Fluoride Salt-Cooled High-Temperature Reactor

FHRs are graphite moderated and are also impacted by library differences for carbon and graphite as they apply to HTGRs. Key nuclear data include $\bar{\nu}$, fission, and the (n,γ) reaction of the major fissile isotopes ^{235}U, ^{239}Pu, and ^{241}Pu. The impact of the update from the ENDF/B-VII.0 to the ENDF/B-VII.1 release of the tritium production cross section for ^{6}Li is significant given the large amount of FLiBe salt present in this type of reactor. The large uncertainty of ^{7}Li (n,γ) is the dominating contributor to most reactivity effects considered in this report. Thermal scattering data uncertainties for both graphite and FLiBe are not available for consideration in uncertainty analyses. The impact of such uncertainties, where available, is expected to be significant for reactivity uncertainty calculations.

6.3   Graphite Moderated Molten Salt Reactor

For graphite-moderated MSRs, the important nuclide reactions impacting reactivity are similar to those identified for FHRs for graphite, FLiBe salt, and fissile nuclides in the fuel. If Ni is used as part of the structural material as in the MSRE, then the (n,γ) reaction of several Ni isotopes can have a significant contribution to reactivity uncertainties, varying between the applied ENDF/B library releases. Because the fuel is circulating through the reactor during operation, the importance of short-lived fission products is significantly increased. An identified nuclear data gap for analysis of MSRs is the data missing for ^{135m}Xe, which can have a large impact on the calculation of the xenon worth. Thermal scattering data uncertainties for both graphite and FLiBe are not available for consideration in uncertainty analysis.

6.4   Molten Chloride Fast Spectrum Reactor

Given that reactor descriptions sufficient for modeling could not be found in the open literature, the observations reported for the molten chloride fast spectrum reactor were made based solely on a literature search. Given the fast neutron spectrum and fuel composition characteristics, the reactivity uncertainty for the molten chloride fast spectrum reactor is mainly driven by the large uncertainty of the ^{239}Pu fission cross section. Other key nuclear data are for fission $\bar{\nu}$ and capture reactions of the fissile nuclides, as well as scattering reactions of the materials within the salt. Notably, a significant update of the ^{35}Cl (n,p) reaction cross section from ENDF/B-VII.0 to ENDF/B-VII.1 was shown to cause reactivity changes greater than 1,000 pcm. Also, a study identified a significant impact of the ^{24}Mg elastic scattering uncertainty due to the abundance of Mg in the chosen reflector material.

6.5   Heat Pipe Reactor

Reactivity in HPRs with enriched uranium fuel is significantly affected by fission (n,γ), $\bar{\nu}$, and scattering cross sections for ^{235}U and ^{238}U, as well as scattering cross sections for nuclides in coolant and structural materials. Large reactivity uncertainties in such fast spectrum system calculations are caused by large uncertainties for the ^{235}U (n,γ) reaction and inelastic scattering of ^{238}U in the fast energy range. The uncertainty of both of these reactions is significantly reduced in the ENDF/B-VIII.0 nuclear data library as compared to ENDF/B-VII.0 and ENDF/B-VII.1. The uncertainties determined for many HPR reactivities, therefore, tends to be smaller in ENDF/B-VIII.0 calculations, although the decrease is partially compensated by increased uncertainties of reactions such as ^{235}U fission and ^{23}Al elastic scattering in the case of Al$_2$O$_3$ reflector materials. Moreover, because a significant change of this uncertainty was made in the ENDF/B-VIII.0 release, the use of different evaluated libraries is expected to have a large impact on uncertainty analyses for this reactor type. A gap identified in the data of importance for fast spectrum systems analysis is the unavailability of angular scattering data uncertainties.

6.6   Sodium-Cooled Fast Reactor

The key nuclear data identified for sodium-cooled fast reactors is similar to that identified for the HPR and the fast spectrum MSR. Fission, (n,γ), scattering, and $\bar{\nu}$, of ^{235}U, ^{238}U, ^{239}Pu, ^{240}Pu, and ^{241}Pu are the key nuclear data for reactivity. The scattering and (n,γ) reactions of ^{56}Fe as part of the structural material and ^{23}Na as the coolant are also important. For uncertainty analyses of SFRs containing mixed U/Pu fuel, the ^{238}U inelastic scattering update from ENDF/B-VII.1 to ENDF/B-VIII.0 plays a major role. For uncertainty analyses of SFRs with highly enriched uranium, the large uncertainty of the ^{235}U (n,γ) reaction in the fast energy range plays a major role, similar to the fast spectrum HPR. The most relevant identified gap is the missing uncertainty data for angular scattering distributions.

Table 6-1 Overview of Key Nominal Nuclear Data for the Selected Advanced Reactor Concepts

Reactor type	Key nuclear data	Missing/discrepant/additional data, important data changes
Thermal spectrum pebble-bed HTGR*	**Fuel:** ^{235}U $\bar{\nu}$, ^{235}U fission, ^{235}U (n,γ), ^{238}U (n,γ), ^{16}O elastic **Moderator:** ^{12}C (n,γ), ^{10}B (n,γ), ^{10}B (n,α) graphite thermal scattering	^{12}C (n,γ) (ENDF/B-VII.0 vs. VII.1), 0%, 10% and 30% graphite porosities in ENDF/B-VIII.0, new SiC thermal scattering data in ENDF/B-VIII.0
Thermal spectrum FHR	**Fuel:** $\bar{\nu}$, fission, and (n,γ) of ^{235}U, ^{239}Pu, and ^{241}Pu (n,γ) of ^{238}U (n,γ), ^{238}U and ^{240}Pu **Coolant:** ^{7}Li (n,γ), ^{7}Lif elastic, ^{6}Li (n,t), ^{19}F (n,γ), ^{19}F elastic, ^{9}Be (n,γ), ^{9}Be (n,2n), ^{9}Be elastic **Moderator:** ^{12}C (n,γ), graphite thermal scattering	^{12}C (n,γ) and ^{6}Li (n,t) (ENDF/B-VII.0 vs. VII.1), 0, 10% and 30% graphite porosities in ENDF/B-VIII.0 New SiC thermal scattering data in ENDF/B-VIII.0 ^{19}F inelastic discrepancies (ENDF/B-VIII.0 vs. JENDL 4.0), no thermal scattering data for salt (e.g., LiF, BeF$_2$)
Thermal spectrum, graphite-moderated MSR*	**Fuel/coolant:** ^{235}U $\bar{\nu}$, ^{235}U fission, ^{235}U (n,γ), ^{238}U $\bar{\nu}$, ^{238}U fission, ^{238}U (n,γ), ^{238}U elastic, ^{19}F elastic, ^{19}F (n,γ), ^{7}Li (n,γ), ^{6}Li (n,γ), ^{6}Li (n,t) **Moderator:** ^{12}C (n,γ), graphite thermal scattering **Structure:** ^{58}Ni elastic, ^{58}Ni inelastic, ^{58}Ni (n,p)	^{12}C (n,γ) and ^{6}Li (n,t) (ENDF/B-VII.0 vs. VII.1), 0%, 10% and 30% graphite porosities in ENDF/B-VIII.0, new SiC thermal scattering data in ENDF/B-VIII.0, no data for ^{135m}Xe, ^{19}F inelastic discrepancies (ENDF/B-VIII.0 vs. JENDL-4.0), no thermal scattering data for salt (e.g., LiF, BeF$_2$)
Fast spectrum, molten chloride MSR	**Fuel and coolant salt:** $\bar{\nu}$ and fission of ^{235}U, ^{238}U, ^{239}Pu, ^{240}Pu, ^{241}Pu, ^{238}U (n,γ), ^{238}U inel., ^{239}Pu (n,γ), ^{37}Cl inelastic, ^{37}Cl elastic, ^{23}Na inelastic, ^{23}Na elastic, ^{35}Cl (n,p), ^{35}Cl (n,γ)	Missing ^{135m}Xe, ^{35}Cl (n,p) (ENDF/B-VII.0 vs. VII.1)
Fast spectrum, oxide and metal fueled HPR*	**Fuel:** ^{235}U $\bar{\nu}$, ^{235}U fission, ^{235}U (n,γ), ^{238}U $\bar{\nu}$, ^{238}U fission, ^{238}U (n,2n), ^{16}O elastic, elastic and inelastic scattering, as well as (n,γ) of ^{238}U, ^{90}Zr, ^{91}Zr, ^{92}Zr, ^{94}Zr, ^{96}Zr **Coolant:** ^{23}Na elastic, ^{23}Na inelastic, ^{39}K capture, ^{39}K (n,p), ^{39}K elastic **Structure/Reflector:** ^{56}Fe (n,γ), ^{56}Fe elastic, ^{56}Fe inelastic, ^{27}Al elastic, ^{9}Be elastic, ^{16}O elastic, ^{10}B (n,γ), ^{10}B (n,α), BeO thermal scattering	

Table 6-1 Overview of Key Nominal Nuclear Data for the Selected Advanced Reactor Concepts (cont.)

Reactor type	Key nuclear data	Missing/discrepant/additional data, important data changes
Fast spectrum, metal and oxide fueled SFR	**Fuel:** $\bar{\nu}$ and fission of ^{238}U, ^{238}Pu, ^{239}Pu, ^{240}Pu, ^{241}Pu, ^{242}Pu, ^{241}Am, ^{242m}Am, ^{243}Am, ^{245}Cm; ^{238}U (n,γ), ^{238}U inelastic, ^{239}Pu (n,γ), ^{241}Am (n,γ), ^{243}Am (n,γ), ^{16}O elastic **Coolant:** ^{23}Na elastic, ^{23}Na inelastic **Structure/Reflector:** ^{52}Cr elastic; elastic and inelastic scattering, as well as (n,γ) of ^{56}Fe, ^{52}Cr, ^{52}Cr, ^{90}Zr, ^{91}Zr, ^{92}Zr, ^{94}Zr, ^{96}Zr	
All concepts	Fission yields, decay constants, branching ratios, energy release per fission, fission spectra, fission products (e.g., Xe, Sm, Gd), fission and capture of actinides that build up during depletion	

* Based on the availability of data, the findings in this report for this reactor type are focused on systems with fresh fuel. Additional relevant reactions are expected for systems including irradiated fuel.

Table 6-2   Overview of Key Nuclear Data Uncertainties for the Selected Advanced Reactor Concepts

Reactor type	Key nuclear data	Missing/discrepant/additional data, important data changes
Thermal spectrum, pebble-bed HTGR*	**Fuel:** ^{235}U $\bar{\nu}$, ^{235}U χ, ^{235}U fission, ^{235}U (n,γ), ^{238}U (n,γ), ^{28}Si (n,γ), ^{28}Si elastic **Moderator:** ^{12}C/graphite: (n,γ), elastic, inelastic, ^{10}B (n,α)	No thermal scattering data uncertainties for graphite
Thermal spectrum, FHR	**Fuel:** $\bar{\nu}$, fission, and (n,γ) of ^{235}U, ^{239}Pu, and ^{241}Pu, (n,γ) of ^{238}U and ^{240}Pu **Coolant:** ^{7}Li (n,γ), ^{7}Li elastic, ^{6}Li (n,t) ^{19}F (n,γ), ^{19}F elastic, ^{9}Be elastic **Moderator:** ^{12}C/graphite (n,γ) and elastic	No thermal scattering data uncertainties for graphite components
Thermal spectrum, graphite-moderated MSR*	**Fuel/coolant:** ^{235}U $\bar{\nu}$, ^{235}U fission, ^{235}U (n,γ), ^{238}U $\bar{\nu}$, ^{238}U fission, ^{238}U (n,γ), ^{238}U elastic, ^{19}F elastic, ^{19}F (n,γ), ^{7}Li (n,γ), ^{6}Li (n,γ), ^{6}Li (n,t) **Moderator:** ^{12}C/graphite (n,γ) and elastic **Structure:** Structure: ^{58}Ni elastic, ^{58}Ni inelastic, ^{58}Ni (n,γ), ^{58}Ni (n,p)	No thermal scattering data uncertainties for graphite or salt components
Fast spectrum, molten chloride MSR	**Fuel and coolant salt:** $\bar{\nu}$ and fission of ^{235}U, ^{238}U, ^{239}Pu, ^{240}Pu, ^{241}Pu, ^{238}U (n,γ), ^{238}U inel., ^{239}Pu (n,γ), ^{37}Cl inelastic, ^{37}Cl elastic, ^{23}Na inelastic, ^{23}Na elastic, ^{35}Cl (n,p), ^{35}Cl (n,γ) **Reflector:** ^{24}Mg elastic	Angular scattering distribution uncertainties: limited availability and usability; ^{238}U inelastic scattering uncertainty ENDF/B-VII.1 vs. VIII.0
Fast spectrum, oxide and metal fueled HPR*	**Fuel:** ^{235}U $\bar{\nu}$, ^{235}U fission, ^{235}U (n,γ), ^{238}U $\bar{\nu}$, ^{238}U fission, ^{238}U (n,2n), ^{16}O elastic; elastic and inelastic scattering, as well as (n,γ) of ^{238}U, ^{90}Zr, ^{91}Zr, ^{92}Zr, ^{94}Zr, ^{96}Zr **Coolant:** ^{23}Na elastic, ^{23}Na inelastic, ^{39}K capture, ^{39}K (n,p), ^{39}K elastic **Structure:** ^{56}Fe (n,γ), ^{56}Fe elastic, ^{56}Fe inelastic, ^{27}Al elastic, ^{9}Be elastic, ^{16}O elastic, ^{10}B (n,γ), ^{10}B (n,α)	Angular scattering distribution uncertainties: limited availability and usability No thermal scattering data uncertainties for BeO; ^{235}U (n,γ) uncertainty ENDF/B-VII.1 vs. VIII.0

Table 6-2 Overview of Key Nuclear Data Uncertainties for the Selected Advanced Reactor Concepts (cont.)

Reactor type	Key nuclear data	Missing/discrepant/additional data, important data changes
Fast spectrum, metal and oxide fueled SFR	**Fuel:** $\bar{\nu}$ and fission of ^{238}U, ^{238}Pu, ^{239}Pu, ^{240}Pu, ^{241}Pu, ^{242}Pu, ^{241}Am, ^{242m}Am, ^{243}Am, ^{245}Cm; ^{238}U (n,γ), ^{238}U inelastic, ^{239}Pu (n,γ), ^{241}Am (n,γ), ^{243}Am (n,γ), ^{16}O elastic **Coolant:** ^{23}Na elastic, ^{23}Na inelastic **Structure/Reflector:** ^{52}Cr elastic; elastic and inelastic scattering as well as (n,γ) of ^{56}Fe, ^{52}Cr, ^{90}Zr, ^{91}Zr, ^{92}Zr, ^{94}Zr, ^{96}Zr	Angular scattering distribution uncertainties: limited availability and usability ^{238}U inelastic scattering uncertainty between ENDF/B releases
All concepts	Fission yields, decay constants, branching ratios, energy release per fission, fission spectra, fission products (e.g., Xe, Sm, Gd), fission and capture of actinides that build up during depletion	Missing correlations between $\bar{\nu}$, fission and χ; ^{235}U/^{239}Pu $\bar{\nu}$ and fission uncertainty ENDF/B-VII.1 vs. VIII.0 Missing $\bar{\nu}$ uncertainty for ^{242}Am, ^{244}Am, ^{244m}Am, ^{243}Pu, ^{237}U, ^{239}U, ^{240}U, ^{241}U

* Based on the availability of data, the findings in this report for this reactor type are focused on systems with fresh fuel. Additional relevant reactions are expected for systems including irradiated fuel.

7   REFERENCES

(Aliberti et al., 2007.) Aliberti, G., Kodeli, I., Palmiotti, G., & Salvatores, M. (2007). *Fission spectrum related uncertainties*. (Technical Report INL/COV-07-13354), Idaho National Laboratory, Idaho Falls, ID.

(Andreades et al., 2014) Andreades, C., Cisneros, A. T., Choi, J. K., Chong, A. Y. K., Fratoni, M., Hong, S., Huddar, L. R., Huff, K. D., Krumwiede, D. L., Laufer, M. R., Munk, M., Scarlat, R. O., Sweibaum, N., Greenspan, E., & Peterson, P. F. (2014). *Technical description of the "Mark 1" Pebble-Bed Fluoride-Salt-Cooled High-Temperature Reactor (PB-FHR) power plant.* (Technical Report UCBTH-14-002). University of California, Berkeley, CA.

(Aures et al., 2017a) Aures, A., Bostelmann, F., Hursin, M., & Leray, O. (2017a). Benchmarking and application of the state-of-the-art uncertainty analysis methods XSUSA and SHARK-X. *Annals of Nuclear Energy, 101,* 262–269.

(Aures et al., 2017b) Aures, A., Bostelmann, F., Kodeli, I., Velkov, K., & Zwermann, W. (2017b). Uncertainty in the delayed neutron fraction in fuel assembly depletion calculations. *EPJ Web of Conferences, International Conference on Nuclear Data for Science and Technology (ND2016), Bruges, Belgium, September 11–16, 2016, volume 146, page 02052.*

(Bailey, 2020) Bailey, T. (2020). Impact of unrealistic or missing cross section covariances. *Workshop for Applied Nuclear Data Activities (WANDA),* Washington DC, March 3–5.

(Batchelder et al., 2019) Batchelder, J. C., Chong, S. A., Morrell, J., Unzueta, M. A., Adams, P., Bauer, J. D., Bailey, T., Becker, T. A., Bernstein, L. A., Fratoni, M., Hurst, A. M., James, J., Lewis, A. M., Matthews, E. F., Negus, M., Rutte, D., Song, K., Van Bibber, K., Wallace, M., and Waltz, C. S. (2019). Possible evidence of nonstatistical properties in the ^{35}Cl (n, p) ^{35}S cross section. *Physical Review C*, 99:044612.

(Bernstein et al., 2019) Bernstein, L. A., Brown, D. A., Koning, A. J., Rearden, B. T., Romano, C. E., Sonzogni, A. A., Voyles, A. S., & Younes, W. (2019). Our future nuclear data needs. *Annual Review of Nuclear and Particle Science, 69*.

(Betzler et al., 2017a) Betzler, B. R., Powers, J. J., Peterson-Droogh, J. L., & Worrall, A. (2017a). Fuel cycle analysis of thermal and fast spectrum molten salt reactors. *GLOBAL International Fuel Cycle Conference, Seoul, Korea, September 24–29.*

(Betzler et al., 2017b) Betzler, B. R., Powers, J. J., & Worrall, A. (2017b). Molten salt reactor neutronics and fuel cycle modeling and simulation with SCALE. *Annals of Nuclear Energy, 101,* 489–503.

(Bostelmann, 2020) Bostelmann, F. (2020). *Systematic sensitivity and uncertainty analysis of sodium-cooled fast reactor systems*. [PhD thesis, École polytechnique fédérale de Lausanne, Switzerland].

(Bostelmann et al., 2020) Bostelmann, F., Celik, C., Williams, M. L., Ellis, R. J., Ilas, G., & Wieselquist, W. A. (2020). SCALE capabilities for high temperature gas-cooled reactor analysis. *Annals of Nuclear Energy, 147,* 107673.

(Bostelmann et al., 2019a) Bostelmann, F., Holcomb, A. M., Clarity, J. B., Marshall, W. J., Sobes, V., and Rearden, B. T. (2019a). *Nuclear data performance assessment for advanced reactors.* (Technical Report ORNL/TM-2018/1033), Oak Ridge National Laboratory, Oak Ridge, TN.

(Bostelmann et al., 2019b) Bostelmann, F., Holcomb, A. M., Marshall, W. J., Sobes, V., and Rearden, B. T. (2019b). Impact of the ENDF/B-VIII.0 Library on Advanced Reactor Simulations. *Transactions of the American Nuclear Society*, Vol. 121, Washington, DC, November 17–21.

(Bostelmann et al., 2021) Bostelmann, F., Skutnik, S. E., Walker, E., Ilas, G., and Wieselquist, W. A. (2021). Modeling of the Molten Salt Reactor Experiment with SCALE. *Nuclear Technology*, submitted.

(Bostelmann and Strydom, 2017) Bostelmann, F. and Strydom, G. (2017). Nuclear data uncertainty and sensitivity analysis of the VHTRC benchmark using SCALE. *Annals of Nuclear Energy*, 110, 317–329.

(Bostelmann et al., 2018) Bostelmann, F., Williams, M. L., Celik, C., Ellis, R. J., Ilas, G., Rearden, B. T., and Carlo, C.-e. M. (2018). Assessment of SCALE capabilities for high temperature reactor modeling and simulation. *Transactions of the American Nuclear Society*, 119, Orlando, Florida, November 11–15.

(Broadhead et al., 2004) Broadhead, B. L. (2004). Sensitivity- and uncertainty-based criticality safety validation techniques. *Nuclear Science and Engineering*, *146*(3), 340–366.

(Brown et al., 2018) Brown, D., Chadwick, M., Capote, R., Kahler, A., Trkov, A., Herman, M., Sonzogni, A., Danon, Y., Carlson, A., Dunn, M., Smith, D., Hale, G., Arbanas, G., Arcilla, R., Bates, C., Beck, B., Becker, B., Brown, F., Casperson, . . . & Zhu, Y. (2018). ENDF/B-VIII.0: The 8th major release of the nuclear reaction data library with CIELO-project cross sections, new standards and thermal scattering data. *Nuclear Data Sheets*, *148,* 1–142.

(Buiron et al., 2019) Buiron, L., Rimpault, G., Sciora, P., Stauff, N., Kim, T. K., Taiwo, T., Bostelmann, F., Pautz, A., Ivanov, K., Trivedi, I., Kereszturi, A., Aures, A., Velkov, K., Zwermann, W., & Mikityuk, K. (2019*). Benchmark for uncertainty analysis in modeling (UAM) for design, operation and safety analysis of SFRs, core definitions, version 1.6*., OECD/NEA.

(Campbell et al., 2016) Campbell, A. A., Katoh, Y., Snead, M. A., & Takizawa, K. (2016). Property changes of G347A graphite due to neutron irradiation. *Carbon*, *109,* 860–873.

(Chadwick et al., 2011) Chadwick, M., Herman, M., Obložinský, P., Dunn, M., Danon, Y., Kahler, A., Smith, D., Pritychenko, B., Arbanas, G., Arcilla, R., Brewer, R., Brown, D., Capote, R., Carlson, A., Cho, Y., Derrien, H., Guber, K., Hale, G., Hoblit, . . . Young, P. (2011). ENDF/B-VII.1 nuclear data for science and technology: cross sections, covariances, fission product yields and decay data. *Nuclear Data Sheets, 112*(12), 2887–2996.

(Chadwick et al., 2006) Chadwick, M., Obložinský, P., Herman, M., Greene, N., McKnight, R., Smith, D., Young, P., MacFarlane, R., Hale, G., Frankle, S., Kahler, A., Kawano, T., Little, R., Madland, D., Moller, P., Mosteller, R., Page, P., Talou, P., Trellue, H.,. . . Van Der Marck, S. (2006). ENDF/B-VII.0: Next generation evaluated nuclear data library for nuclear science and technology. *Nuclear Data Sheets, 107*(12), 2931–3060.

(Cheng et al., 2020a) Cheng, Y., Hao, C., & Li, F. (2020a). Uncertainty quantification of fuel pebble model and its effect on the uncertainty propagation of nuclear data in pebble bed HTR. *Annals of Nuclear Energy, 139*.

(Cheng et al., 2020b) Cheng, Y., Hao, C., & Li, F. (2020b). Uncertainty quantification of fuel pebble model and its effect on the uncertainty propagation of nuclear data in pebble bed HTR. *Annals of Nuclear Energy, 139*.

(Choe et al., 2018) Choe, J., Ivanova, M., LeBlanc, D., Mohaptra, S., & Robinson, R. (2018). Fuel cycle flexibility of terrestrial energy's integral molten salt reactor (IMSR R). *38th Annual CNS Conference and 42nd CNS/CNA Student Conference, June 3–6.*

(Choi and Ha, 2016) Choi, C. and Ha, K. S. (2016). Assessment calculation of MARS-LMR using EBR-II SHRT-45R. *Nuclear Engineering and Design, 307,* 10–29.

(Cisneros, 2013) Cisneros, A. T. (2013). *Pebble bed reactors design optimization methods and their application to the Pebble Bed Fluoride Salt Cooled High Temperature Reactor (PB-FHR).* [PhD thesis, University of California, Berkeley].

(Cisneros, 2021) Cisneros, T. (2021). Molten Chloride reactor experiment nuclear data uncertainty analysis and needs The MCFR roadmap includes non-nuclear and nuclear. I*Workshop for Applied Nuclear Data Activities* (WANDA), Washington, DC, January 25 – Februrary 3.

(Clark et al., 2020) Clark, A., Beeny, B. A., Wagner, K. C., & Luxat, D. L. (2020). *Technical and licensing considerations for micro-reactors.* (Technical Report SAND2020-4609). Sandia National Laboratories, Albuquerque, NM.

(CSEWG, 2018) CSEWG (2018). *Minutes of the 2018 Cross Section Evaluation Working Group Annual Meeting.* (Technical Report BNL-209790-2018-INRE). Brookhaven National Laboratory, Upton, NY.

(CSEWG, 2019) CSEWG (2019). *2019 CSEWG meeting minutes.* (Technical Report BNL-213606-2020-INRE), Brookhaven National Laboratory, Upton, NY.

(Eades et al., 2016) Eades, M. J., Chaleff, E. S., Venneri, P. F., & Blue, T. E. (2016). The influence of Xe-135m on steady-state xenon worth in thermal molten salt reactors. *Progress in Nuclear Energy*, *93,* 397–405.

(Fast Reactor Working Group, 2018) Fast Reactor Working Group (2018). *Nuclear metal fuel: Characteristics, design, manufacturing, testing, and operating history.* (Technical Report White Paper 18-01).

(Fratoni, 2019) Fratoni, M. (2019). Impact of nuclear data on the design of fluoride cooled reactors. In *Workshop for Applied Nuclear Data Activities, Washington D.C., January 22–24.*

(Fratoni et al., 2020) Fratoni, M., Shen, D., Ilas, G., & Powers, J. (2020). *Molten Salt Reactor Experiment benchmark evaluation.* (Technical Report DOE-UCB-8542, 16-10240). University of California, Berkeley, CA.

(Fujimoto et al., 2021) Fujimoto, N., Tada, K., Quan Ho, H., Hamamoto, S., Nagasumi, S., & Ishitsuka, E. (2021). Nuclear data processing code FRENDY: A verification with HTTR criticality benchmark experiments. *Annals of Nuclear Energy, 158,* 108270.

(Glaeser et al., 2012) Glaeser, H., Graf, U., Herb, J., Krzykacz-Hausmann, B. Lerchl, G., Papadimitriou, P., Papukchiev, A., Ringer, F., Scheuerer, M., Schöffel, P., Skorek, T., von der Cron, D., & Weyermann, F. (2012). *Thermal-hydraulic calculation methods for transients and accidents of the reactor cooling system under special consideration of multi-dimensional flows (ATHLET, FLUBOX, CFX).* (Technical report, GRS-A-3644) Gesellschaft für Anlagen- und Reaktorsicherheit, Garching, Germany.

(Hao et al., 2018) Hao, C., Chen, Y., Guo, J., Wang, L., & Li, F. (2018). Mechanism analysis of the contribution of nuclear data to the k_{eff} uncertainty in the Pebble Bed HTR. *Annals of Nuclear Energy*, *120,* 857–868.

(Hawari and Gillete, 2014) Hawari, A. I. & Gillete, V. H. (2014). Inelastic thermal neutron scattering cross sections for reactor-grade graphite. *Nuclear Data Sheets, 118*(1), 176–178.

(Hill and Jeong, 2017) Hill, I. & Jeong, S. (2017). Status and analysis of P1 angular scattering sensitivity data available with the database for ICSBEP (DICE). *M&C 2017, Jeju, Korea, April 16–20.*

(Holcomb et al., 2011) Holcomb, D. E., Flanagan, G. F., Patton, B. W., Gehin, J. C., Howard, R. L., & Harrison, T. J. (2011). *Fast spectrum molten salt reactor options.* (Technical Report ORNL/TM-2011/105), Oak Ridge National Laboratory, Oak Ridge, TN.

(Hu et al., 2019) Hu, G., Hu, R., Kelly, J., & Ortensi, J. (2019). *Multi-physics simulations of heat pipe micro reactor.* (Technical Report ANL-NSE-19/25), Argonne National Laboratory, Argonne, IL.

(IAEA, 2013) IAEA (2013). *Evaluation of high temperature gas cooled reactor performance: Benchmark analysis related to the PBMR-400, PBMM, GT-MHR, HTR-10 and the ASTRA Critical Facility.* (Technical Report IAEA-TECDOC-1694). IAEA.

(Ilas et al., 2012) Ilas, G., Ilas, D., Kelly, R. P., & Sunny, E. E. (2012). *Validation of SCALE for high temperature gas-cooled reactor analysis.* (Technical Report NUREG/CR-7107, ORNL/TM-2011/161). Oak Ridge National Laboratory, Oak Ridge, TN.

(Kiedrowski et al, 2011) Kiedrowski, B. C., Brown, F. B., & Wilson, P. P. (2011). Adjoint-weighted tallies for k-eigenvalue calculations with continuous-energy Monte Carlo. *Nuclear Science and Engineering*, *168*(3), 226–241.

(Kim et al., 2019) Kim, K. S., Williams, M. L., Holcomb, A. M., Wiarda, D., Jeon, B. K., and Yang, W. S. (2019). The SCALE/AMPX multigroup cross section processing for fast reactor analysis. *Annals of Nuclear Energy*, 132, 161–171.

(Kim et al., 2009) Kim, T., Yang, W., Grandy, C., & Hill, R. (2009). Core design studies for a 1000MWth Advanced Burner Reactor. *Annals of Nuclear Energy, 36,* 331–336.

(Kodeli, 2013) Kodeli, I. A. (2013). Sensitivity and uncertainty in the effective delayed neutron fraction (β_{eff}). *Nuclear Instruments and Methods in Physics Research A*, *715,* 70–78.

(Latta et al., 2019) Latta, R., Blaise, C., Hackett, M., Brown, N., Hunn, J., Petrie, C., Gerczak, T., & Helmreich, G. (2019). High Power Irradiation Testing of TRISO Particles in Miniature Fuel Specimens in HFIR. *Transactions of the American Nuclear Society, 121, Washington, DC, November 17–21.*

(Lee et al., 2019) Lee, C., Jung, Y. S., & Cho, H. K. (2019). *Micro reactor simulation using the PROTEUS suite in FY19.* (Technical Report ANL/NSE-19/33). Argonne National Laboratory, Argonne, IL.

(Leppänen, 2007) Leppänen, J. (2007). *Development of a New Monte Carlo reactor physics code.* [PhD thesis, Helsinki University of Technology, Finland].

(Leray et al., 2017) Leray, O., Fiorito, L., Rochman, D., Ferroukhi, H., Stankovskiy, A., & Van den Eynde, G. (2017). Uncertainty propagation of fission product yields to nuclide composition and decay heat for a PWR UO_2 fuel assembly. *Progress in Nuclear Energy, 101,* 486–495.

(Little et al., 2008) Little, R., Kawano, T., Hale, G., Pigni, M., Herman, M., Obložinský, P., Williams, M., Dunn, M., Arbanas, G., Wiarda, D., McKnight, R., McKamy, J., & Felty, J. (2008). Low-fidelity Covariance Project. *Nuclear Data Sheets*, *109*(12), 2828–2833.

(Lum et al., 2018) Lum, E. S., Pope, C. L., Stewart, R., Byambadorj, B., & Beaulieu, Q. (2018). *Evaluation of Run 138B at Experimental Breeder Reactor II, a prototypic liquid metal reactor.* (Technical Report EBR2-LMFR-RESR-001, CRIT, NEA/NSC/DOC[2006]1). Organisation for Economic Co-operation and Development/Nuclear Energy Agency.

(Maioli et al., 2019) Maioli, A. A., Detar, H. L., Haessler, R. L., Friedman, B. N., Belovesick, C. A., Scobel, J. H., Kinnas, S. T., Smith, M. C., Wyk, J. V., & Fleming, K. (2019). *Modernization of Technical Requirements for Licensing of Advanced Non-Light Water Reactors: Westinghouse eVinci^{TM} Micro-Reactor Licensing Modernization Project Demonstration*. (Technical Report SC-29980-202). Southern Company.

(Martinez et al., 2014) Martinez, J. S., Zwermann, W., Gallner, L., Puente-Espel, F., Cabellos, O., Velkov, K., & Hannstein, V. (2014). Propagation of neutron cross section, fission yield, and decay data uncertainties in depletion calculations. *Nuclear Data Sheets,118*, 480–483.

(Matthews et al., 2019) Matthews, C., Laboure, V., Ortensi, J., DeHart, M., Wang, Y., & Martineau, R. C. (2019). *Evaluation of the MOOSE tool-set for analysis of thermo-mechanical-neutronics coupling in micro-reactors.* (Technical Report LA-UR-19-31443). Los Alamos National Laboratory, Los Alamos, NM.

(Mausollf et al., 2021) Mausolff, Z., DeHart, M., and Goluoglu, S. (2021). Design and assessment of a molten chloride fast reactor. *Nuclear Engineering and Design*, 379, 111181.

(Mcclure et al., 2015) Mcclure, P. R., Poston, Irvin, D., Dasari, V. R., & Reid, R. S. (2015). *Design of megawatt power level heat pipe reactors.* (Technical Report LA-UR-15-28840). Los Alamos National Laboratory, Los Alamos, NM.

(Mei et al., 2013) Mei, L., Cai, X., Jiang, D., Chen, J., Zhu, Y., Liu, Y., & Wang, X. (2013). The investigation of thermal neutron scattering data for molten salt FLiBe. *Journal of Nuclear Science and Technology, 50*(7), 682– 688.

(Mulder and Boyes, 2020) Mulder, E. J. & Boyes, W. A. (2020). Neutronics characteristics of a 165 MW$_{th}$ Xe-100 reactor. *Nuclear Engineering and Design*, 357.

(NEA, 2015) . *International handbook of evaluated reactor physics benchmark experiments*. (Technical Report NEA-1765/11). OECD/NEA, Nuclear Energy Agency.

(NEA, 2016) . *Benchmark for neutronic analysis of sodium-cooled fast reactor cores with various fuel types and core sizes.* (Technical Report NEA/NSC/R[2015]9). OECD/NEA.

(Neudecker, 2020) Neudecker, D. (2020). Building a long-range AI / ML vision. *Workshop for Applied Nuclear Data Activities (WANDA)*, Washington DC, March 3–5.

(Otuka et al., 2014) Otuka, N., Dupont, E., Semkova, V., Pritychenko, B., Blokhin, A. I., Aikawa, M., Babykina, S., Bossant, M., Chen, G., Dunaeva, S., Forrest, R. A., Fukahori, T., Furutachi, N., Ganesan, S., Ge, Z., Gritzay, O. O., Herman, M., Hlavač, S., Kato, K., & Zhuang, Y. (2014). Towards a more complete and accurate experimental nuclear reaction data library (EXFOR): International collaboration between nuclear reaction data centres (NRDC). *Nuclear Data Sheets*, *120, 272*–276.

(Pandya et al., 2016) Pandya, T. M., Johnson, S. R., Evans, T. M., Davidson, G., Hamilton, S., & Godfrey, A. (2016). Implementation, capabilities, and benchmarking of shift, a massively parallel Monte Carlo radiation transport code. *Journal of Computational Physics, 308,* 239–272.

(Perfetti et al., 2016) Perfetti, C. M., Rearden, B. T., & Martin, W. R. (2016). SCALE Continuous-energy eigenvalue sensitivity coefficient calculations. *Nuclear Science and Engineering*, *182*(3), 332–353.

(Pigni et al., 2015) Pigni, M. T., Francis, M. W., & Gauld, I. C. (2015). Investigation of inconsistent ENDF/B-VII.1 independent and cumulative fission product yields with proposed revisions. *Nuclear Data Sheets, 123,* 231–236.

(Powers et al., 2018) Powers, J. J., Brown, N. R., Mueller, D. E., Patton, B. W., Losa, E., & Košťál, M. (2018). Sensitivity/uncertainty analyses comparing LR-0 reactor experiments containing FLiBe salt with models for molten-salt-cooled and molten-salt-fueled reactors. *Annals of Nuclear Energy, 120,* 319–332.

(Qualls et al., 2017) Qualls, A. L., Betzler, B. R., Brown, N. R., Carbajo, J. J., Greenwood, M. S., Hale, R., Harrison, T. J., Powers, J. J., Robb, K. R., Terrell, J., Wysocki, A. J., Gehin, J. C., & Worrall, A. (2017). Preconceptual design of a fluoride high temperature salt-cooled engineering demonstration reactor: Motivation and overview. *Annals of Nuclear Energy, 107,* 144–155.

(Radaideh et al., 2019) Radaideh, M. I., Wieselquist, W. A., & Kozlowski, T. (2019). A new framework for sampling-based uncertainty quantification of the six-group reactor kinetic parameters. *Annals of Nuclear Energy*, *127,* 1–11.

(Rearden et al., 2011) Rearden, B. T., Williams, M. L., Jessee, M. A., Mueller, D. E., & Wiarda, D. A. (2011). Sensitivity and uncertainty analysis capabilities and data in SCALE. *Nuclear Technology*, *174*(2), 236–288.

(Rochman et al., 2017) Rochman, D., Leray, O., Hursin, M., Ferroukhi, H., Vasiliev, A., Aures, A., Bostelmann, F., Zwermann, W., Cabellos, O., Diez, C., Dyrda, J., Garcia-Herranz, N., Castro, E., van der Marck, S., Sjöstrand, H., Hernandez, A., Fleming, M., Sublet, J.-C., & Fiorito, L. (2017). Nuclear data uncertainties for typical LWR fuel assemblies and a simple reactor core. *Nuclear Data Sheets*, *139,* 1–76.

(Salvatores, 2002) Salvatores, M. (2002). Future nuclear power systems and nuclear data needs. *Journal of Nuclear Science and Technology*, *39*, (2), 4–12.

(Salvatores and Jacqmin, 2008) Salvatores, M. & Jacqmin, R. (2008). *Uncertainty and target accuracy assessment for innovative systems using recent covariance data evaluations.* (Technical Report NEA/WPEC-26). OECD/NEA.

(Salvatores et al., 2013) Salvatores, M., Palmiotti, G., & McKnight, R. D. (2013). *Methods and issues for the combined use of integral experiments and covariance data.* (Technical Report NEA/WPEC-33). OECD/NEA.

(Shen et al., 2018) Shen, D., Fratoni, M., Aufiero, M., Bidaud, A., Powers, J., & Ilas, G. (2018). Zero-power criticality benchmark evaluation of the Molten Salt Reactor Experiment. *PHYSOR 2018, Cancun, Mexico, April 22–26, 4012–4024.*

(Shen et al., 2019) Shen, D., Fratoni, M., Ilas, G., & Powers, J. J. (2019). *Molten-Salt Reactor Experiment (MSRE) zero-power first critical experiment with U-235.* (Technical Report MSRE-MSR-EXP-001, NEA/NSC/DOC[2006]1), Rev. 0, OECD/NEA.

(Shen et al., 2021) Shen, D., Ilas, G., Powers, J. J., & Fratoni, M. (2021). Reactor physics benchmark of the first criticality in the Molten Salt Reactor Experiment. *Nuclear Science and Engineering*, submitted.

(Shi et al., 2018) Shi, J., Aufiero, M., and Fratoni, M. (2018). Sensitivity and uncertainty analysis of the pebble-bed fluoride-salt-cooled high-temperature reactor (PB-FHR). PHYSOR 2018, Cancun, Mexico, April 22–26.

(Shibata et al., 2012) Shibata, K., Iwamoto, O., Nakagawa, T., Iwamoto, N., Ichihara, A., Kunieda, S., Chiba, S., Furutaka, K., Otuka, N., Ohsawa, T., Murata, T., Matsunobu, H., Zukeran, A., Kamada, S., & Katakura, J.-i. (2012). JENDL-4.0: A new library for nuclear science and engineering. *Journal of Nuclear Science and Technology*, *48*(1), 1–30.

(Sobes et al., 2019) Sobes, V., Marshall, W. B., Wiarda, D., Bostelmann, F., Holcomb, A. M., & Rearden, B. T. (2019). *ENDF/B-VIII.0 covariance data development and testing for advanced reactors.* (Technical Report ORNL/TM-2018/1037). Oak Ridge National Laboratory, Oak Ridge, TN.

(Stauff et al., 2017) Stauff, N. E., Kim, T. K., Taiwo, T. A., Buiron, L., Rimpault, G., Lee, Y. K., Batki, B., Keresztúri, A., Bostelmann, F., Zwermann, W., Fridman, E., Guilliard, N., Lopez, R., Gomez, A., Puente-Espel, F., del Valle, E., Peregudov, A., Semenov, M., Nakahara, Y., Ivanova, T., & Gulliford, J. (2017). Evaluation of the OECD/NEA/SFR-UAM neutronics reactivity feedback and uncertainty benchmarks. *FR17, Yekaterinburg, Russian Federation*, June 26–29, IAEA–CN245–149.

(Sterbentz et al., 2018) Sterbentz, J. W., Werner, J. E., Hummel, A. J., Kennedy, J. C., Brien, R. C. O., Dion, A. M., Wright, R. N., & Ananth, K. P. (2018). *Preliminary assessment of two alternative core design concepts for the special purpose reactor.* (Technical Report INL/EXT-17-43212, Rev. 1). Idaho National Laboratory, Idaho Falls, ID.

(Sublet et al., 2003) Sublet, J.-C., Koning, A. J., Forrest, R. A., & Kopecky, J. (2003). *The JEFF-3.0/A neutron activation file – EAF-2003 into ENDF-6 format.* (Technical Report JEFDOC-982). CEA, France.

(Sunny and Ilas, 2010) Sunny, E. E. & Ilas, G. (2010). SCALE 6 analysis of HTR-10 Pebble-Bed Reactor for initial critical configuration. *PHYSOR 2010*, Pittsburgh, Pennsylvania, USA, May 9–14, 2010.

(Takahashi et al., 1999) Takahashi, R., Toyahara, M., Maruki, S., Ueda, H., and Yamamoto, T. (1999). Investigation of Morphology and Impurity of Nuclear Grade Graphite, and Leaching Mechanism of Carbon-14. In IAEA Technical committee meeting on nuclear graphite waste management, Manchester, United Kingdom, October 18–20.

(Terrapower, 2021) Terrapower (2021). MCFR Project https://www.terrapower.com/resources/#group_1058-5

(Terry et al., 2007) Terry, W. K., Montierth, L. M., Kim, S. S., Cogliati, J. J., & Ougouag, A. M. (2007). Evaluation of the initial critical configuration of the HTR-10 pebble-bed reactor. (Technical Report HTR10-GCR-RESR-001, NEA/NSC/DOC[2006]1, Rev. 0). OECD/NEA.

(DOE, 2002) US DOE Nuclear Energy Research Advisory Committee & the Generation IV International Forum (2002). *A technology roadmap for Generation IV nuclear energy systems* (Technical Report GIF-002-00).

(van Rooijen et al., 2015) van Rooijen, W., Shimazu, Y., & Yamano, N. (2015). Criticality uncertainty dependence on nuclear data library in fast molten salt reactors. *Energy Procedia*, *71,* 3–13.

(Wiarda et al., 2016) Wiarda, D., Dunn, M. E., Greene, N. M., Celik, C., & Petrie, L. M. (2016). *AMPX-6: A modular code system for processing ENDF/B.* (Technical Report ORNL/TM-2016/43). Oak Ridge National Laboratory, Oak Ridge, TN.

(Wiarda et al., 2018) Wiarda, D., Marshall, W. J., Sobes, V., Bostelmann, F., Holcomb, A., & Rearden, B. T. (2018). ENDF/B-VIII.0 covariance testing at Oak Ridge National Laboratory. In *CSEWG meeting 2018, Brookhaven National Laboratory, November 5–7*.

(Wieselquist et al., 2020) Wieselquist, W. A., Lefebvre, R. A., & Jessee, M. A. (2020). *SCALE Code System, Version 6.2.4.* (Technical Report ORNL/TM-2005/39). Oak Ridge National Laboratory, Oak Ridge, TN. https://www.ornl.gov/content/scale-v624

(Williams et al., 2017) Williams, M., Wiarda, D., & Marshall, B. J. (2017). Consistency between ENDF/B cross sections and covariances variation in C/E values is much less than predicted by ENDF/B covariances. In *CSEWG Meeting, Brookhaven National Laboratory,* October 31 – November 9.

(Williams et al., 1986) Williams, M. L. (1986). Perturbation theory for nuclear reactor analysis. Ronen, Y., ed., *Handbook of Nuclear Reactors Calculations, III*, 63–188. CRC Press.

(Williams et al., 2007) Williams, M. L. (2007). Sensitivity and uncertainty analysis for eigenvalue-difference responses. *Nuclear Science and Engineering*, *155*:18–36.

(Williams et al., 2001) Williams, M. L., Broadhead, B. L., & Parks, C. V. (2001). Eigenvalue Sensitivity Theory for Resonance-Shielded Cross Sections. *Nuclear Science and Engineering, 138,* 177–191.

(Williams et al., 2013) Williams, M. L., Ilas, G., Jessee, M. a., Rearden, B. T., Wiarda, D., Zwermann, W., Gallner, L., Klein, M., Krzykacz-Hausmann, B., & Pautz, A. (2013). A statistical sampling method for uncertainty analysis with SCALE and XSUSA. *Nuclear Technology*, *183,* 515–526.

(X-energy, 2021) X-energy (2021). Reactor: Xe-100. https://x-energy.com/reactors/xe-100

(Yan et al., 2020) Yan, B. H., Wang, C., & Li, L. G. (2020). The technology of micro heat pipe cooled reactor: A review. *Annals of Nuclear Energy*, 135:106948.

(Yang, 2012) Yang, W. S. (2012). Fast reactor physics and computational methods. *Nuclear Engineering and Technology*, *44*(2):177–198.

(Zhang et al., 2020) Zhang, L., She, D., & Shi, L. (2020). Influence of graphitization degree of nuclear graphite on HTGR reactor physics calculation. *Annals of Nuclear Energy*, *143:*107458.

(Zhang et al., 2006) Zhang, Z., Wu, Z., Sun, Y., & Li, F. (2006). Design aspects of the Chinese modular high-temperature gas-cooled reactor HTR-PM. In *Nuclear Engineering and Design*, *236*, 485–490. North-Holland.

(Zhu and Hawari, 2017) Zhu, Y. & Hawari, A. I. (2017). Thermal neutron scattering cross section of liquid FLiBe. *Progress in Nuclear Energy*, *101,* 468–475.

APPENDIX A

A.1 HTR-10

This section provides tables listing the contributions to the individual investigated output uncertainties obtained with TSUNAMI corresponding to the images provided in Section 5.1. While the contributors listed for k_{eff} are the top contributors to the k_{eff} uncertainty, this is not necessarily the case for the reactivity differences. Contributions from nonconverged sensitivities were excluded from these tables.

Table A-1   HTR-10: Top Contributions to the k$_{eff}$ Uncertainty[1]

Nuclide	Reaction	ENDF/B-VII.0	ENDF/B-VII.1	ENDF/B-VIII.0	$\frac{VII.1}{VII.0} - 1$	$\frac{VIII.0}{VII.1} - 1$
Graphite	el	0.360%	0.315%	0.403%	-12.4%	27.8%
U-235	$\bar{\nu}$	0.303%	0.380%	0.464%	25.4%	21.9%
Graphite	n,γ	0.228%	0.253%	0.249%	11.4%	-1.8%
U-235	n,γ	0.173%	0.170%	0.033%	-1.3%	80.4%
U-235	χ	0.160%	0.265%.	0.041%	66.1%	-84.5%
U-235	fis/n,γ	0.131%	0.131%	0.000%	0.0%	0.0%
U-235	Fis	0.124%	0.125%	0.173%	1.0%	37.7%
Graphite	n,n$'$	0.092%	0.083%	0.039%	-10.6%	-52.5%
U-238	n,γ	0.059%	0.052%	0.042%	-11.0%	-20.3%
N-14	n,p	0.018%	0.018%	0.018%	-1.8%	-0.9%
B-10	n,α	0.012%	0.004%	0.040%	-64.1%	840.4%
U-238	el	0.016%	0.016%	0.014%	5.1%	-13.0%
U-238	el/n,γ	0.011%	0.011%	0.012%	6.2%	5.2%
Si-28	n,γ	0.011%	0.011%	0.009%	-17.8%	-0.7%

---

[1] Obtained using TSUNAMI in $\Delta k/k$

Table A-2 **HTR-10: Top Contributions to the Uncertainty of the Fuel Temperature Reactivity**

Nuclide	Reaction	ENDF/B-VII.0	ENDF/B-VII.1	ENDF/B-VIII.0	$\frac{VII.1}{VII.0}-1$	$\frac{VIII.0}{VII.1}-1$
U-238	n,γ	0.750%	0.546%	0.545%	-27.2%	-0.3%
U-238	el	0.449%	0.547%	0.340%	21.6%	-37.9%
Graphite	n,γ	0.383%	0.383%	0.325%	0.0%	-15.1%
U-235	$\bar{\nu}$	0.300%	0.378%	0.475%	26.2%	-25.6%
U-235	χ	0.294%	0.530%	0.160%	80.6%	-69.9%
Graphite	n,n$'$	0.240%	0.273%	0.108%	13.9%	-60.4%
O-16	el	0.155%	0.179%	0.029%	15.3%	-83.8%
U-235	fis	0.151%	0.149%	0.236%	-1.5%	58.4%
U-238	n,n$'$	0.037%	0.067%	0.077%	81.3%	14.3%
U-235	el	0.075%	0.077%	0.075%	3.1%	-2.7%
B-10	n,α	0.023%	0.008%	0.063%	-62.7%	649.2%

Table A-3 **HTR-10: TSUNAMI Top Contributions to the Uncertainty of the Pebble Graphite Density Reactivity**

Nuclide	Reaction	ENDF/B-VII.0	ENDF/B-VII.1	ENDF/B-VIII.0	$\frac{VII.1}{VII.0}-1$	$\frac{VIII.0}{VII.1}-1$
U-235	χ	0.367%	0.608%	0.101%	65.8	-83.4%
Graphite	n,γ	0.292%	0.292%	0.291%	0.0%	-0.4%
U-235	$\bar{\nu}$	0.290%	0.370%	0.456%	27.6%	23.4%
Graphite	n,n$'$	0.240%	0.224%	0.019%	-6.7%	-91.4%
U-235	fis	0.148%	0.148%	0.201%	0.0%	-75.5%
U-235	n,γ	0.147%	0.143%	0.035%	-3.0%	-78.4%
U-235	fis/n,γ	0.129%	0.129%	0.028%	-0.2%	-83.6%
U-238	n,γ	0.089%	0.077%	0.063%	-12.7%	-18.0%
U-238	el	0.083%	0.048%	0.049%	-41.6%	1.8%
O-16	el	0.028%	0.049%	0.004%	76.7%	-92.1%
B-10	n,α	0.042%	0.016%	0.144%	-62.7%	818.4%
Si-28	el	0.009%	0.015%	0.053%	75.6%	251.4%
U-238	n,p	0.041%	0.041%	0.041%	0.0%	-1.6%
U-14	el/ n,γ	0.000%	0.021%	0.033%	0.0%	55.4%

Table A-4 **HTR-10: Top Contributions to the Uncertainty of the Pebble Graphite Impurity Reactivity**

Nuclide	Reaction	ENDF/B-VII.0	ENDF/B-VII.1	ENDF/B-VIII.0	$\frac{VII.1}{VII.0}-1$	$\frac{VIII.0}{VII.1}-1$
U-235	X	0.346%	0.512%	0.075%	47.9%	-85.3%
U-235	fis	0.332%	0.332%	0.484%	-0.3%	46.1%
U-235	$\bar{\nu}$	0.299%	0.377%	0.460%	26.1%	22.2%
B-10	n,α	0.234%	0.087%	0.864%	-62.7%	893.3%
Graphite	n,n$'$	0.117%	0.092%	0.182%	-21.2%	98.2%
Graphite	n,γ	0.082%	0.082%	0.084%	0.0%	2.3%
U-235	el/fis	0.049%	0.047%	0.006%	-4.5%	-88.3%
U-238	n,γ	0.046%	0.038%	0.024%	-17.9%	-37.1%
U-238	el	0.046%	0.040%	0.078%	13.6%	95.8%
O-16	el	0.045%	0.097%	0.011%	115.7%	-88.5%
Si-28	el	0.024%	0.068%	0.102%	-187.6%	48.7%
U-235	fis/n,γ	0.030%	0.031%	0.043%	1.1%	41.7%
U-238	el/n,γ	0.021%	0.010%	0.041%	-53.2%	311.0%
U-235/fis	U-238/fis	0.000%	0.001%	0.025%	0.0%	3620.8%

Table A-5 **HTR-10: Top Contributions to the Uncertainty of the Pebble Graphite Temperature Reactivity**

Nuclide	Reaction	ENDF/B-VII.0	ENDF/B-VII.1	ENDF/B-VIII.0	$\frac{VII.1}{VII.0}-1$	$\frac{VIII.0}{VII.1}-1$
U-235	fis	0.467%	0.465%	0.746%	-0.5%	60.6%
U-235	$\bar{\nu}$	0.301%	0.377%	0.458%	25.5%	21.5%
U-235	n,γ	0.244%	0.245%	0.341%	0.2%	39.5%
Graphite	n,γ	0.221%	0.221%	0.193%	0.0%	-12.5%
U-235	X	0.141%	0.240%	0.059%	70.3%	-75.6%
Graphite	n,n$'$	0.138%	0.131%	0.100%	-4.8%	-23.9%
U-235	fis/ n,γ	0.128%	0.128%	0.000%	0.0%	0.0%
U-235	el/fis	0.054%	0.054%	0.029%	-0.4%	-46.0%
U-238	n,γ	0.054%	0.047%	0.032%	-12.7%	-31.8%
B-10	n,α	0.021%	0.008%	0.070%	-62.7%	808.7%
Si-28	el	0.009%	0.016%	0.035%	80.1%	126.8%
U-238	el	0.033%	0.039%	0.032%	18.9%	-17.6%
U-238	el/ n,γ	0.011%	0.009%	0.025%	-22.4%	186.9%

Table A-6 **HTR-10: Top Contributions to the Uncertainty of the Structural Graphite Density Reactivity**

Nuclide	Reaction	ENDF/B-VII.0	ENDF/B-VII.1	ENDF/B-VIII.0	$\frac{VII.1}{VII.0}-1$	$\frac{VIII.0}{VII.1}-1$
Graphite	n,γ	0.622%	0.622%	0.567%	-0.0%	-8.8%
U-235	$\bar{\nu}$	0.289%	0.370%	0.457%	27.8%	23.8%
Graphite	n,n′	0.260%	0.233%	0.185%	-10.6%	-20.5%
U-235	X	0.254%	0.430%	0.112%	69.4%	-73.9%
U-238	el	0.205%	0.138%	0.073%	-32.9%	-47.1%
U-235	fis	0.173%	0.174%	0.226%	0.1%	30.5%
U-238	el/n,n′	0.167%	0.150%	0.000%	-10.5%	0.0%
U-235	fis/n,γ	0.029%	0.129%	0.000%	-0.4%	0.0%
U-235	n,γ	0.022%	0.120%	0.032%	-1.8%	-73.5%
U-238	n,n′/el	0.167%	0.150%	0.000%	-10.5%	0.0%
Si-28	el	0.030%	0.116%	0.162%	282.3%	39.3%
U-238	n,γ	0.076%	0062.%	0.053%	-18.9%	-14.8%
U-238	n,n′	0.093%	0.097%	0.027%	4.6.%	-72.7%
U-235	el	0.056%	0.057%	0.026%	1.0.%	-53.7%
U-235/fis	U-238/fis	0.000%	0.004%	0.020%	0.0%	380.3%

Table A-7 **HTR-10: Top Contributions to the Uncertainty of the Structural Graphite Impurity Reactivity**

Nuclide	Reaction	ENDF/B-VII.0	ENDF/B-VII.1	ENDF/B-VIII.0	$\frac{VII.1}{VII.0}-1$	$\frac{VIII.0}{VII.1}-1$
Graphite	n,γ	0.650%	0.650%	0.660%	-0.0%	1.5%
U-235	χ	0.445%	0.743%	0.122%	66.9%	-83.5%
U-235	$\bar{\nu}$	0.294%	0.374%	0.458%	27.2%	22.4%
Graphite	n,n′	0.217%	0.194%	0.086%	-10.6%	-55.4%
U-235	fis	0.196%	0.196%	0.267%	-0.2%	36.1%
B-10	n,α	0.136%	0.051%	0.483%	-62.7%	850.3%
U-235	fis/n,γ	0.130%	0.129%	0.019%	-0.2%	-85.4%
U-235	n,γ	0.110%	0.107%	0.031%	-2.4%	-71.1%
U-238	n,γ	0.077%	0.064%	0.054%	-16.2%	-15.6%
N-14	n,p	0.029%	0.029%	0.030%	0.0%	3.2%
U-238	el/n,γ	0.009%	0.000%	0.029%	0.0%	0.0%
U-238	el	0.026%	0.033%	0.024%	28.1%	-27.8%
Si-28	el	0.005%	0.011%	0.019%	120.9%	75.1%

Table A-8   HTR-10: Top Contributions to the Uncertainty of the Structural Graphite Temperature Reactivity

Nuclide	Reaction	ENDF/B-VII.0	ENDF/B-VII.1	ENDF/B-VIII.0	$\frac{VII.1}{VII.0} - 1$	$\frac{VIII.0}{VII.1} - 1$
Graphite	n,γ	0.748%	0.748%	0.688%	0.0%	-8.1%
U-235	χ	0.381%	0.649%	0.153%	70.4%	-76.5%
U-235	$\bar{\nu}$	0.295%	0.373%	0.459%	26.2%	23.0%
Graphite	n,n$'$	0.290%	0.237%	0.045%	-18.2%	-80.9%
U-235	n,γ	0.188%	0.187%	0.119%	-0.5%	-36.5%
U-235	fis	0.161%	0.162%	0.261%	0.0%	61.0%
U-235	fis/n,γ	0.148%	0.149%	0.000%	0.3%	0.0%
U-238	el	0.146%	0.086%	0.072%	-40.6%	-17.0%
U-238	n,γ	0.063%	0.054%	0.043%	-14.2%	-20.4%
Si-28	el	0.020%	0.073%	0.101%	262.5%	38.4%
B-10	n,α	0.051%	0.019%	0.166%	-62.7%	771.7%
N-14	n,p	0.044%	0.044%	0.041%	-0.0%	-6.7%
U-235	el	0.027%	0.028%	0.021%	4.4%	-25.6%

A.2 __PB-FHR-MK1__

This section provides details on the generation of representative fuel compositions for the PB-FHR-Mk1 reactor, shows plots usually studied for each uncertainty analysis using Sampler, and provides tables listing the contributions to the output uncertainty obtained with TSUNAMI corresponding to the images provided in Section 5.2.

A.2.1 Generation of Representative Fuel Compositions

As described in Section 4.2, the annular core of the PB-FHR-Mk1 reactor is filled with 470,000 fuel pebbles which travel from the bottom of the core to the top. On average, a fuel pebble completes 8 passes through the core before reaching its final discharge burnup of 180 GWd/MTIHM. This means that at any time during the operation of this reactor, a mixture of pebbles at different burnups is included in each axial zone of the reactor.

To provide a representative model of the PB-FHR-Mk1 for the uncertainty and sensitivity analyses presented in this report, a model with an approximate fuel inventory corresponding to an equilibrium-state of a core with 10 axial regions of equal volume was developed. A flowchart of the iterative approach followed here is shown in Figure A-1.
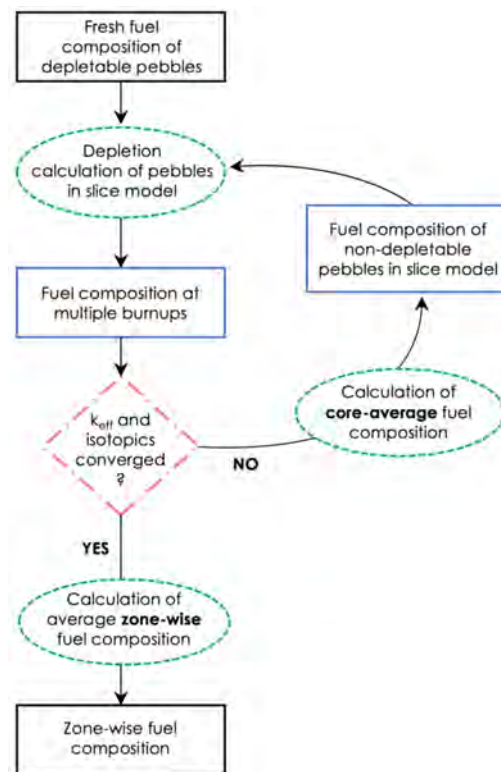
Figure A-1 PB-FHR-Mk1: Flowchart Showing the Process to Determine Fuel Compositions in the Individual Axial Fuel Zones

To obtain burnup-dependent fuel compositions, depletion calculations were performed using a 2D slice model of the reactor with reflective axial boundary conditions and vacuum radial boundary conditions (Figure A-2 and A-3). The axial height of this model was chosen in a way

that retains the correct packing fraction of the pebbles in the annular core. Only the fuel pebbles displayed in red in Figure A-2 were depleted in these calculations; the composition of all other fuel pebbles (lilac) was assumed not to change during depletion. The depletion calculations were performed using SCALE's TRITON sequence. The fuel pebbles were depleted for 540.54 days at a specific power of 333 MW/MTIHM to reach a burnup of 180 GWd/MTIHM.
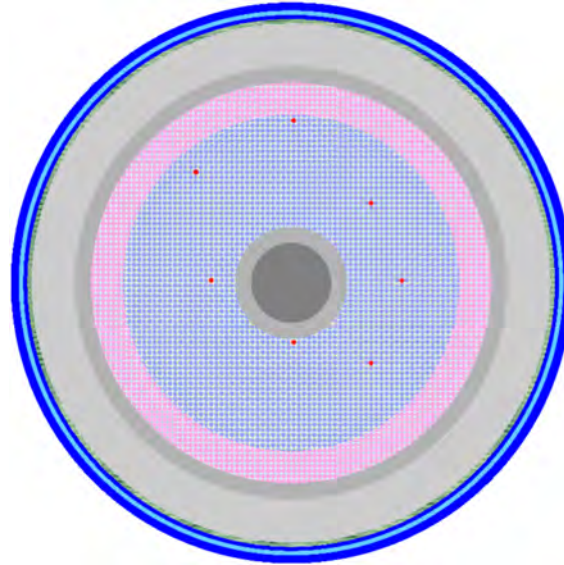
Figure A-2 PB-FHR-Mk1: Horizontal View of the Slice Model used for the Depletion Calculations[2]
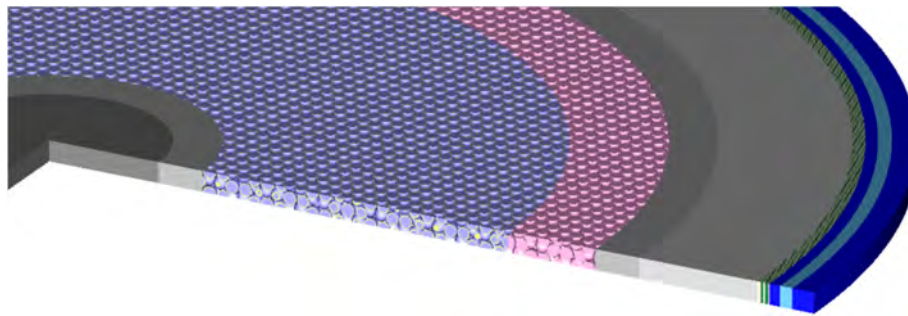
Figure A-3 PBR-FHR-Mk1: 3D View of the Slice Model Used for the Depletion Calculation

In the first iteration, fresh fuel was applied in both the depletable and the non-depletable fuel pebbles. After a depletion calculation under the conditions described above, a core-average fuel composition was determined by averaging the compositions of the depleted fuel pebble at different burnups as described in the next paragraph. For the second iteration, this core-average fuel composition was applied in all non-depletable fuel pebbles. The depletion calculation was then repeated, starting with fresh fuel in the depleted fuel pebbles, but with new spectral conditions due to the changed composition in the non-depletable pebbles. Based

---

[2] The non-depletable fuel pebbles are displayed in lilac, the depletable fuel pebbles in red, the dummy graphite pebbles in pink, the graphite structure in gray, the absorber pins in green, and the outer structure in blue.

on this depletion calculation, a new core-average fuel composition was determined for use in the following iteration. This process was repeated until k_{eff} and the densities of important nuclides reached convergence, meaning that they did no longer change significantly between one iteration and the next iteration. After convergence was reached, the fuel compositions at different burnups from the last iteration were used to calculate average fuel compositions for each zone in the core. Table A-9 shows that convergence was reached after 10 iterations, with k_{eff} changes below 100 pcm and nuclide density changes of relevant nuclides such as [235]U, [239]Pu and relevant fission products below 0.6%.

The average fuel composition in each of the 10 axial zone was calculated through averaging of fuel com- positions at different burnups. Each fuel pebble travels 8 times through 10 axial zones of the reactor until it reaches the final burnup. We assumed that (1) the pebble is exposed to the same neutron flux in each axial zone, (2) each zone is composed of equal fractions of pebbles at different passes (i.e., $1/8$-th of the pebbles are traveling the first time during the reactor, $1/8$-th the second time, etc.), (3) the burnup increases by 22.5 GWd/MTIHM each time a pebble travels through the reactor. Based on these assumptions, a burnup map as displayed in Table A-10 was determined. The average fuel composition of a zone was calculated by averaging the fuel compositions at the burnups indicated for this particular zone. Core-average compositions were determined through averaging the fuel compositions of all zones.

Although this described simplified approach results in only a very rough approximation of fuel compositions during reactor operation, the approach was considered sufficient for the nuclear data assessment studies. The pebbles in the 2D slice model were exposed to representative conditions in the reactor during depletion through a realistic moderator-to-fuel ratio and depleted fuel in adjacent fuel pebbles, and therefore a more realistic neutron flux spectrum environment. The depletion calculations resulted in realistic fuel compositions such that all relevant isotopes in the depleted fuel are included in the model and consequently considered in the nuclear data uncertainty and sensitivity analyses.

Table A-9 PB-FHR-Mk1: Depletion Calculation Iterations Using a Slice Model of the Reactor[3]

i	k_{eff}	$k_i - k_{i-1}$ [pcm]	N_D ^{235}U (atoms/b-cm)	$\frac{N_{D_i}}{N_{D_{i-1}}} - 1$	N_D ^{239}Pu (atoms/b-cm)	$\frac{N_{D_i}}{N_{D_{i-1}}} - 1$
0	1.28646 ± 0.00019	–	1.785e-03	–	0.000E+00	–
1	1.05373 ± 0.00016	-23273	1.054E-03	-40.94%	5.326E-05	–
2	1.01184 ± 0.00019	-4189	9.313E-04	11.64%	5.189E-05	2.56%
3	0.99504 ± 0.00019	-1680	8.873E-04	-4.72%	5.010E-05	3.46%
4	0.98720 ± 0.00019	-784	8.663E-04	-2.37%	4.959E-05	-1.02%
5	0.98290 ± 0.00019	-430	8.564E-04	1.14%	4.871E-05	1.77%
6	0.98107 ± 0.00017	-183	8.513E-04	-0.60%	4.880E-05	0.18%
7	0.97959 ± 0.00019	-148	8.488E-04	-0.29%	4.873E-05	-0.15%
8	0.97971 ± 0.00019	12	8.488E-04	0.00%	4.857E-05	0.32%
9	0.97899 ± 0.00017	-72	8.473E-04	-0.17%	4.847E-05	-0.21%
10	0.97935 ± 0.00017	36	8.470E-04	-0.04%	4.877E-05	0.62%

Table A-10 PB-FHR-Mk1: Fuel Pebble Burnup (GWd/MTIHM) in the Middle of Each Axial Zone Depending on the Pass Through the Core

Axial zone	Pass through the core							
	1	2	3	4	5	6	7	8
10	21.4	43.9	66.4	88.9	111.4	133.9	156.4	178.9
9	19.1	41.6	64.1	86.6	109.1	131.6	154.1	176.6
8	16.9	39.4	61.9	84.4	106.9	129.4	151.9	174.4
7	14.6	37.1	59.6	82.1	104.6	127.1	149.6	172.1
6	12.4	34.9	57.4	79.9	102.4	124.9	147.4	169.9
5	10.1	32.6	55.1	77.6	100.1	122.6	145.1	167.6
4	7.9	30.4	52.9	75.4	97.9	120.4	142.9	165.4
3	5.6	28.1	50.6	73.1	95.6	118.1	140.6	163.1
2	3.4	25.9	48.4	70.9	93.4	115.9	138.4	160.9
1	1.1	23.6	46.1	68.6	91.1	113.6	136.1	158.6

A.2.2 Sampler Uncertainty Analysis

The behavior of the mean values and standard deviations (uncertainties) of each Sampler/ KENO-MG calculation was investigated as a function of the sample size to confirm that a sufficient sample size was used and to rule out any unexpected behavior. Figure A-4 shows this analysis for the axial peak power of the PB-FHR-Mk1. The running mean value already agrees with the final mean value (the mean value after 1,000 samples) after 100 samples and does not

---

[3] For each iteration i, the k_{eff} of the initial neutron transport calculation and the nuclide densities (N_D) as applied in the non-depletable fuel pebbles (from the core-average composition determined from the previous iteration) is displayed.

significantly change with the addition of more samples. The relative uncertainty shows large variations and becomes consistent with the final uncertainty after approximately 600 samples. This is expected, since the relative uncertainty is subject to a statistical uncertainty itself, as indicated through shaded regions in the example plot. For example, the 95% statistical confidence interval of the relative uncertainty is ~5% for a sample size of 1,000, assuming that the output is normally distributed [Bostelmann, 2020].

Interpretation of the *standard deviation* from the 1,000 samples as uncertainty is only valid if the output is normally distributed. Both the Anderson-Darling test and the Shapiro-Wilk test are applied to confirm that the output comes from a normal distribution. Correspondingly, a visual inspection of the probability density function is conducted to confirm the good agreement of the samples with the Gaussian normal distribution based on the final mean value and the standard deviation (see Figure A-5 for the example of the axial power distribution).
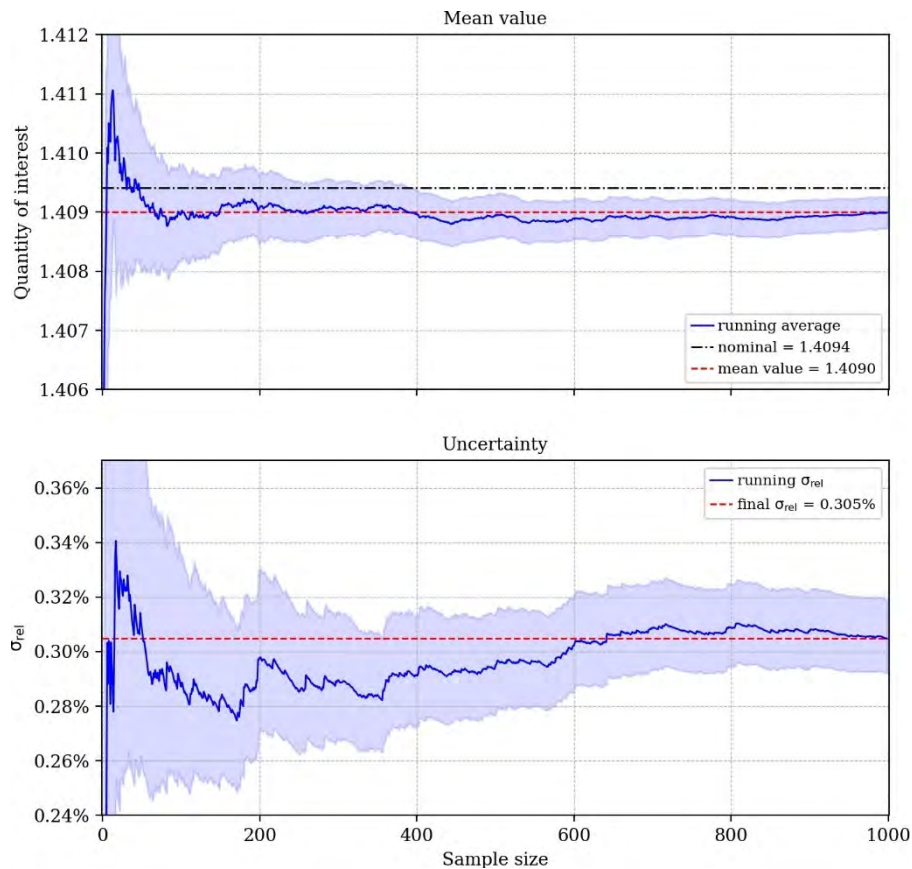
Figure A-4   PB-FHR-Mk1: Development of the Axial Peak Power (Upper Plot) and the Corresponding Relative Uncertainty (lower plot) as a Function of the Sample Size as Determined with Sampler/KENO-MG and ENDF/B-VII.1 Data[4]

---

[4] The shaded regions indicate the corresponding 95% statistical confidence intervals.
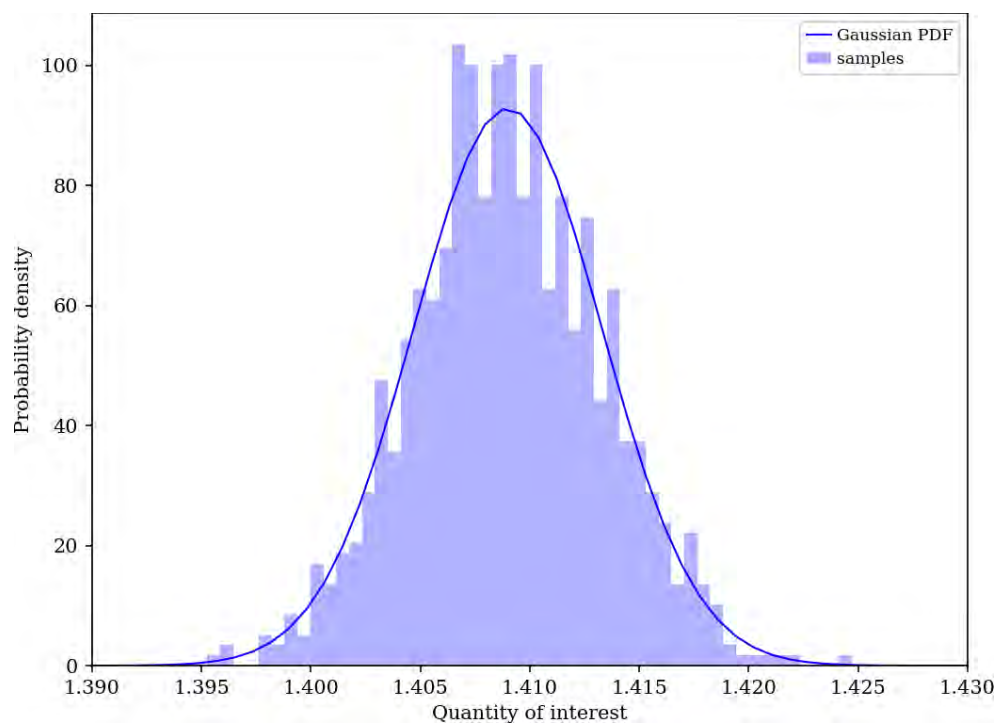
Figure A-5   PB-FHR-Mk1: Distribution of the Axial Peak Power Samples[5]

---

[5] Calculated with Sampler/KENO-MG and ENDF/B-VII.1 data compared to the Gaussian normal distribution using the final mean value and standard deviation.

A.2.3 Comparisons of Contributions to the Calculated Output Uncertainties

While the contributors listed for k_{eff} are the top contributors to the k_{eff} uncertainty, this is not necessarily the case for the reactivity differences. Contributions from nonconverged sensitivities were excluded from these tables.

Table A-11   PB-FHR-Mk1: Top Contributors to the k_{eff} Uncertainty[6]

Nuclide	Reaction	ENDF/B-VII.0	ENDF/B-VII.1	ENDF/B-VIII.0	$\frac{VII.1}{VII.0} - 1$	$\frac{VIII.0}{VII.1} - 1$
Li-7	n,γ	1.218%	1.218%	1.209%	0.0%	-0.8%
U-235	$\bar{\nu}$	0.235%	0.295%	0.362%	25.6%	22.6%
Pu-239	$\bar{\nu}$	0.185%	0.033%	0.056%	-82.1%	70.1%
F-19	n,γ	0.169%	0.169%	0.167%	0.1%	-0.8%
Graphite	el	0.138%	0.142%	0.177%	2.5%	24.9%
Xe-135	n,γ	0.135%	0.135%	0.134%	0.0%	-0.9%
U-238	n,γ	0.132%	0.101%	0.100%	-22.9%	-1.0%
U-235	fis	0.132%	0.131%	0.180%	-0.3%	37.6%
Graphite	n,γ	0.128%	0.128%	0.126%	0.0%	-1.6%
U-235	n,γ	0.110%	0.109%	0.040%	-1.0%	-63.4%
U-235	fis/n,γ	0.109%	0.108%	0.000%	-0.2%	0.0%
Pu-239	n,γ	0.059%	0.060%	0.213%	1.1%	257.0%
Pu-239	fis	0.082%	0.082%	0.212%	0.5%	158.7%
F-19	el	0.102%	0.100%	0.097%	-1.8%	-3.8%
Pu-240	n,γ	0.036%	0.016%	0.061%	-55.1%	276.4%

---

[6] As obtained with TSUNAMI, in Δk/k.

Table A-12   PB-FHR-Mk1: Contributions to the Uncertainty of the Fuel Temperature Reactivity[7]

Nuclide	Reaction	ENDF/B-VII.0	ENDF/B-VII.1	ENDF/B-VIII.0	$\frac{VII.1}{VII.0}-1$	$\frac{VIII.0}{VII.1}-1$
U-238	n,γ	1.642%	1.154%	1.253%	-29.7%	8.6%
Li-7	n,γ	1.261%	1.261%	1.192%	0.0%	-5.4%
F-19	n,n′	0.387%	0.455%	0.479%	17.6%	5.3%
U-238	el/n,γ	0.379%	0.000%	0.277%	0.0%	0.0%
U-238	el	0.370%	0.331%	0.310%	-10.5%	-6.4%
Pu-239	$\bar{\nu}$	0.322%	0.057%	0.094%	-82.2%	63.0%
Pu-240	n,γ	0.251%	0.080%	0.385%	-68.1%	381.1%
U-235	$\bar{\nu}$	0.188%	0.239%	0.304%	26.9%	26.9%
F-19	n,γ	0.175%	0.175%	0.165%	0.1%	-5.5%
Pu-239	fis	0.143%	0.146%	0.362%	2.0%	147.9%
Pu-239	n,γ	0.117%	0.120%	0.394%	2.3%	229.4%

Table A-13   PB-FHR-Mk1 – TSUNAMI Contributions to the Uncertainty of the Salt Temperature Reactivity

Nuclide	Reaction	ENDF/B-VII.0	ENDF/B-VII.1	ENDF/B-VIII.0	$\frac{VII.1}{VII.0}-1$	$\frac{VIII.0}{VII.1}-1$
Pu-239	$\bar{\nu}$	3.378%	0.606%	0.994%	-82.1%	-68.6%
Xe-135	n,γ	2.180%	2.181%	2.059%	0.0%	0.0%
Pu-239	fis	2.116%	2.139%	5.232%	1.1%	160.2%
Pu-239	fis/n,γ	1.987%	2.002%	0.000%	0.8%	0.0%
Pu-239	n,γ	1.584%	1.598%	4.376%	0.9%	192.2%
Li-7	n,γ	1.282%	1.282%	1.130%	0.0%	0.0%
U-235	$\bar{\nu}$	0.799%	0.985%	1.119%	23.2%	52.8%
Eu-155	n,γ	0.160%	1.452%	1.364%	810.4%	810.4%
U-235	fis	0.607%	0.607%	1.400%	-0.0%	145.7%

---

[7] As obtained with TSUNAMI, in ΔR/R, R: response.

Table A-14 PB-FHR-Mk1: TSUNAMI Contributions to the Uncertainty of the Salt Density Reactivity

Nuclide	Reaction	ENDF/B-VII.0	ENDF/B-VII.1	ENDF/B-VIII.0	$\frac{VII.1}{VII.0}-1$	$\frac{VIII.0}{VII.1}-1$
Li-7	n,γ	33.964%	33.964%	33.857%	0.0%	-0.3%
F-19	n,γ	4.698%	4.700%	4.682%	0.0%	-0.4%
Be-9	n,γ	1.249%	1.250%	1.245%	0.1%	-0.4%
U-235	fis	0.751%	0.750%	1.046%	-0.2%	39.5%
Be-9	n,2n	0.715%	0.771%	0.763%	8.0%	-1.0%
U-235	χ	0.712%	1.127%	0.173%	58.2%	-84.7%
F-19	n,α	0.595%	0.612%	0.603%	3.0%	-1.5%
U-238	n,γ	0.578%	0.467%	0.416%	-19.3%	-11.0%
Pu-239	fis	0.312%	0.314%	0.832%	0.5%	165.3%
Pu-239	n,γ	0.203%	0.206%	0.715%	1.1%	248.0%

A.3 MSRE

This section provides tables listing the contributions to the individual investigated output uncertainties obtained with TSUNAMI corresponding to the images provided in Section 5.3. While the contributors listed for k_{eff} are the top contributors to the k_{eff} uncertainty, this is not necessarily the case for the reactivity differences. Contributions from nonconverged sensitivities were excluded from these tables.

Table A-15 MSRE: Top Contributors to the k_{eff} Uncertainty[8]

Nuclide	Reaction	ENDF/B-VII.0	ENDF/B-VII.1	ENDF/B-VIII.0	$\frac{VII.1}{VII.0} - 1$	$\frac{VIII.0}{VII.1} - 1$
U-235	$\bar{\nu}$	0.292%	0.373%	0.458%	27.6%	22.7%
Graphite	el	0.259%	0.264%	0.319%	1.9%	21.0%
Li-7	n,γ	0.207%	0.207%	0.204%	0.0%	-1.7%
U-235	n,γ	0.178%	0.170%	0.063%	-4.4%	-63.1%
Ni-58	n,γ	0.169%	0.106%	0.104%	-37.3%	-1.5%
F-19	el	0.156%	0.152%	0.144%	-2.1%	-5.5%
U-235	χ	0.138%	0.220%	0.034%	59.4%	-84.4%
U-235	fis/ n,γ	0.129%	0.129%	0.000%	-0.3%	0.0%
U-238	n,γ	0.126%	0.093%	0.094%	-26.2%	0.8%
U-235	fis	0.122%	0.121%	0.161%	-0.5%	32.5%
F-19	n,n'	0.099%	0.103%	0.100%	4.5%	-3.4%
Ni-62	n,γ	0.048%	0.099%	0.097%	108.4%	-2.2%
Li-7	el	0.056%	0.056%	0.054%	-0.1%	-3.1%

Table A-16 MSRE: Contributions to the Uncertainty of the CR Worth[9]

Nuclide	Reaction	ENDF/B-VII.0	ENDF/B-VII.1	ENDF/B-VIII.0	$\frac{VII.1}{VII.0} - 1$	$\frac{VIII.0}{VII.1} - 1$
Graphite	el	0.702%	0.720%	1.041%	2.5%	44.6%
Ni-58	n,γ	0.652%	0.315%	0.314%	-51.7%	-0.4%
F-19	el	0.419%	0.406%	0.403%	-3.2%	-0.7%
Gd-155	n,γ	0.276%	0.314%	0.319%	13.8%	1.6%
U-235	$\bar{\nu}$	0.273%	0.359%	0.453%	31.4%	26.4%
U-235	fis	0.232%	0.230%	0.294%	-0.8%	27.7%
Ni-62	n,γ	0.186%	0.446%	0.443%	140.6%	-0.8%
Ni-58	el	0.170%	0.169%	0.183%	-0.1%	8.0%
F-19	n,n'	0.165%	0.194%	0.225%	17.7%	15.8%
U-235	χ	0.163%	0.265%	0.045%	62.4%	-82.9%
Gd-157	n,γ	0.141%	0.237%	0.238%	68.5%	0.4%
Li-7	el	0.150%	0.150%	0.113%	0.0%	-24.4%

---

[8] Obtained with TSUNAMI, in Δk/k.

[9] Obtained with TSUNAMI, in ΔR/R, R: response.

A.4 INL DESIGN A-MET

This section provides tables listing the contributions to the individual investigated output uncertainties obtained with TSUNAMI corresponding to the images provided in Section 5.4.

Table A-17   INL Design A-MET – k$_{eff}$ Uncertainty Contributors

Nuclide	Reaction	ENDF/B-VII.0	ENDF/B-VII.1	ENDF/B-VIII.0	$\frac{VII.1}{VII.0} - 1$	$\frac{VIII.0}{VII.1} - 1$
U-235	n,γ	1.865%	1.915%	0.396%	2.7%	-79.3%
U-238	n,n$'$	0.531%	0.539%	0.076%	1.6%	-85.9%
U-238	el/n,n$'$	0.225%	0.221%	0.000%	-1.8%	0.0%
U-235	fis	0.218%	0.234%	0.625%	7.7%	166.6%
U-235	χ	0.216%	0.354%	0.053%	63.9%	-85.1%
U-238	n,γ	0.205%	0.185%	0.256%	-9.5%	38.3%
U-238	$\bar{\nu}$	0.162%	0.164%	0.168%	1.4%	2.2%
U-235	$\bar{\nu}$	0.130%	0.086%	0.366%	-33.5%	323.9%
Zr-90	el	0.119%	0.027%	0.025%	-77.7%	-6.6%
U-235	el/ n,γ	0.096%	0.106%	0.025%	9.9%	-76.3%
U-238	n,n$'$/el	0.225%	0.221%	0.000%	-1.8%	0.0%
U-238	χ	0.041%	0.137%	0.044%	234.8%	-67.5%
Al-27	el	0.017%	0.088%	0.092%	408.8%	4.4%
U-235/fis	U-238/fis	0.000%	0.064%	0.355%	0.0%	454.8%
U-235	fis/ n,γ	0.011%	0.007%	0.100%	-34.8%	1317.8%
U-238	fis	0.043%	0.043%	0.099%	0.1%	129.5%

Table A-18 INL Design A-MET: Top Contributors to the CD Worth Uncertainty[10]

Nuclide	Reaction	ENDF/B-VII.0	ENDF/B-VII.1	ENDF/B-VIII.0	$\frac{VII.1}{VII.0}-1$	$\frac{VIII.0}{VII.1}-1$
Zr-90	el	1.194%	0.277%	0.291%	-76.8%	4.9%
U-235	n,γ	0.863%	0.629%	0.151%	-27.0%	-76.0%
U-238	n,n′	0.734%	0.757%	1.086%	3.1%	43.5%
U-238	el	0.671%	0.662%	0.757%	-1.3%	14.4%
U-235	χ	0.447%	0.749%	0.117%	67.4%	-84.4%
U-235	fis	0.391%	0.416%	1.000%	6.4%	140.3%
Zr-94	el	0.346%	0.122%	0.125%	-64.6%	2.1%
U-238	$\bar{\nu}$	0.342%	0.346%	0.357%	1.1%	3.1%
U-238	n,γ	0.334%	0.330%	0.264%	-1.0%	-20.1%
U-235	n,n′	0.326%	0.337%	0.112%	3.4%	-66.8%
Fe-56	el	0.312%	1.072%	0.316%	243.9%	-70.5%
U-238	χ	0.144%	0.500%	0.152%	246.8%	-69.7%
U-235/fis	U-238/fis	0.000%	0.150%	0.742%	0.0%	395.7%
U-235	$\bar{\nu}$	0.152%	0.122%	0.495%	-19.4%	305.4%
Cr-52	el	0.238%	0.235%	0.287%	-1.4%	22.0%
U-238	fis	0.123%	0.122%	0.284%	-0.5%	132.8%

Table A-19 INL Design A-MET: Top Contributors to the CR Worth Uncertainty

Nuclide	Reaction	ENDF/B-VII.0	ENDF/B-VII.1	ENDF/B-VIII.0	$\frac{VII.1}{VII.0}-1$	$\frac{VIII.0}{VII.1}-1$
U-238	n,n′	1.316%	1.359%	0.299%	3.2%	-78.0%
U-235	n,γ	0.789%	0.822%	0.116%	4.1%	-85.8%
U-235	χ	0.442%	0.725%	0.112%	63.9%	-84.6%
O-16	elastic	0.346%	0.364%	0.057%	5.2%	-84.3%
U-235	fis	0.326%	0.324%	0.931%	-0.6%	186.9%
U-238	$\bar{\nu}$	0.299%	0.304%	0.312%	1.7%	2.4%
U-238	χ	0.132%	0.430%	0.140%	226.0%	-67.5%
B-10	n,α	0.127%	0.082%	0.088%	-35.4%	8.0%
U-235	$\bar{\nu}$	0.115%	0.070%	0.305%	-39.1%	335.9%
U-234	fis	0.109%	0.089%	0.095%	-18.5%	6.2%
Al-27	el	0.090%	0.517%	0.539%	472.4%	4.1%
Fe-56	n,n′	0.064%	0.136%	0.093%	111.9%	-32.0%
U-235/fis	U-238/fis	0.000%	0.134%	0.689%	0.0%	413.8%
U-238	fis	0.108%	0.109%	0.251%	0.2%	131.4%

---

[10] Obtained with TSUNAMI, in ΔR/R, R: response.

Table A-20   INL Design A-MET: Top Contributors to the Fuel Doppler Uncertainty[11]

Nuclide	Reaction	ENDF/B-VII.0	ENDF/B-VII.1	ENDF/B-VIII.0	$\frac{VII.1}{VII.0}-1$	$\frac{VIII.0}{VII.1}-1$
U-238	n,n′	11.499%	13.407%	1.534%	16.6%	-88.6%
U-238	el	10.485%	10.345%	3.301%	-1.3%	-68.1%
U-235	n,γ	6.461%	2.606%	0.456%	-59.7%	-82.5%
Zr-90	el	5.821%	2.370%	3.658%	-59.3%	-54.4%
Zr-92	el	5.649%	0.341%	2.469%	-94.0%	-623.3%
Fe-56	el	5.315%	8.813%	2.461%	65.8%	-72.1%
U-235	n,n′	4.975%	2.591%	0.671%	-47.9%	-74.1%
Cr-52	el	4.935%	5.558%	3.671%	12.6%	-33.9%
Ni-62	el	3.234%	2.486%	3.107%	-23.2%	25.0%
Zr-94	el	3.121%	2.383%	1.074%	-23.7%	-54.9%
Al-27	el	0.814%	11.121%	1.704%	1266.0%	-84.7%
U-235	el	1.730%	3.102%	1.003%	79.4%	-67.7%
U-235	n,n′/el	0.000%	3.026%	0.000%	0.0%	0.0%
Fe-57	el	2.924%	2.965%	1.516%	1.4%	-48.9%
Ni-58	el	1.775%	2.408%	1.676%	35.7%	-30.4%

Table A-21   INL Design A-MET: Top Contributors to the Radial Expansion Uncertainty

Nuclide	Reaction	ENDF/B-VII.0	ENDF/B-VII.1	ENDF/B-VIII.0	$\frac{VII.1}{VII.0}-1$	$\frac{VIII.0}{VII.1}-1$
U-235	n,γ	1.798%	1.329%	0.256%	-26.1%	-80.7%
U-238	n,n′	1.551%	0.885%	0.795%	-42.9%	-10.2%
Zr-92	el	1.093%	0.092%	0.078%	-91.6%	-14.9%
U-238	el	1.016%	0.445%	0.206%	-56.2%	-53.6%
Fe-56	el	0.683%	0.707%	0.184%	3.6%	-74.0%
U-238	n,γ	0.516%	0.551%	0.360%	6.8%	-34.7%
Zr-90	el	0.458%	0.180%	0.324%	-60.7%	80.0%
Cr-52	el	0.438%	0.979%	0.413%	123.3%	-57.8%
O-16	el	0.425%	0.416%	0.071%	-2.0%	-82.8%
Zr-94	el	0.420%	0.385%	0.061%	-8.2%	-84.3%
U-238	n,n′/el	0.000%	0.765%	0.000%	0.0%	0.0%
Al-27	el	0.229%	0.514%	0.745%	124.5%	44.9%
U-235	fis	0.310%	0.495%	0.800%	59.8%	61.5%
U-238	χ	0.068%	0.441%	0.026%	553.4%	-94.1%
U-235	$\bar{\nu}$	0.170%	0.132%	0.680%	-22.3%	414.7%
U-235/fis	U-238/fis	0.000%	0.090%	0.558%	0.0%	519.6%
Fe-54	el	0.210%	0.184%	0.414%	-12.6%	125.5%
Ni-62	el	0.232%	0.204%	0.414%	-12.3%	103.2%

---

[11] Obtained with TSUNAMI, in ΔR/R, R: response.

Table A-22   INL Design A-MET: Top Contributors to the Axial Expansion Uncertainty[12]

Nuclide	Reaction	ENDF/B-VII.0	ENDF/B-VII.1	ENDF/B-VIII.0	$\frac{VII.1}{VII.0}-1$	$\frac{VIII.0}{VII.1}-1$
U-235	n,γ	1.018%	0.927%	0.146%	-9.0%	-84.2%
U-238	n,n$'$	0.636%	0.757%	0.617%	18.9%	-18.5%
O-16	el	0.323%	0.425%	0.051%	31.4%	-87.9%
Zr-90	el	0.320%	0.165%	0.086%	-48.5%	-47.5%
U-235	fis	0.310%	0.369%	0.890%	19.1%	141.1%
U-238	n,γ	0.244%	0.246%	0.180%	1.1%	-26.8%
Zr-92	el	0.174%	0.046%	0.094%	-73.8%	106.2%
Zr-94	el	0.159%	0.073%	0.017%	-53.7%	-76.4%
U-238	$\bar{\nu}$	0.143%	0.153%	0.140%	7.5%	-8.5%
Fe-56	n,γ	0.135%	0.177%	0.154%	30.8%	-13.0%
Fe-56	el	0.053%	0.718%	0.212%	1245.7%	-70.4%
Al-27	el	0.091%	0.576%	0.505%	531.7%	-12.3%
U-238	el	0.080%	0.328%	0.196%	311.0%	-40.2%
U-235	el/n,γ	0.087%	0.295%	0.021%	237.6%	-92.9%
U-235	χ	0.095%	0.193%	0.041%	103.0%	-78.6%
U-235/fis	U-238/fis	0.000%	0.096%	0.521%	0.0%	440.1%
U-235	$\bar{\nu}$	0.135%	0.091%	0.472%	-32.8%	420.7%
U-238	fis	0.067%	0.070%	0.147%	3.5%	111.2%

---

[12] Obtained with TSUNAMI, in ΔR/R, R: response.

A.5 EBR-II

This section provides tables listing the contributions to the individual investigated output uncertainties obtained with TSUNAMI corresponding to the images provided in Section 5.5.

Table A-23   EBR-II – TSUNAMI Top Contributors to the k_{eff} Uncertainty

Nuclide	Reaction	ENDF/B-VII.0	ENDF/B-VII.1	ENDF/B-VIII.0	$\frac{VII.1}{VII.0} - 1$	$\frac{VIII.0}{VII.1} - 1$
U-235	n,γ	2.036%	2.023%	0.436%	-0.6%	-78.4%
U-235	fis	0.220%	0.226%	0.640%	2.8%	183.1%
Fe-56	el	0.196%	0.510%	0.158%	160.9%	-69.1%
Na-23	el	0.170%	0.306%	0.303%	80.0%	-1.0%
U-235	el/n,γ	0.165%	0.183%	0.042%	10.5%	-77.2%
Cr-52	el	0.143%	0.195%	0.187%	36.3%	-4.2%
U-235	$\bar{\nu}$	0.140%	0.087%	0.398%	-37.8%	358.1%
U-235	n,n'	0.116%	0.116%	0.034%	0.7%	-70.9%
Fe-56	n,γ	0.105%	0.146%	0.112%	39.3%	-23.2%
U-235	χ	0.055%	0.097%	0.016%	76.8%	-84.0%
Ni-58	el	0.033%	0.108%	0.095%	230.8%	-12.4%
U-235/fis	U-238/fis	0.000%	0.036%	0.187%	0.0%	412.7%
U-235	fis/n,γ	0.018%	0.014%	0.124%	-19.6%	761.8%
Fe-54	el	0.050%	0.054%	0.108%	7.0%	101.0%

Table A-24   EBR-II: Top Contributors to the CR Worth Uncertainty[13]

Nuclide	Reaction	ENDF/B-VII.0	ENDF/B-VII.1	ENDF/B-VIII.0	$\frac{VII.1}{VII.0} - 1$	$\frac{VIII.0}{VII.1} - 1$
U-235	n,γ	0.585%	0.329%	0.141%	-43.8%	-57.2%
U-235	fis	0.353%	0.404%	0.946%	14.3%	134.2%
Fe-56	n,γ	0.318%	0.415%	0.262%	30.7%	-36.9%
U-238	n,n'	0.294%	0.262%	0.106%	-11.0%	-59.4%
B-10	n,α	0.290%	0.157%	0.216%	-45.7%	37.6%
U-235	n,n'	0.281%	0.263%	0.091%	-6.5%	-65.5%
Na-23	elastic	0.265%	0.159%	0.160%	-40.0%	0.8%
U-235	$\bar{\nu}$	0.148%	0.111%	0.512%	-25.1%	360.6%
Cr-52	el	0.130%	0.225%	0.155%	73.8%	-31.3%
Fe-56	el	0.115%	0.725%	0.090%	530.5%	-87.6%
U-235	χ	0.100%	0.223%	0.034%	124.2%	-84.8%
Ni-58	el	0.025%	0.201%	0.093%	698.4%	-53.7%
U-235/fis	U-238/fis	0.000%	0.047%	0.278%	0.0%	489.0%
U-235/fis	Pu-239/fis	0.000%	0.045%	0.232%	0.0%	421.3%
Fe-54	el	0.094%	0.088%	0.177%	-6.9%	101.5%

---

[13] Obtained with TSUNAMI, in ΔR/R, R: response.

Table A-25   EBR-II: Top Contributors to the Sodium Void Uncertainty[14]

Nuclide	Reaction	ENDF/B-VII.0	ENDF/B-VII.1	ENDF/B-VIII.0	$\frac{VII.1}{VII.0}-1$	$\frac{VIII.0}{VII.1}-1$
U-235	n,γ	3.205%	2.871%	0.443%	-10.4%	-84.6%
Na-23	el	2.117%	3.750%	3.563%	77.2%	-5.0%
Fe-56	el	0.712%	1.252%	0.594%	75.9%	-52.5%
Na-23	n,n'	0.702%	0.869%	0.828%	23.8%	-4.6%
Cr-52	el	0.634%	0.638%	0.802%	0.7%	25.7%
U-235	X	0.482%	0.789%	0.134%	63.6%	-83.0%
U-235	n,n'	0.450%	0.436%	0.145%	-3.0%	-66.6%
U-235	fis	0.447%	0.481%	1.270%	7.8%	163.8%
Fe-56	n,γ	0.219%	0.284%	0.267%	29.4%	-5.9%
Fe-54	el	0.215%	0.242%	0.497%	12.9%	105.0%
Ni-58	el	0.162%	0.322%	0.444%	99.2%	37.9%
U-235/fis	U-238/fis	0.000%	0.113%	0.518%	0.0%	358.2%
U-235	$\bar{\nu}$	0.179%	0.134%	0.461%	-24.7%	242.6%

---

[14] Obtained with TSUNAMI, in ΔR/R, R: response.

A.6 ABR-1000

This section provides tables listing the contributions to the individual investigated output uncertainties obtained with TSUNAMI corresponding to the images provided in Section 5.6.

Table A-26   ABR1000: Top Contributors to the k_{eff} Uncertainty[15]

Nuclide	Reaction	ENDF/B-VII.0	ENDF/B-VII.1	ENDF/B-VIII.0	$\frac{VII.1}{VII.0} - 1$	$\frac{VIII.0}{VII.1} - 1$
U-238	n,n′	1.006%	1.015%	0.268%	0.9%	-73.6%
Pu-239	$\bar{\nu}$	0.695%	0.058%	0.175%	-91.7%	203.6%
Pu-239	χ	0.279%	0.184%	0.181%	-34.2%	-1.5%
Pu-240	$\bar{\nu}$	0.267%	0.081%	0.088%	-69.6%	7.8%
Pu-238	fis	0.211%	0.010%	0.010%	-95.2%	0.0%
Pu-239	fis	0.194%	0.199%	0.560%	2.8%	181.4%
U-238	n,γ	0.187%	0.172%	0.212%	-7.9%	22.8%
Cm-245	fis	0.183%	0.020%	0.020%	-89.2%	-0.1%
Pu-239	n,γ	0.181%	0.174%	0.166%	-4.1%	-4.3%
Cm-244	fis	0.179%	0.014%	0.017%	-92.1%	17.0%
Na-23	el	0.101%	0.171%	0.182%	70.1%	6.3%
Fe-56	n,n′	0.064%	0.169%	0.113%	164.5%	-33.0%
Fe-56	el	0.038%	0.147%	0.038%	289.7%	-73.9%
U-238	χ	0.046%	0.136%	0.049%	197.4%	-63.6%
U-238	$\bar{\nu}$	0.133%	0.134%	0.136%	1.1%	1.7%
U-238/fis	Pu-239/fis	0.000%	0.053%	0.301%	0.0%	472.2%
Na-23	n,n′	0.104%	0.131%	0.128%	26.9%	-2.7%

---

[15] Obtained with TSUNAMI, in Δk/k.

Table A-27   ABR1000: Top Contributors to the Sodium Density Reactivity Uncertainty[16]

Nuclide	Reaction	ENDF/B-VII.0	ENDF/B-VII.1	ENDF/B-VIII.0	$\frac{VII.1}{VII.0}-1$	$\frac{VIII.0}{VII.1}-1$
U-238	n,n′	5.323%	5.299%	1.807%	-0.5%	-65.9%
Na-23	n,n′	4.197%	5.152%	4.318%	22.7%	-16.2%
Pu-239	$\bar{\nu}$	3.704%	0.436%	0.501%	-88.2%	14.7%
Na-23	el	3.702%	5.853%	5.233%	58.1%	-10.6%
U-238	n,γ	2.710%	2.792%	1.560%	3.0%	-44.1%
Pu-239	n,γ	2.217%	1.930%	2.153%	-12.9%	11.5%
Pu-239	fis	1.307%	1.413%	3.069%	8.1%	117.1%
Pu-240	$\bar{\nu}$	1.039%	0.363%	0.355%	-65.0%	-2.1%
Pu-239	n,n′	0.955%	0.980%	0.912%	2.6%	-6.9%
Pu-238	fis	0.907%	0.052%	0.045%	-94.3%	-13.5%
Fe-56	el	0.871%	3.489%	0.883%	300.4%	-74.7%
Fe-56	n,n′	0.545%	1.702%	0.823%	212.2%	-51.6%
Fe-56	n,γ	0.602%	0.880%	0.714%	46.2%	-18.9%

Table A-28   ABR1000: Top Contributors to the Wrapper Density Reactivity Uncertainty

Nuclide	Reaction	ENDF/B-VII.0	ENDF/B-VII.1	ENDF/B-VIII.0	$\frac{VII.1}{VII.0}-1$	$\frac{VIII.0}{VII.1}-1$
Fe-56	n,n′	10.391%	26.808%	16.659%	158.0%	-37.9%
Fe-56	n,γ	7.285%	10.039%	7.843%	37.8%	-21.9%
U-238	n,n′	6.470%	6.398%	0.893%	-1.1%	-86.0%
Fe-56	el	5.148%	18.635%	4.605%	262.0%	-75.3%
Fe-54	n,γ	1.949%	1.661%	2.059%	-14.8%	24.0%
Cr-52	el	1.707%	2.360%	2.325%	38.3%	-1.5%
Pu-239	$\bar{\nu}$	1.338%	0.153%	0.344%	-88.6%	124.6%
Cr-52	n,n′	1.321%	3.209%	2.874%	143.0%	-10.5%
Cr-52	n,γ	1.031%	0.334%	0.310%	-67.6%	-7.2%
U-238	n,γ	0.920%	0.869%	0.557%	-5.5%	-35.9%
U-238	χ	0.302%	0.941%	0.334%	211.9%	-64.5%
Fe-54	el	0.798%	0.816%	1.748%	2.3%	114.2%
Pu-239	fis	0.517%	0.527%	1.311%	1.9%	148.7%
Fe-54	n,n′	0.559%	0.585%	1.306%	4.8%	123.2%

---

[16] Obtained with TSUNAMI, in ΔR/R, R: response.

Table A-29   ABR1000: Top Contributors to the Cladding Density Reactivity Uncertainty[17]

Nuclide	Reaction	ENDF/B-VII.0	ENDF/B-VII.1	ENDF/B-VIII.0	$\frac{VII.1}{VII.0} - 1$	$\frac{VIII.0}{VII.1} - 1$
U-238	n,n′	5.218%	5.319%	0.654%	1.9%	-87.7%
Fe-56	n,γ	1.234%	1.722%	1.364%	39.6%	-20.8%
Pu-239	$\bar{\nu}$	1.194%	0.133%	0.328%	-88.9%	147.2%
Fe-56	n,n′	1.072%	2.840%	1.836%	164.9%	-35.3%
U-238	n,γ	0.776%	0.733%	0.495%	-5.6%	-32.5%
Pu-239	n,γ	0.580%	0.541%	0.569%	-6.7%	5.2%
Fe-56	el	0.565%	2.356%	0.581%	316.8%	-75.3%
Pu-239	X	0.475%	0.282%	0.273%	-40.7%	-3.1%
Pu-239	fis	0.446%	0.448%	1.192%	0.5%	166.2%
Na-23	n,n′	0.397%	0.363%	0.379%	-8.7%	4.4%
U-238	X	0.254%	0.810%	0.270%	219.2%	-66.6%
Pu-240	n,n′	0.188%	0.365%	0.346%	94.3%	-5.1%
Fe-54	n,γ	0.308%	0.251%	0.353%	-18.3%	40.5%

Table A-30   ABR1000: Top Contributors to the Fuel Density Reactivity Uncertainty

Nuclide	Reaction	ENDF/B-VII.0	ENDF/B-VII.1	ENDF/B-VIII.0	$\frac{VII.1}{VII.0} - 1$	$\frac{VIII.0}{VII.1} - 1$
Pu-239	$\bar{\nu}$	0.636%	0.056%	0.182%	-91.2%	-71.4%
Pu-239	χ	0.296%	0.190%	0.191%	-35.8%	-35.4%
U-238	n,n′	0.279%	0.275%	0.273%	-1.4%	-2.1%
Na-23	n,n′	0.271%	0.263%	0.262%	-3.1%	-3.4%
Pu-238	fis	0.249%	0.011%	0.011%	-95.5%	-95.6%
Pu-239	fis	0.249%	0.262%	0.767%	5.1%	208.0%
U-238	n,γ	0.243%	0.237%	0.157%	-2.6%	-35.4%
Pu-240	$\bar{\nu}$	0.218%	0.054%	0.055%	-75.4%	-74.9%
Cm-244	fis	0.215%	0.017%	0.019%	-92.0%	-91.1%
Fe-56	n,γ	0.193%	0.267%	0.170%	38.2%	-12.1%
Fe-56	n,n′	0.173%	0.353%	0.264%	104.0%	52.4%
Na-23	el	0.121%	0.212%	0.205%	74.8%	69.3%
Fe-56	el	0.073%	0.159%	0.089%	119.4%	23.0%
Pu-239	n,γ	0.189%	0.156%	0.255%	-17.5%	34.9%
U-238/fis	Pu-239/fis	0.000%	0.072%	0.429%	0.0%	0.0%

---

[17] Obtained with TSUNAMI, in ΔR/R, R: response.

Table A-31 ABR1000 – Top Contributors to the Fuel Density and Axial Expansion Reactivity Uncertainty[18]

Nuclide	Reaction	ENDF/B-VII.0	ENDF/B-VII.1	ENDF/B-VIII.0	$\frac{VII.1}{VII.0} - 1$	$\frac{VIII.0}{VII.1} - 1$
Pu-239	$\bar{\nu}$	0.774%	0.085%	0.223%	-89.0%	161.9%
U-238	n,n′	0.641%	1.213%	0.366%	89.2%	-69.8%
U-238	n,γ	0.529%	0.498%	0.310%	-5.9%	-37.6%
Pu-239	n,γ	0.432%	0.363%	0.412%	-16.0%	13.3%
Na-23	n,n′	0.419%	0.335%	0.438%	-20.2%	30.9%
Fe-56	n,γ	0.410%	0.557%	0.370%	35.9%	-33.6%
Pu-239	n,n′	0.360%	0.257%	0.184%	-28.8%	-28.1%
Fe-56	n,n′	0.347%	0.734%	0.498%	111.4%	-32.2%
Pu-239	X	0.303%	0.192%	0.140%	-36.7%	-26.7%
Pu-239	fis	0.301%	0.315%	0.924%	4.8%	193.0%
Fe-56	el	0.171%	0.490%	0.178%	187.0%	-63.6%
Na-23	el	0.250%	0.288%	0.400%	15.0%	39.2%
U-238/fis	Pu-239/fis	0.000%	0.050%	0.320%	0.0%	542.7%

Table A-32   ABR1000: Top Contributors to the Grid Expansion Reactivity Uncertainty

Nuclide	Reaction	ENDF/B-VII.0	ENDF/B-VII.1	ENDF/B-VIII.0	$\frac{VII.1}{VII.0} - 1$	$\frac{VIII.0}{VII.1} - 1$
Pu-239	$\bar{\nu}$	0.660%	0.071%	0.181%	-89.3%	156.0%
U-238	n,n′	0.487%	0.412%	0.560%	-15.2%	35.7%
U-238	n,γ	0.404%	0.415%	0.282%	2.6%	-32.0%
Pu-239	X	0.367%	0.239%	0.244%	-34.8%	2.1%
Pu-239	n,γ	0.335%	0.277%	0.504%	-17.5%	82.1%
Pu-239	fis	0.282%	0.305%	0.900%	7.9%	195.3%
Pu-239	n,n′	0.263%	0.237%	0.263%	-10.1%	11.0%
Na-23	n,n′	0.252%	0.235%	0.279%	-6.6%	18.6%
Fe-56	n,γ	0.212%	0.265%	0.122%	24.8%	-54.0%
Pu-238	fis	0.203%	0.008%	0.008%	-95.9%	-1.0%
Na-23	el	0.188%	0.260%	0.256%	38.3%	-1.3%
Fe-56	n,n′	0.132%	0.243%	0.223%	84.1%	-8.0%
U-238/fis	Pu-239/fis	0.000%	0.067%	0.438%	0.0%	550.9%

---

[18] Obtained with TSUNAMI, in ΔR/R, R: response.

Table A-33   ABR1000: Top Contributors to the CR Worth (5 cm Insertion) Uncertainty[19]

Nuclide	Reaction	ENDF/B-VII.0	ENDF/B-VII.1	ENDF/B-VIII.0	$\frac{VII.1}{VII.0}-1$	$\frac{VIII.0}{VII.1}-1$
U-238	n,n′	2.708%	2.164%	0.348%	-20.1%	-83.9%
Pu-239	$\bar{\nu}$	0.878%	0.072%	0.144%	-91.8%	99.0%
Pu-239	χ	0.662%	0.397%	0.393%	-40.1%	-0.9%
Pu-238	fis	0.512%	0.022%	0.021%	-95.8%	-1.8%
Pu-240	$\bar{\nu}$	0.457%	0.120%	0.129%	-73.8%	7.6%
Cm-244	fis	0.445%	0.035%	0.039%	-92.2%	13.3%
U-238	n,γ	0.386%	0.396%	0.242%	2.5%	-38.9%
Pu-239	fis	0.332%	0.349%	0.920%	5.3%	163.4%
Cm-245	fis	0.289%	0.018%	0.018%	-93.7%	-1.0%
Pu-239	n,γ	0.286%	0.258%	0.328%	-9.7%	27.1%
U-238	χ	0.169%	0.445%	0.162%	163.8%	-63.6%
Pu-240	χ	0.135%	0.420%	0.402%	210.9%	-4.4%
Na-23	el	0.274%	0.310%	0.491%	13.2%	58.6%
Fe-56	n,n′	0.165%	0.271%	0.203%	64.6%	-25.0%
U-238	$\bar{\nu}$	0.253%	0.246%	0.253%	-2.6%	2.6%
U-238/fis	Pu=239/fis	0.000%	0.108%	0.514%	0.0%	377.4%
Pu-241	χ	0.062%	0.225%	0.222%	266.3%	-1.7%

Table A-34   ABR1000: Top Contributors to the CR Worth (Full Insertion) Uncertainty

Nuclide	Reaction	ENDF/B-VII.0	ENDF/B-VII.1	ENDF/B-VIII.0	$\frac{VII.1}{VII.0}-1$	$\frac{VIII.0}{VII.1}-1$
U-238	n,n′	2.294%	2.303%	0.312%	0.4%	-86.5%
Pu-239	$\bar{\nu}$	0.689%	0.048%	0.137%	-93.0%	184.5%
Pu-239	χ	0.606%	0.407%	0.399%	-32.8%	-1.8%
Pu-238	fis	0.475%	0.019%	0.019%	-95.9%	-0.4%
Pu-240	$\bar{\nu}$	0.415%	0.090%	0.097%	-78.4%	7.6%
Cm-244	fis	0.393%	0.031%	0.035%	-92.0%	12.8%
B-10	n,α	0.290%	0.164%	0.217%	-43.5%	32.2%
Pu-239	fis	0.255%	0.262%	0.693%	2.7%	164.6%
U-238	n,γ	0.248%	0.239%	0.213%	-3.7%	-10.9%
U-238	$\bar{\nu}$	0.228%	0.230%	0.234%	1.0%	1.5%
Fe-56	n,n′	0.182%	0.498%	0.312%	173.1%	-37.3%
U-238	χ	0.153%	0.449%	0.164%	193.0%	-63.5%
Pu-240	χ	0.124%	0.423%	0.421%	240.9%	-0.6%
Pu-241	χ	0.059%	0.242%	0.236%	307.3%	-2.3%
Pu-240	n,n′	0.076%	0.212%	0.205%	180.7%	-3.1%
U-238/fis	Pu-239/fis	0.000%	0.100%	0.497%	0.0%	398.5%

---

[19] Obtained with TSUNAMI, in ΔR/R, R: response.

Table A-35   ABR1000: Top Contributors to the Delayed Neutron Fraction Uncertainty[20]

Nuclide	Reaction	ENDF/B-VII.0	ENDF/B-VII.1	ENDF/B-VIII.0	$\frac{VII.1}{VII.0}-1$	$\frac{VIII.0}{VII.1}-1$
U-238	n,n′	1.139%	1.478%	0.226%	29.7%	-84.7%
Pu-239	$\bar{\nu}$	0.684%	0.057%	0.174%	-91.7%	206.6%
Pu-238	fis	0.293%	0.013%	0.013%	-95.5%	-0.9%
Pu-240	$\bar{\nu}$	0.270%	0.082%	0.088%	-69.5%	7.5%
Pu-239	fis	0.239%	0.249%	0.714%	4.2%	187.0%
Cm-244	fis	0.239%	0.019%	0.021%	-92.0%	10.6%
Cm-245	fis	0.214%	0.022%	0.023%	-89.5%	2.7%
U-238	$\bar{\nu}$	0.137%	0.134%	0.137%	-2.1%	2.3%
Na-23	n,n′	0.121%	0.108%	0.085%	-11.3%	-20.8%
Pu-239	n,n′	0.103%	0.083%	0.078%	-19.1%	-6.7%
Fe-56	n,n′	0.093%	0.214%	0.152%	129.4%	-29.1%
Fe-56	el	0.062%	0.176%	0.024%	183.4%	-86.1%
Pu-239	χ	0.093%	0.132%	0.162%	41.8%	22.6%
Pu-240	n,n′	0.046%	0.104%	0.099%	124.8%	-5.3%
Pu-240	χ	0.011%	0.094%	0.102%	717.5%	9.2%
Na-23	el	0.081%	0.091%	0.158%	11.9%	74.2%
U-238/fis	Pu-239/fis	0.000%	0.080%	0.458%	0.0%	469.9%
U-238	fis	0.064%	0.063%	0.146%	-1.3%	131.7%

Table A-36   ABR1000: Top Contributors to the Fuel Temperature Reactivity Uncertainty

Nuclide	Reaction	ENDF/B-VII.0	ENDF/B-VII.1	ENDF/B-VIII.0	$\frac{VII.1}{VII.0}-1$	$\frac{VIII.0}{VII.1}-1$
U-238	n,n′	4.033%	4.085%	2.024%	1.3%	-50.5%
Na-23	el	1.558%	2.549%	2.892%	63.5%	13.5%
Pu-239	$\bar{\nu}$	1.236%	0.145%	0.193%	-88.3%	32.7%
Pu-239	n,γ	1.187%	0.961%	1.536%	-19.0%	59.9%
Pu-239	n,n′	0.898%	0.975%	1.047%	8.5%	7.4%
Pu-239	χ	0.760%	0.555%	0.534%	-27.0%	-3.8%
Pu-239	fis	0.568%	0.598%	1.739%	5.3%	190.7%
Pu-238	fis	0.551%	0.027%	0.028%	-95.0%	1.2%
Pu-240	$\bar{\nu}$	0.528%	0.165%	0.181%	-68.6%	9.4%
Cm-244	fis	0.463%	0.037%	0.042%	-92.0%	11.8%
Fe-56	el	0.342%	1.024%	0.283%	199.5%	-72.4%
Fe-56	n,n′	0.224%	0.758%	0.466%	238.7%	-38.6%
Pu-240	χ	0.151%	0.574%	0.560%	280.3%	-2.4%
U-238	χ	0.192%	0.527%	0.211%	174.5%	-59.9%
U-238/fis	Pu-239/fis	0.000%	0.130%	0.684%	0.0%	427.6%
Fe-54	el	0.270%	0.330%	0.669%	22.2%	103.1%
U-238	el	0.382%	0.418%	0.540%	9.6%	29.1%

---

[20] Obtained with TSUNAMI, in ΔR/R, R: response.

Table A-37   ABR1000: Top Contributors to the Sodium Void Worth Uncertainty[21]

Nuclide	Reaction	ENDF/B-VII.0	ENDF/B-VII.1	ENDF/B-VIII.0	$\frac{VII.1}{VII.0} - 1$	$\frac{VIII.0}{VII.1} - 1$
Na-23	n,n′	6.455%	8.165%	7.276%	26.5%	-10.9%
U-238	n,n′	6.379%	6.236%	2.107%	-2.2%	-66.2%
Na-23	el	5.876%	9.814%	9.611%	67.0%	-2.1%
Pu-239	$\bar{\nu}$	4.846%	0.609%	0.701%	-87.4%	15.1%
U-238	n,γ	3.325%	3.521%	2.087%	5.9%	-40.7%
Pu-239	n,γ	2.756%	2.309%	2.581%	-16.2%	11.8%
Pu-240	$\bar{\nu}$	1.679%	0.490%	0.515%	-70.8%	5.1%
Pu-239	fis	1.637%	1.783%	3.668%	8.9%	105.8%
Cm-244	fis	1.450%	0.120%	0.127%	-91.7%	5.9%
Pu-238	fis	1.362%	0.082%	0.077%	-94.0%	-6.7%
Fe-56	el	0.861%	3.432%	0.929%	298.7%	-72.9%
Fe-56	n,n′	0.580%	1.621%	1.044%	179.3%	-35.6%
Pu-239	n,n′	1.345%	1.406%	1.177%	4.5%	-16.3%
Pu-240	χ	0.323%	0.933%	0.793%	188.9%	-15.1%
Pu-240	n,n'	0.200%	0.931%	0.798%	364.5%	-14.3%

---

[21] Obtained with TSUNAMI, in ΔR/R, R: response.

2. TITLE AND SUBTITLE

Nuclear Data Assessment for Advanced Reactors

3. DATE REPORT PUBLISHED

MONTH	YEAR
March	2022

4. FIN OR GRANT NUMBER

5. AUTHOR(S)

Friederike Bostelmann , Germina Ilas, Cihangir Celik, Andrew M. Holcomb, William A. Wieselquist

6. TYPE OF REPORT

Technical

7. PERIOD COVERED (Inclusive Dates)

8. PERFORMING ORGANIZATION - NAME AND ADDRESS (If NRC, provide Division, Office or Region, U. S. Nuclear Regulatory Commission, and mailing address; if contractor, provide name and mailing address.)

Oak Ridge National Laboratory
Oak Ridge, TN 37831-6283

9. SPONSORING ORGANIZATION - NAME AND ADDRESS (If NRC, type "Same as above", if contractor, provide NRC Division, Office or Region, U. S. Nuclear Regulatory Commission, and mailing address.)

Division of Advanced Reactors and Non-power Production and Utilization Facilities
Office of Nuclear Reactor Regulation
U.S. Nuclear Regulatory Commission
Washington, D.C. 20555-0001

10. SUPPLEMENTARY NOTES

Timothy J Drzewiecki

11. ABSTRACT (200 words or less)

This report identifies key nuclear data that impact the reactor physics and nuclear design of advanced reactors and assesses the data and data gaps for impact on key quantities of interest (e.g., reactivity balance, reactivity coefficients, shutdown margin). An initial assessment is performed based on available literature. This assessment is then enhanced through sensitivity and uncertainty analyses of selected benchmarks to identify and rank the most significant nuclear data contributors to quantifies of interest and their calculated uncertainty. In general, the most important reactions of relevance for reactivity analyses have been found to be the neutron multiplicity ($\bar{\nu}$), fission, the (n,g) reaction of the fissile nuclides of the fuel, and the (n,g) reaction of the fertile nuclides of the fuel. Depending on the spectral conditions and fuel composition, these nuclides are several U and Pu isotopes. In the case of depleted fuel, the neutron capture reactions of relevant fission products are important. Depending on the reactivity control mechanism, neutron capture reactions, including (n,g) and (n,α) of the absorbing material (e.g., Gd or B isotopes), are important. In the case of lighter nuclides with large abundance in the reactor due to their use as moderators, coolants or structural materials, the scattering reactions and (n,g) reactions are relevant. For molten salt reactors additional neutron capture reactions such as (n,p) and (n,t) for components of the salt (e.g., Li and Cl) are important.

12. KEY WORDS/DESCRIPTORS (List words or phrases that will assist researchers in locating the report.)

Nuclear design, nuclear data, reactor physics, advanced reactors

13. AVAILABILITY STATEMENT
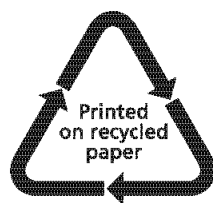
unlimited

14. SECURITY CLASSIFICATION

(This Page)

unclassified

(This Report)

unclassified

15. NUMBER OF PAGES

16. PRICE

UNITED STATES
NUCLEAR REGULATORY COMMISSION
WASHINGTON, DC 20555-0001

OFFICIAL BUSINESS

f

@NRCgov

You Tube

● ●

in